Consolidation Analysis of Sri Lankan Peaty Clay using Elasto-viscoplastic Theory

June 2007

Wanigavitharana Asiri Karunawardena

Abstract

The consolidation of peat is complex due to the resultant large strain associated with the highly compressible nature of natural peat deposits and to the rapid changes in soil properties during the consolidation process. In addition, the consolidation process is further complicated by the occurrence of secondary compression which significantly contributes to the overall settlement of peaty soil. Therefore, it is necessary to take these properties into account in order to obtain better predictions from peat consolidation analyses. In the present study, the consolidation behavior of peaty clay found in Sri Lanka is extensively studied using a model based on the elasto-viscoplastic theory. The model can describe the prominent creep behavior of peaty soil as a continuous process. In addition, the model can accommodate the effect of structural degradation on the consolidation process. The analysis takes into account all the main features involved in the peat consolidation process, namely, finite strain, variable permeability, and the effect of secondary compression. Also, it considers the variable compressibility for stage-constructed embankments which exert high levels of pressure on the peaty subsoil.

The constitutive equations used in the model and the procedure adapted to account for the above-mentioned features of the analysis are described. The constitutive model is based on Perzyna's type viscoplastic theory and the Cambridge elasto-plastic theory combined with empirical evidence. In the finite element formulations, which are based on the finite deformation theory, an updated Lagrangian method is adopted. A description of the material parameters used in the model and the procedures applied to evaluate them, with standard laboratory and field tests, are explained. In addition, a performance of the model incorporating the original and the modified Cam-clay theory is evaluated by simulating triaxial test results. A comparison shows that with the present definition of the parameters, the original model yields more representative results than the model based on the modified Cam-clay theory.

Initially, the capability of the constitutive model to capture the consolidation behavior is verified using the consolidation model test data on peaty clay found in Sri Lanka. It is confirmed that the constitutive model is able to predict the observed creep characteristics and the effect of sample thickness on settlement predictions for the material under consideration.

The performance of the model in predicting the consolidation behavior under field conditions is studied using field data on instrumented earth fill constructed on peaty clay. One-dimensional compression is assumed for the peaty clay due to the large plane area of the fill. Separate analyses are carried out by the model considering the infinitesimal strain theory, the finite strain theory, and the finite strain theory together with the effect of structural degradation in order to explore how these features describe the observed field

behavior. Analyses reveal that it is necessary to consider finite deformation together with the effect of structural degradation in order to successfully simulate the resultant large strain and the stagnated pore water pressure observed in the field.

The construction of road embankments over peat deposits is quite problematic, and thus, it is often done after first improving the properties of the peaty soil through the utilization of appropriate ground-improvement techniques. Understanding the field response of peaty clay during this improvement process is naturally of great importance. A constitutive model is applied to predict the field performance of embankments constructed on peaty clay using different ground-improvement techniques. The back analysis of embankments constructed with the preloading method indicates that the model can be successfully applied to predict both the deformation and the stability of structures constructed on peaty clays. The stability of the embankment during and after construction is verified by investigating the stress-strain characteristics of the subsoil.

The model applications used to predict the consolidation behavior of embankments constructed by the preloading method, combined with other ground-improvement techniques, are then discussed. Embankments constructed with prefabricated vertical drains (PVDs) and sand compaction piles (SCPs) are considered, and finite element analyses are carried out in all cases by converting the actual three-dimensional conditions that exist around the drains into simplified two-dimensional plane strain conditions. The field behavior when PVDs are installed in the peaty clay is simulated using the equivalent vertical permeability for the PVD-improved subsoil. In the case of SCPs, a conversion scheme is used to transform the axisymmetric nature of sand columns into equivalent plane strain conditions. A comparison of the predicted results with the field observations shows a reasonable agreement. An analysis of the PVD-improved foundation indicates that the installation of PVDs not only accelerates the rate of consolidation, but influences the deformation pattern of the subsoil due to embankment loading. The analysis also shows that the use of PVDs can significantly increase embankment stability. The model prediction for the SCP-improved foundation reveals that the stiffness and the area replacement ratio used in the conversion scheme play vital roles in predicting the behavior of SCP-improved soft grounds. The observed improvements in the bearing capacity of the subsoil and in the stability of the embankment, brought about by the installation of SCPs, can be simulated by the model.

Acknowledgements

The research described in this thesis was carried out at the Graduate School of Engineering, Kyoto University, Japan. I wish to express my profound gratitude to the members of the Dissertation Committee, namely, Professor Fusao Oka, Professor Takeshi Tamura, and Associate Professor Sayuri Kimoto, for their discussions, invaluable comments, and constructive suggestions in reviewing this work.

I am extremely grateful to my academic advisor, Professor Fusao Oka, for his enthusiastic guidance and his invaluable help and encouragement in all aspects of this research work. The numerous comments, criticisms, and suggestions he made, based on his deep insight and vast experience in the field of geotechnical engineering, contributed greatly to the success of this work. Also, I am deeply indebted to him for giving me the opportunity to follow the International Doctoral Program in Engineering organized by the Graduate School of Engineering, Kyoto University. I am sure that the confidence I gained being a student of Professor Oka will be a vital asset as I take my career to the next level.

I also owe many thanks to Associate Professor Sayuri Kimoto for her valuable suggestions, constant motivation, and constructive discussions during my doctoral research. Her continuous and ever-present support contributed significantly to my understanding of the constitutive model as well as to the outcome of this research work.

I would like to extend my thanks to Dr. Yosuke Higo, Research Associate in Geomechanics at the Graduate School of Engineering, for his kind help on various occasions. Also, the guidance and the advice on laboratory testing given by Associate Professor Takeshi Kodaka, now at Meji University, Japan is gratefully acknowledged.

I offer my sincere thanks to the all the students who graduated during my period of study. Among them, Dr. Boonlert Siribumrungwong, Dr. Md Rezaul Karim, Mr. Ryosuke Kato, Mr. Hirotaka Suzuki, and Mr. Ryota Asai deserve special recognition. The support given by Mr. Naoaki Takada, who now works for Japan Railways, and Mr. Hideki Kitahara, who now works for Kajima Corporation is highly appreciated and will never be forgotten.

Thanks are also due to Ms Chikako Itou, Secretary of Oka Laboratory, who has been so kind in assisting me with all the official formalities during the research period. I would like to thank all of my friends who are current members of the Oka Laboratory and have helped me in one way or another, including doctor course students Feng Huaiping, Nguen Huy Quoc, and master course students, Tinet Anne-Julie, Mai Sawada , Shinya Yamazaki, Tomohiko Fushita, Hirofumi Ohta , Junya Fukutani and Anna Paula Heitior, who all deserve to be mentioned.

The research presented in this dissertation was financially supported by the MONBUSHO Scholarship Program, provided by the Ministry of Education, Science and Culture, Government of Japan. This program deserves special acknowledgement.

I wish to express my deepest appreciation and gratitude to my supervisor in the Master Degree Program, Dr. S.A.S. Kulathilaka, Senior Lecturer, University of Moratuwa, Sri Lanka, for making arrangements to provide the relevant field and laboratory data used in this research work. Also, I am grateful to the Road Development Authority, University of Moratuwa and the National Building Research Organization of Sri Lanka for providing the necessary data for this research work.

I wish to express my gratitude to the Director General of the National Building Research Organization (NBRO) for granting me a study leave for this research work. The support and the encouragement given by Mr. D.L.C. Welikala, former Director of the Geotechnical Engineering Division of NBRO is highly acknowledged. Special thanks are due to all staff members at NBRO, including Mrs. Karuna De Silva, Mrs. Gayani Samaradiwakara, Mrs.Prashanthi Dissanayake, and Ms Sriyani Munashinghe.

Many thanks go to my friends in Sri Lanka for helping me in various ways to achieve this goal. A special note of sincere appreciation is also extended to Mr. Kishan Sugathapala and his family for their continuing support and good wishes.

I would like to thank all my Sri Lankan friends studying at Kyoto University for their help in many ways. I would also like to extend a huge thank you to Ms. Ryuko Yamaoka and her family, of Ibaraki City, Osaka, for making me feel at home during my stay in Japan.

I offer my heart-felt gratitude to my late father who passed away five months before I started this study program. I am sure that his principles and teachings contributed a great deal to the person I have become. I am indebted to my two brothers and their wives, namely, Sampath and Lali, and Dumindu and Nirosha, for their ever-loving support, patience, and encouragement during this work. Finally, I dedicate this dissertation to my dearest mother who has always inspired me to challenge myself. Her constant love, trust, understanding, and encouragement follow me everywhere.

Table of Contents

List of Figures

List of Tables

Chapter 1

INTRODUCTION

1.1 Background and Objectives

Soft compressible amorphous peat deposits can be found in many places around the country of Sri Lanka, including the capital city of Colombo and its suburbs. The process of urbanization, along with an increasing population and developments associated with this increase, has created the need to utilize these areas for new housing developments, industrial sites, and embankments for roads and highways. However, construction over peaty deposits always creates special problems due to the poor engineering properties of peaty soil. Excessive settlements comprise the major problem associated with the highly compressible nature of peat soil. These settlements appear quickly and may continue for a long period of time due to the dominant creep behavior. In addition, low shear strength often causes stability problems in peat soils when they are subjected to external loading. Therefore, in order to prevent differential settlements and subsequent potential failures, it is necessary to improve the strength and the stiffness properties of natural peat deposits using appropriate ground-improvement techniques. In this process, it is important to understand and to quantify the consolidation response of peaty soils when employing such techniques and to predict the long-term settlements of the structures supported by these soils.

Many research works have been extensively conducted to investigate the consolidation behavior of peaty soils through the use of both empirical and experimental methods in the field and under laboratory conditions. An important conclusion which emerges from these studies is that secondary compression, rapid changes in permeability, and the resultant large strain have a significant influence on the consolidation analysis of peaty soil. The studies also reveal that the composition of natural peat deposits may vary considerably among different sites, as do their mechanical properties (Berry and Poskitt 1972).

Therefore, it is necessary to identify the type of peat under consideration, since the resulting consolidation behavior may be region-specific.

Very little research has been done on this subject, and the research that has been done indicates that the consolidation behavior of the peaty clay found in Sri Lanka could not be satisfactorily modeled by the conventional theory, the Barden model, the Bjerrun model, or the model based on the modified Cam-clay theory. Munasinghe (2001) performed consolidation tests with pore pressure measurements and attempted to model the observed consolidation behavior of peaty clay using Terzaghi's one-dimensional model. As expected, the observed settlement which continued after the full dissipation of excess pore pressure could not be predicted. The application of the Barden model and the Bjerrun model to the same research has shown only limited success.

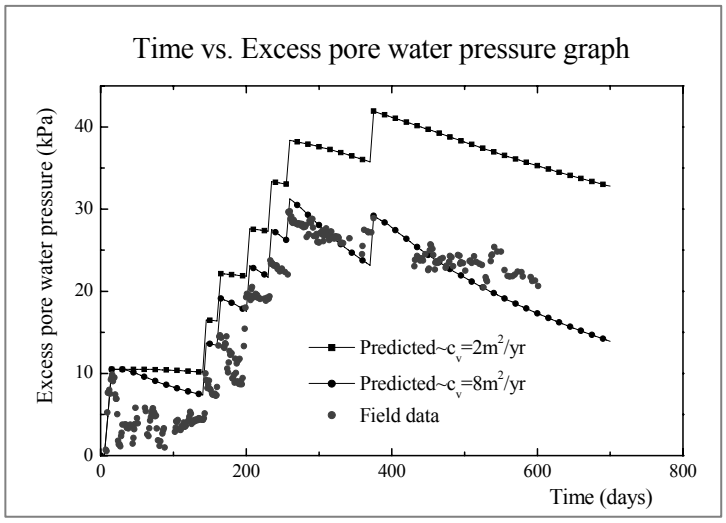

Fig. 1.1: Prediction of excess pore water pressure using Terzaghi's model (Karunawardena 2002)

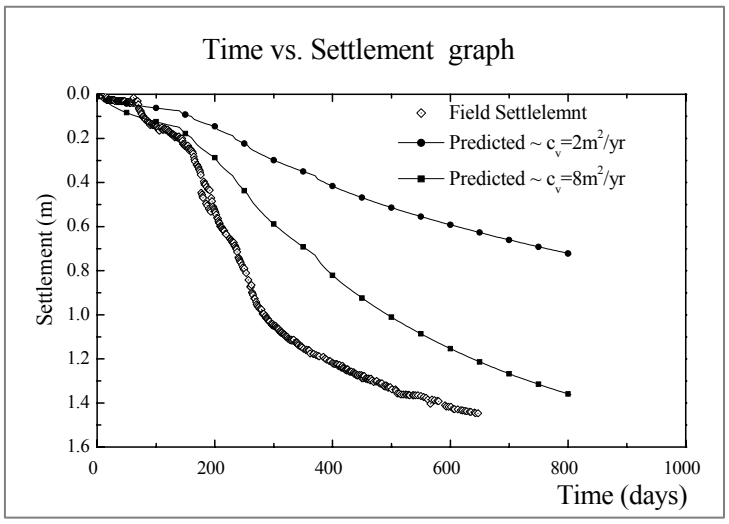

Fig. 1.2: Prediction of settlements using Terzaghi's model (Karunawardena 2002)

Karunawardena (2002), Karunawardena and Kulathilaka (2003) attempted to model the consolidation behavior in the field by back analyzing instrumented earth fill constructed on peaty clay using the model based on Terzaghi's one-dimensional consolidation theory. The predicted and the observed pore water pressure development/dissipation and the settlements of the peaty clay due to the gradual placement of the fill are shown in Figs. 1.1 and 1.2, respectively.

The results indicate that neither the observed excess pore water pressure nor the settlements could be satisfactorily modeled. After reviewing these results, Chew and Ng (2003) commented that the discrepancies were due to the fact that Terzaghi's model does not take into account either the finite strain (a field settlement of 1.5 m was recorded) or the secondary compression which might have taken place simultaneously with the primary consolidation during preloading. There may also be other reasons for the adverse effects on the results, such as the application of constant permeability throughout the process. The effects have been investigated by plotting the coefficient of consolidation, c_v, against the consolidation pressure applied during the consolidation tests. An extreme variation in c_v with the applied pressure has been observed, as indicated in Fig. 1.3. It is primarily due to the drastic changes in the coefficient of permeability, k, with physical reduction of void ratio during the consolidation process. Similar results have been reported by Lea (1958), Forrest and MacFarlane (1969), etc.

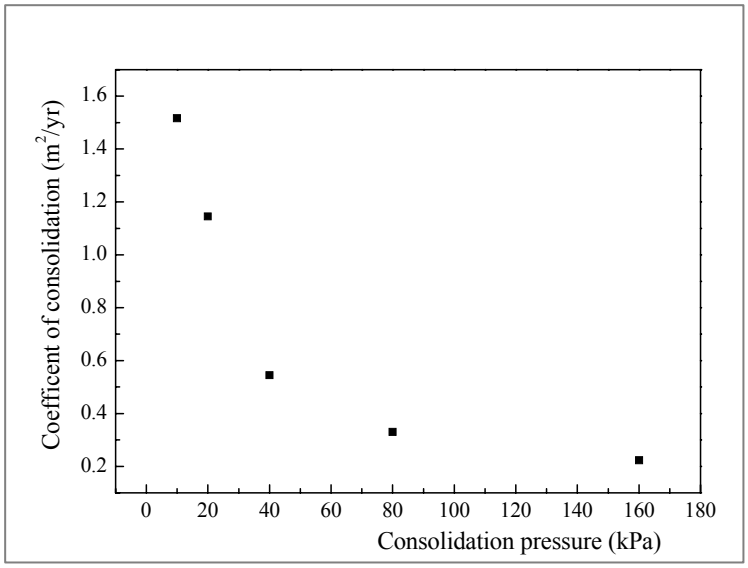

Fig. 1.3: Variation in coefficient consolidation during the consolidation process

Ketheeswaravenayagam (2006) modeled the field performance of embankments constructed on Sri Lankan peaty clay using a model based on the modified Cam-clay theory. The model is based on the infinitesimal strain theory and does not consider the

secondary compression behavior; therefore, it has shown only limited success. The outcome of the above research works indicates the profound necessity for employing a model which can describe the consolidation behavior of the peaty clay found in Sri Lanka.

The approach to the consolidation process for amorphous granular peat has generally been similar to that for clays which exhibit exceptionally large secondary compression effects (Forrest and MacFarlane 1969; Berry and Poskitt 1972). Mesri (1997) proposed a method based on the C_α / C_c concept to predict the consolation behavior of peat and organic soils. Vermeer and Neher (1999) proposed a soft soil model that can account for creep using the logarithmic creep law for the secondary compression and incorporating the concepts of the modified Cam-clay theory and viscoplasticity. However, the above approaches are based on the two-stage concept of consolidation, one terminating at a clearly defined point and the other continuing for a long period of time, leaving something to be desired with reference to peats. The point at which the primary consolidation ends and the secondary compression begins is obscure. Therefore, the application of the above approaches has produced limited success for peats.

Nowadays, it is generally accepted that creep takes place during consolidation and at a constant effective stress. In particular, for materials like peat, which show prominent creep characteristics and a relatively short primary consolidation period during the consolidation process, the assumption of creep as a continuous process provides a more realistic approach to consolidation predictions. Several constitutive models which can consider the creep behavior brought about by viscosity during the primary consolidation (during excess pore water pressure dissipation) were developed in the past (e.g., Adachi and Oka 1982; Katona 1984; Yin and Graham 1989; Kaliakin and Dafalias 1990). Each model has its own features and has shown potential for describing particular types of behavior. Subsequently, Kimoto and Oka (2005) proposed an elasto-viscoplastic model which can consider not only the time-dependent properties of soil, but also the degradation of the microstructure induced by the applied loads.

The main objective of this study is to analyze the consolidation behavior of the amorphous granular type of peaty soil found in Sri Lanka by considering all the main features involved in the process of peat consolidation, namely, secondary compression, finite strain, and changes in permeability and compressibility. In addition to the above features, the effect of structural degradation on the peat consolidation process is investigated. Analyses are conducted using the elasto-viscoplastic model proposed by Oka and Kimoto (2005). The model can describe the secondary compression behavior as a continuous process and it can also account for the effect of structural degradation on the consolidation analysis. Finite element analyses are carried out based on the finite

deformation theory, and the permeability is varied with the void ratio during the analyses. Initially, the applied constitutive model and the analysis methods to simulate the peat consolidation process are validated against the laboratory consolidation test results. Then, the model is applied to predict the consolidation behavior of peaty clay under different field conditions. In this context, firstly, the one-dimensional field consolidation of peaty clay, brought about by the construction of compacted earth fill, is predicted. Then, the peat foundation response upon embankment loading is simulated. The foundation behavior of embankments constructed on natural peaty clay as well as peaty clay which has been improved by different ground-improvement techniques are simulated. In addition, the capability of the model to evaluate the stability of the embankments is investigated by studying the soil behavior in different regions of the foundations and using an observational method.

1.2 Organization of the Dissertation

The introductory chapter, Chapter 1, highlights the importance of this research work. Chapter 2 is devoted to describing the general features of peaty soil. Initially, the physical and the mechanical properties of peat found around the world are explained. Then, the properties of the peaty soil found in Sri Lanka, on which the present study is based, are presented together with some observed correlations.

Chapter 3 presents the elasto-viscoplastic model (Kimoto and Oka 2005) which is extensively used in the present research work. The analysis methods and the model features which are relevant to the peat consolidation analysis are highlighted. A description of the material parameters used in the model and the procedures applied to evaluate them, with standard laboratory and field tests, are explained. Also, the performance of the model in incorporating the modified Cam-clay theory is investigated.

The model validation which was conducted using consolidation model test data is presented in Chapter 4. The settlements monitored in consolidation tests, by maintaining the final load for a long period of time, are predicted by the elasto-viscoplastic model and Terzaghi's model in order to verify the ability of the model to capture creep settlements. The effect of sample thickness on the prediction of settlements is verified using the results of consolidation model tests performed on specimens of different heights. Finally, the validity of the derived relationship between viscoplastic parameter m' and the C_α / C_c ratio of the soil is experimentally confirmed.

In Chapter 5, the model performance in predicting the field consolidation behavior of peaty clay due to one-dimensional compression is studied. The material parameters required for the analysis are determined using the laboratory and the field tests conducted during the project period. Predictions are made with the model based on infinitesimal strain, finite strain, and finite strain together with the effect of structural degradation in order to explore how these features describe the observed field behavior, namely, excess pore water pressure development/dissipation and settlements.

Chapter 6 presents the application of the model to the field performance of an embankment constructed on peaty clay using the preloading method. The versatility of the elasto-vicoplastic model, which considers the effect of structural degradation and is based on the finite deformation theory, is revealed by accurately predicting the observed large strain in the peaty clay brought about by embankment loading. In addition, the ability of the model to verify the stability of the embankment during and after construction is investigated.

Model applications to embankments constructed by preloading, utilizing other ground-improvement techniques, are discussed in Chapter 7. Field performances due to the installation of prefabricated vertical drains (PVDs) and sand compaction piles (SCPs) are simulated. Finite element analyses are carried out for all cases by converting the actual three-dimensional conditions that exist around the drains into simplified two-dimensional plane strain conditions. Model predictions are compared with the observed pore water pressure and settlements measured at different locations under the embankments. The effects on the subsoil response, due to the installation of vertical drains and the influence of the stiffness and the area replacement ratio used in the conversion scheme in the SCP analysis, are studied.

Chapter 8 presents the conclusions of the current research and recommendations for further studies. This last chapter is followed by the References and two Appendices.

Chapter 2

GENERAL FEATURES OF PEATY SOIL

2.1 Introduction

Peat generally refers to natural material which is composed primarily of plant material in various stages of decomposition and which is characterized by high compressibility and low shear strength. Peat is formed in low-lying, water-logged areas or in lakes or ponds with extremely poor drainage when organic (usually plant) matter accumulates more quickly than it humidifies. Peat is usually dark brown to black in color, has the distinctive odor of decaying vegetation, is spongy in consistency without exhibiting distinct plasticity, and has a texture ranging from fibrous to amorphous.

The properties which indicate the state or the condition of peat are the water content, the bulk density, the degree of saturation, the specific gravity, the organic content, the pH value, the liquid limit, the plastic limit, linear shrinkage, and the degree of decomposition as quantified by the von Post humification number. The engineering properties are the permeability, the compression index, the coefficient of secondary compression, and shear strength. Many of these properties are interrelated and most of them appear to have a direct association with the formation process conditions. The properties may also change chemically and/or biologically over time. For example, further humification of the organic constituents alters the mechanical properties of the soil, namely, the compressibility, the shear strength, and the hydraulic conductivity. Lowering the ground water level may cause the shrinking and the oxidation of the peat which leads to humification with a consequent increase in both permeability and compressibility.

In this chapter, the features of peaty soil found around the world will be briefly discussed. Firstly, the physical and the mechanical properties of peat are described on a world scale.

Then, a classification system that can be successfully adopted for engineering purposes to describe the behavior of all peats will be introduced. Finally, the features of the peaty clay found in Sri Lanka, on which the present research is focused, are described together with the observed correlations between its properties.

2.2 Physical Properties of Peaty Soil

Peat is a term commonly used to designate highly organic soil. The term originated from geology and meant vegetable matter in the early stages of coal creation. In the fields of soil science and geotechnical engineering, however, peat is considered to be a kind of soil referred to as peaty soil. Soils with an organic content of more than 50% are generally called peat in soil science. In geotechnical engineering, peat generally includes soils with an organic content of more than 20% (Kogure 1999). Some physical properties of soils with a high organic content (OC), generally of interest to engineers, will be reviewed in this section.

The presence of organic components in peaty soil creates unique physical and mechanical properties in comparison to the properties of inorganic soils, such as clay and sandy soils, which are made up of only soil particles. Soils containing a wide range of organic matter can be found throughout the world.

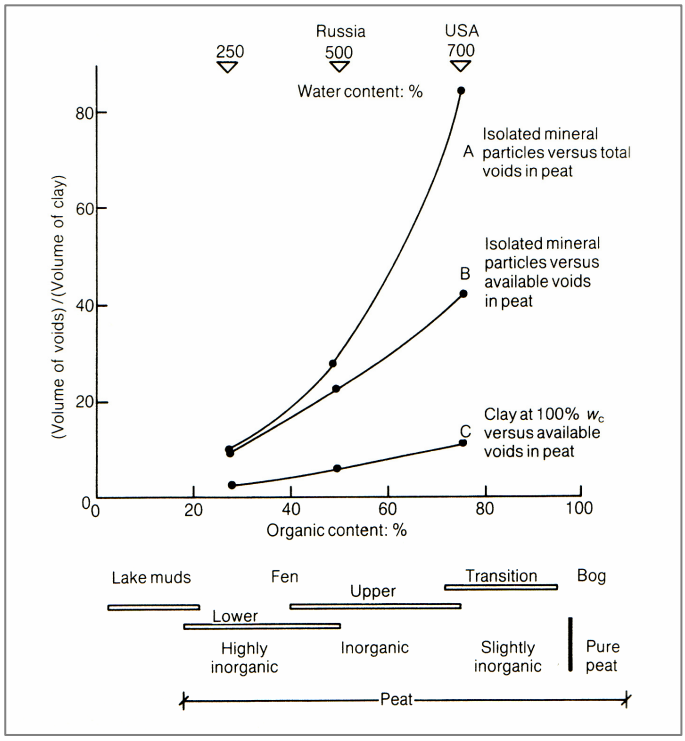

Fig. 2.1: Void ratio vs. organic content for some foreign peats (Hobbs 1987)

Peat that is completely free of extraneous mineral matter may have an ash content as low as 2%, that is, an organic content exceeding 98%. At the other extreme, a lake mud may contain less than 10% organic matter (Hobbs 1986). The organic content of peat is very important geotechnically as most other soil properties greatly depend on it. For example, Hobbs (1986) reported that the water-storing capacity of peat depends largely upon this quantity. Rashid and Brown (1975) reported that the liquid and the plastic limits, as well as the compressibility of peat, increase with an increase in the organic matter content. O'Loughlin et al. (2001) reported that soil with a high organic content leads to pronounced creep characteristics in addition to a more rapid consolidation. The variations in void ratio with the organic content for peat found in Russia and the USA are shown in Fig. 2.1 together with the corresponding range in observed water content for each type. According to this figure and to other reported data, the water content and the compressibility of peats increase with an increase in the organic content.

High water content is the most striking characteristic of natural peat. Hobbs (1986) reported that five meters of fibrous peat may contain 4.7 m of water and as little as 300 mm of solid plant. The water content of peat can vary over a wide range, namely, from a few hundreds percent of dry weight to greater than 2000%. The water content increases with the organic content of the soil. This is because the increase in fibers creates an open cellular structure, which in turn allows for water retention within these organic solids.

The bulk density of peat is low and sometimes appears to be slightly lower than that of water. It was reported that the bulk density increases with the humification of peat and that it generally varies from 14 kN/m^3~8 kN/m^3. The observed bulk density vs. water content relationship for the peat found in the UK is shown in Fig. 2.2.

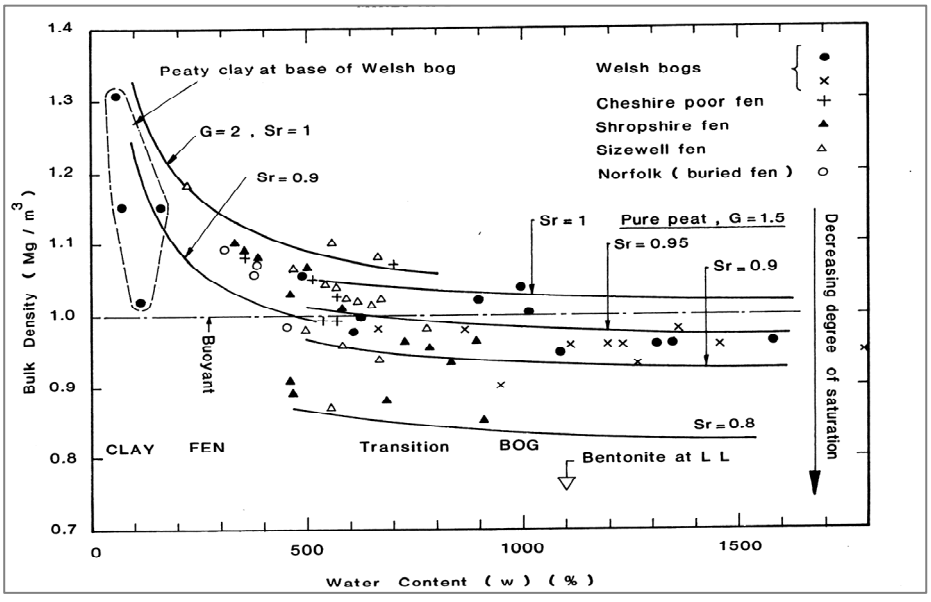

Fig. 2.2: Bulk density vs. water content in some UK peats (Hobbs 1986)

Peat soils have low specific gravity compared to inorganic clays, namely, in the range of 1.5-2.5. It has been observed that the specific gravity increases with an increase in the degree of humification of the peat. Fig. 2.3 shows the specific gravity vs. water content relationship reported by Hobbs (1986) for peat soils found in different parts of the world.

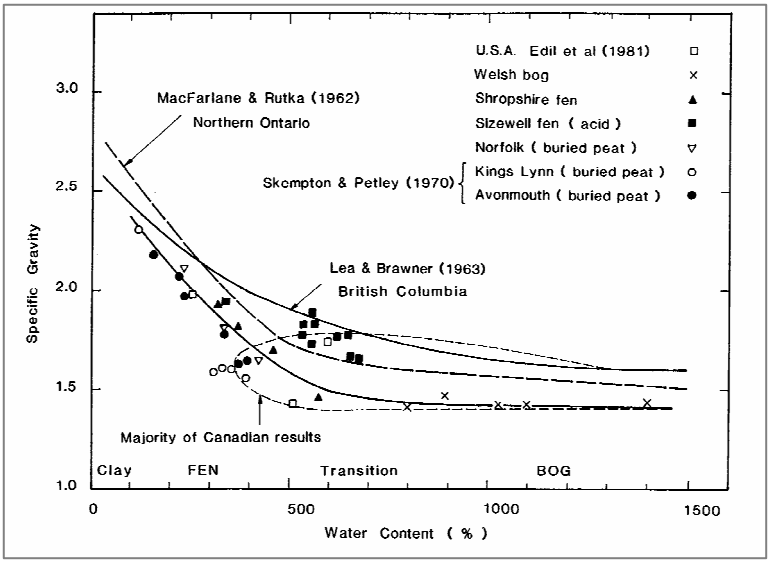

Fig. 2.3: Specific gravity vs. water content relationship in peat soils around the world (Hobbs 1986)

The liquid limit of peat is very high; it is almost equal to the natural water content. The liquid limit vs. water content relationship for different peats reported by Hobbs (1986) is shown in Fig. 2.4. The liquid limit of peat varies with the organic content. The liquid limit of fen peat (low organic content) lies in the range of 200%-600% and that of bog peat (high organic content) lies in the range of 800%-1500%.

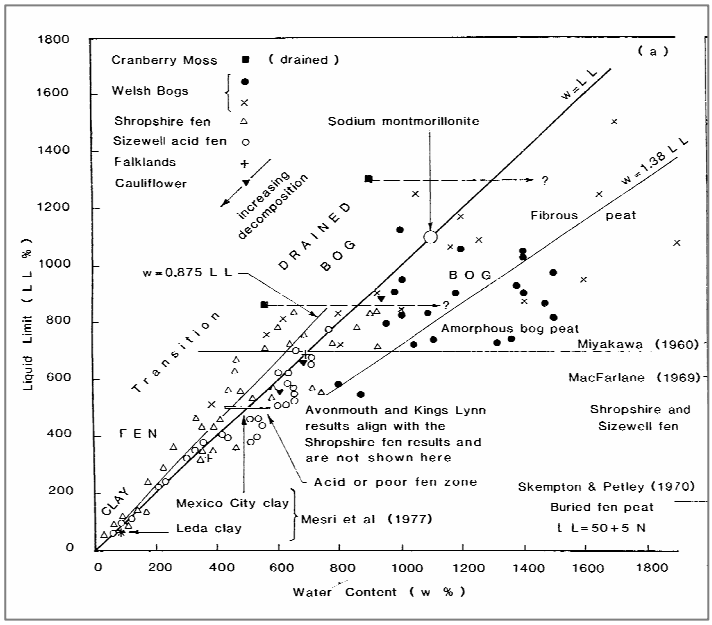

Fig. 2.4: Liquid limit vs. water content relationship for peats (Hobbs 1986)

The organic matter content (≈ ignition loss) vs. liquid limit relationship for the peats found in the different regions reported by Hobbs (1986) is shown in Fig. 2.5. The results indicate an increase in the liquid limit with an increase in the organic content. This is to be expected since organic matter has a higher liquid limit than clay soil.

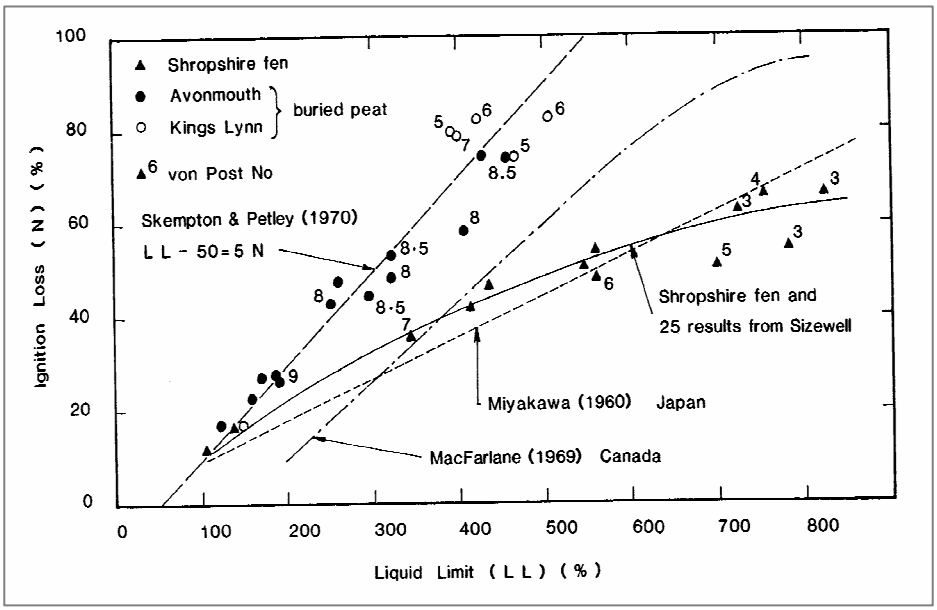

Fig. 2.5: Organic content vs. liquid limit relationship for peats (Hobbs 1986)

The numbers shown in Fig. 2.5 are related to the von Post humification index. The von Post scale of humification is a ten-point scale, from H1 to H10, for which the decomposition increases with an increase in the numerical value. The scale reflects a decomposition range between plant remains that are fresh to those which have become completely decayed amorphous material for which a plant structure can no longer be recognized. As indicated in Fig. 2.5, the relationship between the organic content and the liquid limit varies with the state of the peat's decomposition. The above relationships, as well as most of the other properties, are influenced by this state of decomposition.

2.3 Engineering Properties of Peaty Soil

Peat soil in its natural state has poor engineering properties such as high compressibility and low shear strength. Due to high in situ void ratios, peat deposits display higher values for compression index C_c than clay or silt deposits. The values of the natural water content and the compression index for peats, compared to those for soft clay and silt deposits reported by Mesri et al. (1997), are shown in Fig. 2.6.

The values of C_c in the effective vertical stress (σ'_v) range of $\sigma'_p - 2\sigma'_p$, are plotted against the natural water content where σ'_p is the in situ preconsolidation pressure.

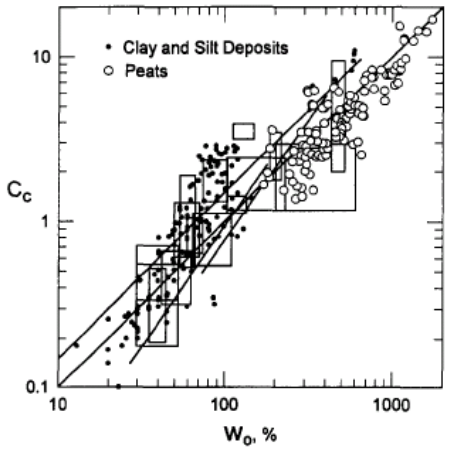

Fig. 2.6: Values of the compression index and the natural water content for peats in comparison to those for soft clay and silt deposits (Mesri et al.1997)

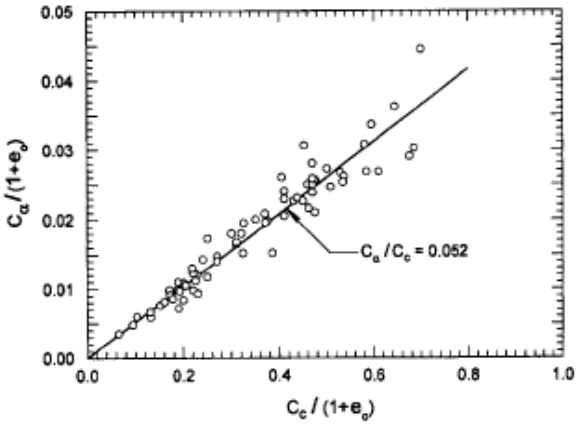

Fig. 2.7: C_α / C_c relationship for Middleton peat, UK (Mesri et al.1997)

Peat soil possesses higher values of compression index C_c and secondary compression C_α than any other soils. Mesri (1997) reported that the secondary compression is prominent in peat deposits because they exist at high void ratios, exhibit high values of C_c, and display the highest values of C_α / C_c among all geotechnical materials. Table 2.1 shows the C_α / C_c values for natural soil deposits. The table clearly indicates that the C_α / C_c ratio increases with an increase in the organic content. Fig. 2.7 shows the observed relationship between the secondary compression index and the compression index for Middleton peat found in the UK.

Table 2.1: Values of C_α / C_c for natural soil deposits (Mesri et al.1977)

Soil (1)	C_α / C_c (2)	Reference (3)
Whangamarino clay	0.03–0.04	Newland and Allely (22)
Norfolk organic silt	0.05	Barber (2)
Calcareous organic silt	0.035–0.06	Wahls (28)
Amorphous and fibrous peat	0.035–0.083	Lea and Brawner (13)
Canadian muskeg	0.09–0.10	Adams (1)
Leda clay	0.03–0.055	Walker and Raymond (31)
Leda clay	0.04–0.06	Walker and Raymond (32)
Peat	0.075–0.085	Weber (33)
Post-glacial organic clay	0.05–0.07	Chang (9)
Soft blue clay	0.026	Crawford and Sutherland (11)
Organic clays and silts	0.04–0.06	Ladd (12)
Sensitive clay, Portland	0.025–0.055	Ladd (12)
Peat	0.05–0.08	Samson and La Rochelle (25)
San Francisco Bay mud	0.04–0.06	Su and Prysock (26)
New Liskeard varved clay	0.03–0.06	Quigley and Ogunbadejo (23)
Silty clay C	0.032	Samson and Garneau (24)
Nearshore clays and silts	0.055–0.075	Brown and Rashid (6)
Fibrous peat	0.06–0.085	Berry and Vickers (3)
Mexico City clay	0.03–0.035	Mesri, et al. (19)
Hudson River silt	0.03–0.06	Mesri, Personal files
Leda clay	0.025–0.04	Present paper
New Haven organic clay silt	0.04–0.075	Present paper

Permeability is a very important engineering property, since it controls the consolidation rate of peat under various loads. The in situ permeability of peat is relatively higher than that of ordinary clays. Mesri (1997) reported that the initial permeability of peat is typically 100-1000 times the initial permeability of soft clay and silt deposits; the initial coefficient of the consolidation of peat, c_{v0}, is 10-100 times larger. Table 2.2 shows the values of the initial coefficient of permeability in the vertical direction, k_{v0}, together with the relevant C_α / C_c values for the different peat deposits reported by Mesri (1986).

Tests comparing vertical and horizontal drainage show peat to be hydraulically anisotropic and the horizontal permeability to generally be greater than the vertical, although not to the extent one would imagine in terms of the manner in which peat accumulates from dead plant matter. It is confirmed that the fresher the peat is, the greater the ratio of horizontal to vertical permeability will be and the more the highly humified peat will be expected to be fairly uniform.

Table 2.2: Values of natural water content, initial vertical coefficient of permeability, and C_α / C_c for peat deposits (Mesri et al.1997)

Peat (1)	w_o % (2)	k_{vo} m/s (3)	C_α/C_c (4)	Reference (5)
Fibrous peat	850	4×10^{-6}	0.06–0.10	Hanrahan (1954)
Peat	520	—	0.061–0.078	Lewis (1956)
Amorphous and fibrous peat	500–1,500	10^{-7}–10^{-6}	0.035–0.083	Lea and Brawner (1963)
Canadian muskeg	200–600	10^{-5}	0.09–0.10	Adams (1965)
Amorphous to fibrous peat	705	—	0.073–0.091	Keene and Zawodniak (1968)
Peat	400–750	10^{-5}	0.075–0.085	Weber (1969)
Fibrous peat	605–1,290	10^{-6}	0.052–0.072	Samson and LaRochell (1972)
Fibrous peat	613–886	10^{-6}–10^{-5}	0.06–0.085	Berry and Vickers (1975)
Amorphous to fibrous peat	600	10^{-6}	0.042–0.083	Dhowian and Edil (1981)
Fibrous peat	660–1,590	5×10^{-7}–5×10^{-5}	0.06	Lefebvre et al. (1984)
Dutch peat	370	—	0.06	Den Haan (1994)
Fibrous peat	610–850	6×10^{-8}–10^{-7}	0.052	Present study (1997)

One of the striking characteristics of peat is the remarkable decline in permeability which accompanies a reduction in the void ratio. It falls by some three orders against a change in the void ratio of a half order.

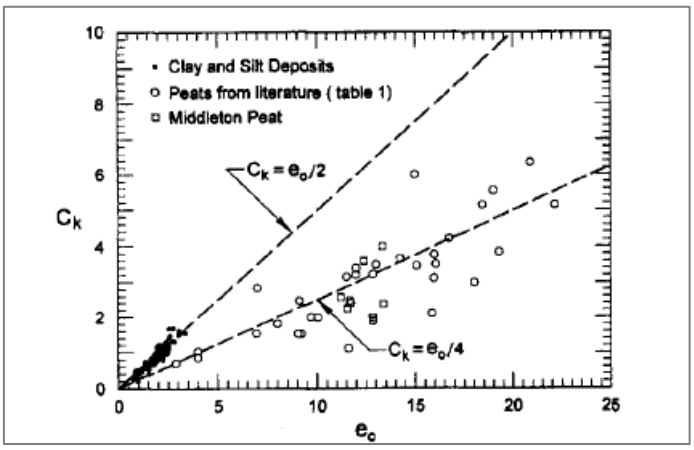

Fig. 2.8: Values of C_k for peats compared to those for soft clay and silt deposits (Mesri et al.1997)

The variation in permeability with the void ratio for peats can be represented in terms of the linear relationship of e vs. $\ln k$ which is used extensively in engineering for soft clay and silt deposits. However, the value of $C_k = \Delta e / \Delta \ln k_v$ for peats is close to $e_0 / 4$ (e_0 is the initial void ratio), whereas $C_k = e_0 / 2$ yields a better agreement compared to those for soft clay and silt deposits. A comparison of the C_k values for peats and for the soft clay and silt deposits reported by Mesri et al. (1997) is shown in Fig. 2.8.

Peat soils are characterized by low shear strength. Landva (1980) reported that in situ vane tests on peats with void ratios of 6.1-11.5 displayed shear strength levels ranging from 5-35 kPa. However, it has been observed that this low strength will increase when the fibers and the particles of the peat come together under compression (Lea and Brawner 1963). Vane shear tests conducted before the construction of an expressway built over peat by preloading (Samson and Rochelle 1972), and at the end of the surcharge stage when the primary consolidation was completed, indicate that the average shear strength of peat in its natural condition was 10 kPa and increased up to 95 kPa. Such a considerable gain in shear strength is attributed to the exceptionally high values of the effective angle of shearing resistance, ϕ', which has been observed in various laboratory tests conducted on several types of peat. The tests have shown that their behavior is essentially frictional, with high friction angles and relatively small cohesion intercepts (Adams 1965; Edil and Dhowian 1981; Yamaguchi et al. 1985). Yamaguchi et al. (1985) found that the friction angle, ϕ', determined with some compression triaxial tests on normally consolidated peat from Japan, varied from 52^0-35^0. Very high values of ϕ' (50^0-57^0), compared to those for inorganic soil, were also observed by Edil and Dhowian (1981).

A significant difference is observed between the values for peats and clays of the coefficient of lateral earth pressure under the condition of no lateral deformation, K_0; the former is much lower due to the presence of fibers. Furthermore, the peat type exerts a significant influence on the measured value of K_0 during loading, namely, 0.53 for amorphous granular peat and about 0.30, a markedly low value, for fibrous peat (Edil and Dhowian 1981). It was also reported that the use of the effective friction angle, ϕ', to make an indirect determination from the empirical expressions was found to yield unacceptable values of K_0 in comparison to those measured in the laboratory. It is apparent that ϕ' is not adequate as a single parameter for reflecting the lateral load transfer mechanisms brought about by the diverse nature of the microstructure in peat soils.

2.4 Classification of Peat for Engineering Purposes

As described in the preceding sections, the properties of peat soil vary over a wide range which may lead to different types of behavior under loading. Therefore, it is necessary to relate any theory for the mechanics of peat to the type of peat under consideration. Since both physical and mechanical properties are naturally and remarkably affected not only by the amount of organic matter, but also by the state of decomposition, it is desirable to adopt a classification system based on these two criteria for engineering applications of peat. Such a classification system has been proposed by MacFarlane and Radforth (1965). In this scheme, amorphous granular peat and fibrous peat are given as the two extreme types between which all other peat derivatives lie. Berry & Poskitt (1972) reported that by proposing consolidation theories for these two materials, it would be possible to bracket the entire scope of consolidation behavior for peaty soils.

Similar to the method proposed by MacFarlane and Radforth (1965), the ASTM standards for the classification of peat are based largely on the organic content and on a visual description (degree of humification) of the samples. According to ASTM standards, soil with a low organic content (less than 25%) is called organic silt or clay. This group has the visual appearance of amorphous material with a high degree of humification. Soil with an organic content in the range of 25%-75% is called muck or amorphous peat. The visual description includes some fibrous organic material in the process of humification covered by amorphous granular particles. Soil with a high organic content (greater than 75%) is called peat, or more precisely, fibrous peat. This type of soil contains mostly fibrous material in the early stages of humification.

In the present research work, the classification of peaty soil is done in accordance with the method proposed by MacFarlane and Radforth (1965). According to their method, fibrous peat generally has a higher organic content than amorphous peat (almost double). In addition, it has been observed that the water content of fibrous peat is almost five times higher than that of amorphous peat. This indicates that as the organic content becomes greater, so does the water content. However, the difference is also due to the higher degree of decomposition of amorphous peat with respect to fibrous peat. In fact, fibrous peat (low humification) has a higher total water content than granular-amorphous peat (high humification). The organic content of peat has a considerable effect on its physical and mechanical properties. In general, as the organic content of peat becomes greater, so do the void ratio, the compressibility, and the in situ permeability.

2.5 Properties of Sri Lankan Peat

Sri Lanka lies in the monsoon region of Southeast Asia. Colombo, the capital city, is situated on the western coast of the island and experiences a humid, tropical climate with an average annual rainfall of 2500 mm. In the Colombo region, the flood plains of Kelani Gaga (Kelani River) lie to the north and bodies of water, such as Kotte Lake, Bolgoda Lake, etc., are found in the coastal belt. The fluctuation of the water table, due to excessive rainfall, provides suitable conditions for the accumulation of peat deposits in these areas which consist of poorly drained grounds. This process has been occurring for a long time and, as a result, there are now around 2500 acres of marshy land underlain with peat in and around Colombo (Fig.2.9). Investigations have revealed that these marshy lands consist of the granular-amorphous type of peat layers, around 5 m-10 m in thickness, which yield the basic properties shown below in Table 2.3.

Table 2.3: Basic properties of Sri Lankan peat

Peat type	Amorphous peat
Water content	200%-800%
Initial void ratio	2.0-8.0
Organic content	20%-50%
Specific gravity	1.5-2.2
pH value	Less than 3.0
Liquid limit	Often less than the natural water content (%)

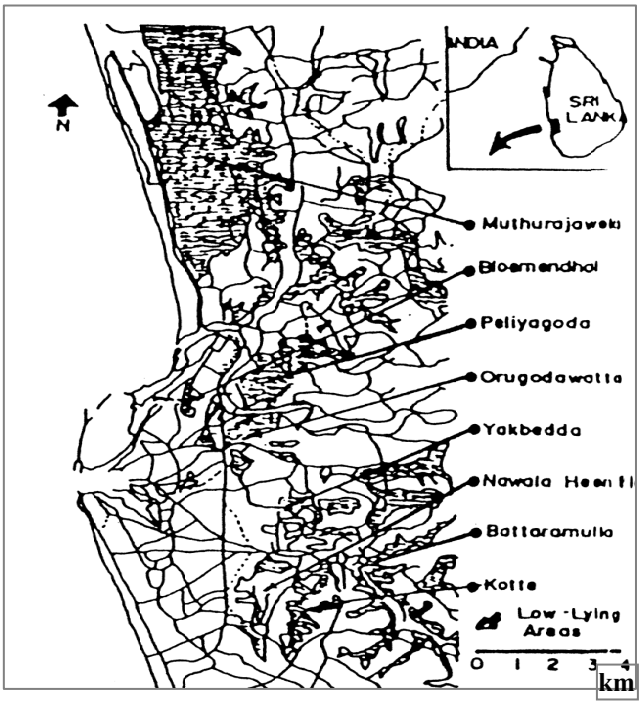

Fig. 2.9: Distribution of peaty areas around Colombo

2.5.1 Empirical Correlations for Sri Lankan Peaty Clay

It is universally accepted that reasonably consistent relationships exist between the engineering parameters and the index properties of normally consolidated inorganic clays. Notwithstanding its very high water content, similar relationships or correlations are found to apply to peat, whatever the morphology, but only in regards to constrained deformation (Hobbs 1986). The preliminary design of structures to be built in/on peats can profit from such empirical correlations, sometimes even more so than when dealing with clays, due to the difficulty of obtaining high quality peat samples and to the extreme variability of peat deposits. There are no well-established or widely-known correlations between the simpler index properties and the more difficult mechanical parameters of peat (Edil and Haan 1994). As such, some observed co-relations for Sri Lankan peaty clays reported by Karunawardena (2000) are presented.

The relationship between compression index C_c and the natural water content (w_0) of Sri Lankan peat is shown in Fig. 2.10. Although there is a customary scatter normally associated with peat, the majority of the results confirm the $C_c = 0.007\, w_0$ relationship for the peat found in Sri Lanka. For comparison, the same relationship was observed for peats found in the UK, Canada, the USA, and Japan, as shown in Fig. 2.11. The figure shows that there is a clear distinction between the UK fen peat and the UK bog peat, the two mean relationships being $C_c = 0.065\, w_0$ for bog peat and $C_c = 0.008\, w_0$ for fen peat (Hobbs 1986). The figure also shows that the observed relationship for the Sri Lankan peat $C_c = 0.007\, w_0$ lies in between the reported values for the fen and the bog peats found in the UK. This is understood since the observed organic content of Sri Lankan peaty soil is generally slightly higher than that of the UK fen peat and much lower than that of the UK bog peat. Moreover, the degree of decomposition is lower than that of the UK fen peat and higher than that of the UK bog peat.

Fig. 2.12 indicates the relationship between compression index C_c and initial void ratio e_0 for Sri Lankan peat. The figure shows that the majority of the results falls into the $C_c = 0.367 e_0$ relationship. The observed and the reported relationship for C_c and e_0 for peats found in the UK was $C_c = 0.45 e_0$ (Hobbs 1986). This is slightly different from the observed value for Sri Lankan peat, and might be due to the effects of secondary compression with the variable loading period, to any variation in vertical consolidation yield stress p_c, and/or to the variation in the relationship between the void ratio and the water content.

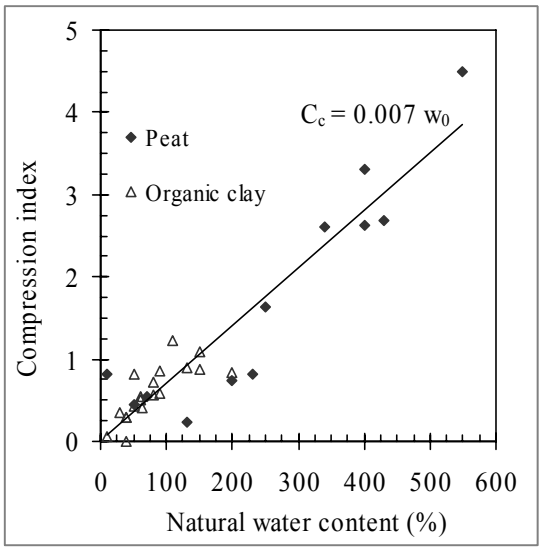

Fig. 2.10: C_c vs. natural water content (%) relationship for Sri Lankan peats

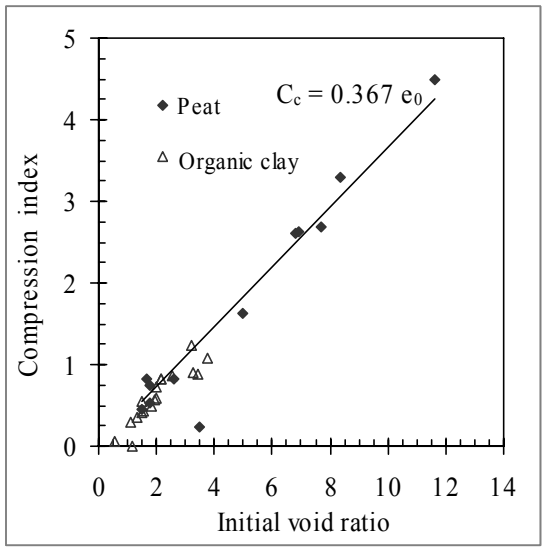

Fig. 2.12: C_c vs. e_0 relationship for Sri Lankan peats

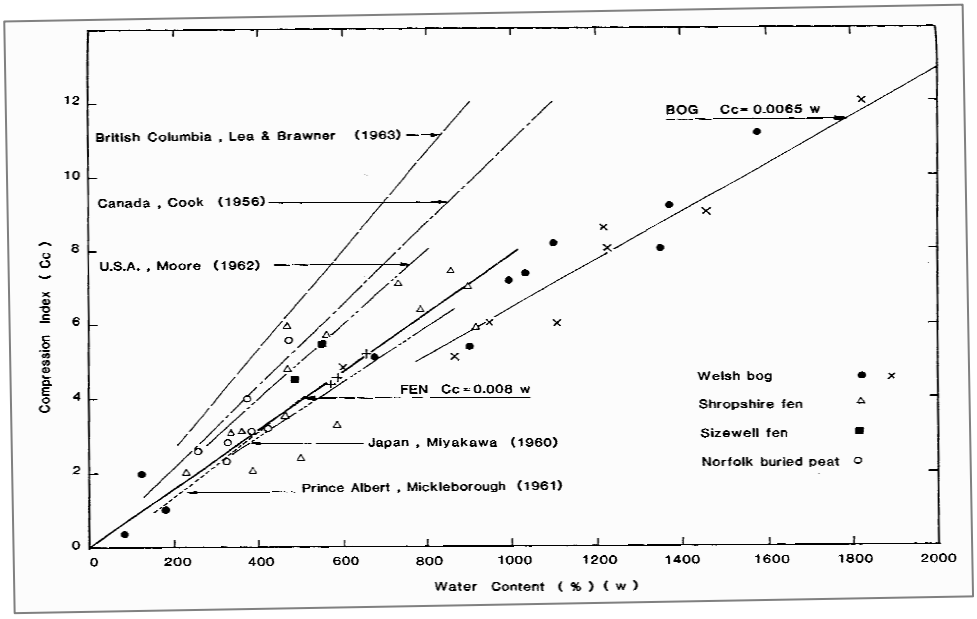

Fig. 2.11: C_c vs. natural water content (%) relationship for foreign peat

The organic content of peat is also an important geotechnical parameter, since it influences most of the peat's physical and mechanical properties. For example, Hobbs (1986) reported that the water-storing capacity of peat depends greatly upon this quantity. Rashid and Brown reported that the liquid and the plastic limits, as well as the compressibility of peat, increase with an increase in the organic matter content (O.M.C.). O'Loughlin et al. (2001) reported that soil with a high organic content leads to pronounced creep characteristics in addition to a more rapid consolidation. The dependence of compressibility and creep characteristics on the organic matter in Sri Lankan peats is shown in Figs. 2.13 and 2.14, respectively.

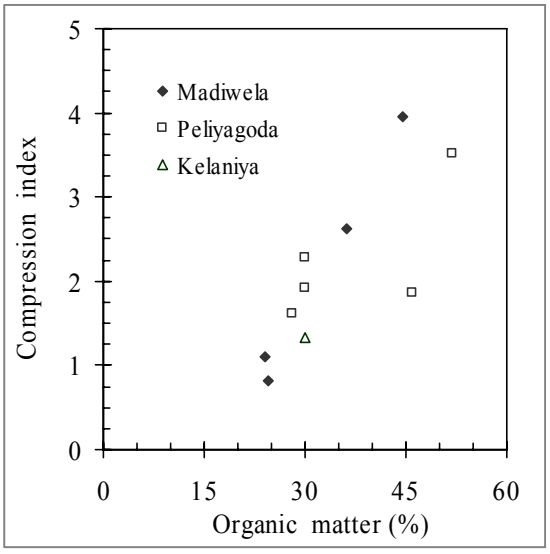

Fig. 2.13: C_c vs. O.M.C. (%) relationship for Sri Lankan peats

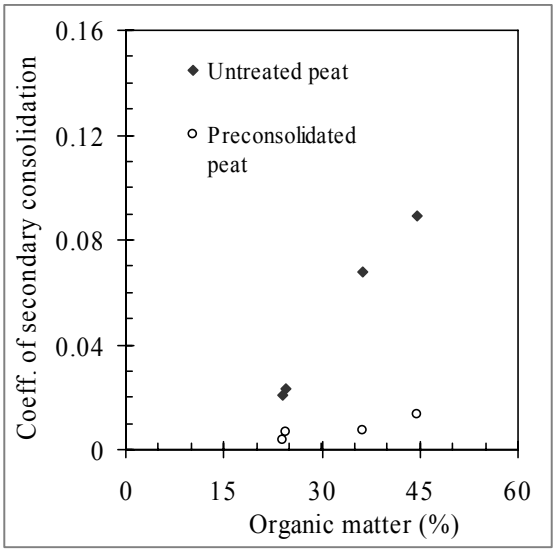

Fig. 2.14: C_α vs. O.M.C. (%) relationship for Sri Lankan peats

As shown in Fig. 2.13, when the data corresponding to different sites is separated, it is clear that the compressibility of the peat found in Sri Lanka also increases with an increase in the organic matter content. Similar to the relationship between the compression index and the organic matter content, the coefficient of secondary consolidation represents the increase in creep characteristics with an increase in the organic matter content, as shown in Fig. 2.14. This figure also indicates that secondary settlements can be significantly reduced by preloading.

Secondary compression is often more significant in peat deposits than in other geotechnical materials (Mesri 1997). Peat deposits have very high natural water contents and void ratios. Peat deposits accumulate at high void ratios because the plant matter that constitutes peat particles is light and holds a considerable amount of water. Due to high in situ void ratios, peat deposits display high values of compression index C_c. In addition, because C_α is directly related to C_c, peat deposits display high C_α. As a result, peaty soil has the greatest C_α / C_c ratio of all geotechnical materials. Moreover, the duration of the primary consolidation for peat is relatively short due to the high initial permeability. For these reasons, the secondary compression is more significant in peaty soils than in inorganic clays.

It has been reported that the C_α / C_c concept of compressibility could be used to explain and to predict the secondary compression behavior of geotechnical materials. As such, the observed C_α / C_c relationship for Sri Lankan peat is shown in Fig. 2.15. In the established correlation of $C_\alpha = 0.0341 C_c$ agrees quite well with the $C_\alpha = 0.035 C_c$ relationship for the amorphous peaty clay observed by Mesri et al. (1997).

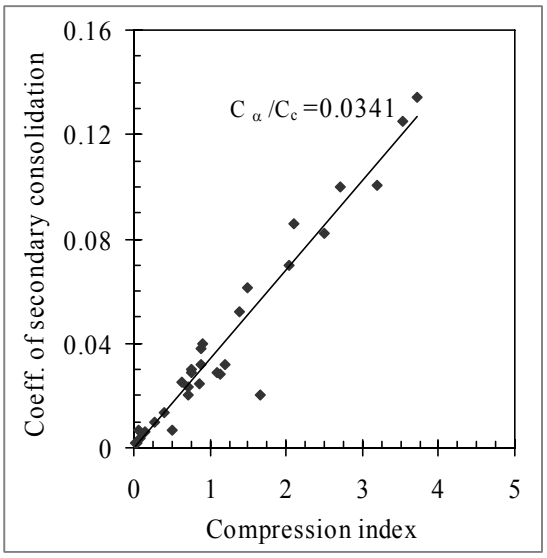

Fig. 2.15: C_α vs. C_c relationship for Sri Lankan peat

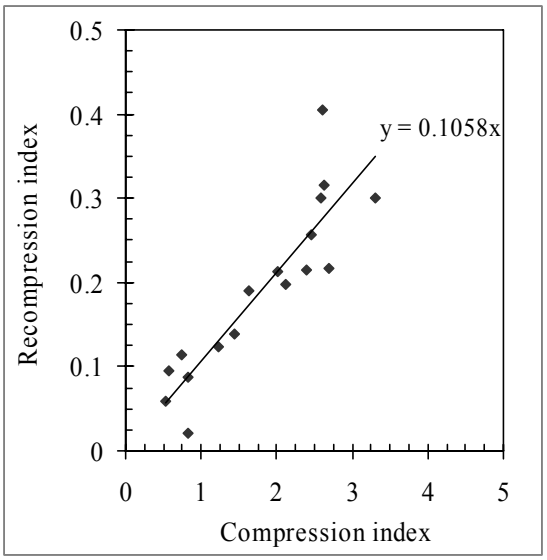

Fig. 2.16: C_r vs. C_c relationship for Sri Lankan peat

Preconsolidation by preloading can be used to improve the engineering properties of peat. It is reasonable to assume that the settlement of natural soil will be proportional to compression index C_c and that the peat improved by precompression will be proportional to recompression index C_r. The relationship between the recompression index and the compression index under laboratory conditions is given in Fig. 2.16. It shows that the two parameters are related and that the average, C_s, is about 10% of C_c.

2.6 Summary

It has been observed that peaty soil composed of fibrous organic matter, i.e., partly decomposed plants such as leaves and stems, shows unique mechanical properties in comparison with those of inorganic soils, i.e., clay and sandy soils made up of soil particles. In the same manner as for the physical properties of peat, the mechanical properties are naturally and remarkably affected not only by the amount of organic matter, but also by their degree of decomposition. Therefore, it is desirable to adopt a classification system that can describe the entire scope of consolidation behavior for peaty soils.

The peaty soils found in Sri Lanka are generally of the amorphous type due to their low organic content. Some useful relationships were established between the stiffness characteristics and the basic index properties of peats found in Sri Lanka. The patterns are seen to agree well with similar results reported in literature, but the numerical values of the correlations are different due to the lower organic matter contents reported for Sri Lankan peaty soil.

Chapter 3

CONSTITUTIVE MODEL AND ANALYSIS METHODS TO SIMULATE PEAT CONSOLIDATION

3.1 Introduction

Simply stated, a material model is a mathematical relationship which describes the stress-strain behavior of the material. It is often called a constitutive model. The formulation of a constitutive model is an important step toward obtaining solutions for practical engineering problems. Once established, the model can be employed in a numerical solution code suitable for the analysis of geotechnical problems with given conditions. Thus, the model should be comprehensive enough to represent all the important types of material behavior observed for a given material, in a quantitative and a qualitative fashion, under the prevailing loading conditions.

The consolidation behavior of peaty soil is extremely complex. This is due to the highly compressible nature of the natural deposits which may undergo a strain of 50% and a hundredfold reduction in macropermeability under loads equivalent to only a few feet of fill. In addition, the consolidation process is complicated by the occurrence of secondary compression which, for certain kinds of peat, shows an essentially linear relationship with log time that appears to extend indefinitely, although it is realized that the settlement must ultimately cease (Beery 1983). Therefore, the constitutive model used to predict the consolidation behavior of peaty soil should be capable of capturing the above main characteristics, in addition to the general features of natural soil deposits.

A variety of constitutive models for clay has been proposed based on the theories of elasticity, plasticity, viscoplasticiy, and combinations of them. The applications of these models to peaty soil have had mixed success. This is because some models resort to idealizing the soil behavior by applying many assumptions and simplifications which are not realistic for peat. For example, it has been observed that the consolidation behavior of peat could not be satisfactorily modeled by Terzaghi's model (Karunawardena 2002) due to the following assumptions made when deriving Terzaghi's one-dimensional theory:

- Linear elasticity
- Small strain
- Relationship between void ratio and effective stress that is independent of time
- Changes in void ratio caused entirely by changes in excess pore water pressure which are independent of time
- Coefficient of permeability which is constant during the consolidation process.

In traditional soil mechanics, based on the theory of elasticity, it has been a common practice to study shear and the consolidation deformation behavior separately. However, this division is artificial and disregards the complete stress-deformation response of the soil. Furthermore, this type of settlement and the rate of settlement analysis based on the elastic soil skeleton may well be in error in situations for which the loading induces significant local yielding.

Elastic-perfectly plastic models, such as the Mohr-Coulomb model which considers non-linear material behavior, have been applied to predict the consolidation behavior of peat in the past (Brinkgreve & Vermeer 1994). Many researchers have tried to model peat behavior using elasto-plastic models based on the critical state theory which considers hardening plasticity by incorporating the expanding yield stress represented by a non-fixed yield surface. Although these models have shown acceptable results for the primary loading phase, their performances in predicting long-term behavior were not as satisfactory as expected. This is mainly due to the fact that none of these models addresses the time-dependent behavior of soil, such as creep settlement, which is a dominant characteristic of peat soil.

The above research works indicate that the model for peat should consider both the plastic nature and the time-dependent behavior of the soil. It is now well accepted that this time-dependent behavior of soil is caused by the viscosity of the soil skeleton (eg., Kim and Lerouil 2001). Therefore, a model based on the viscoplastic approach is much more

realistic and logical for predicting the consolidation behavior of peaty soil. Various constitutive models have been proposed to describe the time-dependent behavior of soil using a viscoplastic approach (Adachi and Okano 1974; Adachi and Oka 1982; Sekiguchi and Ohta 1977; Dafalias and Hermann 1986; Kimoto and Oka 2005).

In this thesis, the elasto-viscoplastic model proposed by Kimoto and Oka (2005) is chosen for an extensive study on the consolidation behavior of peaty clay. The constitutive model is selected for its ability to describe the main features involved in the peat consolidation process, namely, creep settlement, finite strain, and changes in permeability and compressibility. In addition, the fact that it is able to describe the effects of sample thickness phenomena and structural degradation, which influence the consolidation behavior of natural soil deposits, is considered in the selection. In this chapter, firstly, the elasto-viscoplastic model proposed by Kimoto and Oka (2005) is briefly introduced. Secondly, the procedures which consider the main features of the peat consolidation analysis in the numerical analysis will be explained. Thirdly, the parameters required for the analysis and the procedures applied to evaluate them, with standard laboratory and field tests, are explained. In the last section, the performance of the model in incorporating the modified Cam-clay theory is investigated and compared with the original model.

3.2 Elasto-viscoplastic Constitutive Model

The elasto-viscoplastic model proposed by Kimoto and Oka (2005) is based on Perzyna (1963) type viscoplastic theory and the Cambridge elasto-plastic theory (Roscoe et al.1963) together with empirical evidence. The most important assumption taken from the derivation of the model is that "At the end of consolidation, the state of the clay does not reach the static equilibrium state but is in a non-equilibrium state" (Oka 2005). In this model, Terzaghi's effective stress is used in the following form:

$$\sigma'_{ij} = \sigma_{ij} - u_w \delta_{ij} \tag{3.1}$$

where σ_{ij} is the total stress tensor, σ'_{ij} is the effective stress tensor, u_w is the pore pressure, and δ_{ij} is Kronecker's delta.

Total strain rate tensor $\dot{\varepsilon}_{ij}$ consists of elastic strain rate tensor $\dot{\varepsilon}^e_{ij}$ and viscoplastic strain rate tensor $\dot{\varepsilon}^{vp}_{ij}$

$$\dot{\varepsilon}_{ij} = \dot{\varepsilon}^e_{ij} + \dot{\varepsilon}^{vp}_{ij} \tag{3.2}$$

3.2.1 Constitutive Equation for Geomaterials

The stress-strain relation of geomaterials denotes non-linearity due to their (visco) plastic properties (Oka et al.1986). The non-linear stress-strain relation of geomaterials used in the model is schematically illustrated in Fig. 3.1.

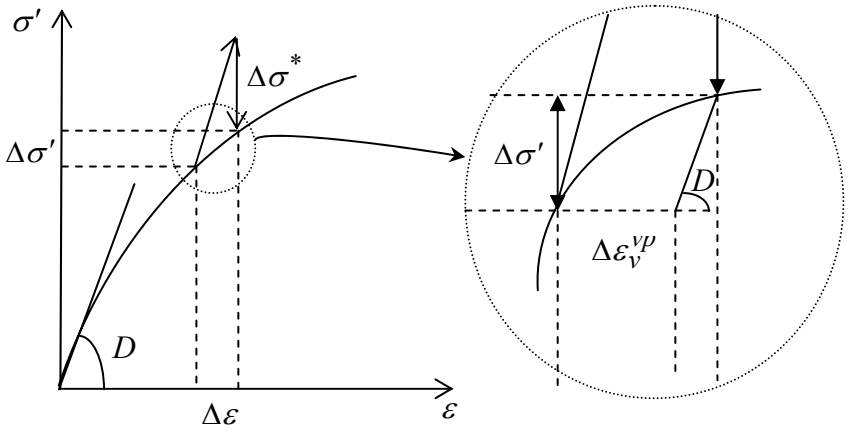

Fig. 3.1: Stress-strain relationship used in the model

Assuming that the effective stress increment, $\Delta\sigma'$, develops only due to the elastic response, the following relationship can be obtained:

$$\{\Delta\sigma'\} = [D]\{\Delta\varepsilon^e\} \tag{3.3}$$

Therefore, by using the relationship for the total strain increment mentioned in Eq. (3.2), the above equation yields

$$\{\Delta\sigma'\} = [D](\{\Delta\varepsilon\} - \Delta\varepsilon^{vp})$$

$$\{\Delta\sigma'\} = [D]\{\Delta\varepsilon\} - \{\Delta\sigma^*\}$$

$$\{\Delta\sigma^*\} = [D]\{\Delta\varepsilon^{vp}\} \tag{3.4}$$

in which $[D]$ is the elastic modulus and $\{\Delta\sigma^*\}$ is the relaxation stress.

3.2.2 Elastic Strain Rate

Elastic strain rate tensor $\dot{\varepsilon}_{ij}^e$ is given by a generalized Hooke type of law and is derived as follows:

$$\dot{\varepsilon}_{ij}^{e} = \dot{e}_{ij}^{e} + \frac{1}{3}\dot{\varepsilon}_{v}^{e}\delta_{ij} \tag{3.5}$$

in which $\dot{e}_{ij}^{e}$ is the deviatoric component of the elastic strain rate tensor and $\dot{\varepsilon}_{v}^{e}$ is the elastic volumetric strain rate.

The elastic deviatoric strain rate is given by

$$\dot{e}_{ij}^{e} = \frac{1}{2G}\dot{S}_{ij} \tag{3.6}$$

where G is the elastic shear modulus and S_{ij} is the deviatoric stress tensor defined as follows:

$$S_{ij} = \sigma'_{ij} - \sigma'_{m}\delta_{ij} \tag{3.7}$$

The elastic volumetric strain rate tensor is calculated using the relationship between void ratio e and logarithm mean effective pressure σ'_m obtained in the isotropic swelling process, namely,

$$\dot{\varepsilon}_{v}^{e} = \frac{\kappa}{1+e_0}\frac{\dot{\sigma}'_{m}}{\sigma'_{m}} \tag{3.8}$$

where κ is the swelling index and e_0 is the initial void ratio.

Based on the above equations, elastic strain rate $\dot{\varepsilon}_{ij}^{e}$ can finally be expressed as

$$\dot{\varepsilon}_{ij}^{e} = \frac{1}{2G}\dot{S}_{ij} + \frac{\kappa}{3(1+e_0)\sigma'_{m}}\dot{\sigma}'_{m}\delta_{ij} \tag{3.9}$$

3.2.3 Overconsolidated Boundary Surface

The model hardening rule is based on the overconsolidated (OC) boundary surface which delineates the OC region ($f_b < 0$) from the normally consolidated (NC) region ($f_b \geq 0$) and is given as follows:

$$f_b = \overline{\eta}^{*} + M_{m}^{*}\ln\left(\frac{\sigma'_{m}}{\sigma'_{mb}}\right) = 0 \tag{3.10}$$

In the above equation, $\overline{\eta}^*$ is the stress parameter that represents the anisotropic consolidation history defined by

$$\overline{\eta}^* = \sqrt{(\eta_{ij}^* - \eta_{ij(0)}^*)(\eta_{ij}^* - \eta_{ij(0)}^*)} \tag{3.11}$$

in which, for $\eta_{ij}^* = S_{ij} / \sigma'_m$, η_{ij}^* is the pressure normalized deviatoric stress tensor and $\eta_{ij(0)}^*$ is the value of η_{ij}^* before the deformation occurs (initial state). M_m^* is the value of $\sqrt{\eta_{ij}^* \eta_{ij}^*}$ when the volumetric strain increment changes from compression to swelling, σ'_{mb} is the hardening parameter, and σ'_{mbi} is the initial value of σ'_{mb} which is defined as the isotropic consolidation yield stress.

The schematic diagram for the OC boundary surface described in Eq. (3.10), with respect to the triaxial state, is shown in Fig. 3.2.

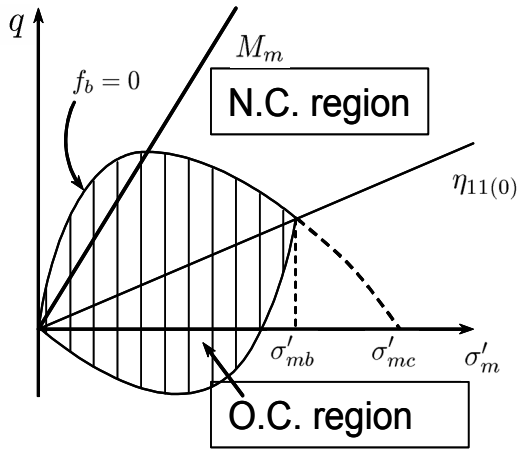

Fig. 3.2: Overconsolidated boundary surface under triaxial conditions (Kimoto 2002)

3.2.4 Static Yield Function and Viscoplastic Potential Function

The Cam-clay static yield function is used to describe the mechanical behavior of clay at its static equilibrium state, namely,

$$f_y = \overline{\eta}^* + \tilde{M}^* \ln\left(\frac{\sigma'_m}{\sigma'^{(s)}_{my}}\right) = 0 \tag{3.12}$$

In the above equation, $\sigma'^{(s)}_{my}$ denotes the mean effective stress in the equilibrium state, where stress may be reached after an infinite period of time. Accordingly, $f_y = 0$

represents the static state in which no viscoplastic deformation occurs (Kimoto 2002). $\overline{\eta}^*$ is the stress parameter that represents the anisotropic consolidation history defined by Eq. (3.11).

The viscoplastic potential function is

$$f_p = \overline{\eta}^* + \widetilde{M}^* \ln\left(\frac{\sigma'_m}{\sigma'_{mp}}\right) = 0 \tag{3.13}$$

where $\widetilde{M}^*$ is defined as

$$\widetilde{M}^* = \begin{cases} M^*_m & : f_b \geq 0 \\ -\dfrac{\sqrt{\eta^*_{ij}\eta^*_{ij}}}{\ln(\sigma'_m / \sigma'_{mc})} & : f_b < 0 \end{cases} \tag{3.14}$$

in which σ'_{mc} denotes the mean effective stress at the intersection of the OC boundary surface and the σ'_m axis. It can be expressed as

$$\sigma'_{mc} = \sigma'_{mb} \exp \frac{\sqrt{\eta^*_{ij(0)}\eta^*_{ij(0)}}}{M^*_m} \tag{3.15}$$

According to the above equation, σ'_{mc} equals σ'_{mb} in the case of isotropic consolidation.

The overconsolidated boundary surface, $f_b = 0$, the static yield function, $f_y = 0$, and the viscoplastic potential function, $f_p = 0$, for $\eta^*_{ij(0)} = 0$, are schematically described in the σ'_m~ $\sqrt{S_{ij}S_{ij}}$ space for the NC and the OC regions in Figs. 3.3(a) and (b), respectively.

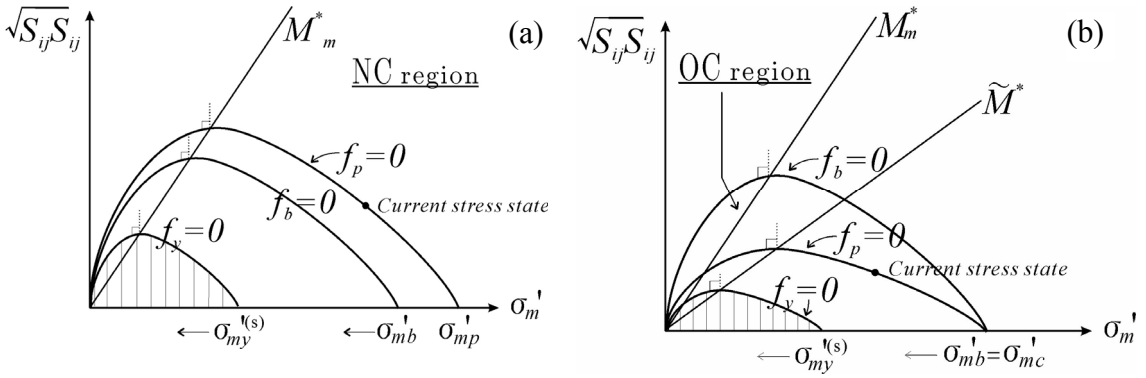

Fig. 3.3: OC boundary surface, static yield function, and viscoplastic potential function

3.2.5 Account of the Effect of Structural Degradation

Originally, the hardening rule for the OC boundary surface was defined only with respect to the viscoplastic volumetric strain as

$$\sigma'_{mb} = \sigma'_{mbi} \exp\left(\frac{1+e_0}{\lambda - \kappa} \varepsilon_v^{vp} \right) \tag{3.16}$$

where e_0 is the initial void ratio, λ is the slope of the $e - \ln \sigma'_m$ line for the consolidation tests, κ is the swelling index, and ε_v^{vp} is the viscoplastic volumetric strain.

However, it has been observed that the behavior of natural soils is influenced by the degradation of the microstructure induced by the applied loads (Burland 1990). This effect has been incorporated into the model by introducing viscoplastic strain softening in addition to strain hardening with viscoplastic volumetric strain. This process is explained in Kimoto and Oka (2005) as follows:

$$\sigma'_{mb} = \sigma'_{ma} \exp\left(\frac{1+e_0}{\lambda - \kappa} \varepsilon_v^{vp} \right) \tag{3.17}$$

$$\sigma'_{ma} = \sigma'_{maf} + \left(\sigma'_{mai} - \sigma'_{maf} \right) \exp\left(-\beta z \right) \tag{3.18}$$

where σ'_{ma} is assumed to decrease with an increasing viscoplastic strain, and σ'_{mai} and σ'_{maf} are the initial and the final values for σ'_{ma}, respectively. σ'_{mai} corresponds to the consolidation yield stress and σ'_{maf} is determined from the difference between the peak and the residual stress rates. Structural parameter β controls the rate of structural changes and z is the accumulation of the second invariant of the viscoplastic strain rate, namely,

$$z = \int_0^t \dot{z} dt \tag{3.19}$$

$$\dot{z} = \sqrt{\dot{\varepsilon}_{ij}^{vp} \dot{\varepsilon}_{ij}^{vp}} \tag{3.20}$$

Due to this modification, the degradation of the soil structure leads to the shrinking of the overconsolidated (OC) boundary surface with the viscoplastic deformation. In the above equation, ε_v^{vp} is the viscoplastic volumetric strain and the superimposed dot denotes the time differentiation.

In the original model (Oka 1981, Adachi and Oka 1982), changes in the size of $\sigma'^{(s)}_{my}$ were given as

$$\sigma'^{(s)}_{my} = \sigma'^{(s)}_{myi} \exp\left(\frac{1+e_0}{\lambda-\kappa}\varepsilon^{vp}_v\right) \tag{3.21}$$

In a similar way for OC boundary surface $f_b = 0$, the effect of structural degradation is taken into account by changing $\sigma'^{(s)}_{my}$ in the static yield function (Eq. 3.12). The procedure adopted to consider the degradation effect, Eq. (3.21), has been modified by Kimoto (2002) as follows:

$$\sigma'^{(s)}_{my} = \frac{\left\{\sigma'_{maf} + \left(\sigma'_{mai} - \sigma'_{maf}\right)\exp\left(-\beta z\right)\right\}}{\sigma'_{mai}} \sigma'^{(s)}_{myi} \exp\left(\frac{1+e_0}{\lambda-\kappa}\varepsilon^{vp}_v\right) \tag{3.22}$$

Accordingly, the decrease in $\sigma'^{(s)}_{my}$ leads to the shrinking of the static yield function depending on the structural collapse.

3.2.6 Viscoplastic Flow Rule

The viscoplastic strain rate tensor is calculated using the following flow rule based on Perzyna's overstress type of viscoplastic theory:

$$\dot{\varepsilon}^{vp}_{ij} = \gamma\left\langle\Phi_1(f_y)\right\rangle\frac{\partial f_p}{\partial\sigma'_{ij}} \tag{3.23}$$

where
$$\left\langle\Phi_1\left(f_y\right)\right\rangle = \begin{cases}\Phi_1\left(f_y\right) & ; f_y > 0\\ 0 & ; f_y \le 0\end{cases} \tag{3.24}$$

in which Φ_1 is a material function indicating rate sensitivity, $f_y = 0$ denotes the static yield function, and $f_p = 0$ is the viscoplastic potential function. Herein, the value of f_y is assumed to be positive for any stress state. In other words, viscoplastic deformation always occurs (Kimoto 2002) since the stress state for this model always exists outside of the static yield function.

Based on the experimental results of strain-rate constant triaxial tests, material function Φ_1 is defined as follows (Oka 2005):

$$\gamma\Phi_1(f_y) = C_0\sigma'_m \exp\left\{ m'\left(\overline{\eta}^* + \widetilde{M}^* \ln\frac{\sigma'_m}{\sigma'^{(s)}_{my}} \right) \right\}$$

$$= C\sigma'_m \exp\left\{ m'\left(\overline{\eta}^* + \widetilde{M}^* \ln\frac{\sigma'_m}{\sigma'_{mb}} \right) \right\} \tag{3.25}$$

$$C = C_0 \exp\left\{ m'\widetilde{M}^* \ln\frac{\sigma'_{mai}}{\sigma'^{(s)}_{myi}} \right\} \tag{3.26}$$

where m' is related to the coefficient of secondary compression, $\alpha(=\mathrm{d}v^p/\mathrm{d}\ln t)$, which will be explained in detail later, and C is the viscoplastic parameter related to the initial volumetric strain rate, $\dot{v}^p_{(0)}$, through the following relation (Adachi and Oka 1982, Oka et al.1986):

$$\dot{v}^p_{(0)} = M^*_m C \tag{3.27}$$

Finally, the viscoplastic strain rate can be calculated using the following equation based on Eqs. (3.23) and (3.25):

$$\dot{\varepsilon}^{vp}_{ij} = C\sigma'_m \exp\left\{ m'\left(\overline{\eta}^* + \widetilde{M}^* \ln\frac{\sigma'_m}{\sigma'_{mb}} \right) \right\} \frac{\partial f_p}{\partial \sigma'_{ij}} \tag{3.28}$$

Based on the above equations, the viscoplastic deviatoric strain rate and the viscoplastic volumetric strain rate are obtained by

$$\dot{e}^{vp}_{ij} = C \exp\left\{ m'\left(\overline{\eta}^* + \widetilde{M}^* \ln\frac{\sigma'_m}{\sigma'_{mb}} \right) \right\} \frac{\eta^*_{ij} - \eta^*_{ij(0)}}{\overline{\eta}^*} \tag{3.29}$$

$$\dot{\varepsilon}^{vp}_{v} = C \exp\left\{ m'\left(\overline{\eta}^* + \widetilde{M}^* \ln\frac{\sigma'_m}{\sigma'_{mb}} \right) \right\} \left(\widetilde{M}^* - \frac{\eta^*_{ij}\left(\eta^*_{ij} - \eta^*_{ij(0)}\right)}{\overline{\eta}^*} \right) \tag{3.30}$$

3.3 Features of the Analysis Related to the Consolidation Process for Peat

The methods applied in the numerical analysis to simulate the peat consolidation process, such as variable permeability and compressibility, the relationship between model parameter m' and the compressibility parameters of the soil, and the adopted procedure for the finite deformation, are described in this section.

3.3.1 Variable Permeability and Compressibility

Changes in permeability k are taken into account using Taylor's empirical formula (1948). In relation to that, the coefficient of permeability k depends on void ratio e in the following form:

$$k = k_0 \exp(e - e_0)/C_k \tag{3.31}$$

in which k_0 is the initial value for k at $e = e_0$ and C_k is the material constant governing the rate of changes in permeability subjected to changes in the void ratio. C_k is the permeability change index.

The elastic shear modulus increases with an increase in the mean effective stress of the soil as follows:

$$G = G_0 \sqrt{\frac{\sigma'_m}{\sigma'_{mo}}} \tag{3.32}$$

in which G_0 is the value for G when $\sigma'_m = \sigma'_{mo}$

In the present research work, the variable compressibility is considered in the analysis of stage-constructed embankments which exert high levels of pressure on the peaty subsoil. The necessity of considering the variable compressibility parameters with an increase in the effective vertical stress in the analysis of stage-loading embankments was emphasized by Mesri and Choi (1985). They explained that, in general, the compression $e - \log\sigma_v$ curve for most soft clays is highly nonlinear and is inadequate for characterizing the compression curve by a single value of C_c. The C_c values for different effective vertical stress levels used in the analysis of the Olga B embankment in Canada, as reported by Mesri and Choi (1985), are shown in Fig. 3.4. These values were calculated using the basic $e - \log\sigma_v$ curves obtained from the oedometer test results.

This nonlinear nature of $e-\log\sigma_v$ is more evident in peaty soil due to the significant decrease in compressibility as a physical reduction in the void ratio during the peat consolidation process. Hobbs (1986) observed that the lines of $e-\log\sigma_v$ tend to flatten out at higher pressures. The typical shape of the $e-\log\sigma_v$ curve for Sri Lankan peaty clay is shown in Fig. 3.5.

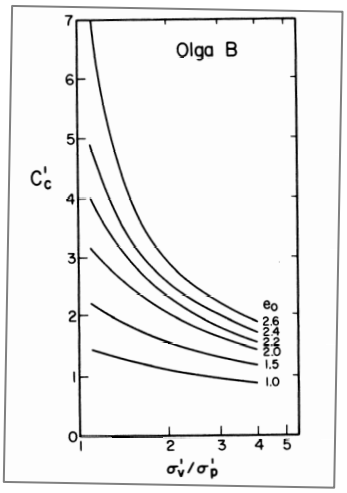

Fig. 3.4: Different C_c values for Olga clay (Mesri 1985)

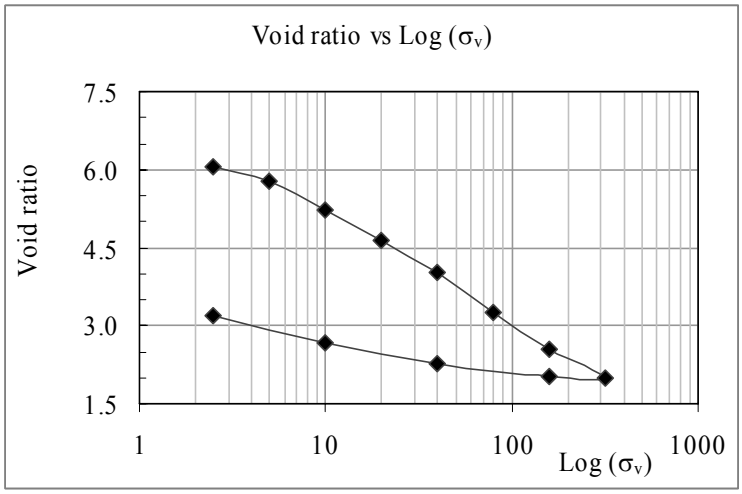

Fig. 3.5: Typical $e-\log\sigma_v$ curve for Sri Lankan peaty clay (STDP*-2003, HAV 27)

Therefore, the selection of the representative compressibility parameters corresponding to any void ratio and effective vertical stress level is essential when analyzing stage-constructed embankments which exert high levels of pressure on peaty subsoil. However, for the embankment analysis which will be described in Chapters 6 and 7, there are not enough consolidation test results to determine the compressibility parameters for each stress level. Thus, these parameters are determined by the following equations which assume that the compressibility parameters are varied in proportion to changes in the specific volume of the peaty soil.

$$\lambda' = \lambda\left(\frac{1+e}{1+e_0}\right) \tag{3.33}$$

$$\kappa' = \kappa\left(\frac{1+e}{1+e_0}\right) \tag{3.34}$$

where λ and κ are the compression index and swelling index, respectively, determined through the basic $e-\log\sigma_v$ curve using Eqs. 3.100 and 3.101 which will be explained later in Section 3.4, e_0 is the initial void ratio, and λ', κ', and e are the respective parameters at any stress level.

*Sourthern Transport Development Project -Kurundugahahethekma To Matara

Using the above equations, it is possible to vary the compressibility parameters throughout the compressible layer according to changes in the specific volume.

3.3.2 Relationship between Viscoplastic Parameter m' and C_α / C_c

The C_α / C_c concept of compressibility explains and predicts the secondary compression behavior of geotechnical materials (Mesri and Godlewski 1977, 1979; Mesri and Castro 1987; Mesri 1987; Mesri and Feng 1991). Mesri (1973) considered the relationship between C_α and C_c, and concluded that soils which are highly compressible in the primary phase would show high compressibility in the secondary phase as well. In the extensive research carried out by Mesri and his co-workers, as well as in other research works, it was discovered that the values of C_α / C_c were generally high for peat, somewhat lower for organic clay, medium for clay and organic silt, and low for certain types of clay and silt.

In the model, the secondary compression is taken into account by viscoplastic parameter m' and it is thought to occur as a continuous process. Parameter m' and the C_α / C_c concept that was proposed by Mesri et al. (1997) to predict the secondary consolidation, are interrelated by Oka (2005) and Adachi et al. (1984) as shown below.

Under isotropic consolidation ($S_{ij} = 0$), viscoplastic volumetric strain rate $\dot{\varepsilon}_v^{vp}$ can be evaluated by

$$\dot{\varepsilon}_v^{vp} = CM_m^* \exp\left\{ m' M_m^* \ln\left(\frac{\sigma'_m}{\sigma'^{(s)}_m} \right) \right\} \tag{3.35}$$

In the derivation of the above equation, M_m^* is the value of $\widetilde{M}^*$ in the normally consolidated region.

Also, viscoplastic volumetric strain ε_v^{vp} is satisfied by the following relationship:

$$d\varepsilon_v^{vp} = \frac{\lambda - \kappa}{(1+e)} \frac{d\sigma'^{(s)}_m}{\sigma'^{(s)}_m} \tag{3.36}$$

where σ'_m is the mean effective stress and (s) denotes the static equilibrium state. All other symbols have their usual meanings, as previously defined.

Supposing that the conditions of $\sigma_m'^{(s)} = \sigma_m'$ and $\varepsilon_v^{vp} = \varepsilon_{v(\infty)}^{vp}$ exist at the end of the secondary compression under a pressure of σ'_m, Eq. (3.36) leads to the following results by integration:

$$\varepsilon_{v(\infty)}^{vp} - \varepsilon_v^{vp} = \frac{\lambda - \kappa}{(1+e)} \ln \frac{\sigma_m'}{\sigma_m'^{(s)}} \tag{3.37}$$

Substituting Eq. (3.37) into Eq. (3.35) yields

$$\begin{aligned}
\dot{\varepsilon}_v^{vp} &= CM_m^* \exp\left\{ \frac{1+e}{\lambda - \kappa} m' M_m^* (\varepsilon_{v(\infty)}^{vp} - \varepsilon_v^{vp} \right\} \\
&= CM_m^* \exp\left(\frac{1+e}{\lambda - \kappa} m' M_m^* \varepsilon_{v(\infty)}^{vp} \right) \exp\left(- \frac{1+e}{\lambda - \kappa} m' M_m^{vp} \varepsilon_v^{vp} \right) \\
&= CM_m^* \exp\left(\frac{1}{\alpha} \varepsilon_{v(\infty)}^{vp} \right) \exp\left(- \frac{1}{\alpha} \varepsilon_v^{vp} \right) \\
\dot{\varepsilon}_v^{vp} &= C_1 \exp\left[- \frac{1}{\alpha} \varepsilon_v^{vp} \right]
\end{aligned} \tag{3.38}$$

in which

$$C_1 = CM_m^* \exp\left(\frac{1+e}{\lambda - \kappa} m' \varepsilon_{kk(\infty)}^{vp} \right) = CM_m^* \exp\left(\frac{1}{\alpha} \varepsilon_{kk(\infty)}^{vp} \right) \tag{3.39}$$

$$\alpha = \frac{\lambda - \kappa}{m'(1+e) M_m^*} \tag{3.40}$$

Assuming that C_1 is a constant value during the process, Eq. (3.38) can be integrated under the condition of $\varepsilon_v^{vp} = \varepsilon_{v(0)}^{vp}$ at time $t = t_0$.

$$\varepsilon_v^{vp} = \alpha \ln(t / t_0) + \varepsilon_{v(0)}^{vp} \tag{3.41}$$

or more precisely,

$$\alpha = \frac{\varepsilon_v^{vp} - \varepsilon_{v(0)}^{vp}}{\ln(t) - \ln(t_0)} = \frac{\Delta \varepsilon_v^{vp}}{\Delta \ln t} \tag{3.42}$$

where $\varepsilon_{v(0)}^{vp} = \alpha \ln(\alpha / C_1 t_0)$.

Therefore, it is clearly seen from Eqs. (3.40) and (3.42) that viscoplastic parameter m' and secondary consolidation rate α are interrelated.

In terms of the coefficient of secondary consolidation, c_α, Eq. (3.40) can be expressed as

$$m' = \frac{C_c - C_s}{C_\alpha M_m^*} \tag{3.43}$$

in which C_c and C_s are the compression index and the swelling index, respectively, determined through oedometer tests. In peat soils, $C_s \approx 0.1 C_c$, $M_m^* \approx 1$, and the viscoplastic parameter can often be approximated as $m' = 0.9 C_c / C_\alpha$.

Leroueil and Hight (2003) also experimentally verified the relationship between strain rate parameter m' and the C_α / C_c values for the soil reported by Mesri et al. (1995) and concluded that the two approaches used for describing the viscous behavior of soils during secondary consolidation are equivalent.

3.3.3 Account of a Finite Deformation

In finite element formulations based on the finite deformation theory, the updated Lagrangian method is adopted with the objective Jaumann rate of Cauchy stress for a weak form of the equilibrium equation (Oka et al. 2000, Oka et al. 2002, Kimoto et al. 2004, Higo et al. 2006). An eight-node quadrilateral element, with reduced Gaussian two-point integration, is employed for the displacement. Biot's two-phase mixture theory is used with a velocity-pore pressure formulation, and the pore water is defined at the four corner nodes of the element (see Fig. 3.6). In this section, the finite element formulation using the finite deformation theory is explained. A discretization of the equilibrium equation is presented followed by the continuity equation.

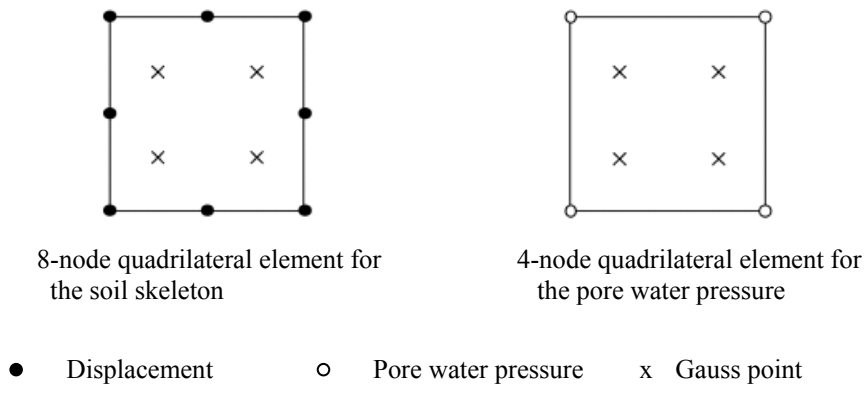

Fig. 3.6: Finite elements and Gauss integration points

In the model, Terzaghi's effective stress concept is used in the following form:

$$T_{ij} = T'_{ij} + u_w \delta_{ij} \tag{3.44}$$

$$\dot{T}_{ij} = \dot{T}'_{ij} + \dot{u}_w \delta_{ij} \tag{3.45}$$

in which T_{ij} denotes the total Cauchy stress tensor, T'_{ij} denotes the effective Cauchy stress tensor, u_w denotes the pore water pressure, δ_{ij} denotes Kronecker's delta, and the superimposed dot denotes the time differentiation.

The relationships between the normal stress rate tensor and the effective normal stress tensor are given by the following equations:

$$\dot{S}_{ij} = \dot{T}_{ij} + L_{kk} T_{ij} - T_{ik} L_{jk} \tag{3.46}$$

$$\dot{S}'_{ij} = \dot{T}'_{ij} + L_{kk} T'_{ij} - T'_{ik} L_{jk} \tag{3.47}$$

where $\dot{S}_{ij}$ is the total nominal stress rate tensor, $\dot{s}'_{ij}$ is the effective nominal stress rate tensor, and L_{ij} is the velocity gradient tensor. The relation between total nominal stress rate tensor $\dot{S}_{ij}$ and effective nominal stress rate tensor $\dot{S}'_{ij}$ can be obtained by substituting Eqs. (3.44) and (3.45) into Eq. (3.46), namely,

$$\dot{S}_{ij} = \dot{S}'_{ij} + \dot{u}_w \delta_{ij} + B_{ij} \tag{3.48}$$

$$B_{ij} = L_{kk} u_w \delta_{ij} - u_w \delta_{ik} L_{jk} \tag{3.49}$$

Assuming fully saturated conditions, the weak form of the equilibrium equation for the whole fluid-solid mixture in domain V can be expressed as

$$\int_V \dot{S}_{ij,j} \delta v_i dV = 0 \tag{3.50}$$

where δv_i is the virtual velocity vector component. Using the relation

$$(\dot{S}_{ij} \delta v_i)_{,j} = \dot{S}_{ij,j} \delta v_i + \dot{S}_{ij} \delta v_{i,j} \tag{3.51}$$

Eq. (3.50) can be rewritten as

$$\int_V \left(\dot{S}_{ij} \delta v_i\right)_{,j} dV - \int_V \dot{S}_{ij} \delta v_{i,j} dV = 0 \tag{3.52}$$

Applying the Gauss principle to the first term and substituting velocity gradient tensor L_{ij} for $v_{i,j}$ in the second term of Eq. (3.52), the relation yields

$$\int_{\Gamma} \left(\dot{S}_{ij}\delta v_i\right) n_j d\Gamma - \int_V \dot{S}_{ji}\delta L_{ij} dV = 0 \tag{3.53}$$

where Γ denotes the total boundary of the problem.

Incorporating the relationship for the total nominal stress rate tensor and the effective nominal stress rate tensor given in Eq. (3.48) into Eq. (3.53) yields

$$\int_V \dot{S}'_{ji}\delta L_{ij} dV + \int_V \dot{u}_w \delta_{ij}\delta L_{ij} dV + \int_V B_{ij}\delta L_{ij} dV = \int_{\Gamma} \left(\dot{S}_{ji}\delta v_i\right) n_j d\Gamma \tag{3.54}$$

According to Cauchy's stress principle, the nominal stress rate tensor, $\dot{S}_{ij}$, is related to the nominal traction vector, $\hat{S}_{ti}$, as follows:

$$\hat{S}_{ti} = \dot{S}_{ji} n_j \tag{3.55}$$

Substituting Eq. (3.55) and using relationship $\delta_{ij}\delta L_{ij} = \delta L_{kk} = \delta D_{kk}$, Eq. (3.54) is obtained as follows:

$$\int_V \dot{S}'_{ji}\delta L_{ij} dV + \int_V \dot{u}_w \delta D_{kk} dV + \int_V B_{ij}\delta L_{ij} dV = \int_{\Gamma} \hat{S}_{ti}\delta v_i d\Gamma \tag{3.56}$$

where D_{ij} is the stretching tensor which can be expressed in terms of the symmetric Cauchy stress rate and the velocity gradient tensor as

$$\dot{T}'_{ij} D_{ij} = \frac{1}{2}\dot{T}'_{ij}(L_{ij} + L_{ji}) = \dot{T}'_{ij} L_{ij} \tag{3.57}$$

Finally, by substituting Eqs. (3.47) and (3.57) into Eq. (3.56), a weak form of the equilibrium equation can be obtained.

$$\begin{aligned} \int_V \dot{T}'_{ij}\delta D_{ij} dV + \int_V A_{ij}\delta L_{ij} dV + \int_V L_{kk} T'_{ij}\delta L_{ij} dV + \int_V \dot{u}_w \delta D_{kk} dV \\ + \int_V B_{ij}\delta L_{ij} dV = \int_{\Gamma} \hat{S}_{ti}\delta v_i d\Gamma \end{aligned} \tag{3.58}$$

in which

$$A_{ij} = -\dot{T}'_{jk} L_{ik} \tag{3.59}$$

In the finite element formulation using the finite deformation theory, the objective Jaumann rate of Cauchy stress rate tensor $\hat{T}'_{ij}$ is defined by means of Cauchy stress rate tensor $\dot{T}'_{ij}$ and spin tensor W_{ij} as

$$\hat{T}'_{ij} = \dot{T}'_{ij} - W_{ik} T'_{kj} + T'_{ik} W_{kj} \tag{3.60}$$

The total stretching tensor, D_{ij}, is assumed to be composed of an elastic stretching tensor, D^e_{ij}, and a viscoplastic stretching tensor, D^{vp}_{ij}, namely,

$$D_{ij} = D^e_{ij} + D^{vp}_{ij} \tag{3.61}$$

The relation between the Jaumann rate of Cauchy stress $\hat{T}'_{ij}$ and elastic stretching tensor D^e_{ij} is

$$\hat{T}'_{ij} = C^e_{ijkl} D^e_{kl} \tag{3.62}$$

where C^e_{ijkl} is the elastic tangential stiffness matrix. Using the relations given in Eqs. (3.61) and (3.62), the following equation can be obtained:

$$\hat{T}'_{ij} = C^e_{ijkl} (D_{kl} - D^{vp}_{kl}) \tag{3.63}$$

Viscoplastic stretching tensor D^{vp}_{ij} is given as

$$D^{vp}_{ij} = \gamma \left\langle \Phi(f_y) \right\rangle \frac{\partial f_p}{\partial T'_{ij}} \tag{3.64}$$

in which f_y and f_p are static yield and potential functions, respectively, as outlined in Section 3.2.4. The tangent modulus method proposed by Peirce et al. (1984) is implemented to obtain viscoplastic stretching tensor D^{vp}_{ij}.

The relation outlined in Eq. (3.63) for the Jaumann rate vector of Cauchy stress $\left\{\hat{T}'\right\}$ and stretching vector $\{D\}$ can be written in the following matrix form:

$$\left\{\hat{T}'\right\} = [C]\{D\} - \{Q\} \tag{3.65}$$

where $[C]$ is the tangential stiffness matrix and $\{Q\}$ is the relaxation stress vector. Using the definition for $\left\{\hat{T}'\right\}$, mentioned in Eq. (3.60), Eq. (3.65) can be written as

$$\{\dot{T}'\} = [C]\{D\} - \{Q\} + \{W^*\} \tag{3.66}$$

where $\{W^*\}$ is the vector defined as $\{W^*\} = \{WT - TW\}$.

For the discretization of the weak form of the equilibrium equation, the following relations are defined:

$$\{v\} = [N]\{v^*\} \tag{3.67}$$

$$\{D\} = [B]\{v^*\} \tag{3.68}$$

$$\{L\} = [B_M]\{v^*\} \tag{3.69}$$

$$trD = \{B_v\}^T \{v^*\} \tag{3.70}$$

$$\dot{u}_w = \{N_h\}\{\dot{u}_w{}^*\} \tag{3.71}$$

where $\{v\}$ is the velocity vector in an element, $[N]$ is the shape function of the eight-node quadrilateral element, $\{v^*\}$ is the nodal velocity vector, $[B]$ is the matrix which transforms the nodal velocity into the stretching vector, $\{L\}$ is the velocity gradient vector, $[B_M]$ is the matrix which transforms the nodal velocity into the velocity gradient vector, and $[B_v]$ is the vector which transforms the nodal velocity into the trace of D. In Eq. (3.71), $\dot{u}_w$ is the pore pressure rate, $\{\dot{u}_w^*\}$ is the nodal pore pressure rate vector, and $[N_h]$ is the shape function of the four-node quadrilateral element.

Incorporating Eq. (3.66) into Eq. (3.58) and using the relations mentioned in Eqs. (3.67)~(3.71), the final weak form of the equilibrium equation becomes

$$[K]\{v^*\} - \int_V [B]^T \{Q\} dV + \int_V [B]^T \{W^*\} dV + [K_L]\{v^*\} + [K_v]\{\dot{u}_w^*\} = \{\dot{F}\} \tag{3.72}$$

in which

$$[K] = \int_V [B]^T [C][B] dV \tag{3.73}$$

$$[K_L] = \int_V [B_M]^T [D_s'][B_M] dV + \int_V [B_M]^T [U][B_M] dV + \int_V [B_M]^T \{T'\}\{B_v\}^T dV \tag{3.74}$$

$$[K_v] = \int_V \{B_v\}\{N_h\}^T dV \tag{3.75}$$

$$\{\dot{F}\} = \int_\Gamma [N]^T \{\hat{S}_t\} d\Gamma \tag{3.76}$$

$$[A] = [D_s'][B_M]\{v^*\} \tag{3.77}$$

$$[B] = [U][B_M]\{v^*\} \tag{3.78}$$

The relation between nodal velocity vector $\{v^*\}$ and nodal displacement vector $\{\Delta u^*\}$ is given by Euler's approximation as

$$\{v^*\} = \frac{\{\Delta u^*\}}{\Delta t} \tag{3.79}$$

Similarly, the pore water pressure can be obtained as

$$\{\dot{u}_w^*\} = \frac{\{u_w^*\}_{t+\Delta t} - \{u_w^*\}_t}{\Delta t} \tag{3.80}$$

Substituting Eqs. (3.79) and (3.80) into Eq. (3.72), the discretization of the equilibrium equation is finally obtained.

$$\begin{aligned}[[K] + [K_L]]\{\Delta u^*\} + [K_v]\{u_w^*\}_{t+\Delta t} = \Delta t\{\dot{F}\} + [K_v]\{u_w^*\}_t + \\ \Delta t \int_V [B]^T \{Q\} dV - \Delta t \int_V [B]^T \{W^*\} dV\end{aligned} \tag{3.81}$$

The discretzation procedure for the continuity equation is described below. It assumes that the compressibility of the soil particles and the pore water pressure is negligible.

Consider a boundary surface Γ of a closed domain V which can be separated into two components, namely,

$$\Gamma = \Gamma_p + \Gamma_v \tag{3.82}$$

Γ_p, the boundary at which the pore pressure is specified, and Γ_v, the boundary at which the flow of water is specified, are given by

$$u_w = \bar{u}_w \qquad \text{on} \qquad \Gamma_p \tag{3.83}$$

$$v_i = \bar{v}_i \qquad \text{on} \qquad \Gamma_v \tag{3.84}$$

The continuity equation for the fluid phase can be derived from the mass conversation equation for the soil-water mixture as follows:

$$\frac{k}{\gamma_w} u_{w,ii} + D_{ii} = 0 \tag{3.85}$$

where k is the coefficient of permeability, D_{ii} is the stretching tensor, and γ_w is the density of water.

The weak form of the continuity equation is given as

$$\int_V \left(\frac{k}{\gamma_w} u_{w,ii} + D_{ii} \right) \hat{u}_w dV = \frac{k}{\gamma_w} \int_V u_{w,ii} \hat{u}_w dV + \int_V D_{ii} \hat{u}_w dV = 0 \tag{3.86}$$

where $\hat{u}_w$ is the test function for the pore water pressure. Using the relation

$$u_{w,ii} \hat{u}_w = \left(u_{w,i} \hat{u}_w \right)_{,i} - u_{w,i} \hat{u}_{w,i} \tag{3.87}$$

Eq. (3.86) can be rewritten as

$$\frac{k}{\gamma_w} \int_V \left(\hat{u}_w u_{w,i} \right)_{,i} dV - \frac{k}{\gamma_w} \int_V \hat{u}_{w,i} u_{w,i} dV + \int_V \hat{u}_w D_{ii} dV = 0 \tag{3.88}$$

By applying Gauss's theorem, the above equation can be expressed as

$$\frac{k}{\gamma_w} \int_{\Gamma_v} \hat{u}_w u_{w,i} n_i d\Gamma - \frac{k}{\gamma_w} \int_V \hat{u}_{w,i} u_{w,i} dV + \int_V \hat{u}_w D_{ii} dV = 0 \tag{3.89}$$

in which n is the unit normal vector to boundary surface Γ. The following vectors and matrices are defined for the discretization:

$$u_w = \{N_h\}^T \left\{ u_w^* \right\} \quad , \quad \hat{u}_w = \{N_h\}^T \left\{ \hat{u}_w^* \right\} \tag{3.90}$$

$$\{u_{w,i}\}=\{N_{h,i}\}^T\left\{u_w^*\right\}=[B_h]\left\{u_w^*\right\}\quad,\quad \{\hat{u}_{w,i}\}=[B_h]\left\{\hat{u}_w^*\right\} \tag{3.91}$$

$$[N_{h,i}]=\nabla\{N_h\} \tag{3.92}$$

$$D_{ii}=trD=\{B_v\}^T\left\{v^*\right\} \tag{3.93}$$

Substituting Eqs. (3.90) ~ (3.93) into Eq. (3.89) and considering the arbitrariness of the unconstrained test function, $\left\{\hat{u}_w^*\right\}^T$, we get the following equation:

$$\begin{aligned}\frac{k}{\gamma_w}\int_\Gamma\{N_h\}^T\{n\}^T\{B_h\}d\Gamma\left\{u_w^*\right\}-\frac{k}{\gamma_w}\int_V[B_h]^T[B_h]dV\left\{u_w^*\right\}\\ +\int_V\{N_h\}^T\{B_v\}^T dV\left\{v^*\right\}=0\end{aligned} \tag{3.94}$$

Substituting Eq. (3.79) into Eq. (3.94) yields the discrete form of the continuity equation as

$$[K_v]^T\left\{\Delta u^*\right\}-\Delta t([K_h]+[V])\left\{u_w^*\right\}_{t+\Delta t}=0 \tag{3.95}$$

where

$$[K_h]=\frac{k}{\gamma_w}\int_V[B_v]^T[B_h]dV \tag{3.96}$$

$$[K_v]^T=\int_V\{N_h\}\{B_v\}^T dV \tag{3.97}$$

$$[V]=-\frac{k}{\gamma_w}\int_\Gamma\{N_h\}\{n\}^T[B_h]d\Gamma \tag{3.98}$$

The final system of the equation for the FEM analysis, based on the finite deformation theory, is obtained by combining Eqs. (3.81) and (3.95) as

$$\begin{aligned}&\begin{bmatrix}[K]+[K_L] & [K_v]\\ [K_v]^T & -\Delta t([K_h])\end{bmatrix}\begin{Bmatrix}\Delta u^*\\ u_{w,t+\Delta t}^*\end{Bmatrix}\\ &=\begin{Bmatrix}\Delta t\{\dot{F}\}+[K_v]\left\{u_w^*\right\}_t+\Delta t\int_V[B]^T\{Q\}dV-\Delta t\int_V[B]^T\left\{W^*\right\}dV\\ \Delta t[V]\end{Bmatrix}\end{aligned} \tag{3.99}$$

3.4 Determination of the Model Parameters

The material parameters required for the analysis are determined as follows:

- Initial void ratio e_0 can be obtained from the physical properties.

- For the compression index and the swelling index

$$\lambda = C_c / \ln 10 = 0.434 C_c \tag{3.100}$$

$$\kappa = C_s / \ln 10 = 0.434 C_s \tag{3.101}$$

  where C_c and C_s are the compression and the recompression indices, respectively, determined from oedometer tests.

- The initial permeability coefficient (k_0) of the soil can be determined by directly measuring the soil permeability with consolidation tests under laboratory conditions. Otherwise, the initial vertical permeability (k_{v0}) can be calculated with the relationship given in Terzaghi's one-dimensional theory of consolidation using the following relationship:

$$k_v = m_v c_v \gamma_w \tag{3.102}$$

  where m_v is the coefficient of volume compressibility, c_v is the coefficient of consolidation, and γ_w is the unit weight of water.

  However, it has been observed that the permeability calculated with the above relationship often underestimates the field value. On the other hand, the in situ horizontal permeability coefficient (k_h) can be reliably evaluated through in situ tests. Field permeability tests conducted on Sri Lankan peaty clay indicated that the in-situ value for k_h is in the order of 10^{-7}m/s.

- Permeability change index C_k can also be deduced from the variations in permeability and void ratio observed from the above-described methods. In addition, Mesri et al. (1997) reported that the peat deposit value of $C_k = \Delta e / \Delta \log k_v$ was close to $e_0/4$, in which e_0 is the in situ void ratio.

- The stress ratio at maximum compression M_m^* is defined as the stress ratio whereby maximum occurs in the drained compression tests. For clay, however, it has been assumed to equal the stress ratio at the critical state. Herein, M_m^* is determined from the stress ratio at the residual state on the undrained triaxial compression tests and

$M_m^* = \sqrt{\frac{2}{3}}\, M_m$ where M_m is the slope of the critical state line obtained from the triaxial test.

- Viscoplastic parameter m' is related to the coefficient of secondary compression, $\alpha (= \mathrm{d}v^p / \mathrm{d}\ln t)$, and can be determined using the following relationship:

$$m' = \frac{C_c - C_s}{C_\alpha M_m^*} \tag{3.103}$$

for which all the symbols are the same as previously defined. It has been observed that the C_α determined from the long-term consolidation tests can provide a more representative value in the case of peaty clay.

- The values used here for the coefficient of earth pressure at rest, K_0, are based on the report by Edil and Dhowian (1981). They pointed out that the K_0 calculated from the empirical correlations, based on the measured value of the angle of internal friction for soil (e.g., Jaky 1948), rarely agrees with the measured value of K_0 for peat. Thus, it is suggested that the following values be used for engineering purposes.

Fibrous peat - $K_0 = 0.3$ Amorphous peat - $K_0 = 0.53$

- The compression yield stress, σ'_{mbi}, is assumed to be equal to the preconsolidation pressure determined through oedometer tests.

- Viscoplastic parameter C is related to the initial volumetric strain rate, $\dot{v}_{(0)}^p$, through the following relation:

$$\dot{v}_{(0)}^p = M_m^* C \tag{3.104}$$

Parameter C also reflects the effect of the duration of the preceding secondary compression, i.e., quasi-overconsolidation. A heavily aged clay stratum has a large value for the initial volumetric strain compared to the value for normally consolidated clay, i.e., young clay. Conversely, if the value of the initial volumetric strain is assumed to be zero for both types of clay at the beginning of consolidation, then the value of C for aged clay is smaller than that for young clay (Oka et al.1986). In the present research work, viscoplastic parameter C was determined by simulating triaxial test results.

- Degradation parameter β, structural parameter σ'_{maf}, initial shear modulus G_0, and above-mentioned viscoplastic parameter C are determined by curve fitting the stress-strain curve of the undrained triaxial tests.

3.5 Performance of the Elasto-viscoplastic Model with the Modified Cam-clay Theory

In the model by Kimoto and Oka (2005), the mechanical behavior of clays in the static equilibrium is described in the original Cam-clay model by Roscoe et al. (1963), Roscoe and Schofield (1963). The viscoplastic potential function is also in the shape of the original Cam-clay type. Since the development of the modified Cam-clay theory by Roscoe and Burland (1968), however, the modified Cam-clay theory has probably been more widely used for numerical predictions. In this section, therefore, the performance of the model by Kimoto and Oka (2005), which incorporates the modified Cam-clay theory, is studied and compared with the original model which is based on the original Cam-clay theory.

The basic difference between the original and the modified Cam-clay models comes from the expression for dissipated work, δW , given as follows.

In the original Cam-clay theory, the increment of work dissipated per unit bulk volume of an isotropic continuum during deformation was expressed as

$$\delta W = p' \delta \varepsilon_{vol} + q \delta \varepsilon_q \tag{3.105}$$

where p' and q are the mean effective stress and the shear stress, respectively, and $\delta \varepsilon_{vol}$ and $\delta \varepsilon_q$ are the corresponding strain increments associated with p' and q .

In the derivation of the modified Cam-clay theory, Roscoe and Burland (1968) suggested that it was reasonable to assume that under an isotropic stress of $q = 0$, there is no distortion ($\delta \varepsilon_q = 0$) in normally consolidated clay. Since normally consolidated clay can deform irrecoverably under isotropic stress, Eq. (3.105) becomes

$$(\delta W_{dissipated})_{q=0} = p' \delta \varepsilon_{vol,p} \tag{3.106}$$

At the critical state condition, $q / p = M$ and $\delta \varepsilon_{vol,p} = 0$, so that Eq. (3.105) becomes

$$(\delta W_{dissipated})_{q=Mp} = Mp' \delta \varepsilon_q \tag{3.107}$$

A generalization of the conditions in Eqs. (3.106) and (3.107) is

$$\delta W_{dissipated} = p' \sqrt{(\delta \varepsilon_{vol,p})^2 + (M \delta \varepsilon_q)^2} \tag{3.108}$$

This is the expression for work dissipation used in the modified Cam-clay theory.

Employing the above expression (3.108) and the normality condition (Roscoe and Burland 1968), the equation for the yield locus of the modified Cam-clay can be obtained as

$$f_y = \frac{p'}{p'_0} - \frac{M^2}{\eta^2 + M^2} = 0 \tag{3.109}$$

where η is the value of the stress ratio (q/p) and M is the value when the stress ratio reaches the critical state. $p' = p'_0$ at $\eta = 0$ (isotropic normal compression).

Eq. (3.109) represents an ellipse in the q, p space with its center at $p_0/2$.

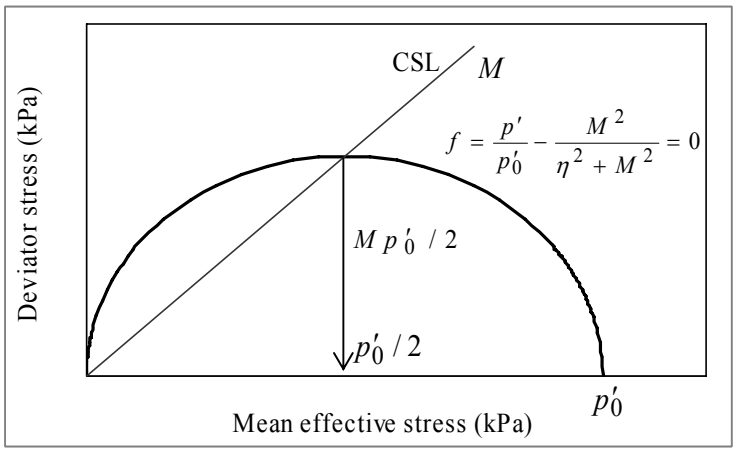

Fig. 3.7: Modified Cam-clay yield locus

3.5.1 Derivation of the Viscoplastic Volumetric and the Deviatoric Strain Rates

In this section, the derivation of the viscoplastic volumetric strain rate and the viscoplastic deviatoric strain rate for the Kimoto and Oka (2005) model, incorporating the modified Cam-clay theory, is described.

The yield function given in Eq. (3.109) can be generalized as

$$f_y = \ln\left(\frac{\sigma'_m}{\sigma'^{(s)}_{my}}\right) + \ln\left(\frac{\overline{\eta}^{*2} + \widetilde{M}^{*2}}{\widetilde{M}^{*2}}\right) = 0 \tag{3.110}$$

where all the symbols have their usual meanings, as previously defined.

As described in Section 3.2.6, the model proposed by Kimoto and Oka (2005) for the viscoplastic strain rate is given by the following equation which is based on the overstress type of viscoplastic theory (Oka 2005; Perzyna 1963):

$$\dot{\varepsilon}_{ij}^{vp} = \gamma\left\langle \Phi_1(f_y) \right\rangle \frac{\partial f_p}{\partial \sigma'_{ij}} \tag{3.111}$$

where

$$\left\langle \Phi_1(f_y) \right\rangle = \begin{cases} \Phi_1(f_y) & ; f_y > 0 \\ 0 & ; f_y \le 0 \end{cases} \tag{3.112}$$

When the modified yield function (Eq. 3.110) incorporates material function Φ_1

$$\gamma\Phi(f_y) = C\sigma'_m \exp\left\{ m'\left(\ln\left(\frac{\sigma_m{}'}{\sigma'_{mb}} \right) + \ln\left(\frac{\overline{\eta}^{*2} + \widetilde{M}^{*2}}{\widetilde{M}^{*2}} \right) \right) \right\} \tag{3.113}$$

The derivative of $\dfrac{\partial f_p}{\partial \sigma_{ij}}$ is

$$\frac{\partial f_p}{\partial \sigma_{ij}} = \left\{ \frac{1}{\sigma'_m} - \frac{2\eta^*_{kl}\,(\eta^*_{kl} - \eta^*_{kl(0)})}{\sigma'_m\,(\overline{\eta}^{*2} + \widetilde{M}^{*2})} \right\} \frac{1}{3}\delta_{ij} + \left\{ \frac{2\,(\eta^*_{ij} - \eta^*_{ij(0)})}{\sigma'_m\,(\overline{\eta}^{*2} + \widetilde{M}^{*2})} \right\} \tag{3.114}$$

Using the above equations, therefore, viscoplastic deviatoric strain rate $\dot{e}_{ij}^{vp}$ can be calculated as follows:

$$\dot{e}_{ij}^{vp} = C\sigma'_m \exp\left\{ m'\left(\ln\left(\frac{\sigma_m{}'}{\sigma'_{mb}} \right) + \ln\left(\frac{\overline{\eta}^{*2} + \widetilde{M}^{*2}}{\widetilde{M}^{*2}} \right) \right) \right\} \frac{\partial f_p}{\partial S_{ij}}$$

$$\dot{e}_{ij}^{vp} = C \exp\left\{ m'\left(\ln\left(\frac{\sigma_m{}'}{\sigma'_{mb}} \right) + \ln\left(\frac{\overline{\eta}^{*2} + \widetilde{M}^{*2}}{\widetilde{M}^{*2}} \right) \right) \right\} \left\{ \frac{2\,(\eta^*_{ij} - \eta^*_{ij(0)})}{(\overline{\eta}^{*2} + \widetilde{M}^{*2})} \right\} \tag{3.115}$$

Viscoplastic volumetric strain rate $\dot{\varepsilon}_v^{vp}$ is obtained as follows:

$$\dot{\varepsilon}_v^{vp} = C\sigma'_m \exp\left\{ m'\left(\ln\left(\frac{\sigma_m{}'}{\sigma'_{mb}} \right) + \ln\left(\frac{\overline{\eta}^{*2} + \widetilde{M}^{*2}}{\widetilde{M}^{*2}} \right) \right) \right\} \frac{\partial f_p}{\partial \sigma'_{kk}}$$

$$\dot{\varepsilon}_v^{vp} = C' \exp\left\{ m'\left(\ln\left(\frac{\sigma_m{}'}{\sigma'_{mb}} \right) + \ln\left(\frac{\overline{\eta}^{*2} + \widetilde{M}^{*2}}{\widetilde{M}^{*2}} \right) \right) \right\} \left\{ 1 - \frac{2\eta^*_{ij}(\eta^*_{ij} - \eta^*_{ij(0)})}{(\overline{\eta}^{*2} + \widetilde{M}^{*2})} \right\} \tag{3.116}$$

Table 3.1 summarizes the yield function, the viscoplastic deviatoric strain rate, and the volumetric strain rate based on the original and the modified Cam-clay theories.

Table 3.1: Comparison of original Cam-clay and modified Cam-clay theories

	Original Cam-clay	Modified Cam-clay
Yield function	$f_y = \bar{\eta}^* + \tilde{M}^* \ln\left(\frac{\sigma'_m}{\sigma'^{(s)}_{my}}\right)$	$f_y = \ln(\frac{\sigma_m{}'}{\sigma'^{(s)}_{my}}) + \ln(\frac{\bar{\eta}^{*2} + \tilde{M}^{*2}}{\tilde{M}^{*2}})$
Viscoplastic deviatoric strain	$= C\exp\left\{m'\left(\bar{\eta}^* + \tilde{M}^* \ln\left(\frac{\sigma'_m}{\sigma'_{mb}}\right)\right)\right\}\frac{(\eta^*_{ij} - \eta^*_{ij(0)})}{\bar{\eta}^*}$	$=C\exp\left\{m'\left(\ln\left(\frac{\sigma_m{}'}{\sigma'_{mb}}\right)+\ln\left(\frac{\bar{\eta}^{*2}+\tilde{M}^{*2}}{\tilde{M}^{*2}}\right)\right)\right\}\left\{\frac{2(\eta^*_{ij} - \eta^*_{ij(0)})}{(\bar{\eta}^{*2} + \tilde{M}^{*2})}\right\}$
Viscoplastic volumetric strain	$= C\exp\left\{m'\left(\bar{\eta}^* + \tilde{M}^* \ln\left(\frac{\sigma'_m}{\sigma'_{mb}}\right)\right)\right\}\left\{\tilde{M}^* - \frac{\eta^*_{ij}(\eta^*_{ij} - \eta^*_{ij(0)})}{\bar{\eta}^*}\right\}$	$= C\exp\left\{m'\left(\ln\left(\frac{\sigma_m{}'}{\sigma'_{mb}}\right)+\ln\left(\frac{\bar{\eta}^{*2}+\tilde{M}^{*2}}{\tilde{M}^{*2}}\right)\right)\right\}\left\{1-\frac{2\eta^*_{ij}(\eta^*_{ij} - \eta^*_{ij(0)})}{(\bar{\eta}^{*2} + \tilde{M}^{*2})}\right\}$

It should be noted that the expression for calculating viscoplastic parameter m' from the strain-controlled triaxial tests, using the model based on the modified Cam-clay theory, is different than that based on the original Cam-clay theory. This is because the two models yield different expressions for viscoplastic deviatoric strain rate $\dot{e}^{vp}_{ij}$.

For the model which incorporates the modified Cam-clay theory, the expression for determining m' from the strain-controlled triaxial tests becomes

$$\ln\left\{\frac{\left[\left[\frac{q^{(1)}}{\sigma'^{(0)}_m}\right]^2 + M^2\right]\dot{e}^{(1)}_{11}/q_1}{\left[\left[\frac{q^{(2)}}{\sigma'^{(0)}_m}\right]^2 + M^2\right]\dot{e}^{(2)}_{11}/q_2}\right\} = m'\left\{\ln\left[\left[\frac{q_1}{\sigma'^{(0)}_m}\right]^2 + M^2\right] - \ln\left[\left[\frac{q_2}{\sigma'^{(0)}_m}\right]^2 + M^2\right]\right\} \quad (3.117)$$

As mentioned in Kimoto (2003), the expression for m' in the original Cam-clay case is

$$m' = \sqrt{\frac{3}{2}}\frac{\ln\dot{\varepsilon}^{(1)}_{11} - \ln\dot{\varepsilon}^{(2)}_{11}}{\left(\frac{q}{\sigma'_m}\right)^{(1)} - \left(\frac{q}{\sigma'_m}\right)^{(2)}} \quad (3.118)$$

The m' values generated by the two methods are experimentally verified. For this purpose, the results of strain-controlled triaxial tests (Fig.3.8 and Fig.3.9) conducted on Aji clay from Osaka, Japan are used.

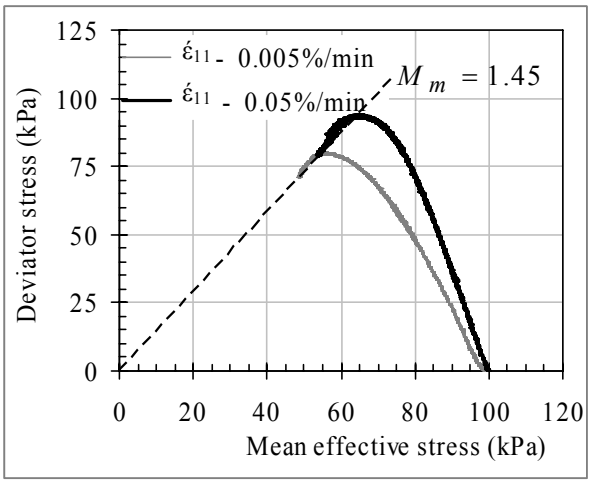

Fig. 3.8: Stress paths

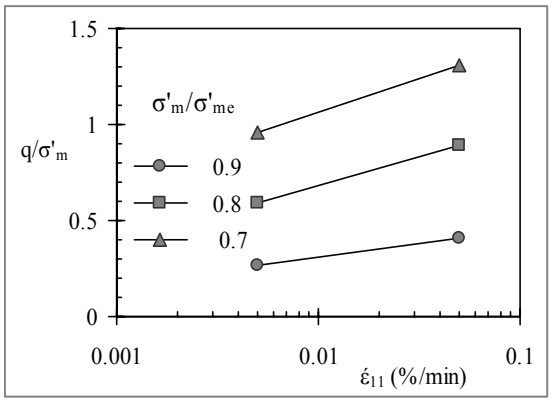

Fig. 3.9: q/σ'_m vs. $\dot{\varepsilon}_{11}$ relationship

Table 3.2: m' calculated from the experimental results

σ'_m(kPa)	σ'_m/σ'_{me}	q(kPa)	q/σ'_m	$\dot{\varepsilon}_{11}$(%/min)	m'(original)	m'(modified)
90	0.9	24.17	0.268556	0.005		
90	0.9	36.97	0.410778	0.05	23.48	44.19
80	0.8	47.42	0.59275	0.005		
80	0.8	71.45	0.893125	0.05	11.12	12.33
70	0.7	67.35	0.962143	0.005		
70	0.7	91.72	1.310286	0.05	9.59	9.59

The experimental results indicate that the m' values calculated by the model incorporating the modified and the original Cam-clay theories are almost equal, except for during the initial stage.

3.5.2 Evaluation of the Model Performance

The performance of the model to incorporate the modified Cam-clay theory is evaluated and compared with the model based on the original Cam-clay theory by simulating the triaxial test results. For this purpose, the stress-strain behavior obtained from the triaxial tests conducted on soft marine clay found near the Aji River in Osaka, Japan is used. The required parameters for the simulation, such as the compression index, the swelling index, the initial void ratio, and the compression yield stress, are taken from consolidation test data on the same clay. As indicated in Table 3.2, the calculated m' values are based on the two methods and are almost equal, except during the initial stage. Therefore, it is

reasonable to assume common average values for both models as m' is a constant for a particular soil (Mesri et al.1977; Oka et al.1984).

Table 3.3: Parameters used in the simulation

Parameters			Values
Strain rate	$\dot{\varepsilon}$	(%/min)	0.05
Initial void ratio	e_0		1.727
Initial elastic shear modulus[#]	G_0	(kPa)	3100
Compression index	λ		0.3201
Swelling index	κ		0.0482
Stress ratio at critical state	M_m^*		1.184
Compression yield stress	$\sigma'_{mbi}(\sigma'_{mai})$	(kPa)	100
Viscoplastic parameter	m'		20
Viscoplastic parameter[#]	C	(1/s)	4.0x 10^{-11}
Structural parameter [#]	σ'_{maf}	(kPa)	66
Structural parameter [#]	β		3

[#] From the triaxial test stress–strain relationship

The simulation is initially carried out using the model based on the original Cam-clay theory. The parameters used in the simulation are listed in Table 3.3. Then, using the same parameters, an analysis is performed with the model based on the modified Cam-clay theory. The obtained results are shown in Figs. 3.10 and 3.11. As shown in Figs. 3.10 and 3.11 when the results predicted by the model based on the original Cam-clay theory correlate well with the observed stress-strain behavior, the results produced by the model based on the modified Cam-clay theory deviate significantly from the experimental data and the failure stress is overpredicted for the same parameters.

In order to obtain better results by the model with the modified Cam-clay theory, a simulation is carried out using a higher value for viscoplastic parameter C. The analysis indicates that when parameter C is equal to 2 x 10^{-7} s^{-1}, the predictions show a better correlation with the experimental results.

However, the value for parameter C, which produces better results with the model based on the modified Cam-clay theory, is considerably high. With such a high C value, the numerical stability of the analysis declines. Thus, it seems that the application of the constitutive model incorporating the modified Cam-clay theory has some limitations. Furthermore, even with the use of a higher C value, there is no significant improvement in the prediction of the stress path which shows a considerable deviation from that in the

experimental results during the initial stage. Considering the above facts, the model incorporating the original Cam-clay theory is found to be more suitable to predicting the stress–deformation behavior of soil with the present definition of the parameters.

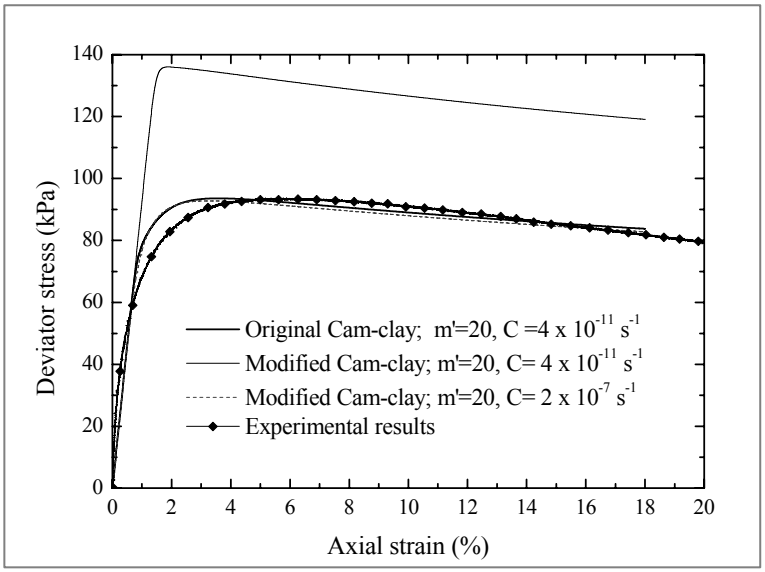

Fig. 3.10: Comparison of the stress-strain behavior

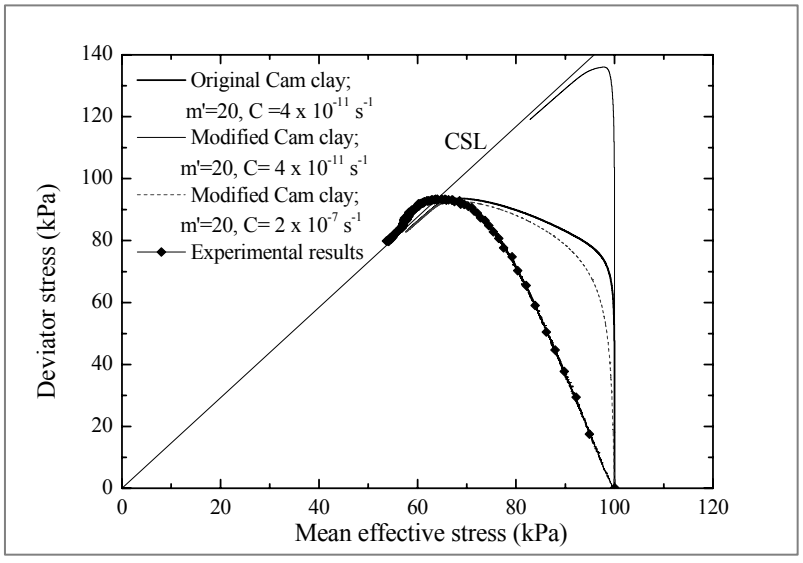

Fig. 3.11: Comparison of the stress paths

3.6 Summary and Remarks

In this chapter, the viscoplastic model and the analysis methods used to simulate the peat consolidation process were described. The constitutive model (Kimoto and Oka 2005) is based on Perzyna's type of viscoplastic theory and the Cambridge elasto-plastic theory combined with empirical evidence. In the model, the static yield function, the viscoplastic potential function, and the overconsolidated boundary surface which delineates the overconsolidated region from the normally consolidated region are in the shape of the original Cam-clay type. In the model, the secondary compression is taken into account by viscoplastic parameter m', which is related to the C_α / C_c ratio of the soil. Also, it was found that the model can accommodate the effect of structural degradation on consolidation by introducing viscoplastic strain softening in addition to strain hardening with viscoplastic volumetric strain.

The variable permeability was considered in the analysis by varying the coefficient of permeability with the void ratio of the soil. The compressibility parameters were proposed to vary with the specific volume of the soil in the analysis of stage-constructed embankments which exert high levels of pressure on the peaty clay. In the finite element formulations, which are based on the finite deformation theory, an updated Lagrangian method was adopted.

The material parameters required for the analysis and the procedures applied to evaluate them, with standard laboratory and field tests, were explained. Some material parameters could be directly evaluated from the test data. However, some model parameters, such as the initial shear modulus, viscoplastic parameter C, and the structural parameters, were determined by simulating the stress-strain curve of the triaxial tests.

The performance of the model to incorporate the original and the modified Cam-clay theories was evaluated by simulating the stress-strain characteristics of clay in triaxial tests. The results predicted by the model based on the original Cam-clay theory were found to correlate well with the observed stress-strain behavior, whereas the results produced by the model based on the modified Cam-clay theory deviated significantly from the experimental data and the failure stress was overpredicted for the same parameters. It was confirmed, therefore, that the model which incorporates the original Cam-clay theory is more suitable to predicting the stress–deformation behavior of soil with the present definition of the parameters.

Chapter 4

MODEL VALIDATION USING LABORATORY CONSOLIDATION TEST RESULTS

4.1 Introduction

The successful application of any constitutive model has to be verified in the modeling of simple problems, such as laboratory tests, before it can be applied to full-scale problems. The verification of a proposed model against laboratory one-dimensional consolidation or triaxial tests gives some insight into the behavior of the model and enables a previous understanding of its capabilities and limitations. However, such verifications do not guarantee the model's predictive ability to deal with full-scale problems which may include complicated boundary conditions in the field.

The main focus of this chapter is to study the predictive capability of the elasto-viscoplastic model to capture two important phenomena that have been identified in the peat consolidation process. One phenomenon is the one-dimensional strain-time relationship, including creep (or secondary) settlement, which is known to contribute significantly to the overall settlement of peaty soil. The other phenomenon is the influence of specimen thickness (length of the drainage path) on settlement predictions. Model performances to grasp these two phenomena are verified against the experimental observations in consolidation model tests conducted on peaty clay and reported by Kugan et al. (2003). In addition, the mathematically derived relationship between model parameter m' and the C_α / C_c ratio of the soil is experimentally verified using data from laboratory tests on soft marine clay found in Osaka, Japan. This chapter consists of the following sections:

1) Application of the model to predict laboratory consolidation behavior
2) Model performance of settlement prediction considering different layer thicknesses
3) Experimental verification of the relation between parameter m' and C_α / C_c.

4.2 Application of the Model to Predict Laboratory Consolidation Behavior

The elasto-viscoplastic constitutive model (Kimoto and Oka 2005) was validated using laboratory consolidation test results. For this purpose, data on medium-scale consolidation tests with the 2-day time increment reported by Kugan et al. (2003) were used. The specimen was 203 mm in diameter and 275 mm in height. Drainage was permitted only at the top surface of the sample during the tests. The tests were conducted on reconstituted peaty clay obtained from sites along the Colombo-Katunayaka Expressway (CKE) project. A load of 30 kN/m^2 was applied in steps of 5 kN/m^2 with time intervals of two days. An incremental load application was adopted to avoid shear failure in the peaty clay in case a full load was applied all at once. The one-dimensional normally consolidated behavior for load increments of 5-30 kPa was predicted using the elasto-viscoplastic model and Terzaghi's model, and compared with the measured strains.

4.2.1 Determination of the Model Parameters for the Analysis

The parameters required for the elasto-viscoplastic model analysis for load increments of 5-30 kPa were determined as shown below.

The compression index and the swelling index were determined by following the method outlined in Section 3.4 and using the results of the oedometer tests conducted under the same experimental program. The results of the void ratio vs. log (σ'_v) relation obtained in the oedometer tests are shown in Fig. 4.1.

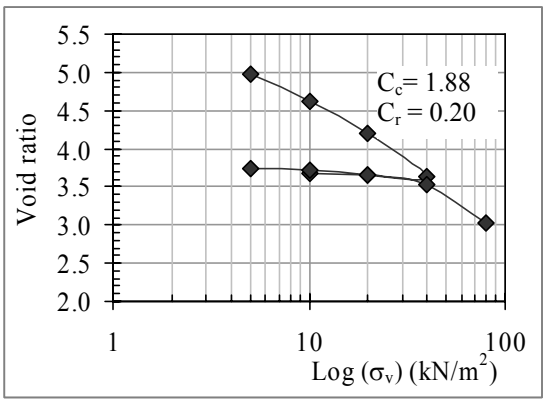

Fig. 4.1: Void ratio vs. Log (σ'_v) relationship

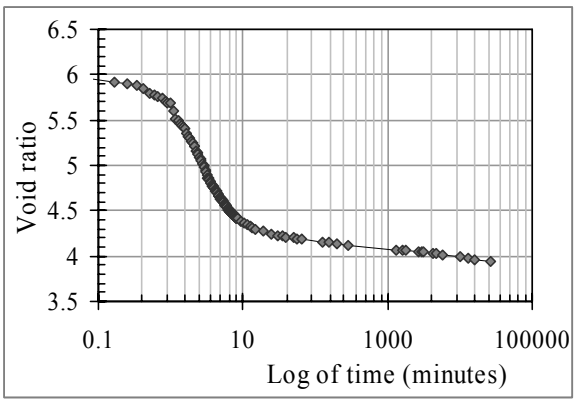

Fig. 4.2: Void ratio vs. Log (time) relationship

The initial permeability coefficient, k_0, was calculated using Eq. (3.102) in Section 3.4. For that, the required coefficient of volume compressibility, m_v, and the coefficient of consolidation, c_v, were calculated from the time-settlement curve for load increments of 5-10 kPa. The respective values were found to be 0.031 m^2/kN and 4.1 m^2/year, and yielded a k_0 value of 4 x 10^{-8} m/s. The permeability change index, C_k, was calculated from the gradient of the $e - \ln k$ graph deduced from the oedometer test results. Viscoplastic parameter m' was calculated using Eq. (3.103) in Chapter 3. The required compression index, swelling index, and coefficient of secondary consolidation were taken from the consolidation test results shown in Figs. 4.1 and 4.2. The compression yield stress, σ'_{mbi}, was determined by considering the previous load (5 kPa) and the coefficient of lateral earth pressure at rest used in the analysis. The coefficient of lateral earth pressure at rest, K_0, was 0.53, as recommended by Edil and Dhowian (1981) for amorphous peat. Realistic values were assumed for viscoplastic parameter C and structural parameters σ'_{maf} and β. The parameters required for Terzaghi's model, namely, the coefficient of volume compressibility, m_v, and the coefficient of consolidation, c_v, were calculated with the consolidation test results. The initial conditions of the sample, together with the parameters used for both the elasto-viscoplastic model and Terzaghi's model, are listed in Table 4.1.

Table 4.1: Parameters used in the model validation

Parameters for the elasto-viscoplastic model			
Initial void ratio	e_0		5.80
Initial vertical effective stress	$\sigma'_{22(0)}$	(kPa)	5.0
Coefficient of earth pressure at rest	K_0		0.53
Coefficient of permeability	k_0	(m/s)	4 x 10^{-8}
Change of permeability index	C_k		0.95
Initial shear modulus	G_0	(kPa)	450
Compression index	λ		0.8207
Swelling index	κ		0.08946
Stress ratio at critical state	M_m^*		0.98
Compression yield stress	$\sigma'_{mbi}(\sigma'_{mai})$	(kPa)	3.5
Viscoplastic parameter	m'		18
Viscoplastic parameter	C	(1/s)	1.0x 10^{-9}
Structural parameter	σ'_{maf}	(kPa)	3.0
Structural parameter	β		5
Parameters for Terzaghi's model			
Coefficient of volume compressibility	m_v	(kN/m^2)	0.010
Coefficient of consolidation	c_v	(m^2/year)	5.0

4.2.2 Comparison of Terzaghi's Model and the Elasto-viscoplastic Model

The prediction made with Terzaghi's model was conducted according to the procedure outlined in Karunawardena (2002). The analysis using the elasto-viscoplastic model was conducted with the finite element method based on the finite deformation theory.

The laboratory test results, along with the predictions made with the two above models, are shown in Figs. 4.3 and 4.4. The excess pore water pressure development/dissipation predicted with these models is shown in Fig. 4.4.

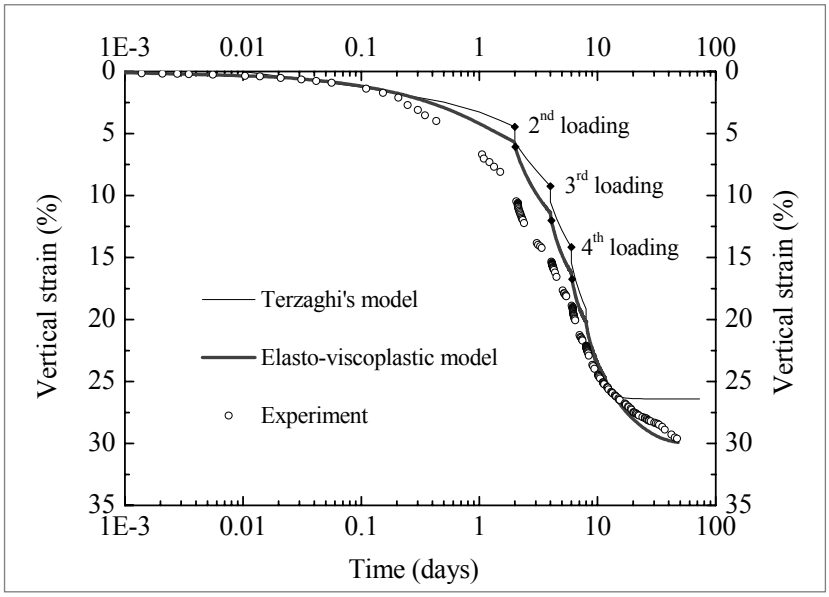

Fig. 4.3: Vertical strain vs. time profile

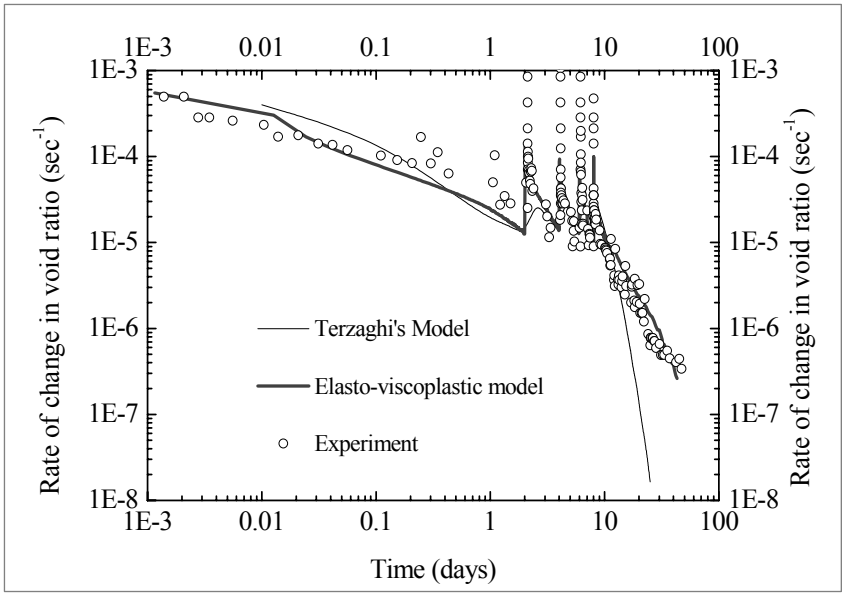

Fig. 4.4: Rate of change in void ratio vs. time profile

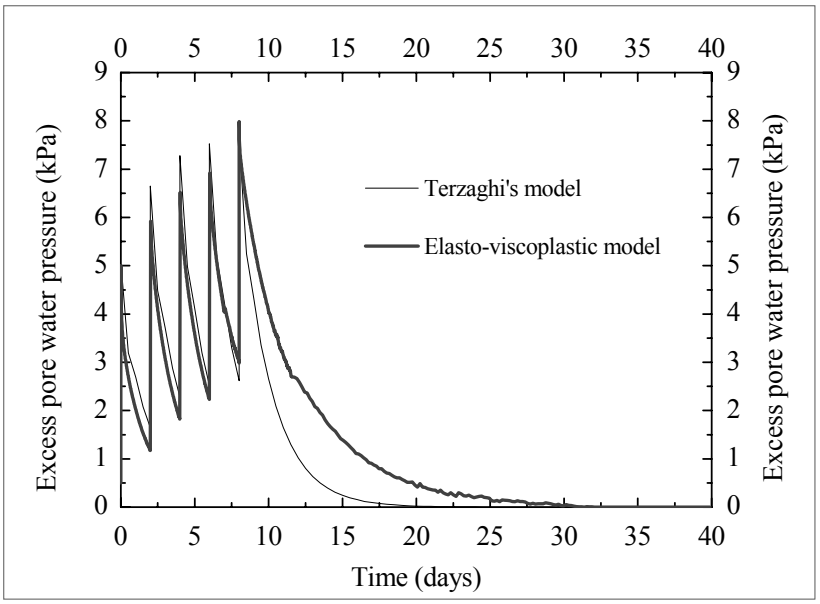

Fig. 4.5: Predicted excess pore water pressure behavior

It can be seen that the strain rates predicted by the two models match the experimental results well, during the initial period. However, with the progress of time and at the end of each incremental load, the strain predicted by the elasto-viscoplastic model is higher than that predicted by Terzaghi's model and more correlated with the experimental results. In addition, the development of strain ceases in Terzaghi's model after the dissipation of excess pore water pressure, whereas the development of strain continues at a slow rate in the elasto-viscoplastic model. These results confirm the assumption that the occurrence of creep behavior is a continuous process and show that the model is capable of predicting the observed creep behavior of peaty soil quite well during and after the complete dissipation of excess pore water pressure. The rates for the void ratio match reasonably well at the beginning, but drop drastically to zero at the end of Terzaghi's solution, as shown in Fig. 4.4

4.3 Model Performance of Settlement Prediction Considering Different Layer Thicknesses

In the previous section of this chapter, it was shown that the model is capable of predicting the observed creep behavior of peaty soil. This section is devoted to verifying the model's performance in predicting the effect of sample thickness on the consolidation analysis of peaty soil. Firstly, the importance of the effect of sample thickness on the consolidation analysis is explained together with relevant research findings. Then, this phenomenon is numerically simulated by the elasto-viscoplastic model using the method

proposed by Oka (2005). Finally, the model's performance in predicting the effect of sample thickness is verified against the results of consolidation tests on specimens with different specimen heights.

4.3.1 Importance of the Effect of Sample Thickness on the Consolidation Analysis

Defining a relevant field compression curve plays an important role in predicting field settlements. This has been well discussed after observing that the deformations of clay in the field are different from those predicted by the conventional methods using the laboratory consolidation test results (e.g., Suklje 1969; Aboshi 1973; Ladd et al. 1977; Oka et al. 1986; Tang and Imai 1995; Leroueil 1996; Oka 2005). The discrepancy might be due mainly to the fact that the clay layer in the field may be several meters thick and that the settlements may take place over a long period of time, whereas the clay specimen tested in the laboratory is only a few centimeters thick and the settlement is usually only monitored over an approximately 24-hour period.

In this regard, Ladd et al. (1977) and Jamiolkowski et al. (1985) indicated that there are two extreme possibilities for the effect of sample thickness on a consolidation analysis, namely, Hypothesis A and Hypothesis B. Hypothesis A assumes that creep occurs only after the end of the primary consolidation (i.e., the complete dissipation of excess pore water pressure). The results are shown by Curve A in Fig. 4.6 and are supported by the findings of Mesri and Rokhsar (1974). Ladd et al. (1977) explained that Hypothesis A is based on the simple relationship in which the strain-log time relationship is displaced in proportion to the thickness (H) squared, an assumption used in conventional consolidation analyses. Hypothesis B assumes that creep occurs during the whole consolidation process and, as a result, the strain at the end of the primary consolidation is not unique. However, it increases with sample thickness due to the time-dependant properties of the soil. The results of this hypothesis are shown by Curve B and are supported by the experimental studies of Barden (1969), Leroueil et al. (1985), Kabbaj et al. (1986), etc.

Meanwhile, Oka et al.(1986) pointed out that the effect of sample thickness on a consolidation analysis is mainly due to the rate-sensitive behavior of soil and that it can be successfully predicted by considering the difference in initial strain rates. Furthermore, he emphasized that it is necessary to determine the initial volumetric strain rates accurately, in order to account for the effect of sample thickness on the consolidation analysis. This is because the initial volumetric strain of a thick sample in the field may differ from that of the thin sample used in the laboratory tests under a one-dimensional condition. Aboshi (1973) experimentally observed that the initial strain rate for thick

sample is lower than that for the thin one. Aboshi's (1973) experimental results indicate that the real behavior of soil appears to correspond to Curve C, which lies between Curves A and B, as shown in Fig. 4.6.

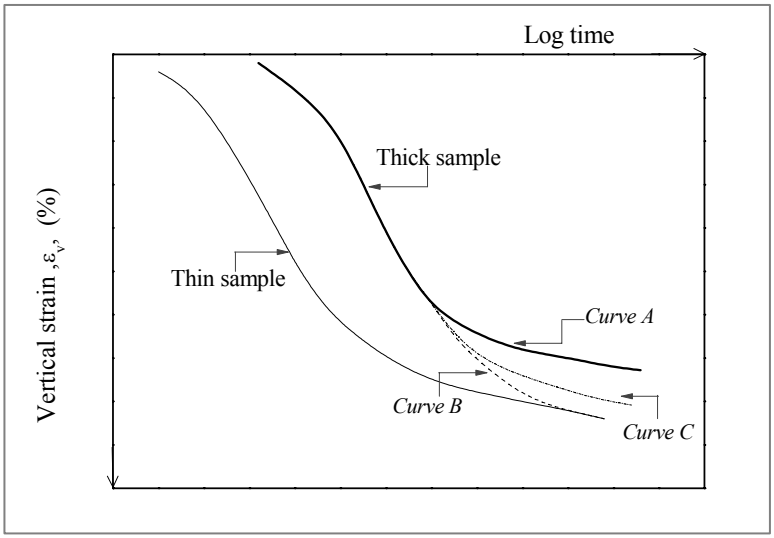

Fig. 4.6: Consolidation of clay layers of different thicknesses according to Hypotheses A and B

4.3.2 Numerical Simulation of the Effect of Sample Thickness on a Consolidation Analysis

The effect of sample thickness on a peat consolidation analysis was numerically simulated by the model, considering the difference in the initial strain rates of the samples. In the model, viscoplastic parameter $C(=\dot{v}^p_{(0)} / M^*_m)$ is related to the initial volumetric strain rate ($\dot{v}^p_{(0)}$). As such, parameter C, which represents $\dot{v}^p_{(0)}$, is used to verify the effect of sample thickness on consolidation, as outlined by Oka (2005).

In the numerical simulation, a one-dimensional consolidation analysis was carried out using the finite element method based on the finite strain theory, as given in Section 3.3.3. The finite strain theory was applied since large deformations were expected in the peat consolidation process. The analysis was conducted using a finite element mesh with an element size of 0.4 cm x 0.4 cm in all cases. The top surface of the specimen was set to be permeable, while the bottom and the side surfaces were set to be impermeable. Assuming normally consolidated behavior, settlements were predicted for samples, 2 cm and 20 cm in thickness, using the typical parameters for peaty clay found in Sri Lanka.

Table 4.2: Parameters used in the numerical simulation of the effect of sample thickness

Parameter			Value
Initial mean effective stress	$\sigma'_{m(0)}$	(kPa)	12
Coefficient of earth pressure	K_0		0.53
Initial pore water pressure	$u_{w(0)}$	(kPa)	24
Coefficient of permeability	k_0	(m/s)	1 x 10^{-8}
Permeability change index	C_k		0.95
Elastic shear modulus	G_0	(kPa)	800
Compression index	λ		1.7176
Swelling index	κ		0.1145
Initial void ratio	e_0		6.0
Compression yield stress	$\sigma'_{mbi}(\sigma'_{mai})$	(kPa)	12
Stress ratio at maximum compression	M^*_m		0.9
Viscoplastic parameter	m'		20
Viscoplastic parameter	C	($1/s^1$)	5 x 10^{-9} s^{-1},5 x 10^{-11}, 5 x 10^{-10}
Structural parameter	σ'_{maf}	(kPa)	10.0
Structural parameter	β		5.0

The parameters and the initial conditions of the analysis are shown in Table 4.2. An excess pore water pressure of 25 kPa (two times greater than the compression yield stress) was applied as the initial load in all cases (Oka 2005).

In the first analysis, the same $C(=C_0)$ value was assumed for both samples in spite of the different thicknesses. In other words, it was assumed that the initial volumetric strain rate ($\dot{v}^p_{(0)}$) was the same for both the thick and the thin samples. The predicted strain for the thick sample is shown as Curve B in Fig. 4.7. It indicates that the final strain for the thick sample is almost the same as that for the thin sample; these results agree with Hypothesis B explained by Ladd et al. (1977). In the second analysis, it was assumed that the initial volumetric strain rates were inversely proportional to the square of the drainage length of the samples and that this relationship yields an initial volumetric strain rate for the thick sample that is 100 times smaller than that for the thin sample. In this case, the model prediction for the thick sample follows Curve A in Fig. 4.7, and the resultant final strain of the thick sample is less than that of the thin sample. This behavior is similar to that in Hypothesis A described by Ladd et al. (1977), however, a quantitative difference can be observed. In the final analysis, the initial volumetric strain of the thick sample was assumed to be 10 times smaller than that of the thin sample, and thus, Curve C is obtained. As indicated in Fig. 4.7, the predicted results are very sensitive to the value of

$C\,(=\dot{v}^{p}_{(0)}/M^{*}_{m})$. Using the different C values by assuming the different initial strain rate relationships for thin and thick samples, the following types of behavior can be obtained:

$$C = C_0(H_0/H)^2 \qquad \text{for Curve A}$$
$$C_0(H_0/H)^2 < C < C_0 \qquad \text{for Curve C}$$
$$C = C_0 \qquad \text{for Curve B}$$

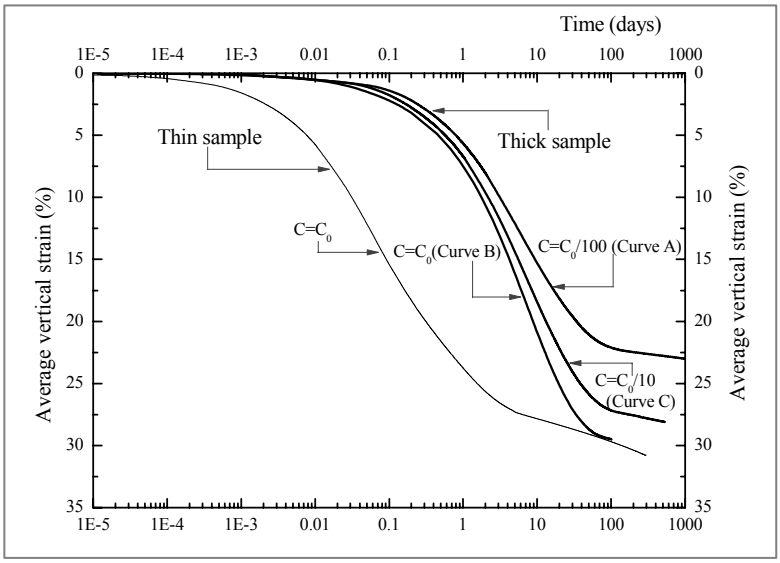

Fig. 4.7: Numerical simulation of the effect of sample thickness on settlement predictions

4.3.3 Consolidation Data for Peaty Soil with Different Sample Heights

Data from the consolidation model tests conducted on samples with different specimen heights were reported by Kugan et al (2003). Tests were conducted using remolded peaty clay obtained from sites along the Colombo-Katunayake Expressway project. The sample thicknesses were 700 mm, 275 mm, and 20 mm, and labeled as large, medium, and small, respectively. For the small-scale tests, a conventional oedometer was used, while for the large- and medium-scale models with diameters of 500 mm and 203 mm, respectively, locally fabricated devices with direct loading were adopted. A description of the test setup used in the experimental work is given in Table 4.3, and the schematic diagram of the large-scale model is shown in Fig. 4.8.

Table 4.3: Description of the test setup

Name	Large scale	Medium scale	Small scale*
Height (mm)- H	700	275	20
Diameter (mm)- D	500	203	50
H/D ratio	1.4	1.35	0.4
Drainage condition	Top	Top	Top and bottom
Load	Direct loading	Direct loading	Loading lever

* A conventional oedometer was used.

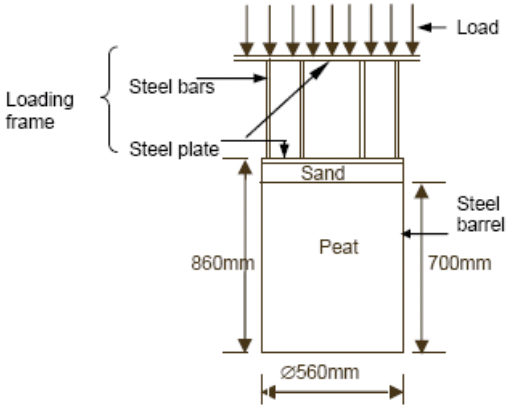

Fig. 4.8: Schematic diagram of the large scale model

In the large- and medium-scale tests, drainage was allowed only at the top, while in the small-scale test, drainage was allowed at both the top and the bottom of the sample. In all the tests, the load was applied in increments of 5 kN/m^2, up to a final pressure of 30 kPa. In this testing program, it was assumed that the time required for a certain degree of consolidation is proportional to the square of the drainage length of the samples.

$$\frac{t_l}{(H_l)^2} = \frac{t_m}{(H_m)^2} = \frac{t_s}{(H_s)^2} \tag{4.1}$$

where indices l,m,s refer to the large-, the medium-, and the small-scale models, respectively. In the large-scale model, load incrementing was done at a time interval of 2 days. According to Eq. (4.1), the degree of consolidation that was achieved in the large-scale model due to maintaining a particular load over a 2-day time period, can be achieved in the medium–scale test by maintaining the same load for 7 hours and 25 minutes. For the small-scale test, the drainage length of the sample is 10 mm and the corresponding time interval for the load increment becomes 30 s. After reaching the final load of 30 kPa, the samples were allowed to consolidate for a long period of time while maintaining the identical conditions; the settlements were monitored during that time.

It can be seen in the above experimental data that the large-scale and the medium-scale tests provide the most comparable data for investigating the effect of the sample thickness phenomena. As indicated in Table 4.3, both tests have almost equal height/diameter ratios, drainage conditions, etc. Not only were the above conditions controlled, but the duration of the preparatory consolidation was controlled in such a way that suited a comparison of the effects of sample thickness on a consolidation analysis.

The importance of controlling the preparatory consolidation time in verifying the effect of sample thickness tests has been emphasized by Mesri (1985). It can be illustrated using the following figure.

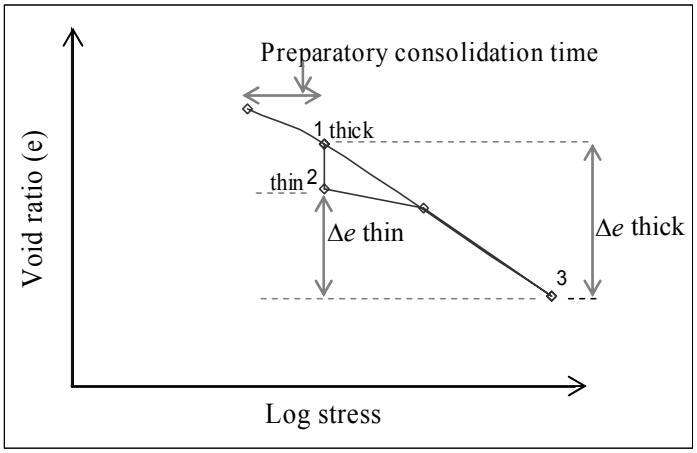

Fig. 4.9: Importance of controlling the preparatory consolidation time

There is a strong possibility that the thin sample will experience a larger secondary compression under the preparatory load than the thick sample, if the consolidation period is not carefully monitored. This is due to the much shorter duration of the primary consolidation stage for the thin sample. As indicated in Fig. 4.9, this might result in the thin sample being compressed (point 2) more than the thick sample (point 1) in the preparatory consolidation. Under this condition, the thick sample would compress more than the thin sample during the next loading increment. Comparing the strain-log time relationships of the two samples would not be appropriate, as their initial conditions are different. The above description indicates that it is necessary to carefully control the preparatory consolidation period in order to have the same initial conditions for both the thin and the thick samples for the load increments considered for comparison here.

In the above experiments, the preparatory consolidation time for the thick sample was 2 days and that for the thin sample was selected using Eq. (4.1). Therefore, if we assume that a simple H^2 law is valid for consolidation, then both thin and thick samples underwent the same degree of consolidation due to the preparatory consolidation load.

4.3.4 Prediction of the Observed Settlements

The observed consolidation behavior for the large- and the medium-scale models, due to load increments of 5-30 kPa, was numerically simulated using the model. An initial load increment of 0-5 kPa was taken as the preparatory consolidation. At the end of the preparatory consolidation period, each sample yielded the following conditions.

Table 4.4: Preparatory consolidation data

	Medium scale	Large scale
Time duration	7 hours and 25 min	2 days
Initial void ratio	5.960	6.283
Initial sample thickness	275 mm	700 mm
Settlement	9.15 mm	31.48 mm
Void ratio at the end of consolidation	5.728	6.051
Sample height at the end of consolidation	265.8 mm	668.5 mm
Strain at the end of consolidation	3.33%	4.49%
Average strain rate	7.477×10^{-3} %/min	1.561×10^{-3} %/min

The initial conditions required for the analysis of the consolidation behavior for load increments of 5-30 kPa were evaluated using the data listed in Table 4.4. The finite element meshes were based on the new sample heights used in the analysis and are shown in Fig. 4.10.

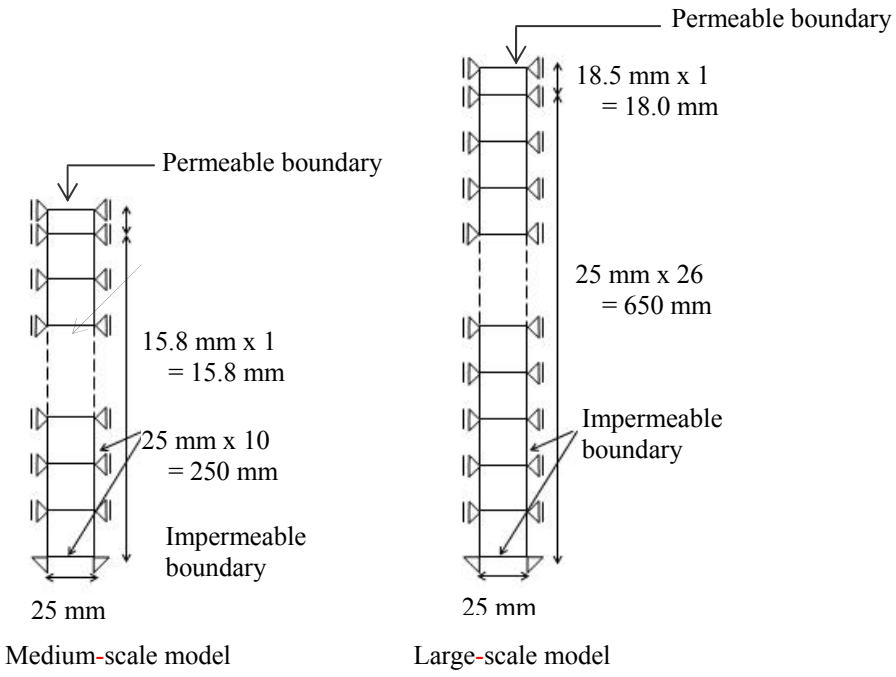

Fig. 4.10: Finite element meshes used in the analysis

The parameters applied in the analysis are listed in Table 4.5. It should be noted that all the parameters, except for viscoplastic parameter C, are the same as those listed in Table 4.1 which was used in the model validation. Initially, the simulation was done for the medium-scale sample. When the value of viscoplastic parameter C was equal to 5.0 x $10^{-9}s^{-1}$, a good correlation was found between the model predictions and the experimental results. Then, the prediction was made for the large-scale model using the same material parameters, except for the initial void ratio and viscoplastic parameter C. The initial void ratio was taken from the experimental results, while parameter C was derived from the observed initial strain rate ratio between the large- and the medium-scale tests. According to the values in Table 4.4, the ratio of the initial strain rates for the medium- to large-scale tests was found to be around 5. In proportion to that, the initial viscoplastic strain rate for the large-scale tests became 1.0x $10^{-9}s^{-1}$ with reference to the medium-scale value of 5.0 x $10^{-9}s^{-1}$. The predicted results using the above values and the experimental data are shown in Fig. 4.11. It can be seen that the strain rates predicted by the model, considering the difference in initial volumetric strain rates, agree well with those in the experimental data.

Table 4.5: Parameters used in the settlement prediction of peat samples with different thicknesses

Parameter			Value
Initial void ratio	e_0		5.98^{+}, $5.728^{\#}$, 6.051^{*}
Initial vertical effective stress	$\sigma'_{v(0)}$	(kPa)	5
Coefficient of earth pressure	K_0		0.55
Coefficient of permeability	k_0	(m/s)	4 x 10^{-8}
Permeability change index	C_k		0.95
Elastic shear modulus	G_0	(kPa)	450
Compression index	λ		0.8207
Swelling index	κ		0.08946
Compression yield stress	$\sigma'_{mbi}(\sigma'_{mai})$	(kPa)	3.5
Stress ratio at maximum compression	M^*_m		0.98
Viscoplastic parameter	m'		18
Viscoplastic parameter	C	(1/s)	1x 10^{-8+}, 5x$10^{-9\#}$, 1x 10^{-9*}
Structural parameter	σ'_{maf}	(kPa)	3.0
Structural parameter	β		5.0

+ small scale model # medium scale model * large scale model

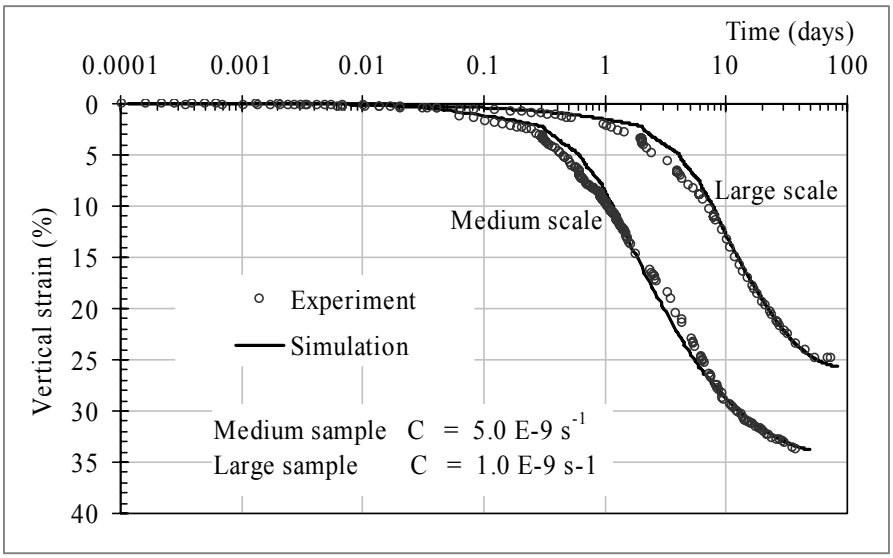

Fig. 4.11: Strain predicted by considering the difference in initial strain rates

At the same time, an analysis was carried out by selecting a parameter C that was inversely proportional to the square of the drainage length of the samples. In this case, the C value for the thick sample became about 6 times smaller than that for the thin sample. Since this value was closer to the C value used in the previous analysis (the C value was based on the difference in initial volumetric strain rates between the thin and the thick samples), the predicted results are almost equal to those of the previous analysis.

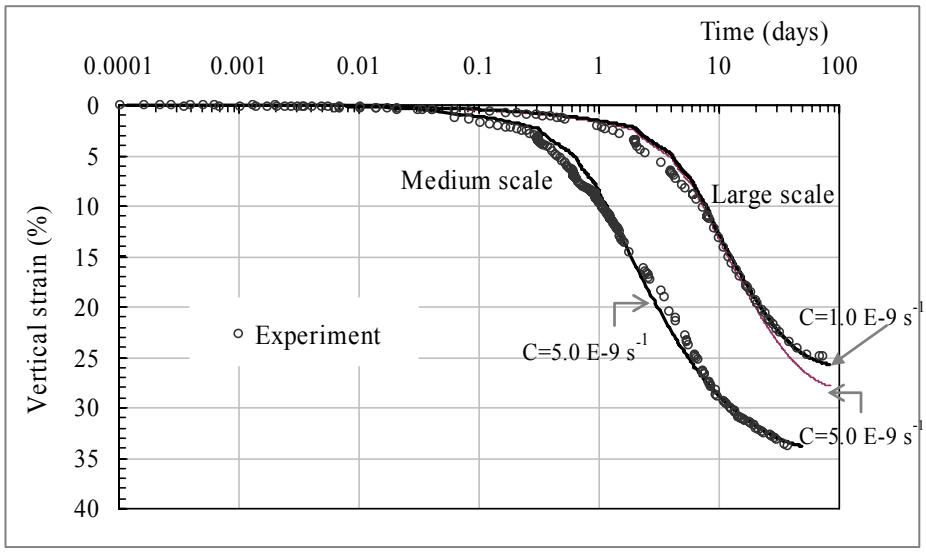

Fig. 4.12: Strain predicted by considering the same initial strain rates for the thick and the thin samples

Fig. 4.12 shows the predictions made by assuming the same value for C, namely, 5 x 10^{-9} s^{-1}, in other words, by considering the same initial volumetric strain rates for both the thin and the thick samples. In this case, the predicted strain for the thick sample overestimates

the observed strain rates. The numerical analysis performed in Section 4.3.2 indicates that the results of an analysis conducted by the model and using the same initial volumetric strain rates (the same C) correspond to the results based on Hypothesis B mentioned in Ladd et al.(1977). As indicated in Fig. 4.12, therefore, the unique strain-log time relationship based on Hypothesis B does not produce representative results for the present analysis.

Fig. 4.13 compares the measured and the predicted strain rates, using the elasto-viscoplastic model for the normally consolidated behavior for load increments of 5–30 kPa in the oedometer tests. The same parameters listed in Table 4.5 are used for the analysis, except for viscoplastic parameter C. In this case, the specimens were 50 mm in diameter and 20 mm in height, and drainage was allowed from both ends. These test conditions were quite different from those which prevailed in the medium- and the large-scale model tests (different drainage conditions and different heights/diameters). Due to these different test conditions, a direct comparison of the initial strain rates between the oedometer tests and the medium- or the large-scale tests was not logical. However, the results of this experiment, as well as those from other research works, indicate that thin samples exhibit higher initial strain rates than thick samples. Considering this fact, a higher C value for 1 x $10^{-8}s^{-1}$ was used in the predictions. As shown in Fig. 4.13, the predicted results for the small-scale sample with a higher C value than those of the large- and the medium-scale samples, agree reasonably well with the experimental data.

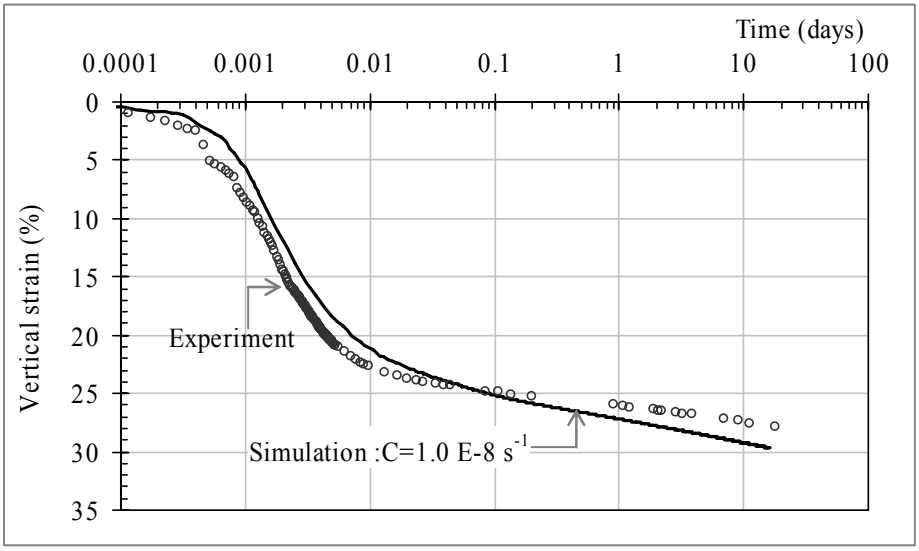

Fig. 4.13: Predicted settlement for the oedometer tests considering high initial strain rate

Fig. 4.14 shows the predicted strain-log time relationship for oedometer, medium- , and large-scale tests considering the difference in the initial volumetric strain rates ($\dot{v}^{p}_{(0)}$)

together with the relevant experimental results. The predicted results show a reasonable agreement with the experimental data. It can be concluded, therefore, that the effect of sample thickness on the consolidation analysis of peaty clay, can be successfully predicted by the model considering the difference in initial strain rates among the samples.

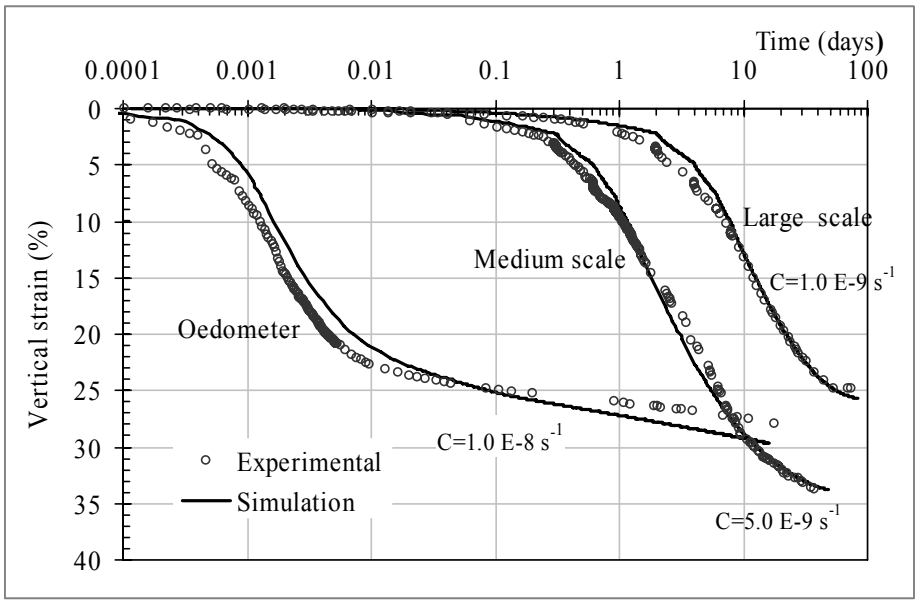

Fig. 4.14: Model performance of the settlement prediction for different layer thicknesses

Therefore, it can be concluded that the effect of using the results of laboratory tests on a thin soil specimen to predict the development of strain with time for thick soil layers in the field can be successfully predicted by the model having considered the difference in initial strain rates.

4.4 Experimental Verification of the Relation between Parameter m' and C_α / C_c

In this section, the validity of the interpretation of parameter m' and the C_α / C_c ratio, described in Section 3.2.2, is experimentally verified. As derived in Section 3.2.2, parameter m' and the C_α / C_c ratio of the soil are interrelated as follows:

$$m' = \frac{C_c - C_s}{C_\alpha M_m^*} \tag{4.2}$$

The validation is done by comparing the m' values calculated from the original definition (Eq. 4.4) and the relationship given by Eq. 4.2.

As outlined by Kimoto (2003), the original definition of parameter m' is based on the results of undrained triaxial compression tests with different strain rates. When undrained triaxial tests with different strain rates, namely, $\dot{\varepsilon}_{11}^{(1)}$ and $\dot{\varepsilon}_{11}^{(2)}$, are performed, the following equations are obtained at the point where the mean effective stress takes the same value in the stress path.

$$\frac{\dot{\varepsilon}_{11}^{(1)}}{\dot{\varepsilon}_{11}^{(2)}} = \exp\left\{ m'\sqrt{\frac{2}{3}}\left(\left(\frac{q}{\sigma'_m}\right)^{(1)} - \left(\frac{q}{\sigma'_m}\right)^{(2)} \right) \right\} \tag{4.3}$$

$$m' = \sqrt{\frac{3}{2}} \frac{\ln\dot{\varepsilon}_{11}^{(1)} - \ln\dot{\varepsilon}_{11}^{(2)}}{\left(\frac{q}{\sigma'_m}\right)^{(1)} - \left(\frac{q}{\sigma'_m}\right)^{(2)}} \tag{4.4}$$

A series of stage-loading consolidation tests, long-term consolidation tests, and strain-controlled undrained triaxial compression tests were carried out for soft clays found in the Aji River area and Higashi Osaka, Osaka, Japan. The results for each type of clay are given in Figs. 4.15 and 4.16, respectively, and the material parameters determined from the results are listed in Table 4.6.

The void ratio e vs. log of the vertical effective stress, σ'_v, relationship obtained from the stage-loading oedometer tests is shown in (a) of each figure, and material parameters λ and κ were determined from the $e - \log\sigma'_v$ relation.

The void ratio for the e vs. log time, obtained from the long-term consolidation tests, is shown in (b) of each figure, and material parameter C_α was determined from the slope after the primary consolidation of the $e - \log Time$ relation.

The stress paths obtained from the undrained triaxial tests with two different strain rates are shown in (c) of each figure, and critical state parameter M_m^* was obtained from the slope of the critical state line. The relation between the stress ratio, q/σ'_m, and the logarithm of the axial strain is shown in (d) of each figure, and rate parameter m' was obtained from the straight lines given in (d) by applying the method described in Eq. (4.4). The lines in the figure are not rigorously parallel to each other. However, m' was determined as an average value by assuming m' as a constant value for a particular type of soil (Mesri et al.1977; Adachi et al.1984).

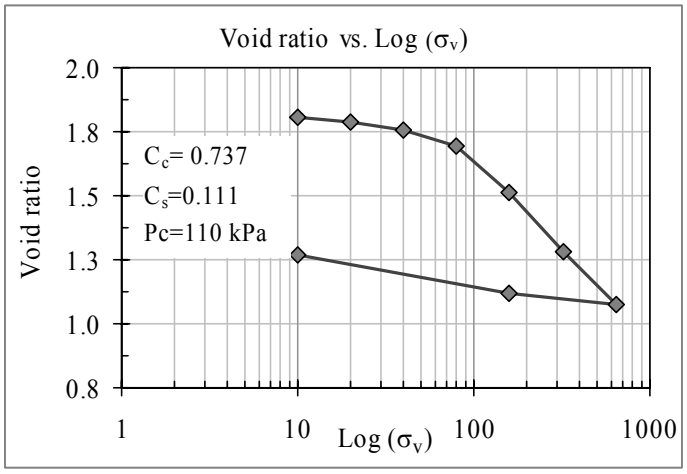

Fig. 4.15(a): Void ratio vs. Log (stress) relationship

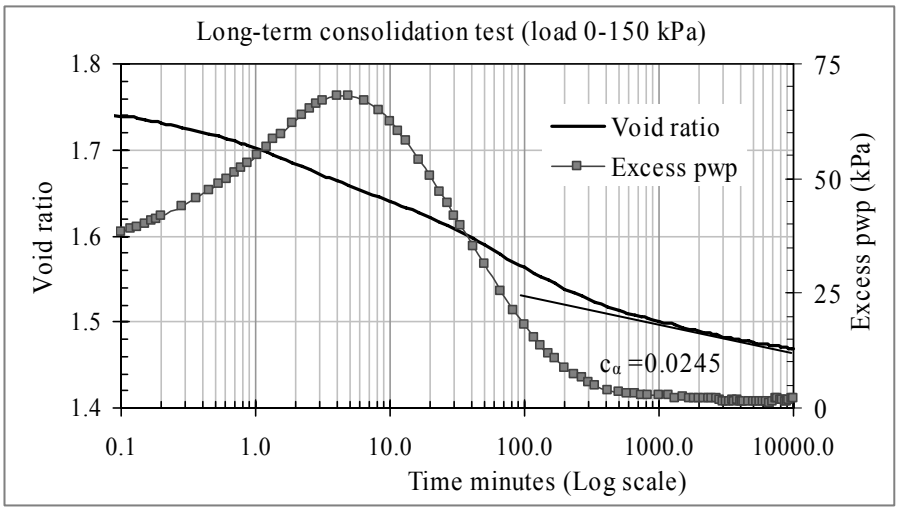

Fig. 4.15(b): Void ratio vs. Log (time) relationship in long-term consolidation tests

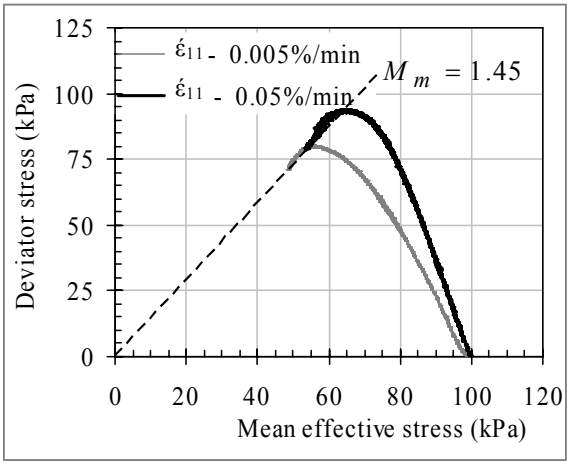

Fig. 4.15(c): Stress paths

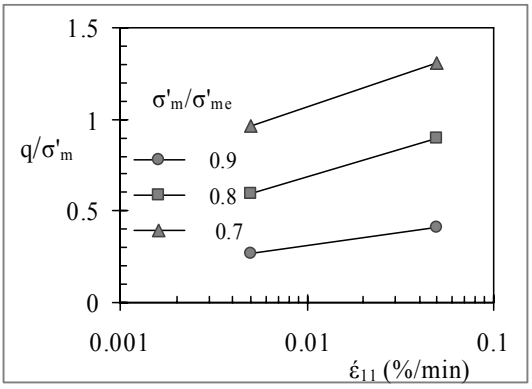

Fig. 4.15(d): q/σ'_m vs. $\dot{\varepsilon}_{11}$ relationship

Fig. 4.15: Experimental results for soft marine clay found around Aji River, Osaka, Japan

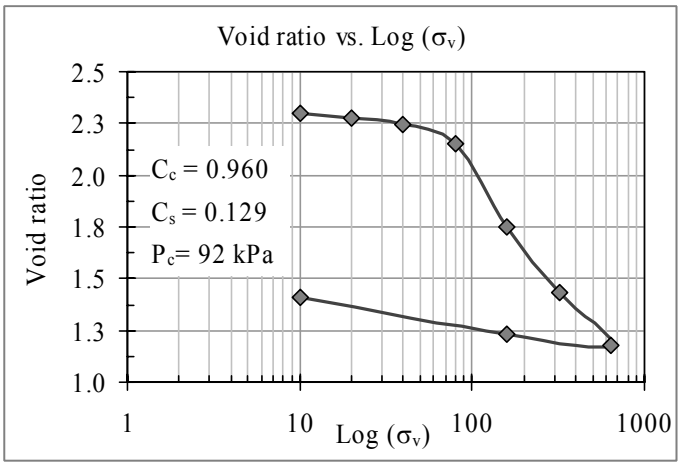

Fig. 4.16(a): Void ratio *vs*. Log (stress) relationship

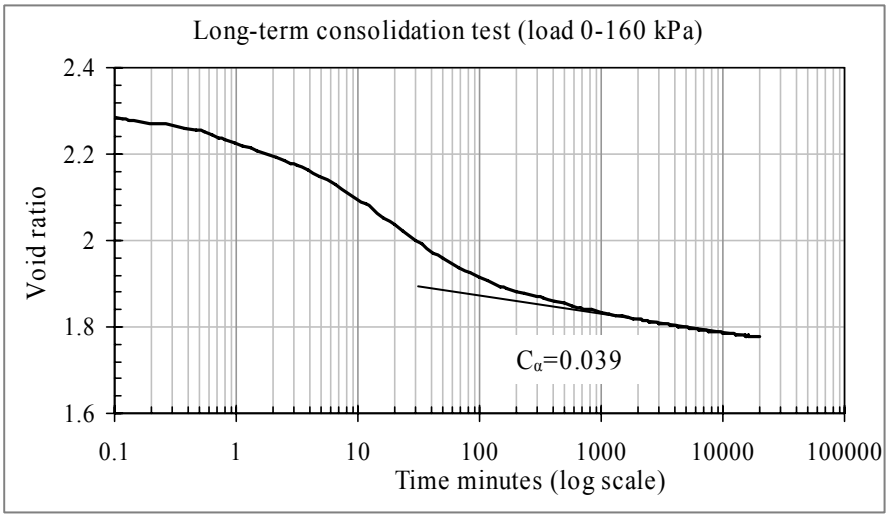

Fig. 4.16(b): Void ratio *vs*. Log (time) relationship in long-term consolidation tests

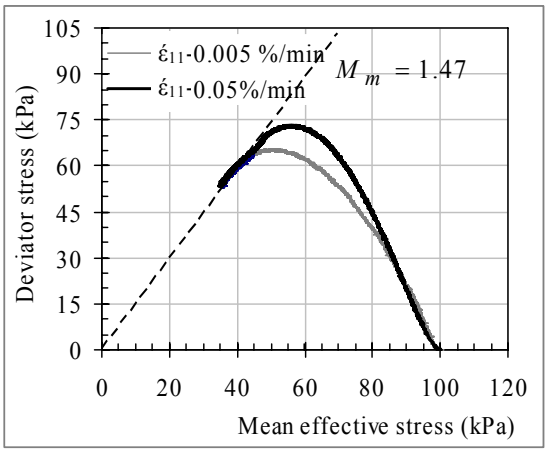

Fig. 4.16(c): Stress paths

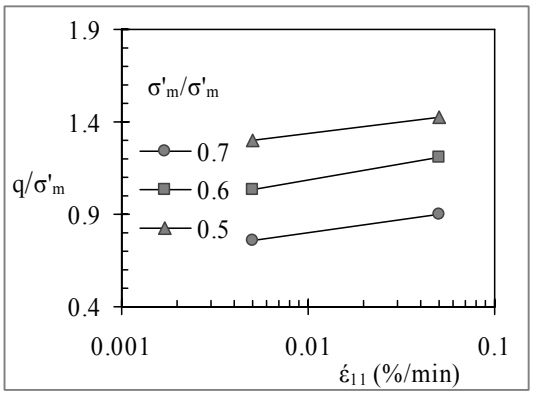

Fig. 4.16(d): q/σ'_m *vs*. $\dot{\varepsilon}_{11}$ relationship

Fig. 4.16: Experimental results for soft marine clay found in Higashi Osaka, Osaka, Japan

The determined material parameters and the calculated m' values, using the above two methods, are listed in Table 4.6. The calculated results for the two methods have shown a reasonable agreement.

Table 4.6: Summary of the test results and the estimated m' values

	Aji clay	Higashi Osaka clay
C_c	0.737	0.960
C_s	0.111	0.129
C_α	0.025	0.039
M_m^*	1.45	1.47
$m' = \dfrac{C_c - C_s}{M_m^* C_\alpha}$	21	18
$m' = \sqrt{\dfrac{3}{2}} \dfrac{\ln\dot{\varepsilon}_{11}^{(1)} - \ln\dot{\varepsilon}_{11}^{(2)}}{\left(\dfrac{q}{\sigma'_m}\right)^{(1)} - \left(\dfrac{q}{\sigma'_m}\right)^{(2)}}$	23	22

Mesri et al. (1997) reported that the C_α / C_c concept of compressibility explains and predicts the secondary compression behavior of geotechnical materials. Mesri (1973) also considered the relationship between C_α and C_c, and concluded that soils which are highly compressible in the primary phase would show high compressibility in the secondary phase as well. The experimental results indicated in Table 4.6 agree well with this conclusion of Mesri et al. (1973). Higashi Osaka clay, which shows a highly compressible primary characteristic (high C_c), yields high creep settlements compared to Aji clay which shows a lower compression index and coefficient of secondary consolidation. Subsequently, model parameter m' yields a lower value for highly compressible Higashi Osaka clay than that for lowly compressible Aji Clay.

4.5 Summary and Remarks

In this chapter, the elasto-viscoplastic model has been validated against laboratory consolidation test data on peaty soil.

- A model prediction was made to simulate the observed one-dimensional consolidation settlements, and then the settlements were compared to those predicted by Terzaghi's consolidation theory. The results indicate that the model is

capable of predicting observed creep settlements quite well, indicating that the model assumption for creep behavior as a whole process is more realistic for peat consolidation.

- The model performance of the effect of sample thickness in the prediction of settlements was verified against the consolidation model tests on specimens with different heights. The simulation confirms that the effect of using the results of laboratory tests on a thin soil specimen to predict the development of strain with time for thick soil layers in the field can be successfully predicted by the model having considered the difference in initial strain rates.
- The mathematically derived relationship between viscoplastic parameter m' and C_α / C_c was experimentally validated by simultaneously conducting laboratory consolidation tests and triaxial tests on soft marine clay. Therefore, the determination of viscoplastic parameter m', based on consolidation test results, is acceptable.

Chapter 5

PREDICTION OF THE ONE-DIMENSIONAL CONSOLIDATION BEHAVIOR OF PEATY CLAY IN THE FIELD

5.1 Introduction

The elasto-viscoplastic model was described and validated in Chapters 3 and 4, and its performance in predicting the field consolidation behavior of peaty clay due to one-dimensional compression is verified in this chapter. For this purpose, the model is used to back analyze instrumented earth fill constructed on peaty clay. Approximating the soil strain as one dimensional is reasonable for this project, because the dimensions of the loaded area are significantly large relative to the thickness of the compressible layer. Karunawardena (2002), Karunawardeana and Kulathilaka (2003) attempted to analyze the same problem using the finite difference program based on Terzaghi's one-dimensional consolidation theory. The observed settlements were found to be greater than the predicted ones, indicating the possibility that some amount of secondary consolidation had taken place even before the excess pore water pressure was completely dissipated. In addition, even predictions made through the use of different coefficients of consolidation could not match the observed pattern of excess pore water pressure generation/dissipation.

Therefore, with the understanding of the limitations and the shortcomings of Terzaghi's theory of consolidation for peat consolidation problems, the same problem is analyzed using the elasto-viscoplastc model. The work is aimed at confirming the importance of considering applied analysis methods, such as finite strain, when modeling the field

consolidation behavior of peat. In order to do that, computations are made by the model based on the infinitesimal strain and the finite strain theories to explore how these two approaches describe the observed behavior. Moreover, the influence of the degradation of the microstructure induced by the applied loads on the consolidation of peat is verified by performing a separate analysis which considers finite strain together with the degradation effect. Details are given on the geotechnical profile, field instrumentation, laboratory test results, and the determination of the soil parameters for the numerical modeling.

5.2 Description of the Project

An area of marshy land, mainly comprised of peaty soil, was reclaimed for an infrastructure development project near the capital of Sri Lanka in the year 2000. The average original ground elevation varied from 0.2 m above MSL to 0.5 m above MSL. The ground water table was almost at surface level and the site was subjected to frequent flooding. Therefore, it was necessary to raise the ground level above the anticipated highest flood level by filling prior to any construction. It was also necessary to improve the highly compressible nature of the peaty soil in order to make it suitable for supporting the infrastructural developments which had been proposed under the project. In order to accomplish these objectives, controlled earth fill was constructed and monitored both during and for a long period after the construction.

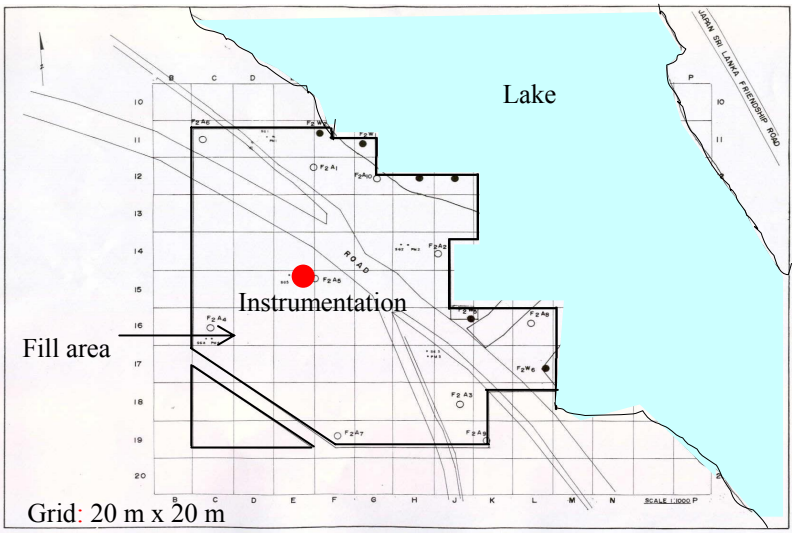

Fig. 5.1: Plan view of the fill and the instrumentation location

The plane view of the fill and the location of the instruments which were considered in the analysis are shown in Fig. 5.1. As shown in the figure, the extent of the fill area is about 2.4 hectares and the instruments are located around the center of the fill area. The

fill was placed and compacted in layers under controlled conditions. The earth fill was constructed by placing fill material in uniform layers not exceeding 300 mm in loose lift thickness per layer. Then, each layer was compacted to a minimum of 95% of the standard proctor maximum density. The loading curve that denotes the construction history of the fill is shown in Fig. 5.2. The stress in the loading curve was calculated as the product of the fill thickness and the total unit weight of the fill based on field records. The field density test results indicate that the total unit weight of the fill varied from 15 kN/m^3 to 18 kN/m^3.

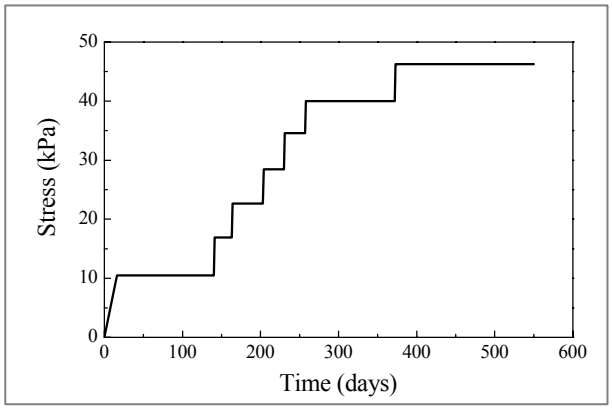

Fig. 5.2: Construction history of the fill

The field rate of consolidation was evaluated in this project by the independent field monitoring of the pore pressure and the settlements. Piezometers were installed in the middle of the peat layer (depth: 2.5 m). The pore pressure development in the peat layer with further placement of the fill and the subsequent dissipation with time were monitored daily. Settlement gauges were set just above the peat layer after the placement of nominal fill 300 mm in thickness. The settlement of the peat layer during the additional filling and during the consolidation phase was captured through these settlement gauges. The locations of the instruments are shown in Fig. 5.3.

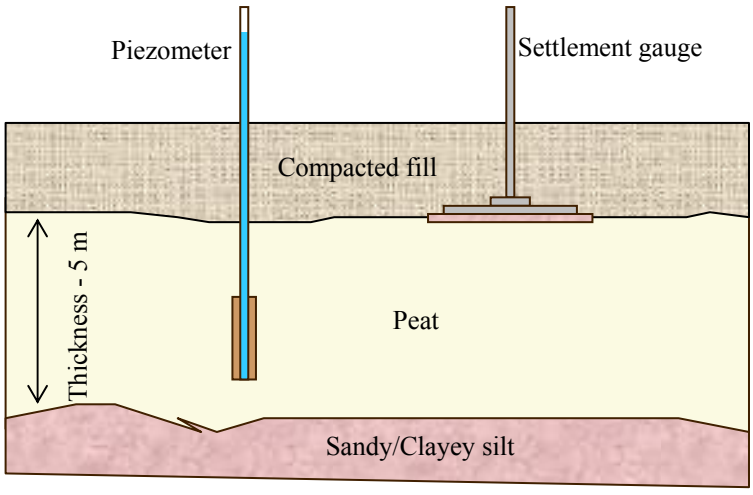

Fig. 5.3: Locations of the field instruments

Before the filling was started, a detailed soil investigation program was conducted in order to establish the relevant soil parameters. The subsoil condition in the instrumented fill area was investigated with 3 boreholes and 8 auger holes, and undisturbed samples were taken for use in the laboratory tests. The assumed subsoil profile was based on the borehole log data, and is shown in Fig. 5.4. It consists of a clay/silty sand layer, about 0.5 m in thickness, as the top soil with roots of vegetation. However, this layer was removed before filling process was begun. Below that, a very soft peat layer, about 5 m in thickness, is encountered. The peat is underlain by a relatively incompressible fine to medium sandy silt, about 2.5 m in thickness, overlying the dense to very dense sand layer which was found to exist up to the termination depth of boreholes. The average physical properties of the peat layer are also given in Fig. 5.4.

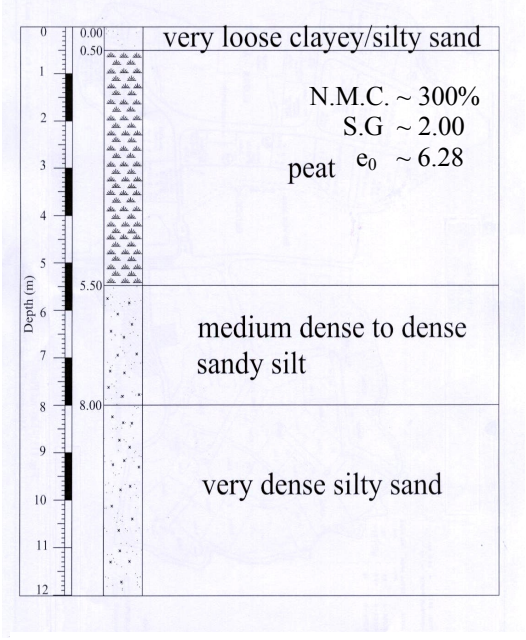

Fig. 5.4: Subsurface profile at the site

5.3 Determination of the Soil Parameters

The parameters for the analysis were determined using the laboratory and the field tests conducted during the project period, following the procedure outlined in Section 3.4.

The compression index, λ, and the swelling index, κ, are determined using the oedometer test results. The value of the initial coefficient of permeability, k_0, was assumed to be equal to the value obtained from the field permeability tests conducted on peaty clay, with similar physical properties, found in the vicinity of the site. The permeability change index, C_k, was deduced from the variations in permeability and the void ratio observed in the oedometer test (Fig. 5.5). The value of stress ratio $\sqrt{\eta_{ij}^* \eta_{ij}^*}$ at

the critical state, M_m^*, was determined from the slope of the critical state line of the triaxial tests. The viscoplastic parameter, m', was determined using the relationship mentioned in Eq. (3.103). For that, required compression index λ and swelling index κ were taken from the stage-loading oedometer test, and the coefficient of secondary consolidation was taken from the long-term consolidation test results. The coefficient of lateral earth pressure at rest, K_0, was 0.53, as recommended by Edil and Dhowian (1981) for amorphous peaty clay.

The results of the stage-loading oedometer test and the long-term consolidation test, conducted on undisturbed peaty samples collected from the site, are shown in Figs. 5.6 and 5.7, respectively.

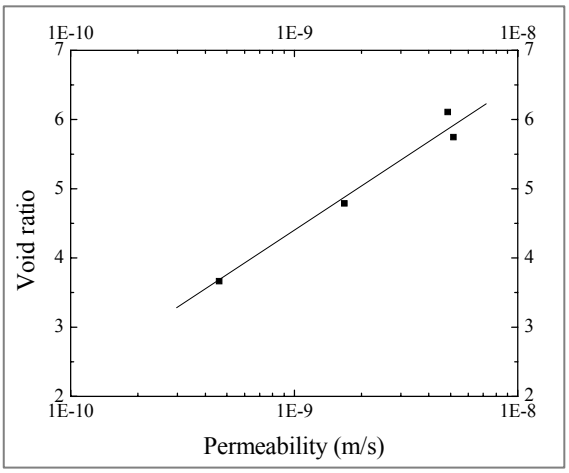

Fig. 5.5: Observed relationship for the permeability vs. void ratio obtained through consolidation test.

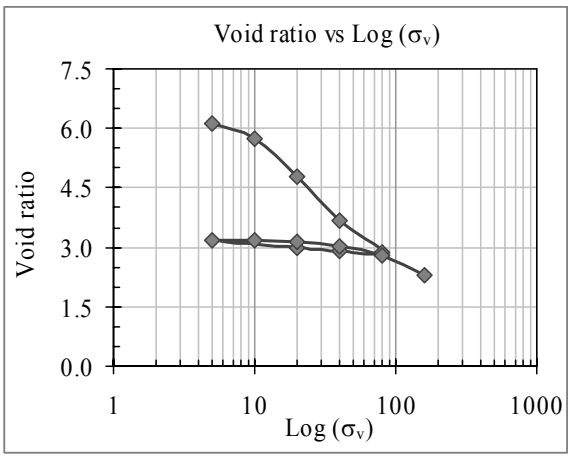

Fig. 5.6: Void ratio vs. vertical effective stress relationship obtained through stage-loading consolidation test

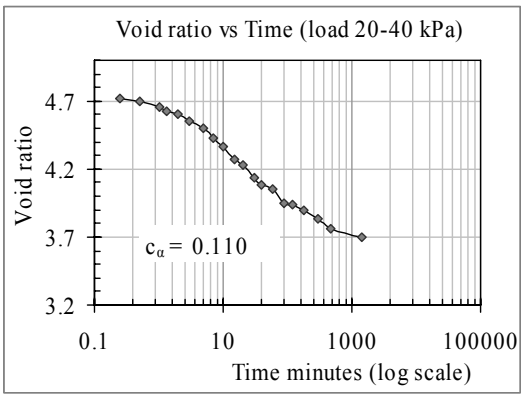

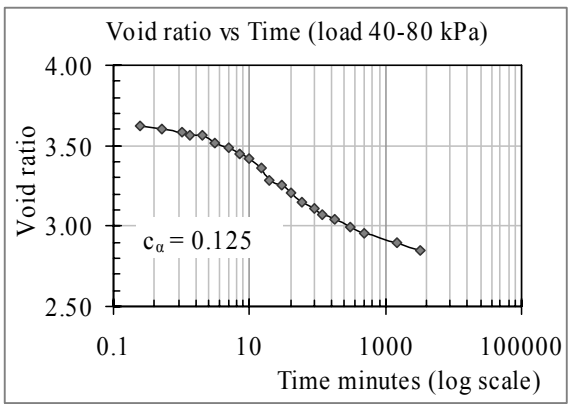

Fig. 5.7: Void ratio-logarithmic time curves from stage-loading consolidation test

The compression yield stress, σ_{mbi}, was related to the preconsolidation pressure determined through the oedometer test. The viscoplastic parameter, C, the degradation

parameter, β, the structural parameter, σ_{maf}, and the initial shear modulus, G_0, were determined by simulating the stress-strain curves of the undrained triaxial tests. For this purpose, data on triaxial tests with different confining pressure levels, conducted on undisturbed peaty samples collected from the peat layer at the site, were used. These tests were performed to evaluate the shear strength of the soil, which is necessary in order to specify the construction program during the design stage of the fill.

Numerical simulations of undrained triaxial compression tests were performed using a one-element program based on the constitutive relations of the model. The program was developed by employing a numerical approximation, namely, the Runge-Kutta method, and giving compressive strain rates of $(\dot{\varepsilon}_{11}, \dot{\varepsilon}_{22}, \dot{\varepsilon}_{33}) = (\dot{\varepsilon}_{11}, -\frac{1}{2}\dot{\varepsilon}_{11}, -\frac{1}{2}\dot{\varepsilon}_{11})$ under the triaxial stress state (Kimoto 2002). The strain rate of 0.11%/min was maintained in all three triaxial tests and simulations were conducted using the same rate. The parameters used in the simulation are listed in Table 5.1.

Table 5.1: Parameters used in the triaxial simulation

Parameters			Values
Strain rate	$\dot{\varepsilon}$	(%/min)	0.11
Initial void ratio	e_0		5.7, 5.4, 5.0
Initial elastic shear modulus[#]	G_0	(kPa)	800
Compression index	λ		1.7163
Swelling index	κ		0.1151
Stress ratio at critical state	M_m^*		0.95
Compression yield stress	$\sigma'_{mbi}(\sigma'_{mai})$	(kPa)	35, 50, 75
Viscoplastic parameter	m'		22
Viscoplastic parameter[#]	C	(1/s)	1.0x 10^{-10}
Structural parameter [#]	σ'_{maf}	(kPa)	0.7 σ'_{mbi}
Structural parameter [#]	β		5

[#] From the triaxial test stress–strain relationship

The results of the numerical simulation of the triaxial test results are shown in Figs. 5.8 and 5.9. The results of the simulation of the stress-strain behavior agree well with the experimental data when the values mentioned in Table 5.1 are assumed for parameters C, β, σ_{maf}, and G_0. The initial part of the stress path predicted by the numerical simulation deviates quite a bit from that in the experimental results; however, the prediction for the failure condition was satisfactory. Due to the present impossibility of measuring the effective stress directly, it is determined as the difference between the total stress and the pore pressure by measuring the increment of the pore pressure when a load

is applied. Subsequently, the pore pressure being measured by the present method is the pressure in the water being squeezed out. The actual pressure of the bound water between the particles remains unknown until it begins to be squeezed out. For the above reasons, the measured pore pressure might not have represented the actual pore pressure and the application of the stress path could lead to inaccuracies in the experiments.

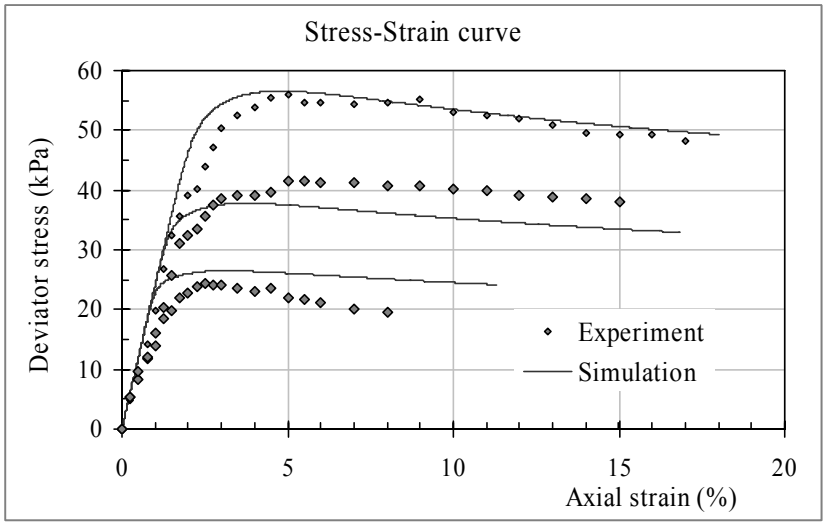

Fig. 5.8: Simulation of the stress-strain behavior

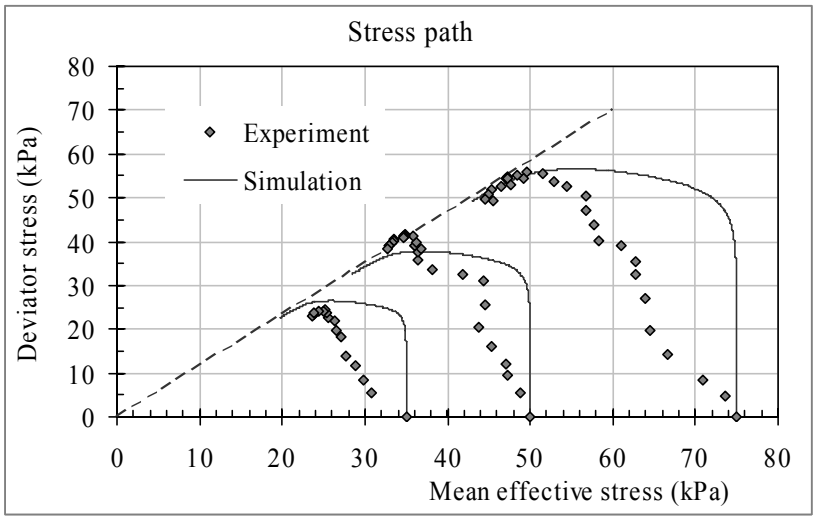

Fig. 5.9: Simulation of the stress paths

In addition, the specimen tested may not be representative of the insitu material due, for example, to sample disturbance, changes in moisture content between the field and the laboratory, also the specimen may not be representative of the poorer performing insitu peat under consideration.

The complete set of parameters used in the simulation of the field consolidation behavior due to the construction of compacted earth fill is shown in Table 5.2. All the analyses described in the following sections are based on these parameters.

Table 5.2: Parameters used in the analysis of a one-dimensional field consolidation problem

Parameters			Values
Initial void ratio	e_0		6.28
Initial vertical effective stress	$\sigma'_{22(0)}$	(kPa)	10.25[#]
Coefficient of earth pressure at rest	K_0		0.53
Coefficient of permeability	k_0	(m/s)	1.5 x 10^{-7}
Change in permeability index	C_k		0.8
Initial shear modulus	G_0	(kPa)	800
Compression index	λ		1.7163
Swelling index	κ		0.1151
Stress ratio at critical state	M^*_m		0.95
Compression yield stress	$\sigma'_{mbi}(\sigma'_{mai})$	(kPa)	12.5[#]
Viscoplastic parameter	m'		22
Viscoplastic parameter	C	(1/s)	1.0x 10^{-10}
Structural parameter	σ'_{maf}	(kPa)	0.7 σ'_{mbi}
Structural parameter	β		5

[#] At a depth of 2.5 m

5.4 Numerical Details for the Analysis

The finite element mesh, the boundary conditions, the time increment, and the initial conditions used in both analyses are described in the following section.

The subsurface profile indicates that a peat layer, about 5 m in thickness, is underlain by a relatively rigid and permeable layer, as shown in Fig. 5.4. Under the same conditions, the peat layer is inelastic and much more compressible than the other layers. Therefore, only the peat layer was considered in the modeling. The peat layer was assumed to be subjected to one-dimensional compression as the dimensions of the loaded area were significantly large relative to the thickness of the peat layer. A finite element mesh with twenty-five elements was used to discretize the peat layer in the analyses. The size of each element was 0.2 m x 0.5 m. The bottom boundary was assumed to be perfectly drained due to the existence of a medium-dense to dense sandy silt layer. Further

investigation revealed that the compacted fill behaved as in impermeable layer, and therefore, the top boundary was assumed to be impermeable for simulating the field conditions. The bottom boundary was ascribed the condition of zero displacement. The horizontal displacement was fixed, but vertical movement was allowed. The finite element mesh and the boundary conditions used in all the analyses are shown in Fig. 5.10.

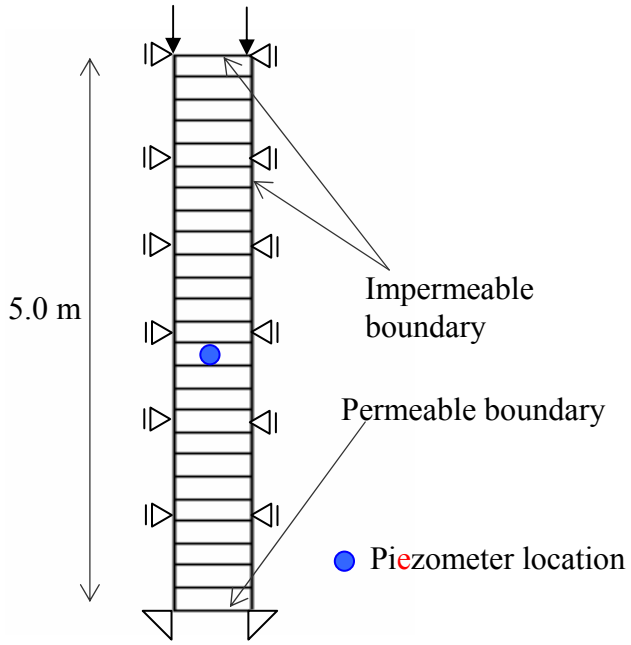

Fig. 5.10: Finite element mesh and boundary conditions

The excess pore water pressure was initially assumed to be zero in all the analyses. Numerical calculations were performed to model the actual construction sequence for the fill, which was raised up to a thickness of about 3 m, as shown in Fig. 5.2. The filling process was simulated by applying incremental vertical loads to the upper boundary. The time increments for the analyses were selected as follows: a small time increment of Δt = 10 s was used in all the loading stages. For the other stages, a relatively large time increment of 100 s was adopted.

5.5 Prediction of the Field Behavior using the Infinitesimal Strain Theory

The numerical analysis of the consolidation behavior of the instrumented earth fill constructed on peaty clay (reported in Section 5.2), using the elasto-viscoplastic model which considers the infinitesimal strain theory, is explained in this section. In the analysis, the degradation of the microstructure induced by the applied loads is not considered.

For the infinitesimal deformation analysis, a basic kinematics assumption exists whereby the difference between the reference configuration and the subsequent configuration is negligible. This means that in the infinitesimal strain analysis, it is assumed that both the size and the position of the element remain the same over time and that any deformations that do take place in the soil element are assumed to be small in comparison to the size of the element. In this case, the selection of stress and strain measurements is unique. Since any local rotations can be ignored, the material time derivatives for stress and strain are objective, and therefore, can be directly applied in the constitutive formulation. Due to these features, the constitutive model can usually be formulated in a concise mathematical form based on infinitesimal theories.

In the finite element formulation, it is assumed that the soil is a two-phase porous medium in which the pores are completely saturated with water, and that the soil particles and the pore water are incompressible. For a boundary value problem related to a soil-water coupled consolidation problem, the finite element method based on Biot's two-phase mixture theory (Biot 1962) is adopted. A four-node quadrilateral element with a reduced Gaussian two-point integration is used for the displacement (Fig. 5.11), and the pore water pressure is defined at the center of each element based on Akai and Tamura (1978).

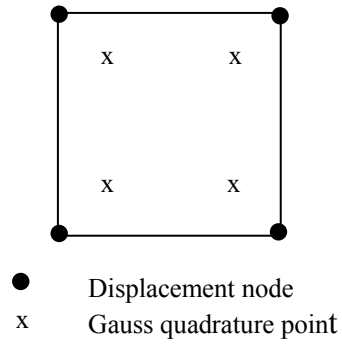

Fig. 5.11: Four-node isoparametric element for displacement interpolation

The procedures for discretizing the equilibrium equation, the continuity equation, and the governing equation, which combines the discretized form of both the equilibrium and the continuity equations used in the finite formulation which assumes the infinitesimal strain theory, are described in Appendix A1. The constitutive equations outlined in Section 3.2 are incorporated into the aforementioned finite element formulation and the analysis is carried out to simulate the excess pore water and the cumulative settlements observed in the field due to the gradual construction of the compacted earth fill. In the analysis, the material parameters listed in Table 5.2 are used, and the adopted numerical details are given in Section 5.4. It should be noted that the structural parameters are not used ($\beta = 0$), since the effect of the structural degradation is not considered in the present analysis.

The observed field behavior, namely, the cumulative settlement and the excess pore water pressure, were compared with the calculated results. The predicted and the observed excess pore water pressure in the middle of the peat layer (depth: 2.5 m) are presented in Fig. 5.12. The field pore water pressure measurements show the sudden rise in pore pressure associated with stage loading and reach around 30 kPa at the completion of the fill. When this behavior is compared with the predicted behavior, assuming infinitesimal strain in the initial stages, the predicted results agree to some extent with the observed results. However, the predicted pore water pressure gradually deviates from the observed values with further loading and significantly overestimates the monitored values at the completion of the fill.

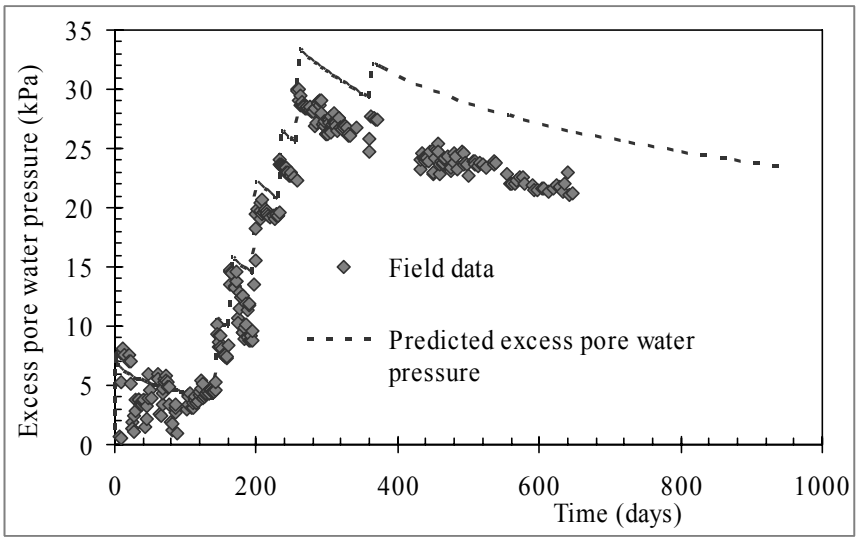

Fig. 5.12: Excess pore water prediction assuming infinitesimal strain

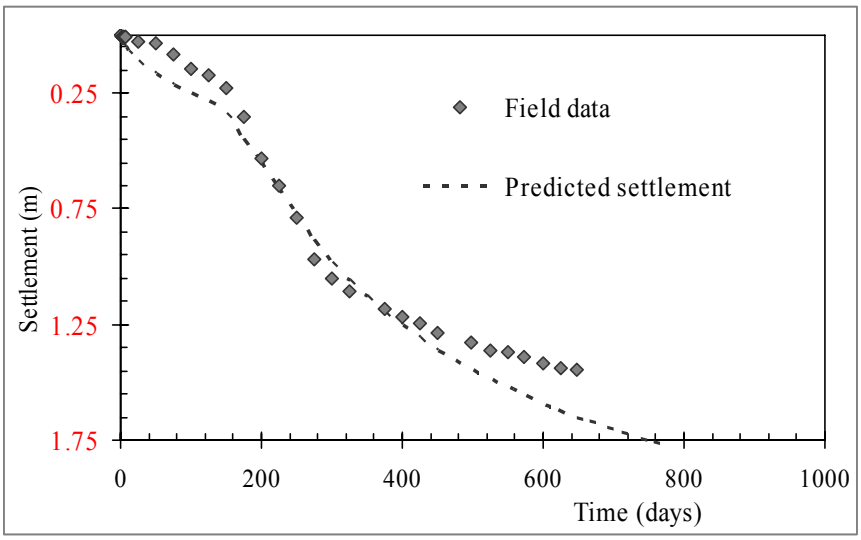

Fig. 5.13: Settlement prediction assuming infinitesimal strain

The predicted settlements which assume infinitesimal deformations are compared with the representative field settlements in Fig. 5.13. The figure indicates that during the initial period in which smaller loads were being applied, the difference between the predicted and the observed settlements are not so distinguishable. However, once the loading is increased with time, due to the gradual placement of the fill, the observed settlements are significantly overestimated by the prediction.

5.6 Prediction of the Field Behavior using the Finite Deformation Theory

It is understood that the analysis based on the infinitesimal strain theory has produced poor simulation results due to the observed large strain in the field (a field settlement of 1.5 m was recorded). The analysis confirms that, in the case of peaty soils, finite deformation is more important than infinitesimal deformation. This is because these soils are easy to deform even under small stress levels and the magnitude of the deformation at the end of the loading is large. Taking all of this into account, the analysis was carried out using the model based on the finite deformation theory.

For finite strain problems, the difference between the reference configuration and all the subsequent configurations cannot be disregarded as with infinitesimal strain problems. The rigid rotation and the objectivity of the material must be carefully treated in the constitutive formulations. The selection of stress and strain measures is not unique, and the material time derivatives of the spatial stress and strain rates are no longer objective. All these facts complicate the mathematical formulation and the numerical analysis of the model based on finite strain.

In the present analysis, finite deformation is taken into account using the updated Lagrangian method with the objective Jaumann rate of Cauchy stress for a weak form of the equilibrium equation. An eight-node quadrilateral element with reduced Gaussian two-point integration is used for the displacement. Biot's two-phase mixture theory is used with a velocity pore pressure formulation and the pore water pressure is defined at the four corner nodes of the element. The finite element formulation was based on the finite deformation theory and was shown in detail in Section 3.3.3. Following the described finite element formulation, the elasto-viscoplastic model presented in Chapter 3 was formulated for the finite deformation and the analysis was conducted to simulate the observed field behavior. The material parameters and the numerical details are the same as for the infinitesimal strain analysis.

The predicted excess pore water pressure and the settlement based on the finite deformation theory are shown in Figs. 5.14 and 5.15, respectively, together with the corresponding measured data. The predicted results obtained from the infinitesimal strain analyses are also shown for comparison in these figures. As shown in Fig. 5.14, the predicted excess pore water pressure using finite strain shows a poor agreement with the observed field data which reached around 30 kPa at the completion of the fill load of 46 kPa, and dissipated only about 10 kPa during the following year. These results indicate that the predicted pore water pressure is less than the observed value from the beginning and, as a result, the observed maximum field pore water pressure at the completion of the fill is highly underestimated by the prediction.

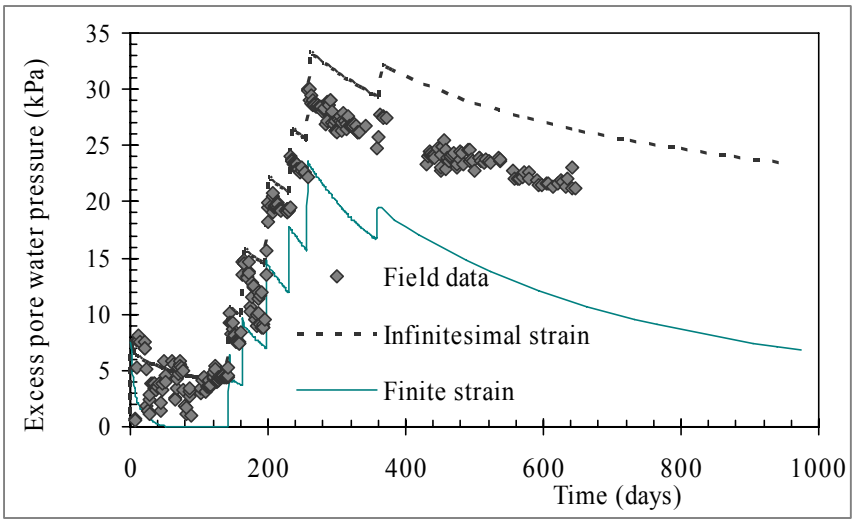

Fig. 5.14: Prediction of excess pore water pressure based on finite strain, infinitesimal strain, and the corresponding field data

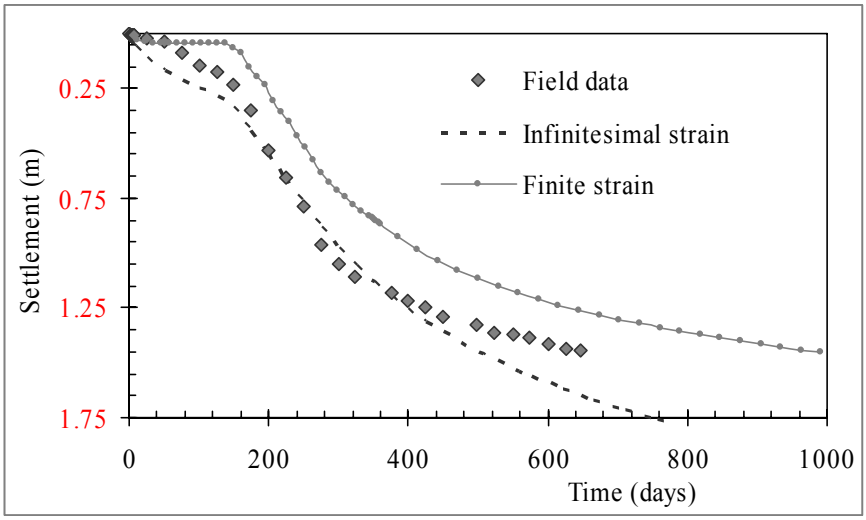

Fig. 5.15: Prediction of settlements based on finite strain, infinitesimal strain, and the corresponding field data

Unlike the excess pore water prediction, the comparison of the field settlements and the predicted settlements with the finite deformation theory shows a good qualitative agreement even though it underestimates quantitatively (Fig. 5.15). However, the field settlement that advanced at a much faster rate during the early stages of loading could not be captured by the prediction.

5.6.1 Comparison of the Results from Finite Strain with Infinitesimal Deformation Analyses

In order to gain insight into whether or not the finite deformation theory must be applied in peat consolidation problems, the results predicted with finite deformation are compared with those made with the infinitesimal strain theory. As can be clearly seen in Fig. 5.14, the predicted excess pore water pressure is less for the finite deformation solution than for the small deformation solution. Fig. 5.15 shows that the settlements predicted by the finite deformation theory are always smaller than those predicted by the infinitesimal deformation theory. Also, as seen in Fig. 5.15, the difference in the predicted settlements between the finite deformation computations and the infinitesimal deformation computations increases with an increasing magnitude of load with time. This stiffening nature in finite deformation computations comes from changes in the geometry (i.e., decrease in soil layer height) which in turn cause a decrease in drainage due to the applied compressive force. A decrease in the drainage path would result in lower pore water pressure for the finite deformation analysis than for the infinitesimal case. This behavior in the finite deformation analysis reveals that changes in the geometry cause the rate of consolidation to become faster than that in the infinitesimal deformation case.

5.7 Prediction of the Field Behavior using the Finite Strain Theory and Considering the Effect of Degradation

As presented in the above figures, the field pore water pressure measurements show a sudden rise in pore pressure with stage loading and reach around 30 kPa at the completion of the fill. After the completion, no significant dissipation of excess pore water pressure actually takes place in the field. However, field settlements advance without any significant dissipation of excess pore water pressure. As a result of this contradictory tendency, the predicted results, particularly the excess pore water pressure described in

the proceeding sections, show completely different types of behavior during the consolidation period.

This unusual phenomenon, namely, the settlement advances without significant dissipation in the excess pore water pressure, has been observed during many construction projects on soft soil deposits around the world. For example, Lavellee et al. (1992) reported that the pore water pressure measured by several piezometers beneath the Olga-C test embankment was seen to become stagnant during the period of no construction. During this period, significant settlement was also reported along the center line of the embankment. Jardine and Hight (1987) reported that a significant settlement occurred in spite of the slow rate of dissipation in pore water pressure observed after the end of the embankment construction over the soft clay. There are various possible explanations for this kind of unusual pore water pressure dissipation and continuing deformation after the end of construction. Mesri and Choi (1979, 1985) pointed out that the additional pore water pressure appearing during consolidation is generated due to the collapse of the clay structure. In 20th Terzaghi Lecture, Mitchell (1986) described that this phenomenon occurs during consolidation as a result of the structural degradation of soft overconsolidated clay when the current stress state exceeds the preconsolidation pressure.

Kimoto and Oka (2005) have numerically simulated this phenomenon by introducing the degradation of the microstructure induced by applied loads in the consolidation process. They proposed a method to account for the effect of structural degradation, by introducing viscoplastic strain softening in addition to strain hardening with viscoplastic volumetric strain. As a result, the degradation of the soil structure induces a slower increase in size of the hardening surface and the static yield surface than that of the pure volumetric hardening case. The detailed procedure for taking the structural degradation effect into account was described in Section 3.2.5. By adopting the same procedure for the finite deformation theory, the analysis was carried out to simulate the field behavior of the peaty clay layer due to the construction of compacted earth fill described in the above sections. The material parameters used for the analysis are listed in Table 5.2. The numerical details, such as the finite element mesh and the boundary conditions, are the same as those used for the previous analysis and described in Section 5.4.

The excess pore water pressure predicted by considering finite deformation and the effect of degradation is shown in Fig. 5.16 with the corresponding field measurements. The observed behavior is predicted accurately by the model during and after the construction of the fill. The sharp peaks of the simulated results, which represent sudden increases in pore pressure associated with loading, show a good agreement with the field measurements. In addition to the observed maximum pore pressure due to the

construction of the fill, the stagnated type of pore pressure dissipation observed after the construction is predicted well by the model.

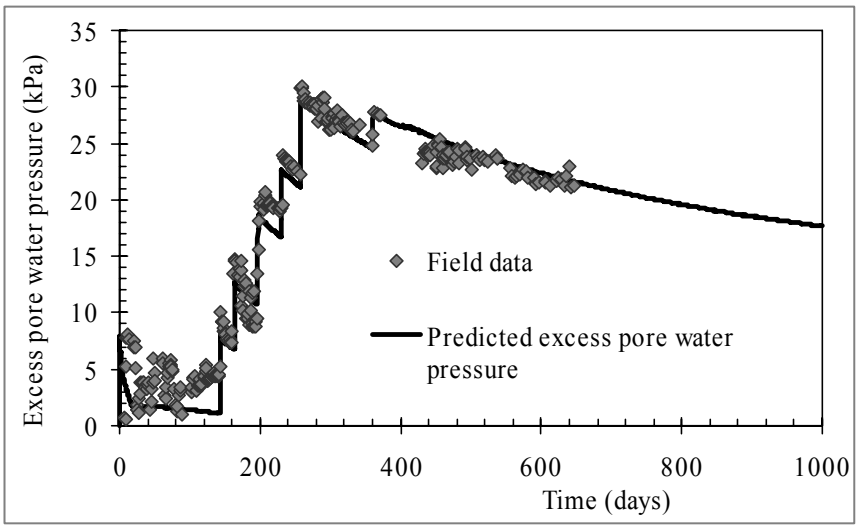

Fig. 5.16: Excess pore water prediction based on finite strain considering the effect of degradation

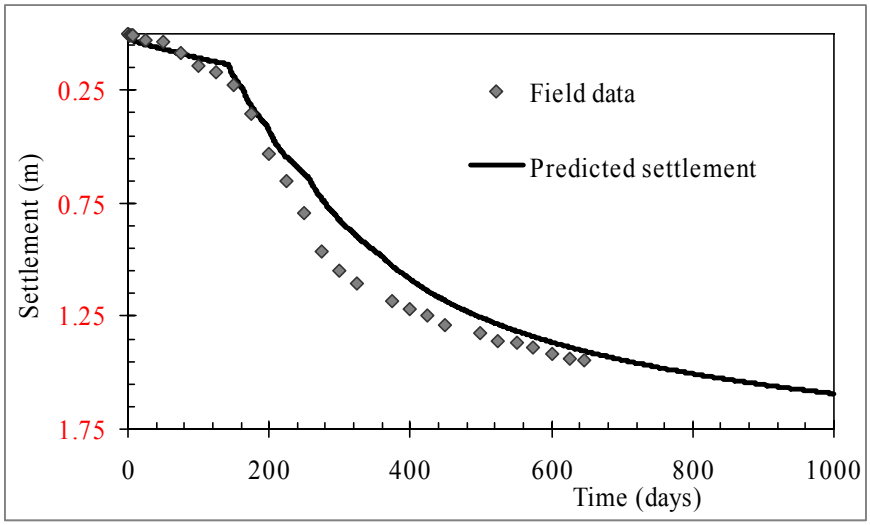

Fig. 5.17: Settlement prediction based on finite strain considering the effect of degradation

The measured and the simulated surface settlement–time curves are shown in Fig. 5.17. Unlike the settlements predicted by the model based on the finite strain alone (Fig. 5.15), the early stage settlements due to the initial loading are captured well by the model, once it considers the effect of degradation with finite strain. This might be due to the ability of the model to account for the sudden increase in settlements associated with the degradation of the soil structure, which plays an important role in predicting the consolidation settlements of natural soil deposits. Also, as indicated in Fig. 5.17, the

predicted settlements advance in a similar way to the field measurements, providing a better agreement.

5.8 Comparison of the Results and a Discussion

The excess pore water pressure in the middle of the peat layer (depth: 2.5) predicted by the model considering infinitesimal strain, finite strain alone, and finite strain together with the effect of structural degradation is shown in Fig. 5.18 with the corresponding field measurements. The loading curve showing the construction history of the fill (Fig. 5.2) is also given in the figure for clarification.

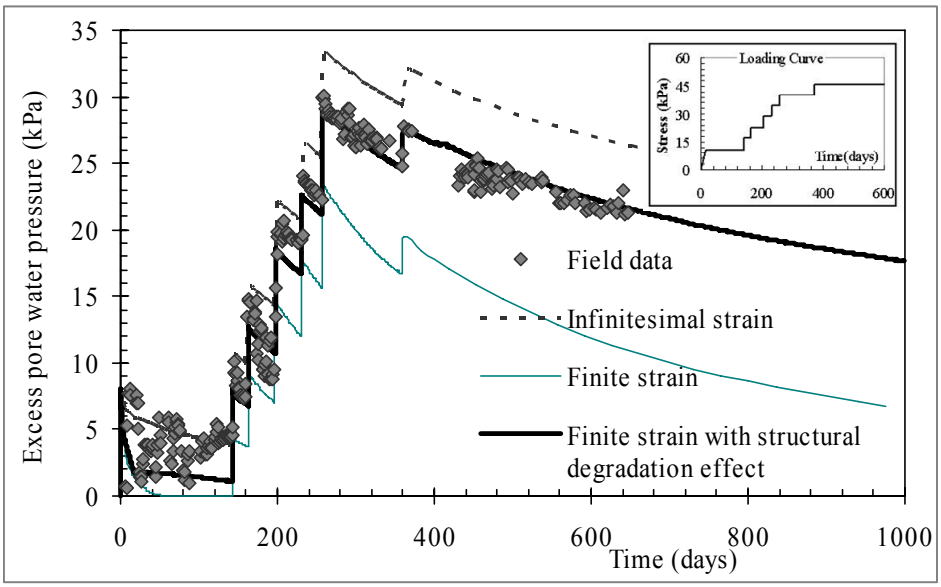

Fig. 5.18: Excess pore water pressure-time profile

The curve indicates that the field pore water pressure reached around 30 kPa at the completion of the fill due to a load of 46 kPa. After the completion of the fill, the quantity of dissipated excess pore water pressure was only about 10 kPa during the following year. When this behavior is compared with the predicted behavior, it is seen that the prediction made by the infinitesimal strain theory overestimates the observed excess pore water pressure. In contrast, the finite strain theory underestimates this value when it is compared with the observed field data. Only the predictions made by the finite strain theory with structural degradation show a remarkable agreement with the observed field behavior. The above results indicate that when predicting excess pore water pressure behavior in highly compressible materials like peat, it is necessary to consider changes in the geometry (decrease in soil layer height) in order to account for the correct drainage

path. Moreover, it is essential to consider the effect of structural degradation along with other variables in order to simulate the stagnated pore pressure observed after the construction.

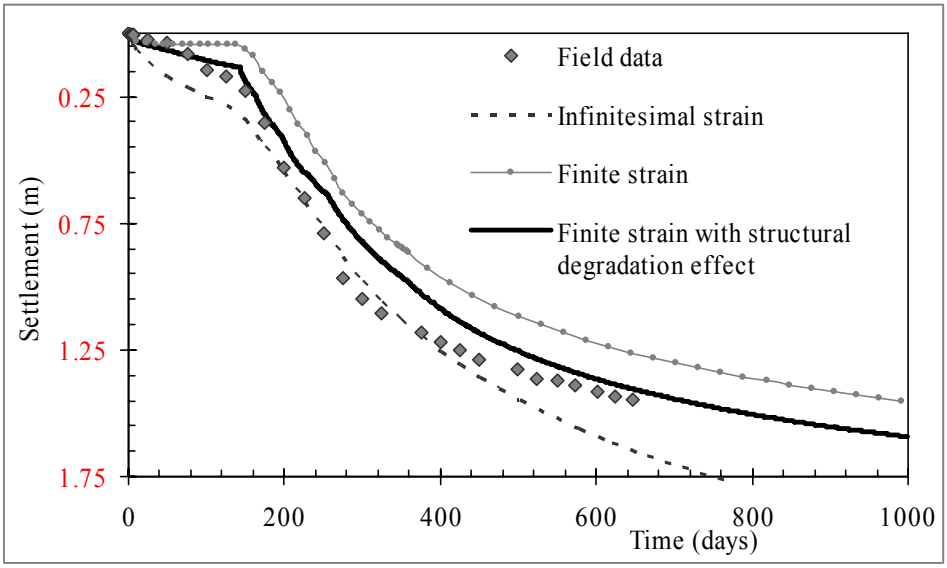

Fig. 5.19: Settlement-time profile beneath the fill

A comparison of the predicted and the actual settlements is presented in Fig. 5.19. The field settlement data indicates that the settlement advances even with the existence of stagnated excess pore water pressure in the field. The comparison shows that, as expected, the settlement predicted by assuming infinitesimal strain gives a higher value than that assuming finite strain. And, in this case, the difference is more significant due to the resultant large strain of around 20% in the field. The prediction made by the infinitesimal theory overestimates the field settlement, whereas the prediction made by the finite strain theory shows a qualitative agreement with the observed data, even though it quantitatively underestimates the actual settlement. Similar to the pore water pressure predictions, the finite strain with structural degradation shows better qualitative and quantitative agreements with the observed field data for the parameters used in the analysis.

5.8.1 Importance of Considering the Effect of Degradation

The performance of the model which considers the finite strain with the effect of structural degradation can be clearly seen in this analysis. Fig. 5.18 shows the predicted settlement for the case in which the degradation effect advances faster than that for the

case without the degradation effect, but the difference in the advance in settlement between the two is not so significant. On the other hand, a big difference is clearly seen in Fig. 5.19 in the prediction of the excess pore water pressure in the peat layer. Although only a slight difference exists for the advance in settlement between the two cases, the excess pore water pressure for the case which considers the effect of degradation remains almost constant even after the end of loading, while the excess pore water pressure for the case which does not consider the effect of degradation starts to dissipate significantly at the completion of loading. This indicates that when analyzing the consolidation behavior of natural soil deposits, the degradation effect of the structure cannot be ruled out in order to simulate realistic in situ behavior. As shown in Figs. 5.18 and 5.19, the unusual behavior whereby the settlement advances without any significant dissipation of excess pore water pressure, can be described by introducing the effect of the structural degradation into the elasto-viscoplastic finite element analysis based on the finite deformation. Unless this kind of model is adopted in the consolidation analysis, it is almost impossible to assess the above-mentioned behavior that is often observed in natural soil deposits.

5.9 Summary and Remarks

The simulation of the field consolidation behavior of peaty clay due to the construction of compacted earth fill reveals that the finite deformation theory is more representative than the infinitesimal strain theory for the consolidation analysis of materials like peat which is highly compressible in nature. In the finite strain analysis, changes in geometry affect the ground rigidity and the rate of consolidation. Therefore, the finite strain analysis always predicts lower levels of excess pore water pressure and settlements than the infinitesimal strain analysis. The difference between the two methods becomes significant with the occurrence of large strain. The effect of structural degradation has a significant influence on the predictions of the observed settlements and the stagnated excess pore pressure occurring simultaneously in the field. The results of the analysis confirm that when analyzing the consolidation behavior of natural soil deposits, it is essential to consider the effect of the degradation of the structure of the deposits in order to describe realistic in situ behavior.

Chapter 6

SIMULATION OF FIELD BEHAVIOR DUE TO EMBANKMENT CONSTRUCTION ON NATURAL SUBSOIL

6.1 Introduction

The construction of embankments on peat soils gives rise to special problems due to their poor engineering properties such as high compressibility and low shear strength. The most obvious problem is the possible occurrence of large deformations during and after the construction period, both vertically and horizontally. Settlements often appear quickly, and may continue for very long periods of time due to creep. Post-construction settlements lead to significant problems for roads with high standards. The low shear strength of peat soils often causes stability problems, and consequently, the load sometimes has to be placed in stages. Therefore, it is essential to reclaim these highly compressible deposits suitable for supporting embankment foundations.

The design of highway embankments on peat deposits usually offers many alternative solutions from which engineers must make a judicious choice. In so doing, they have to take into consideration the cost and the technical feasibility of the different alternatives. Generally speaking, the methods which deal with construction over peat include techniques such as replacing the peat with inorganic materials, transferring the foundation loads down to a better stratum, and utilizing improved peat as the foundation material. Before engineers began to understand the way in which peat behaves under loads, it was generally agreed that when a high standard road was aligned on a peat deposit, the peat

had to be removed either by an excavation or by other displacement methods due to the high compressibility of this material. In some cases, the foundation loads were transferred to an underlying dense layer or rock through a system of piled foundations. With an understanding of the behavior of peat under loads, methods which can improve the engineering properties of in situ peat, so that it can be utilized as foundation material, are becoming more and more common as these methods are not only economical, but they are also technically advantageous for highway projects in which large areas of peaty soils are encountered.

The preloading concept is the most commonly used method for the in situ improvement of the engineering properties of peat in geotechnical engineering practices. The preloading technique, in which a surcharge load is placed on a site prior to construction, has proved to be very effective in reducing the settlement to acceptable levels. Furthermore, the precompression of peat is advantageous in that it results in an appreciable increase in shear strength which makes the preloading technique extremely interesting for different engineering applications (Lea & Brawner 1963; Jonas 1964; Johnson 1970; Samson & La Rochelle 1972; Berry 1983; Kulathilaka 1999). However, the application of the preloading method to the construction of embankments on peat deposits raises certain problems related to the maximum load which can be applied at one time, to the total settlement to be expected, and to the time and magnitude of the preloading required to insure that only tolerable settlements will occur during the life of the structure. Therefore, the efficient use of this technique requires the ability to predict, in advance, the behavior of peat with particular reference to:

(1) Final settlements expected under different loads

(2) Rates at which such settlements occur

(3) Long-term settlements due to creep behavior

(4) Stability of the embankment during and after construction.

The first two considerations are controlled primarily by the consolidation characteristic of peat. Consolidation and the increase in shear strength are related through the rate of pore pressure dissipation. Predictions of long-term settlements are very important to the construction of super-grade highways on peat soil as post-construction settlements will lead to significant problems in service conditions. The verification of the stability during construction is of major importance in preloading projects with a stage-construction embankment; time and money can be saved if the increase in strength of the peat layer beneath the embankment can be accurately predicted.

As such, the model performance in describing the above behavior of peaty clay due to embankment construction is verified using field monitoring data on embankments constructed in the Colombo-Katunayake Expressway (CKE) project in Sri Lanka. Two-dimensional plane strain elasto-viscoplastic finite element analyses are carried out considering finite deformation together with the effect of structural degradation on consolidation.

In this chapter, the model is applied to predict the field behavior of peaty clay brought about by an embankment constructed on natural peaty clay using the preloading technique. Initially, a brief description of the CKE project is presented. Then, details are given on the geotechnical profile, the field instrumentation, the laboratory and the field tests, the determination of the soil parameters, the loading curve, and the finite element mesh used in the analysis. The predicted behavior is compared with the observed data, and the stability of the embankment is verified.

6.2 Project Description

The Colombo–Katunayake Expressway (CKE) is the first proposed major highway in Sri Lanka. It will connect the International Airport at Katunayake to the capital city of Colombo. The total length of the expressway will be 25.8 km, and the majority of the road will traverse flood plain and marshy ground consisting of very soft peat, organic soils, and clays up to 15 m in thickness. The construction of road embankments over these soils involves risks of embankment instability and excessive settlements. Soft ground treatments adopted to overcome the problems include methods of preloading and surcharging, prefabricated vertical drains, sand compaction piles, and stone columns. The instrumenting and the monitoring of the road embankment are also being implemented during construction using settlement plates, settlement stakes, piezometers, observation wells, and inclinometers. Extensive geotechnical investigations, including borehole tests, cone penetration tests, vane shear tests, and laboratory tests, have been carried out to investigate the subsurface profile and the soil properties (Hsi et al.2005).

6.2.1 Subsoil Condition and Embankment Construction

The trial embankment at Ch.11+950 in the CKE project was constructed using preloading with surcharging as the ground-improvement technique; details of the embankment are described in following section.

Based on the drilled borehole logs, the embankment foundation was roughly stratified into the layers shown in Fig. 6.1 (Ketheeswaravenayagam 2006). On top, there is a highly compressible peaty clay layer, 1 m in thickness, followed by a very loose silt layer, up to 2 m in depth. Below that, a soft silty sand/clay layer with pockets of peat, approximately 4.5 m in thickness, is encountered. These compressible layers are underlain by layers of loose to medium-dense sand which extend to a depth of 13.5 m. Then, there is a layer of stiff clayey silt, about 2 m in thickness, overlying a dense sand layer, up to an investigation depth of 20.0 m from the existing ground level.

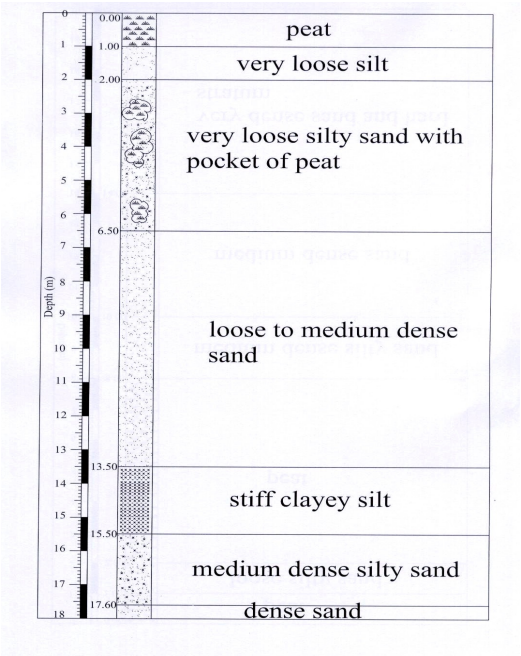

Fig. 6.1: Subsurface profile beneath the embankment (Ketheeswaravenayagam 2006)

A loading curve that denotes the construction history of the embankment is shown in Fig. 6.2.

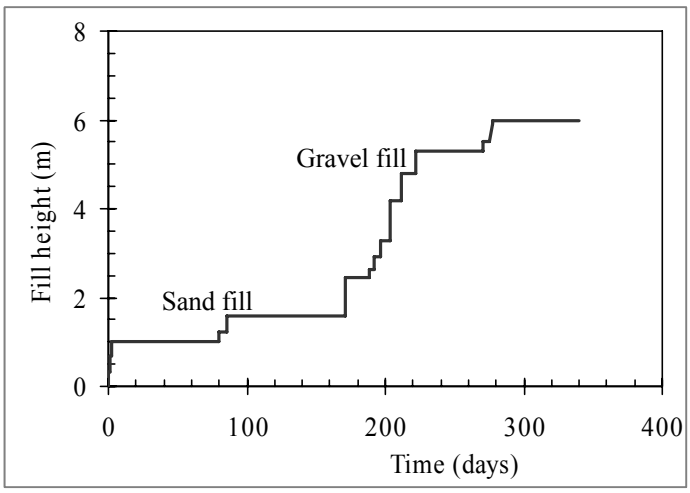

Fig. 6.2: Loading curve

The embankment has a height of 5.69 m (with surcharge fill of 0.94 m), a crest width of 13.6 m, and 1:2 side slopes. The general construction sequence for the trial embankment consisted of the laying of geotextiles over the full width of the embankment at ground level, the placing of a sand mat about 1.5 m in thickness, the installation of instruments, and finally, the construction the embankment from gravel fill.

6.3 Material Parameters

Table 6.1: Parameters used in the embankment analysis on natural soil

Parameters		Values for peats	Values for inter-mediate silt layer
Initial void ratio	e_0	6.5#	1.8
Initial vertical effective stress	$\sigma'_{22(0)}$ (kPa)	9.0#	12.0
Coefficient of earth pressure at rest	K_0	0.53	0.5
Coefficient of permeability	k_0 (m/s)	8.0 x 10^{-7}#	5.5 x 10^{-7}
Change in permeability index	C_k	1.0	0.9
Initial elastic shear modulus	G_0 (kPa)	800	1000
Compression index	λ	1.505	0.203
Swelling index	κ	0.096	0.011
Stress ratio at critical state	M_m^*	0.95	1.1
Compression yield stress	$\sigma'_{mbi}(\sigma'_{mai})$ (kPa)	9.0#	12.0
Viscoplastic parameter	m'	22	30
Viscoplastic parameter	C (1/s)	1.0x 10^{-9}	1.0x 10^{-10}
Structural parameter	σ'_{maf} (kPa)	0.7 σ'_{mbi}	0.7 σ'_{mbi}
Structural parameter	β	5	5.0

At a depth of 1 m

The material parameters required for the analysis are determined based on the data reported by Ketheeswaravenayagam (2006) and research findings related to amorphous peaty soil. The initial vertical effective stress, $\sigma'_{22(0)}$, for each layer is determined based on the results of in situ density profiles. Compressibility parameters λ and κ, critical state parameter M_m^*, and the initial coefficient of permeability k_0 are obtained from the data reported by Ketheeswaravenayagam (2006), and are based on previous laboratory results and publications. The coefficient of lateral earth pressure at rest, K_0, is taken as 0.53, as recommended by Edil and Dhowian (1981) for amorphous peat. According to Ketheeswaravenayagam (2006), the in situ peat layer yields almost the same physical and mechanical properties as the peat considered in the back analysis of the instrumented

earth fill described in Chapter 5. Therefore, the same values as those in the above-mentioned analysis are used for viscoplastic parameter m', initial elastic shear modulus G_0, and structural parameters σ'_{maf} and β, in the present analysis, as corresponding triaxial stress-strain curves for peat are not available. However, viscoplastic parameter C is set at a slightly higher value than in the prediction described in Chapter 5, considering the state of the peaty soil at the site (the C value for young clays is higher than that for aged clays). There are no available test data for silt and sand layers due to inadequate in situ testing and sampling. Therefore, realistic values are assumed for all silt and sand layers in the analysis. The model parameters used for the peaty clay are listed in Table 6.1. It should be noted that the very soft silty clay/peat layer indicated in the subsurface profile is modeled in the analysis using the same properties for the peaty clay by considering the observed large settlement. This assumption is further confirmed by the borehole data at Ch.11+900.

6.4 Finite Element Analysis of the Embankment Foundation

In the finite element analysis, the problem is solved as a two-dimensional plane strain consolidation problem with a symmetry condition applied at the centerline of the embankment. A computation domain, 15.5 m in the vertical direction and 97 m in the horizontal direction (from the axis of symmetry), is discretized into 420 elements, as shown in Fig. 6.3. The width of the area selected for the numerical modeling is large enough (more than three times the embankment width) for the boundary on the right side to have a negligible influence on the results.

The prescribed boundary conditions are as follows. The horizontal displacements and the water fluxes on the left-hand side (the axis of symmetry in Fig. 6.3) are set at zero in order to achieve the condition of symmetry. The bottom boundary is ascribed the condition of zero displacement and imperviousness. Also, a horizontal displacement is constrained at the right-hand side vertical boundary which is assumed to be impervious. At the ground surface, conditions of free drainage and unconstrained displacement apply. The excess pore water pressure is initially assumed to be zero in the subsoil.

The distribution of initial effective stress for the foundation used in the analysis is shown in Fig. 6.4. It should be noted here that a surcharge load of magnitude 9 kN/m2 was introduced over the foundation to enable the computation of the elasto-viscoplastic finite element analysis based on the finite deformation. Otherwise, the top elements of this

normally consolidated peat soil would reach the critical state during a very early stage of loading, due to low mean pressure, and hence, the deformation computation would later become impossible.

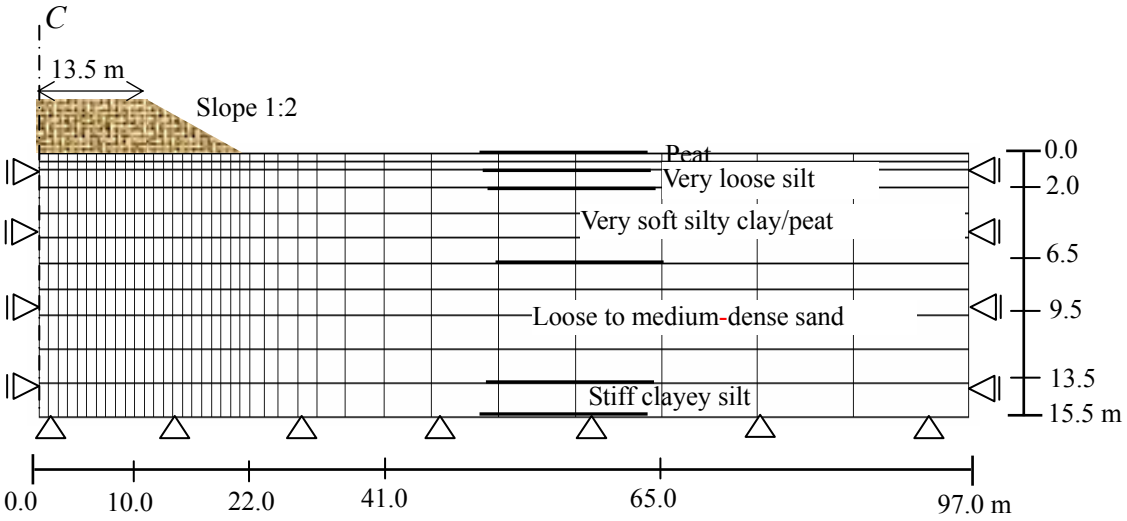

Fig. 6.3: Finite element configuration

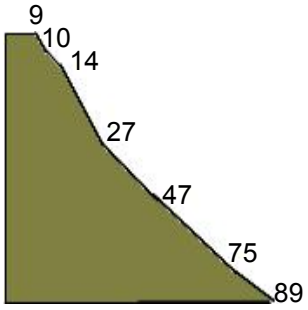

Fig. 6.4: Initial vertical effective stress profile (kPa)

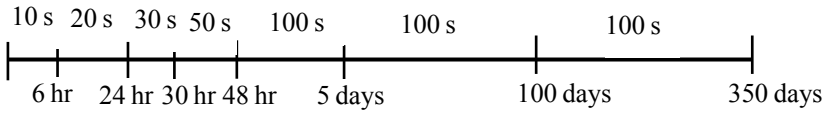

Fig. 6.5: Time increment used in the analysis

The embankment loading is simulated by applying incremental vertical loads to the upper boundary according to the sequential construction history of the embankment (Fig. 6.2). The embankment loads are calculated as the product of the fill thickness and the total unit weight of the fill. For this purpose, total unit weights of 20 kN/m^3 and 17.4 kN/m^3 are assumed for the initial sand mat and the subsequent gravel fill, respectively, as shown in Fig. 6.2.

The time increments used in the analysis are shown in Fig. 6.5. A small time increment is adopted by considering the expected large volumetric strain rate in the initial loading period. However, the time increment gradually increases with time, and finally, a constant time increment is used in the rest of the analysis.

A finite element analysis is performed using the elasto-viscoplastic model described in Chapter 3, to simulate the observed field behavior. The analysis was carried out by considering the finite deformation theory together with the effect of structural degradation. The parameters used in the analysis are listed in Table 6.1. In the modeling, the behavior of the peat, the very loose sand, the soft silty sand/clay, and the stiff clay was assumed to be elasto-viscoplastic, while the behavior of the loose to dense sand was assumed to be elastic. The grass mat existing on the original ground surface, which gave additional strength to the subsoil, was modeled as a thin elastic element. The final height of the embankment was about 6 m (Fig. 6.2) and the average unit weight of the fill material was around 17.5 kN/m^3. Thus, the expected increase of vertical stress under the embankment foundation was more than 100 kPa. The embankment was constructed in stages and the total construction period was fairly long, as shown in Fig. 6.2. Therefore, by considering the highly nonlinear nature of the $e - \log \sigma'_v$ curve in peaty soil, as well as the reduction in compressibility at higher stress levels associated with the peat consolidation process, the compressibility parameters were varied with the specific volume of the soil using Eqs. (3.33) and (3.34) mentioned in Chapter 3.

6.5 Prediction of Field Behavior

6.5.1 Deformation Behavior of Subsoil

The field settlement was monitored by a settlement gauge installed just beneath the center of the embankment 8 days after the construction was started. The recorded settlement before the installation was 0.661 m due to the initial embankment loading. Fig. 6.6 shows the predicted and the measured settlements just below the center of the embankment.

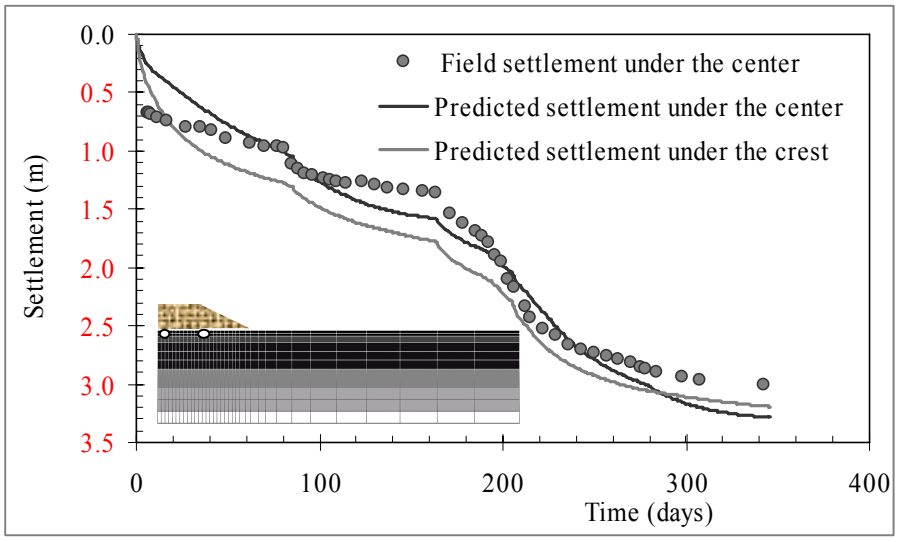

Fig. 6.6: Comparison of settlement predictions

The measured value for the settlement just below the center of the embankment is 3.0 m; the corresponding predicted settlement is around 3.2 m at the end of the monitoring period. The initial discrepancy indicated in the predicted and the observed results under the center is possibly due to the effect of the surcharge introduced in the initial stress distribution of the foundation for the numerical stability of the computation. Under loads that exceeded the initial surcharge, the calculated results show a good agreement with the observed data. This indicates that the resultant large strain in the field is captured well by the model.

In the development of settlement under an embankment at ground level, it is usually taken for granted that the maximum settlement always occurs at the center. While this is true for most soft soil foundations of average dimensions, the calculated results here indicate that the predicted settlements under the shoulder area is greater than that of central area of the embankment during the construction period. The predicted settlement under the crest area (12.5 m away from the center) of the embankment is shown in Fig. 6.6. A comparison of this predicted settlement pattern was not possible as the measured surface settlement under the crest area is not available for this embankment. However, similar field observations have been made for some wide embankments constructed on soft soil elsewhere in the world (e.g., Indraratna et al. 1992). Zhang (1999) discussed the four possible settlement patterns according to the characteristics of the shear stress increment distributions, namely, one-dimensional, sagged, transitional, and typical (the maximum settlement occurs at the centerline and the soil heaves symmetrically outside the slope). If an embankment is extremely wide, compared to its height, the stress condition in the central area of the foundation is approximately one dimensional and the condition in the shoulder area is two dimensional. In many cases, the width of an embankment is not large enough to result in a shear-free central area, but also not small enough to cause the formation of a typical settlement basin (i.e., maximum in the center); this is probably valid for the dimensions of the embankment considered in the present analysis. The higher settlement that was predicted under the shoulder area of the embankment foundation was possibly due to the result of local shear-induced displacement.

Zhang (1999) reported that one settlement pattern might change into another settlement pattern as the construction or the surcharge progresses. The deformed geometrical patterns of the embankment foundation, due to loading, are shown in Fig. 6.7. The figure indicates that the maximum settlement was predicted beneath the side slope of the embankment during the construction period. Then, the location of the maximum settlement gradually shifted toward the centerline, as indicated in Fig. 6.7, after the embankment construction was completed.

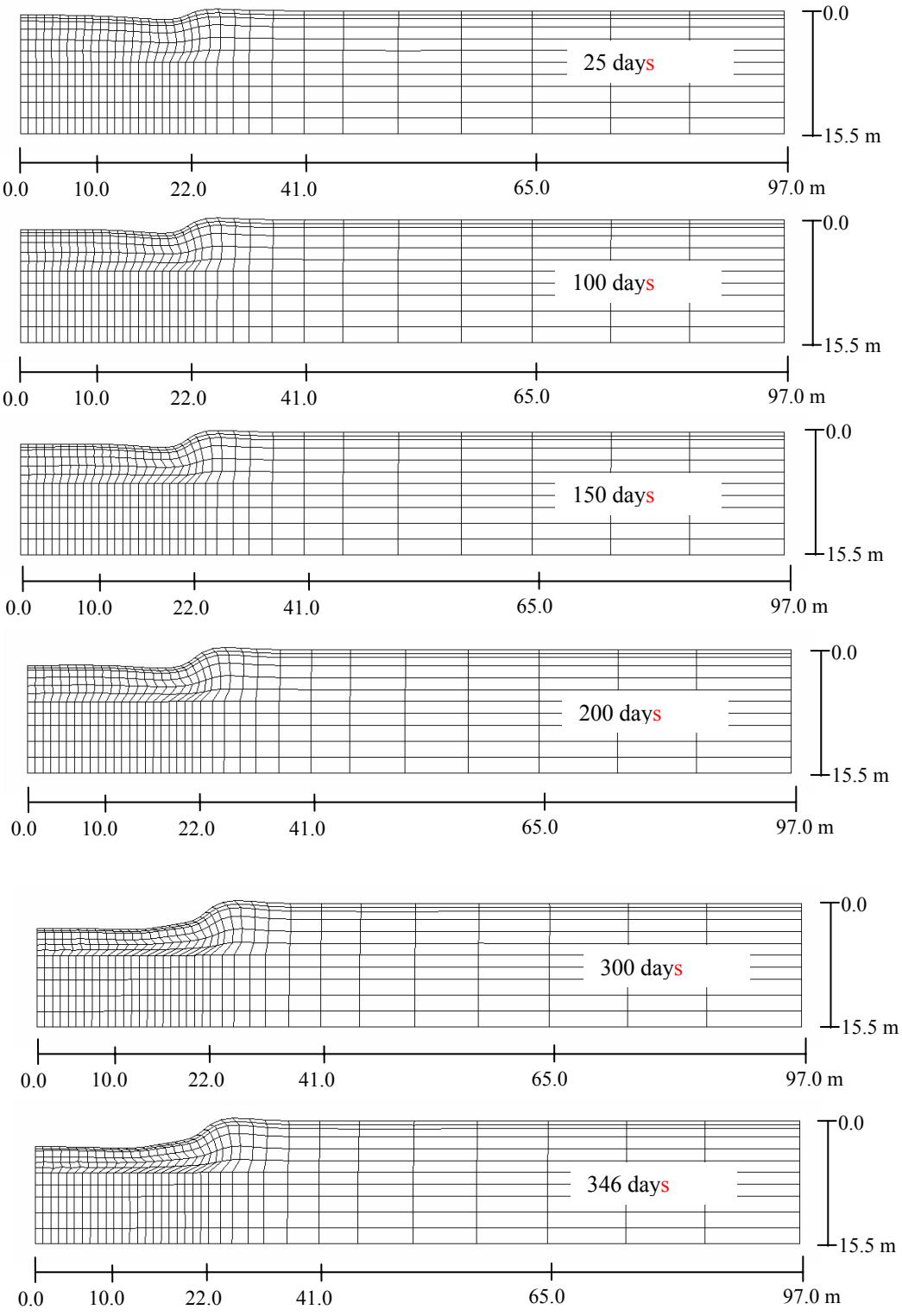

Fig. 6.7: Deformation patterns of the subsoil

6.5.2 Excess Pore Water Pressure

The predicted excess pore water pressure levels at different locations beneath the embankment are shown in Fig. 6.8. A loading curve with the construction history of the embankment is also shown in the figure.

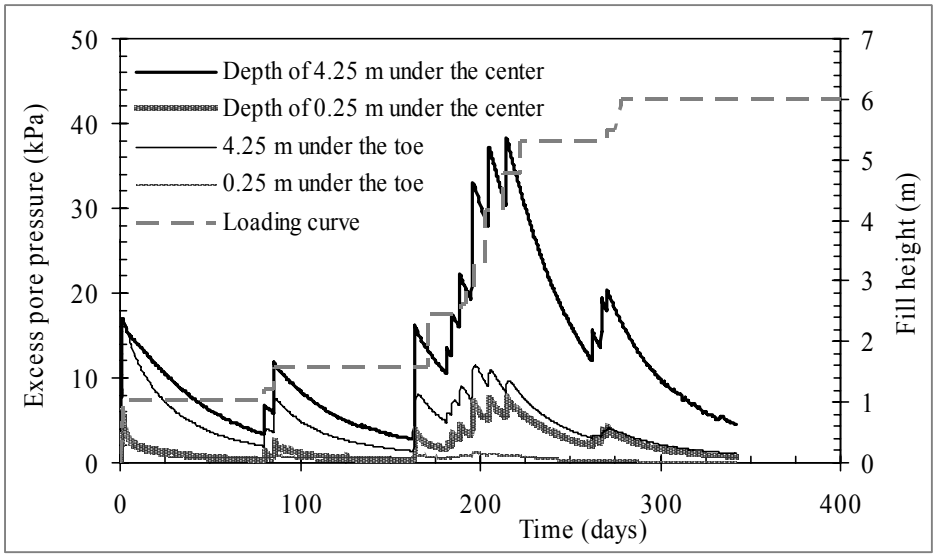

Fig. 6.8: Predicted excess pore water pressure beneath the embankment

The anticipated total load on the subsoil, due to the embankment construction, was around 107 kPa (sand mat of 1.04 x 20 kN/m^3 + gravel fill of 4.95 x 17.4 kN/m^3). This load was applied in stages, as shown in Fig. 6.8. The predicted maximum excess pore water pressure is about 40 kPa in the middle of the peat layer (depth: 4.25 m) due to the stage construction of the embankment. The predicted results indicate that the dissipation of excess pore water pressure is initially quite high due to the high initial permeability of peaty clay. With continued loading, however, the permeability of the peat decreases as a result of the physical reduction in the void ratio during the consolidation process. For this reason, the rate of dissipation of the excess pore water pressure gradually decreases with time.

As described earlier, the maximum settlement has been predicted not under the center, but under the crest area of the embankment. However, the maximum excess pore water pressure dissipation is always predicted around the center. The predicted excess pore water pressure distributions in the subsoil, due to the embankment construction, are shown in Fig. 6.9 for different numbers of days.

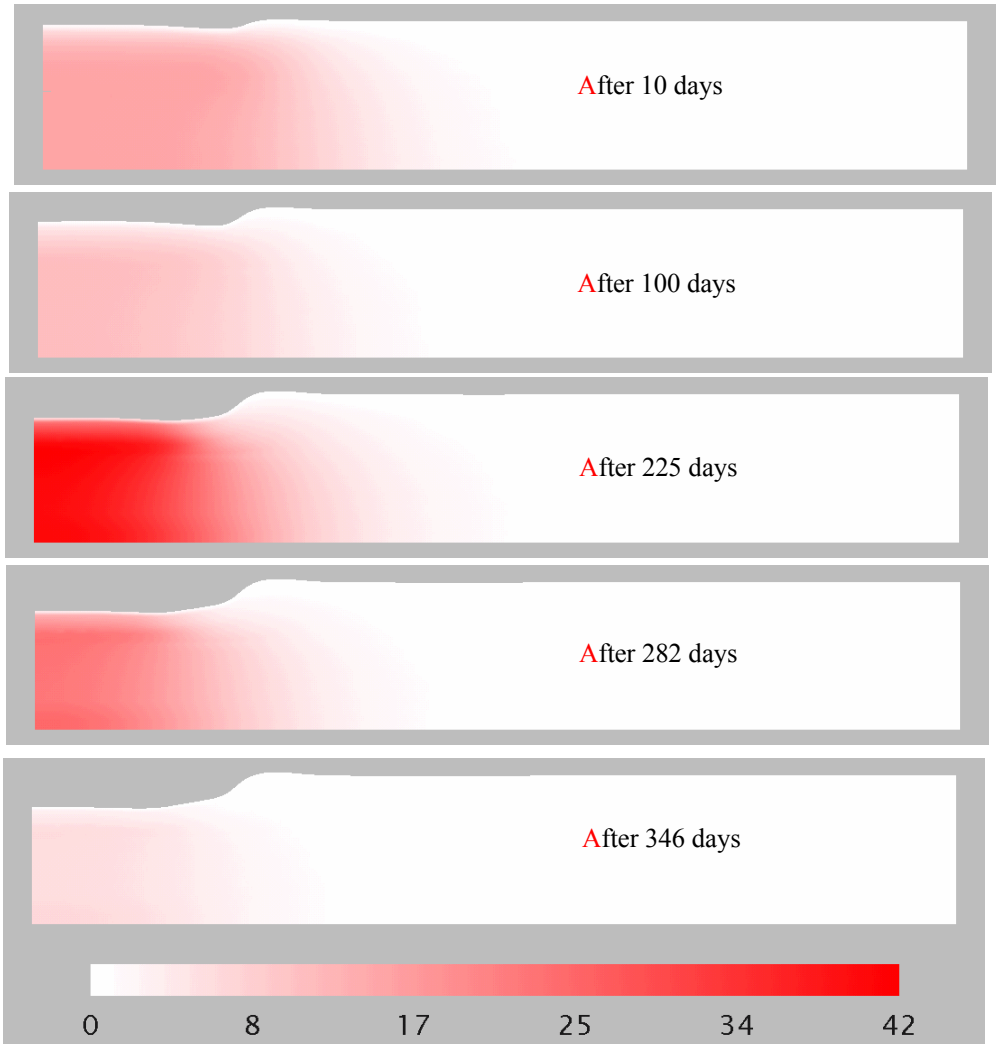

Fig. 6.9: Distribution of excess pore water pressure beneath the embankment (kPa)

6.6 Verification of the Embankment Stability

In addition to excessive settlements, embankments constructed on peaty clays are subjected to large outward lateral displacements. As indicated in Fig. 6.7, a large lateral deformation occurred beneath the toe of the embankment. This lateral deformation was mainly caused by the shear stress induced by the embankment load. If this shear stress is large enough, it will cause shear failure within the subsoil. Therefore, the stability of an embankment built on peaty soil is very important due to the soft consistency of peat.

In traditional soil mechanics, the analysis of an embankment is divided into two distinct parts, namely, an investigation of the stability and an investigation of the settlement of the

foundation. This division is artificial and ignores the complete stress-deformation response. In addition, it gives no indication of the safety of the embankment when the loading rate is too slow for the soil to be considered undrained and yet too fast for it to be considered drained. On the other hand, the present analysis is based on a soil-water coupled boundary value problem and creates the inter-relationship among strength, stiffness, and consolidation which produces more realistic behavior. Moreover, an analysis which considers finite deformation provides better results in the verification of instability problems where the deforming body undergoes significant changes in geometry.

In the present research work, the stability of an embankment is studied by investigating the soil behavior of the embankment foundation considering the following aspects:

1) Effective stress path followed by different soil elements

2) Stress-strain behavior of the soil elements

3) Volume change behavior of the soil elements

4) Pore pressure response

5) Distribution of the accumulated viscoplastic shear strain distribution.

The 'stress path method' was described by Lambe (1967) as a systematic approach to stability and deformation problems in soil mechanics. When a load is applied to a mass of soil in the ground by a foundation, each element of the soil experiences changes in its state of stress. A stress path gives a continuous representation of the relationship between the components of stress at any given point as they change. Use of a stress path provides geotechnical engineers with an easily recognizable pattern which assists them in identifying the mechanism of soil behavior. As such, by analyzing the effective stress paths followed by different soil elements, the actual foundation behavior can be accurately visualized. In the present analysis, the stress path is defined as using the following variables:

The mean effective stress $$\sigma'_m = \frac{\sigma'_{11} + \sigma'_{22} + \sigma'_{33}}{3} \tag{6.1}$$

The deviatoric stress invariant considered here is the second invariant of the deviatoric stress tensor, $\sqrt{2J_2}$, and calculated as

$$\sqrt{2J_2} = (S_{ij}S_{ij})^{1/2} = \left[\begin{array}{r} (\sigma'_{11} - \sigma'_m)^2 + (\sigma'_{22} - \sigma'_m)^2 + \\ (\sigma'_{33} - \sigma'_m)^2 + 2(\tau_{12}^2) \end{array} \right]^{1/2} \tag{6.2}$$

where σ'_{11}, σ'_{22}, and σ'_{33} are the effective normal stress values, and τ_{12} is the shear stress which corresponds to the two-dimensional plane strain condition.

The stress-strain behavior of the embankment foundation is investigated by plotting the deviatoric stress vs. accumulated viscoplastic shear strain, ε_q^{vp}, defined as follows:

$$\varepsilon_q^{vp} = \int (de_{ij}^{vp} de_{ij}^{vp})^{1/2} \tag{6.3}$$

where de_{ij}^{vp} is the viscoplastic shear strain increment tensor.

As with metal plasticity, the saturated soil behavior cannot be understood only through either stress-strain variations or stress paths. The volume change behavior must be simultaneously considered. This is due to the fact that the shear behavior is closely related to the volume change behavior, which in turn is governed by Darcy's law. In the present analysis, the volume change behavior of soil is investigated by observing the changes in the viscoplastic volumetric strain vs. accumulated viscoplastic shear strain ratio of the soil element underneath the embankment.

The pore water response brought about by embankment loading is studied with the accumulated shear strain of the foundation soil. The behavior of the pore water pressure in the foundation provides useful data for identifying an impending failure. This identification would allow measures to be taken to avoid a potential failure. Measures include the stopping of construction to allow time for the pore pressure induced by the embankment to dissipate and the foundation to gain strength.

The localization of the inelastic deformation is a widely observed phenomenon occurring in the behavior of a broad class of geomaterials when approaching the failure state. Well-known practical examples involve the failure governed by the initiation and the propagation of rupture surfaces or shear bands in slopes, foundations, etc. The localization can be understood as instability in the macroscopic constitutive description of the inelastic deformation of the material. Specifically, instability is realized in the sense that the constitutive relations may allow the homogeneous deformation of an initially uniform material to lead to a point at which a non-uniform deformation can be incipient in a planer band under conditions of a continuous equilibrium and a continuous homogeneous deformation outside the zone of localization. In fact, with changes in the geometry of the body, the onset of instability is progressive. In order to investigate the possible localization in a foundation, which would result in embankment instability, the strain distribution of the embankment foundation is verified. For this purpose, the accumulated viscoplastic shear-strain distribution of the subsoil due to embankment loading is examined.

6.6.1 Results and Discussion

The effective stress paths followed by elements at different locations in the embankment foundations are shown in Figs. 6.10(a), 6.11(a), 6.12(a), 6.13(a), 6.14(a), and 6.15(a). The elements considered for the plots are indicated in these figures. In the elements under the center and 10 m away from the center, starting from the K_0 condition, the stress path rises towards the critical state line (CSL) during the load application. After the end of loading, it moves away from the CSL and follows the K_0 path. In the same area, the effective stress path of the peaty clay elements rises only slightly from the K_0 line, whereas in silty soil (Fig. 6.13(a)), the rise of the stress path is significant during loading. It should be noted that the initial permeability and the initial void ratio for the peaty clay layer are higher than those of the slit layer. Thus, it is clear that the drain behavior in a peaty clay layer is prominent compared to that in a silty layer. Also, the influence of the embankment load becomes smaller towards the bottom of the peat layer. The rise in the stress path from the K_0 line is less than that of the top layers and almost follows the K_0 path from the beginning, as shown in Figs. 6.10(a) and 6.11(b).

The behavior of the effective stress paths for the elements under the slope (at the toe and 16 m away from the center) is different from that in the central area of the embankment. As shown in Figs. 6.10(a) ~ 6.15(a), the stress path for the elements under the toe area rises sharply towards the CSL during the early loading stages. The elements in the bottom part of the peat layer almost reach the CSL due to the initial loading (Fig. 6.10(a) ~ Fig. 6.13(a)). However, the stress path of the elements close to the drainage boundary at the top does not reach the CSL, as shown in Figs. 6.14(a) and 6.15(a). This may possibly be due to the easy drainage conditions. With the passage of time, the stress paths of the toe elements move away from the CSL due to the possible drainage. The stress paths of the above-mentioned areas (under the toe and under the slope) close to the loading surface show distinct behavior after several loading stages (Figs. 6.14(a) and 6.15(a)). The paths move in between K_0 and CSL, indicating that the principal stress planes experience a development of shear stress as the embankment is built.

The stress path analysis of the embankment foundation suggests that the toe area is more prone to plastic instability than the central area under this embankment geometry.

The stress-strain behavior of the embankment foundation is shown in Figs. 6.10(b) ~ Fig. 6.15(b). For the elements in the center and the elements located 10 m away from the center, the deviatoric stress increases with the shear strain. For the top elements close to the loading surface, a sharp increase in deviatoric stress is observed during the loading stages. In the same area, for the elements near the bottom of the peat layer, the stress-strain behavior is smooth and an increasing trend is observed throughout the process.

However, the increasing trend of the deviatoric stress with shear strain cannot be seen in the soil elements under the toe. In this area, shear strain increases under an almost constant deviatoric stress. The deeper peat elements under the toe area show a slight decrease in deviatoric stress with an increasing shear strain, due to the initial loading, and then a sudden drop in deviatoric stress is observed in some of the subsequent loadings. Looking over these figures, it is evident that different parts of the foundation respond differently to the embankment loading.

The volume change behavior with respect to predominant viscoplastic volumetric strain and viscoplastic shear strain is shown in Figs. 6.10(c) ~ 6.15(c). All the elements under the center area of the embankment undergo volume compression. The behavior of the elements in the embankment toe area shows a clear difference from that of the center elements. During the early stages of loading, the volumetric strain increases with shear strain. With continued loading, however, the soil behaves in an almost undrained manner without a change in the viscoplastic volumetric strain, as shown in Figs. 6.10(c), 6.14(c), and 6.15(c). It is also seen that the increments in viscoplastic volumetric strain to shear strain ($d\varepsilon_v^{vp} / d\varepsilon_q^{vp}$) of some elements under the toe area approach zero; this is an indication of instability during some stages of the embankment construction.

The excess pore pressure behavior with viscoplastic shear strain for some soil elements under the embankment is shown in Figs. 6.10(d) ~ 6.15(d). A rise in pore pressure with shear strain is seen during the load application. During the constant load consolidation, it gradually dissipates. However, not much of a difference is seen in the present analysis between the pore water pressure behavior at the center and that in the toe elements.

In order to investigate the possible localization during and after construction, which would result in the instability of the embankment foundation, the distribution of accumulated viscoplatic shear strain is plotted with the embankment construction. From the deformation pattern of the embankment foundation after the initial loading, one can expect shear strain localization particularly beneath the slope during construction. As shown in Fig. 6.16, this is captured very well by the model. The progression of the localized shear deformation begins in the region directly under the embankment slope and, with further loading, the deformations become concentrated in a relatively narrow band, as shown in Fig. 6.16. The stress-strain behavior of highly sheared elements in this zone indicates that those elements have already reached their limit strength and are not altered with further strain. The stress path for these particular elements (Fig. 6.10(a)) approaches the CSL and $d\varepsilon_v^{vp} / d\varepsilon_q^{vp}$ approaches zero (Fig. 6.10(c)). All these features, together with the deformed mesh, clarify that the toe area is subjected to plastic instability during some stages of the embankment construction.

However, this local instability of particular soil elements does not imply a general failure of the embankment. The general failure of an embankment occurs only if a mechanism of failure exists through the soil beneath the embankment. This requires many soil elements to have reached the critical state, which we do not observe in the present analysis.

In addition, as presented in Fig. 6.17, the distribution of accumulated viscoplastic shear strain after construction has not shown such a localization behavior in the foundation soil. It is understood that the foundation would again become safer, after showing signs of instability, by an increase in the effective stress due to the gradual dissipation of excess pore water pressure, as indicated in Figs. 6.10(d) ~ 6.15(d). Based on the above discussion, it can be concluded that although a limited region may shows signs of instability, the foundation itself is safe and no catastrophic failure is evident.

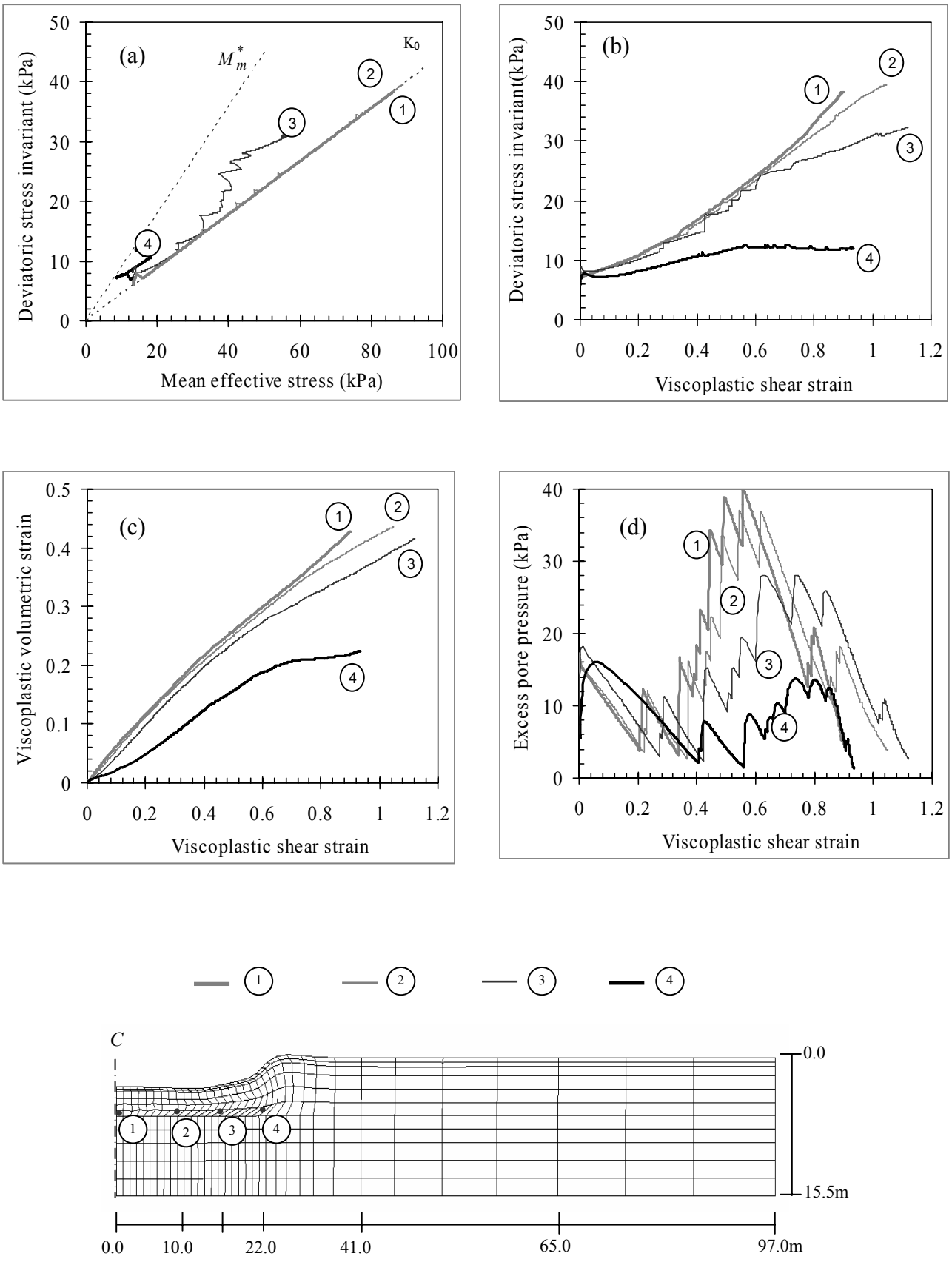

Fig. 6.10: Soil element behavior under the embankment – silty clay/ peat 5.75 m depth

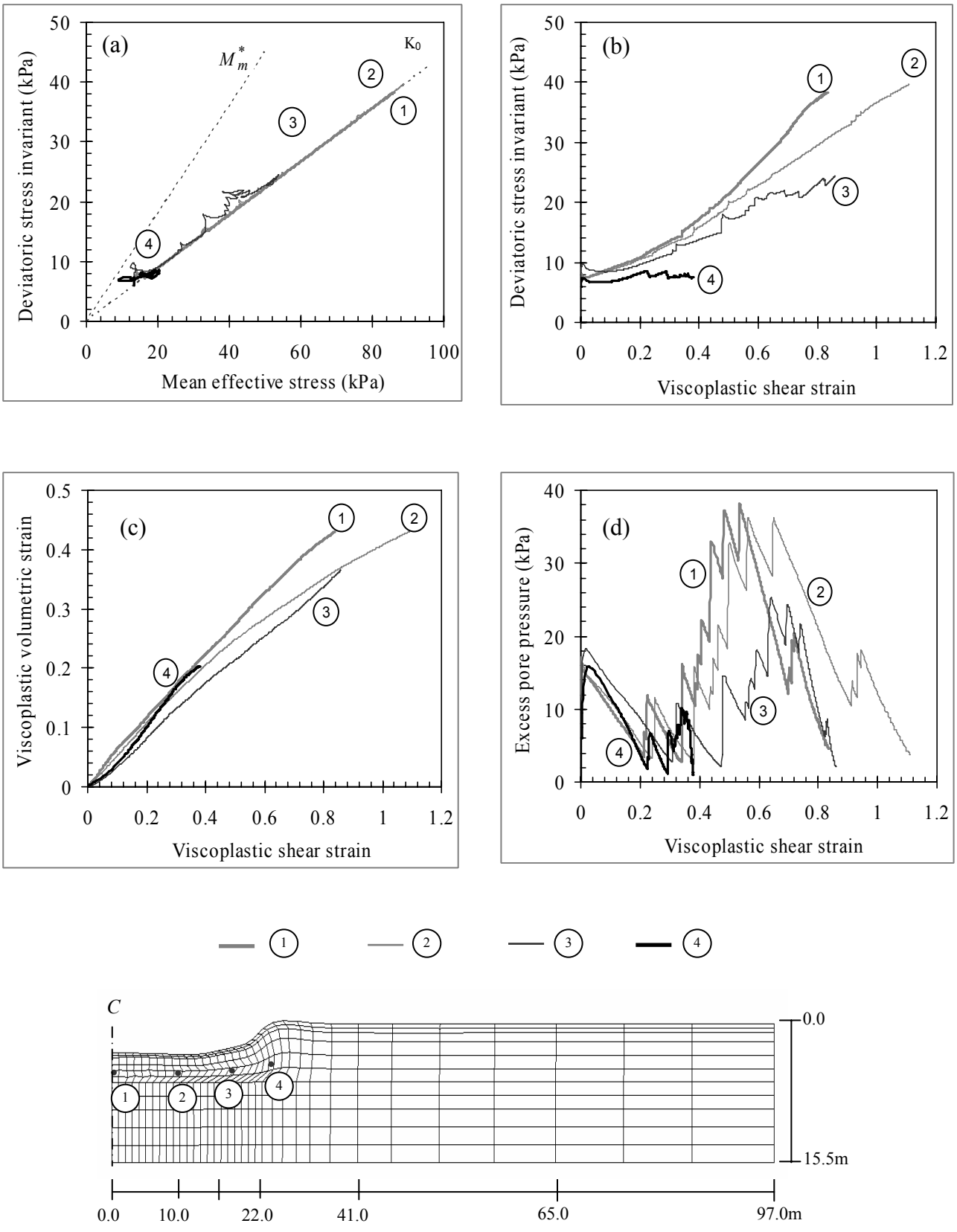

Fig. 6.11: Soil element behavior under the embankment – silty clay/peat 4.25 m depth

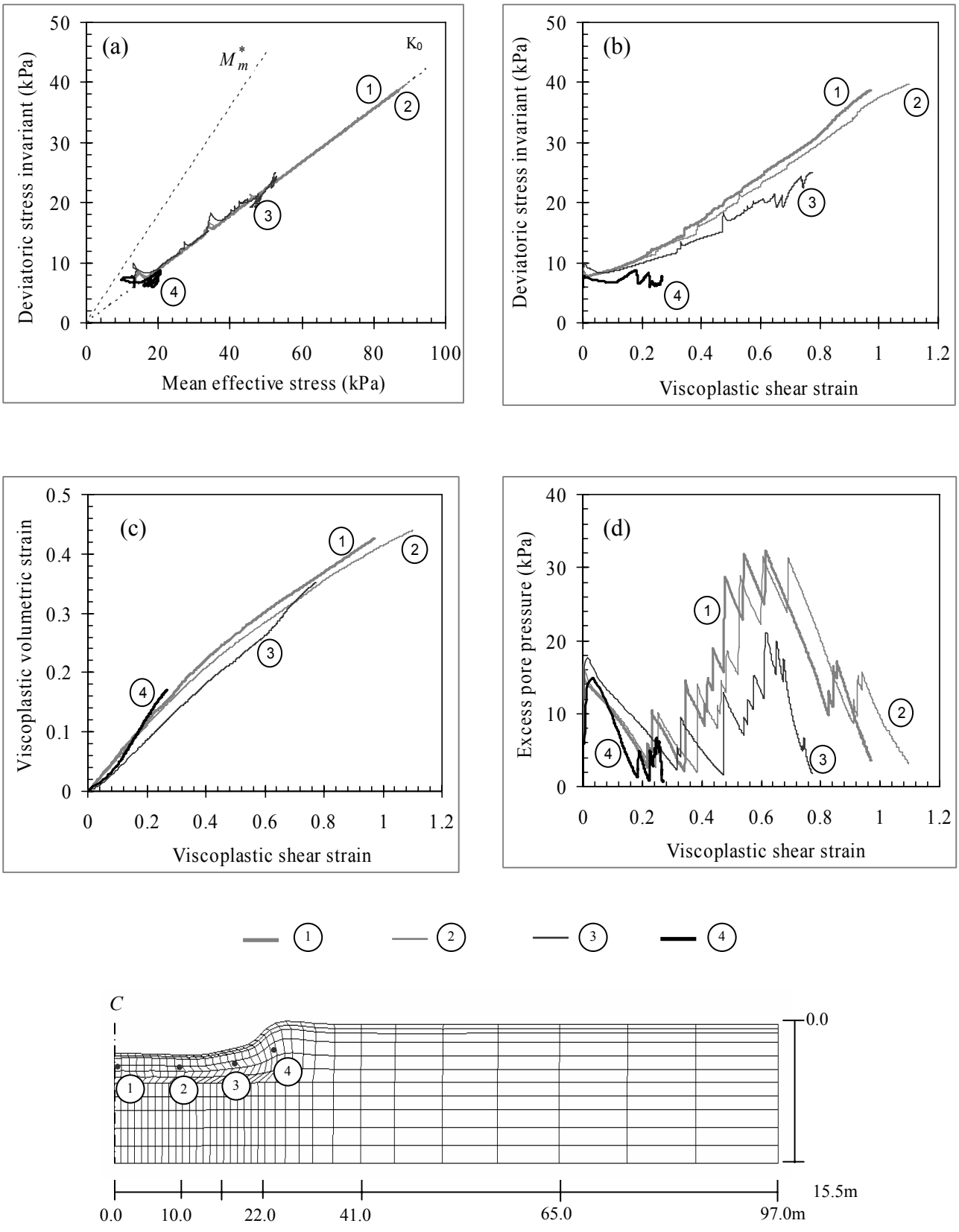

Fig. 6.12: Soil element behavior under the embankment – silty clay/peat 2.75 m depth

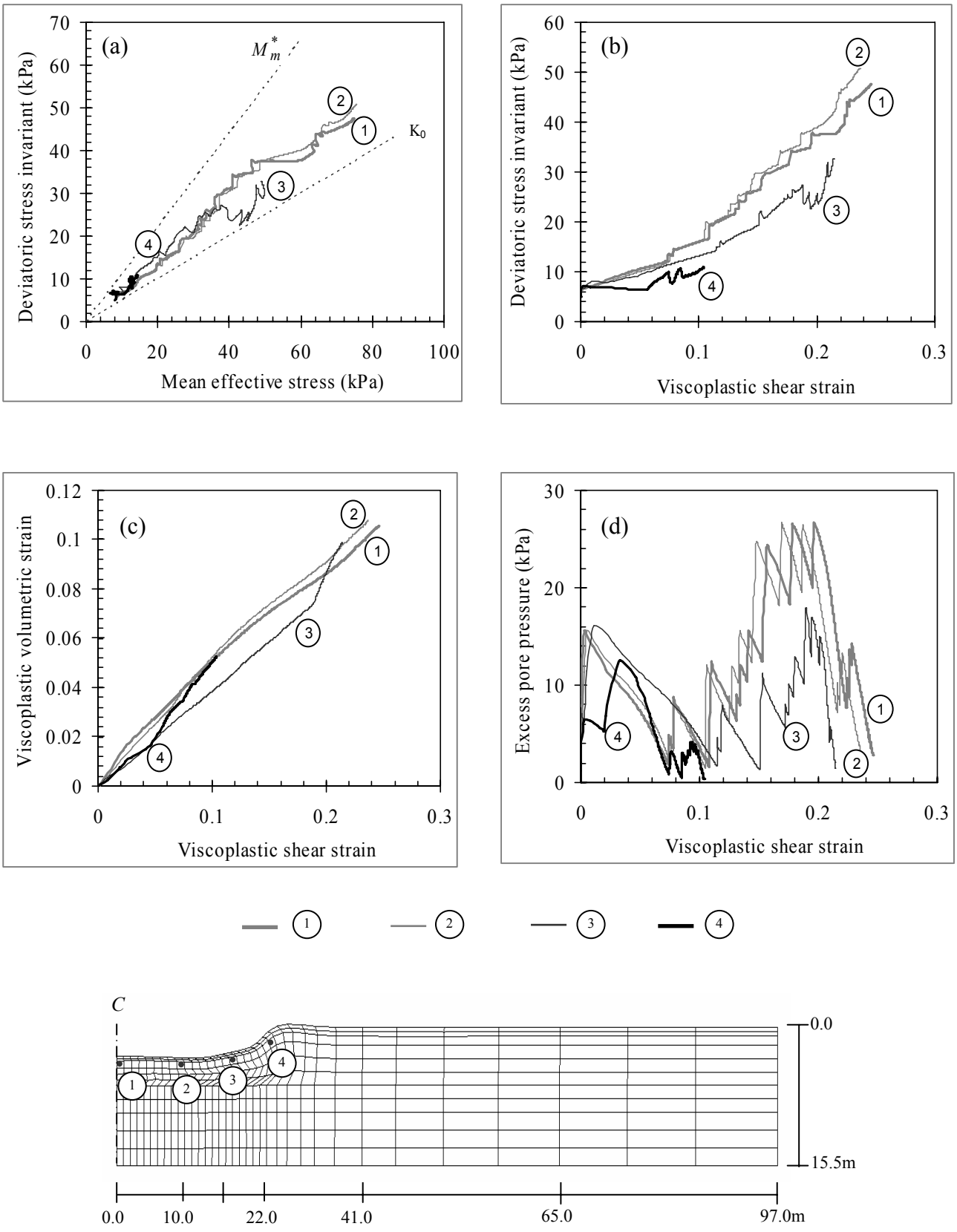

Fig. 6.13: Soil element behavior under the embankment – silt 1.5 m depth

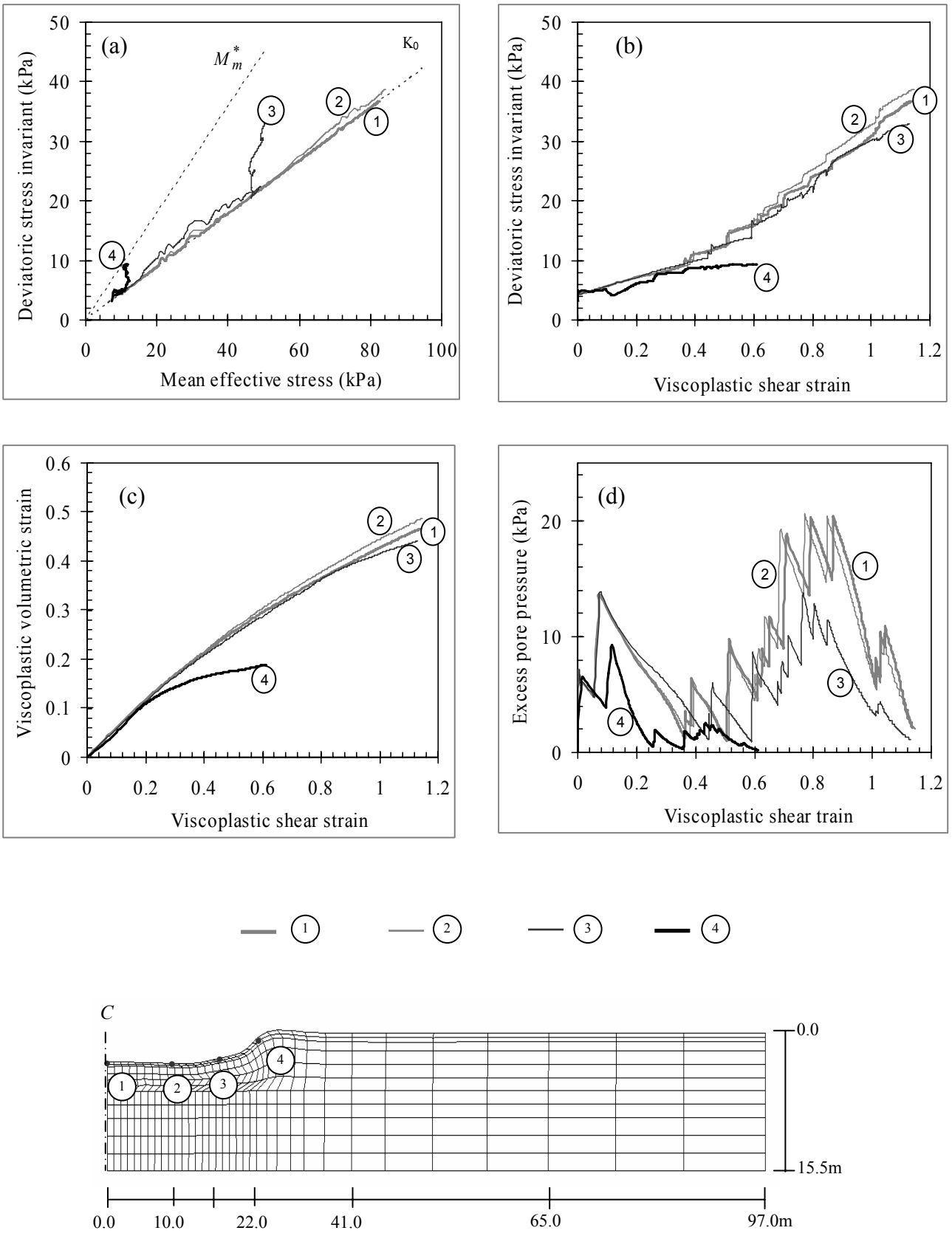

Fig. 6.14: Soil element behavior under the embankment – peat 0.75 m depth

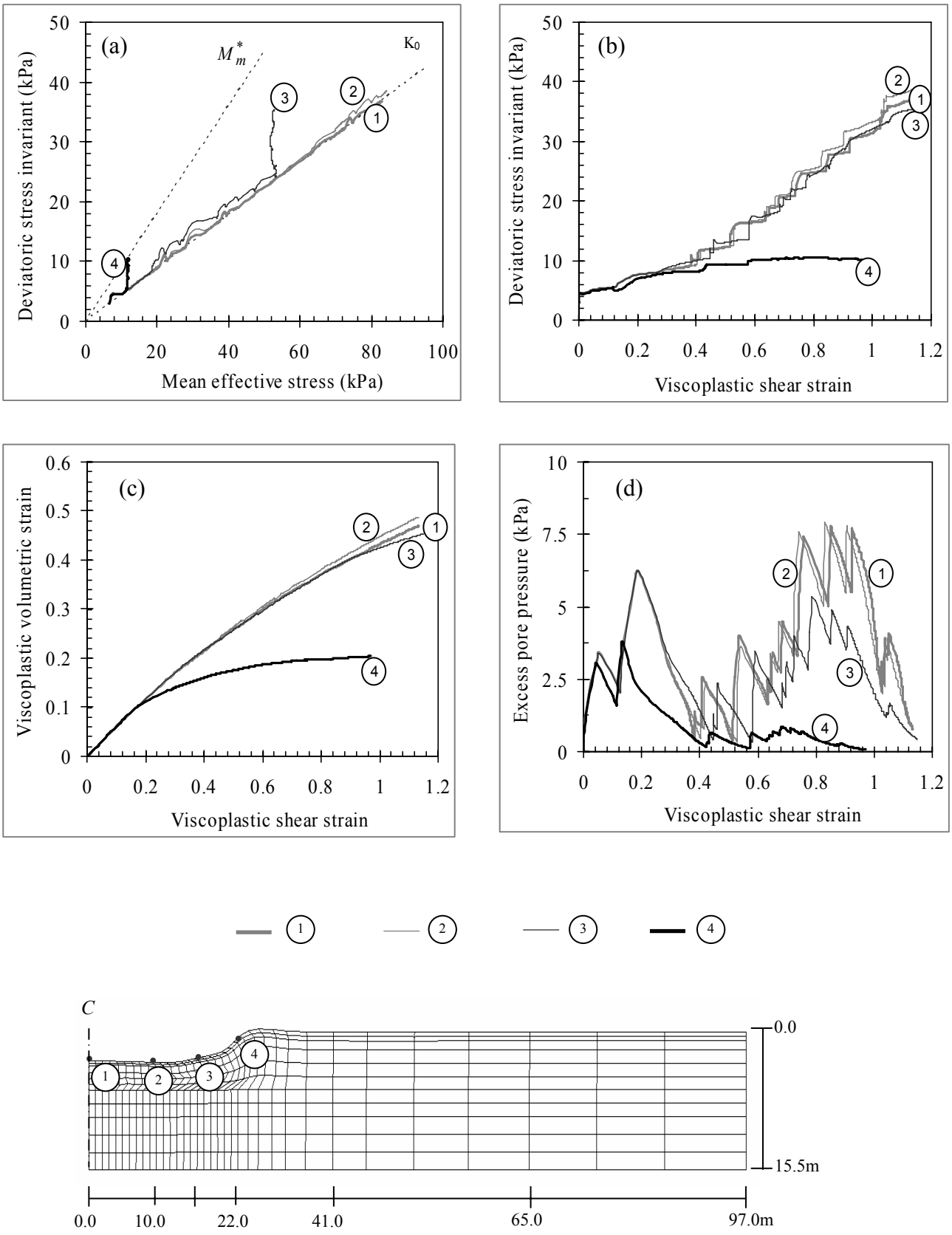

Fig. 6.15: Soil element behavior under the embankment – peat 0.25m depth

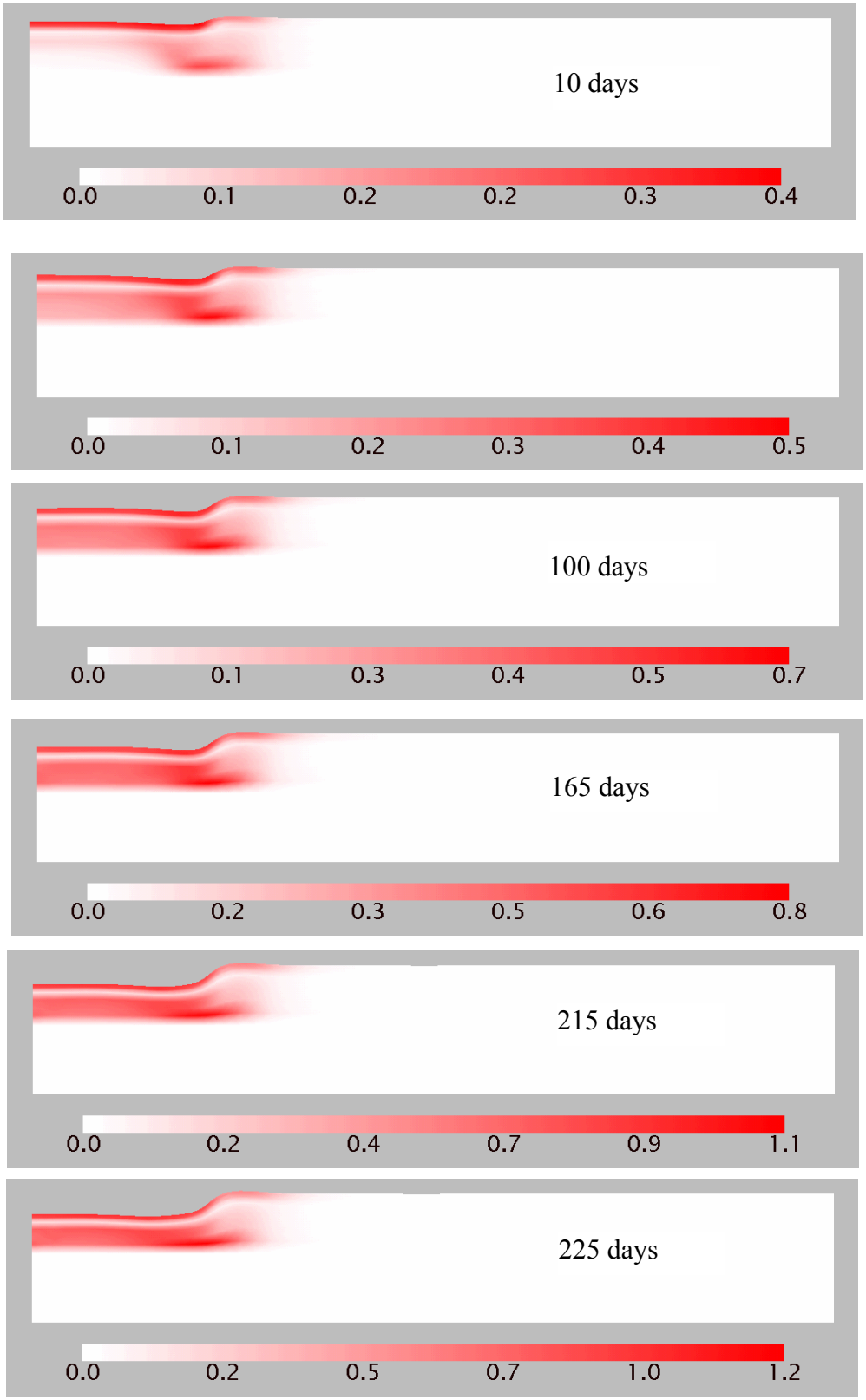

Fig. 6.16: Variation in accumulated viscoplastic shear strain during construction

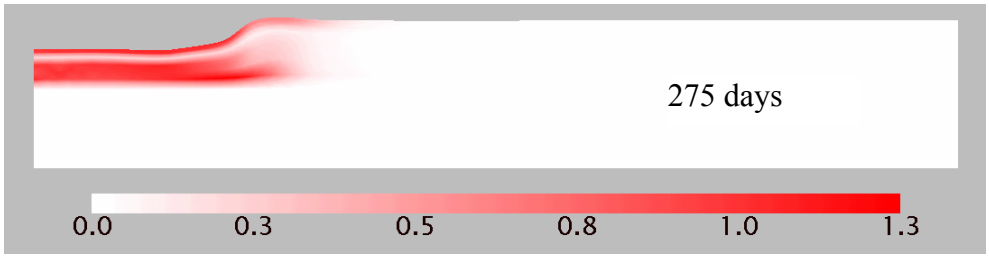

Fig. 6.16: Variation in accumulated viscoplastic shear strain during construction

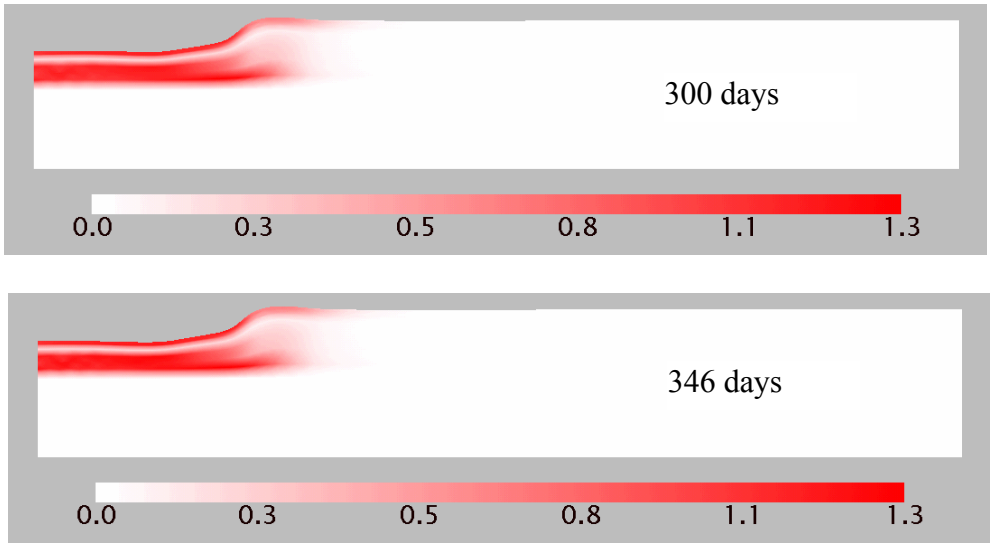

Fig. 6.17: Variation in accumulated viscoplastic shear strain after construction

6.7 Summary and Remarks

In this chapter, the deformation and the stability of a peat foundation due to embankment construction were investigated through use of the elasto-viscoplastic model. The material parameters for the peaty clay were determined based on laboratory and field tests carried out during the project period, and empirical correlations were used when reliable data was not available. The settlements in the field advanced rapidly even during the embankment construction. The predicted results have shown a good agreement with the measured data, except for during the early stages of the embankment construction. The observed discrepancy in the settlements might have occurred due to the effect of the surcharge introduced in the initial stress distribution of the foundation for the numerical stability of

the computation. Under the loads that exceeded the initial surcharge, a good quantitative and qualitative agreement was obtained. This indicates that the observed large strain in the field was captured by the model. In addition, because of the good agreement obtained between the measured and the predicted settlements, the proposed method for considering variable compressibility seems to be realistic in the analysis of stage-constructed embankments which exert high levels of pressure on the peaty subsoil.

The predicted settlement pattern for the embankment was different from the typical one in which always the maximum settlement occurs at the center. The predicted settlement under the crest area (12.5 m away from the center) is greater than that of central area of the embankment during the construction period. This might be due to the fact that the stress condition in the central area of the foundation is approximately one dimensional and that in the edge area is two dimensional as the embankment has a large width compared to its height. The higher settlement that was predicted under the shoulder area of the embankment foundation was possibly due to the result of local shear-induced displacement. The location of the maximum settlement gradually shifted towards the centerline as construction of the embankment proceeded. However, the maximum excess pore water pressure was always predicted around the central area.

The stability of the embankment during and after construction was verified by investigating the stress-strain characteristics of the subsoil. The stress paths of the elements under the central area moved along the K_0 path, whereas the stress paths of the elements under the toe area rose towards the critical state line. This indicates that the toe area was more prone to plastic instability than the central region under this embankment geometry. This was further illustrated by the distribution of accumulated viscoplastic shear strain of the embankment foundation and the viscoplastic volumetric strain vs. shear strain graphs. In the elements underneath the toe area, localized strain developed in the same elements and the increment in viscoplastic volumetric strain to the shear strain approached zero during some stages of the embankment construction. However, a general failure was not anticipated as the signs of instability appeared in a very limited region under the embankment.

Chapter 7

SIMULATION OF FIELD BEHAVIOR DUE TO EMBANKMENT CONSTRUCTION ON IMPROVED SUBSOIL

7.1 Introduction

In the previous chapter, predictions of the foundation behavior of an embankment constructed on natural peaty clay using the preloading method were described. The predictions indicated that, in spite of the high in situ permeability of peaty soil, a significant amount of excess pore water pressure exists in the deeper peat layers even some time after the completion of the embankment construction. Also, previous analyses indicated that some areas of the embankment foundation showed signs of instability during the construction. In most field problems, since a free drainage boundary condition prevails at the ground surface, excess pore water pressure resulting from the preload often drains out only from the top part of the soft layer. Subsequently, the stress of the preload is initially transferred to the top part of the soft layer. This means that the top part of the layer gets more compressed than the middle or the bottom part of the soil layer. Hence, permeability in the top region becomes lower than that in bottom region of the layer. Due to this low permeable zone, created between the free drainage boundary and the bottom part of the peat layer, the dissipation of excess pore water pressure takes a considerably long time even though the bottom part of the layer still has high permeability. Therefore, the consolidation process takes a long time, and subsequently, both the embankment

stability and the potential to allow for the construction of substantially higher embankments in considerably shorter periods of time are decreased.

It is evident that these problems become more complicated when very high embankments are constructed on peat deposits with high layer thickness. In such cases, it is necessary to place the preloading surcharge at a sufficiently slow rate so as to prevent shear failure and plastic flow in the peaty soil. In doing so, it takes a long time to complete the project which leads to delays and financial losses in the construction. Therefore, when constructing high embankments on peaty soil with high layer thickness, the application of preloading alone is not sufficiently effective.

In order to overcome these problems, the preloading method is often employed in conjunction with other ground-improvement techniques. For example, the preloading technique is often combined with vertical drains to accelerate the consolidation process. Sometimes applications of vacuum pressure with surcharge loading can further accelerate consolidation while reducing the surcharge fill material. Sand compaction piles (SCPs) are employed with preloading in order to increase the bearing capacity and to accelerate the consolidation rate of the foundation soil. The selection of the most appropriate method for a particular project depends on various factors, including the type of peaty soil to be improved, the level of improvement needed, the magnitude of the improvement attainable by the method, the required depth, and the extent of the area to be treated.

In the present chapter, model applications employed to predict the consolidation behavior of embankment foundations stabilized with prefabricated vertical drains (PVDs) and sand compaction piles (SCPs) are described. Finite element analyses are carried out in all cases by converting the actual three-dimensional conditions that exist around the drains into simplified two-dimensional plane strain conditions. The field behavior when PVDs are installed in the peaty clay is simulated using equivalent vertical permeability and, in the case of SCPs, a conversion scheme is used to transform the axisymmetric nature of the SCPs into equivalent plane strain conditions.

7.2 Modeling of PVD-improved Subsoil under Plane Strain Conditions

Preloading with vertical drains is the most commonly used ground-improvement technique in low lying reclamation. Vertical drains are used in soft clays and silts, as well as in peaty soil, to accelerate the primary consolidation in order to: (a) increase shear

strength to allow rapid construction, (b) decrease the time for preloading to minimize post–construction settlements, and (c) reduce differential settlements during the primary consolidation stage. Although sand drains and prefabricated band-shaped drains were both introduced in the mid 1930s, the former were mainly employed until the early 1970s. Then, for economic and other reasons, the latter gained popularity and became the most widely used ground-improvement technique (Mesri and Lo 1991).

Various approaches are available for modeling vertical drains in plane strain finite element analyses (Sekiguchi et al. 1986; Zeng et al. 1987; Hird et al. 1992; Indratna et al. 2001). However, all the methods either employ a one-dimensional drainage element or adopt a special formulation for the FEM program. Due to these particularities, conducting a FEM analysis for PVD-improved subsoil is very time-consuming (Olson 1998). Thus, in the present research work, a simple method proposed by Chai et al. (2001) is used to analyze the PVD-improved subsoil. It can analyze the improved subsoil in the same way as for the unimproved subsoil.

The method proposed by Chai et al. (2001) is based on the equivalent vertical hydraulic conductivity for PVD-improved soil. From a macro point of view, vertical drains increase the mass hydraulic conductivity of subsoil in the vertical direction. Thus, it is logical to try to establish a value for the vertical hydraulic conductivity which can approximately represent both the effect of the vertical drainage of natural soil and the effect of the radial drainage due to the existence of PVDs. Under this condition, the PVD-improved subsoil can be analyzed in the same way as for the unimproved subsoil. The equivalent value of vertical hydraulic conductivity k_{ve} is derived based on the equal average degree of consolidation under one-dimensional conditions. Carrillo's theoretical solution (1942) is used to combine the effects of vertical and radial drainage.

$$U_{vr} = 1 - (1 - U_v)(1 - U_r) \tag{7.1}$$

where U_{vr} is the average degree of consolidation for the PVD-improved subsoil, U_r is the average degree of consolidation due to radial drainage, and U_v is the average degree of consolidation due to vertical drainage. The value of U_r is calculated by Hansbo's solution (1981) as follows:

$$U_r = 1 - \exp\left(-\frac{8}{\mu} T_h\right) \tag{7.2}$$

where T_h is the time factor given by $C_h t / D_e^2$ in which C_h is the coefficient of consolidation in the horizontal direction and D_e is the diameter of the unit cell. The value of μ is related to the drain properties and will be explained later.

The average degree of vertical consolidation is estimated with an approximation of Terzaghi's solution.

$$U_v = 1 - \exp(-C_d T_v) \tag{7.3}$$

where T_v is the time factor for the vertical direction given by $C_v t / H^2$ in which C_v is the coefficient of consolidation in the vertical direction, H is the vertical drainage length, and c_d is a constant which can be determined by comparing the values of Terzaghi's exact solution with the approximated solution (7.3).

Using the above equations, the equivalent vertical hydraulic conductivity of the PVD-improved subsoil, k_{ve}, can be expressed as

$$k_{ve} = \left(1 + \frac{2.5l^2}{\mu D_e^2}\frac{k_h}{k_v}\right)k_v \tag{7.4}$$

$$\mu = \ln\left(\frac{n}{s}\right) + \frac{k_h}{k_s}\ln(s) - \frac{3}{4} + \pi\frac{2l^2 k_h}{3q_w} \tag{7.5}$$

In the above-mentioned formulas, D_e is the diameter of the unit cell (containing a PVD and its improvement area), $n = D_e/d_w$ (d_w is the drain diameter), $s = d_s/d_w$ (d_s is the smear zone diameter), k_h and k_s are the hydraulic conductivities of the natural soil and the smear zone, respectively, k_v is the vertical hydraulic conductivity of the natural soil, l is the drainage length of a PVD, and q_w is the discharge capacity of a PVD.

The essentials of the equivalent vertical permeability of the PVD-improved zone given in Eq. (7.4) are presented in Appendix A2.

The modified approach is used in this study for the equivalent drain diameter, d_w, of the band-shaped PVD considering the corner effect. It can be calculated using the following equation proposed by Rixner et al. (1986):

$$d_w = \frac{a+b}{2} \tag{7.6}$$

where a is the width of a PVD and b is the thickness of a PVD.

The equivalent diameter of a unit PVD-influenced zone, D_e, is calculated on the basis of the equivalent cross sectional areas (Rixner et al. 1986). For drains in a square grid pattern with drain spacing S,

$$\pi D_e^2 / 4 = S^2 \quad ; \quad D_e = 1.13S \tag{7.7}$$

When a PVD is installed in a soft ground using a mandrel, a disturbed zone called a smear zone forms around the mandrel, and the hydraulic conductivity is reduced significantly. Two parameters are needed to evaluate the smear effect, namely, (i) the diameter of the smear zone, d_s , and (ii) the hydraulic conductivity ratio, k_h / k_s , i.e., the value in undisturbed zone k_h over the value in smear zone k_s . Since no test data are available to evaluate the smear zone, $d_s \approx 4d_m$ is assumed in this study by considering the very soft consistency of peaty soil. In the above relationship, d_m is equivalent in diameter to the cross sectional area of the mandrel.

Many uncertain factors affect the value of k_h / k_s (Chai and Miura 1999). Hansbo (1987) reported that the value of k_h / k_s varies from 1 to 5 for soft clay. For this research, k_h / k_s was assumed to be 4. The discharge capacity quantitatively denotes the well resistance of PVDs, and a typical value of 100 m^3/year was assumed for the capacity in the present work.

7.2.1 Verification of the Method Using Large-scale Model Test Data

The performance of the model in incorporating the above method to predict the consolidation behavior of PVD-improved soil has been verified using the data reported by Kugan et al. (2003). They conducted laboratory tests to study the behavior of PVDs installed in peaty clay using a large-scale consolidation test apparatus with a centrally located prefabricated drain. Fig. 7.1 shows the schematic diagram of the large-scale consolidation apparatus with a devise for measuring the excess pore water pressure in the middle of the sample which has a thickness of 700 mm and a diameter of 500 mm. The load was applied in increments of 5 kPa over a 2-day time interval, up to a final pressure of 30 kPa. The settlement and the excess pore water pressure were monitored for a long period of time, namely, about 75 days.

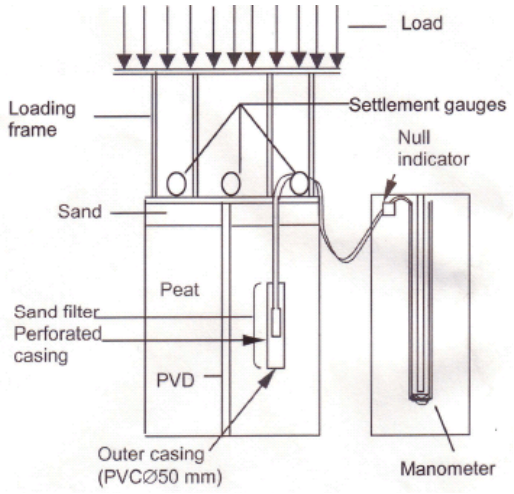

Fig. 7.1: Arrangement of the test apparatus (Kugan et al. 2003)

One-dimensional normally consolidated behavior for load increments of 5-30 kPa for the PVD-improved soil was predicted by the elasto-viscoplastic model using the above-described mass vertical hydraulic conductivity of the PVD-improved zone. The initial conditions required for the finite element analysis were evaluated from load increments of 0-5 kPa, which are considered as preparatory consolidation for the analysis of the consolidation behavior for load increments of 5-30 kPa. The material parameters used for the peaty clay were taken from Kugan et al. (2003) and Ketheeswaravenayagam et al. (2006). Since the tests were conducted with the same remolded peaty soil as that used in the model tests considered for the model validation (Chapter 4), all the material parameters are the same as those listed in Table 4.1 and again in Table 7.1.

Table 7.1: Material parameters for the large-scale peaty soil model with PVD

Parameters			Values
Initial void ratio	e_0		5.80
Initial vertical effective stress	$\sigma'_{22(0)}$	(kPa)	5.0
Coefficient of earth pressure at rest	K_0		0.53
Coefficient of permeability	k_0	(m/s)	4 x 10^{-8}
Change in permeability index	C_k		0.95
Initial shear modulus	G_0	(kPa)	450
Compression index	λ		0.8207
Swelling index	κ		0.08946
Stress ratio at critical state	M^*		0.98
Compression yield stress	$\sigma'_{mbi}(\sigma'_{mai})$	(kPa)	3.5
Viscoplastic parameter	m'		18
Viscoplastic parameter	C	(1/s)	1.0x 10^{-9}
Structural parameter	σ'_{maf}	(kPa)	3.0
Structural parameter	β		5

A band-shaped prefabricated vertical drain was used in the experiment. The cross section of the drain was 100 mm in width (a) and 3 mm in thickness (b). Therefore, the equivalent drain diameter, d_w, was determined as 51.5 mm (Eq. 7.6). The effective diameter of the PVD-influenced zone, D_e, was considered as the diameter of the consolidation cell. The drain parameters used to calculate the equivalent vertical permeability are listed in Table 7.2. Using these parameters, Eq. (7.4) yields an equivalent vertical hydraulic conductivity of 8.01 k_v.

Table 7.2: Drain parameters used in the analysis

d_w (m)	D_e (m)	d_s (m)	k_h/k_s	k_h/k_v	q_w (m^3/yr)
.0515	0.25	0.4	4	1	100

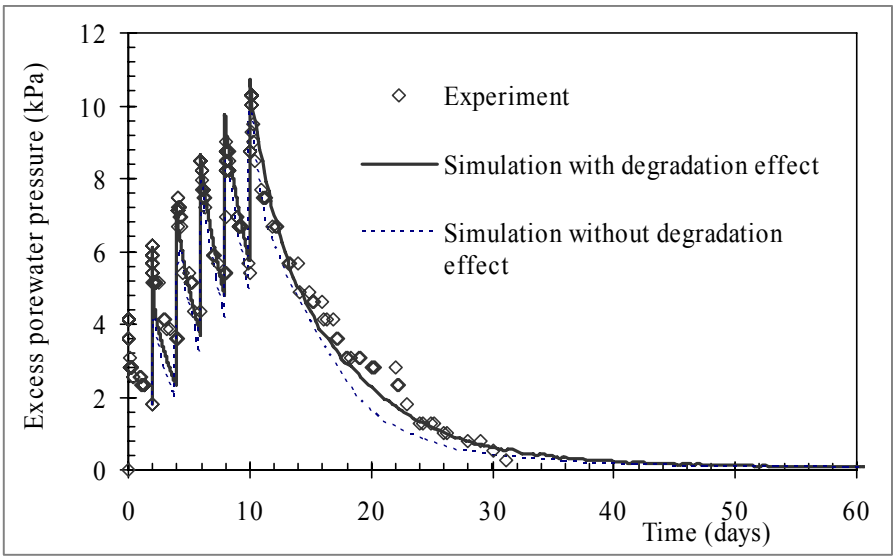

Fig. 7.2: Comparison of excess pore water pressure

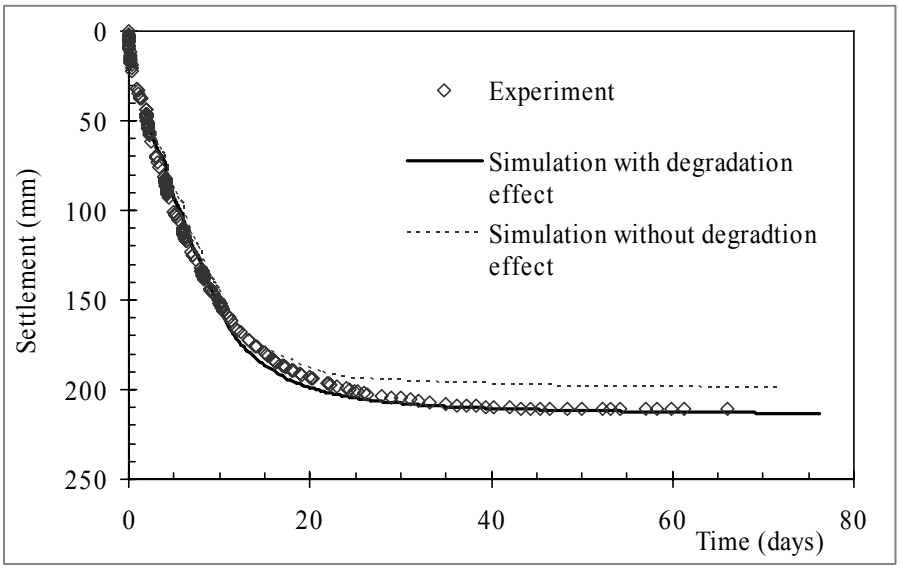

Fig. 7.3: Comparison of the settlements

Model predictions for the excess pore water pressure development/dissipation and the settlements are presented together with the experimental observations in Figs. 7.2 and 7.3, respectively. The figures indicate that the model predictions made with the equivalent vertical permeability, calculated using the described method, can reproduce both the observed settlements and the excess pore water pressure behavior quite well. Furthermore, the figures reveal that taking the effect of structural degradation into account leads to better results for both the observed settlements and the excess pore water behavior.

7.3 Analysis of an Embankment Constructed on PVD-improved Subsoil

Following the initial laboratory simulation of large-scale consolidation model test data, an attempt was made to predict the observed consolidation behavior of an embankment constructed in peaty soil using preloading with vertical drains. Predictions were made to simulate the observed settlements and the excess pore water pressure due to the embankment construction and to compare them with the corresponding measured data obtained through settlement gauges and piezometers installed in the field. Moreover, the influence of the deformation pattern of the subsoil due to the installation of PVDs is verified.

7.3.1 Details of the Embankment and the Subsoil Profile

The trial embankment at Ch.11+250 in the CKE project, Sri Lanka was constructed on PVD-improved subsoil.

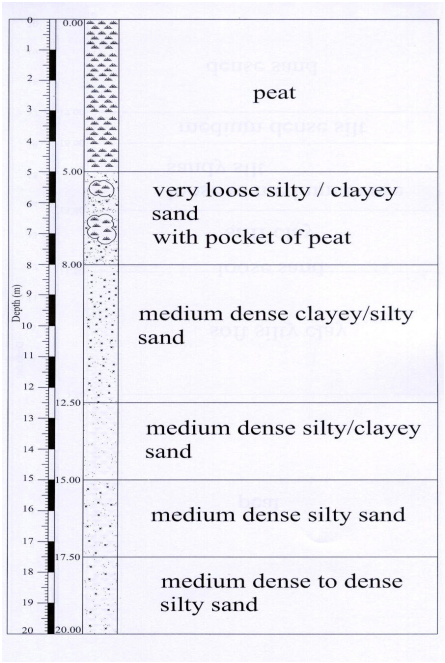

Fig. 7.4: Subsurface profile at the site

The subsoil conditions at the site were reported in detail by Ketheeswaravenayagam (2006) and shown in Fig. 7.4. The subsoil profile consists of a surface peat layer about 5 m in thickness. The surface peat layer is underlain by a layer of soft silty/clay sand, approximately 3 m in thickness, with pockets. Below this soft layer is a medium-dense clayey/silty sand layer, about 4 m in thickness, followed by a medium-dense to dense

silty/clay sand layer, up to a depth of 15 m from the ground surface. A dense sand layer is encountered below a depth of 15 m.

The embankment has a height of 7.99 m with a crest width of 13.6 m and 1:2 side slopes. The height of the initial sand mat was about 1.6 m, and thereafter, gravel fill was placed over a period of 373 days with different loading stages, as indicated in Fig. 7.5.

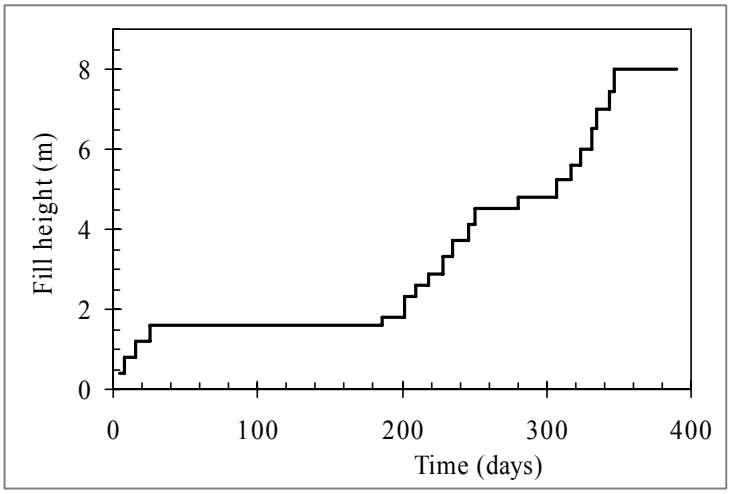

Fig. 7.5: Loading curve

The PVDs were installed 108 days after the construction was started. They were installed to a depth of around 8 m from the original ground surface in a square pattern with a spacing of 1.1 m.

The settlement plates and the piezometers were installed 28 and 148 days after the filling was initiated. The settlements and the excess pore water pressure were monitored over a period of 444 days.

7.3.2 Finite Element Analysis

In the finite element method (FEM) analysis, plane strain conditions were assumed. The modeled range was 15 m in the vertical direction and 78 m in the horizontal direction away from the embankment centerline. The displacement boundary conditions were as follows: both vertical and horizontal displacements were fixed at the bottom, while the horizontal displacement was fixed at the left and the right vertical boundaries. The adopted drainage boundary conditions were as follows: the ground surface was drained while the bottom boundary was undrained. The left and the right boundaries were undrained. The finite element mesh, indicating the displacement boundary conditions for the PVD-improved zone, is shown in Fig. 7.6. The subsurface profile considered in the analysis is also given in this figure.

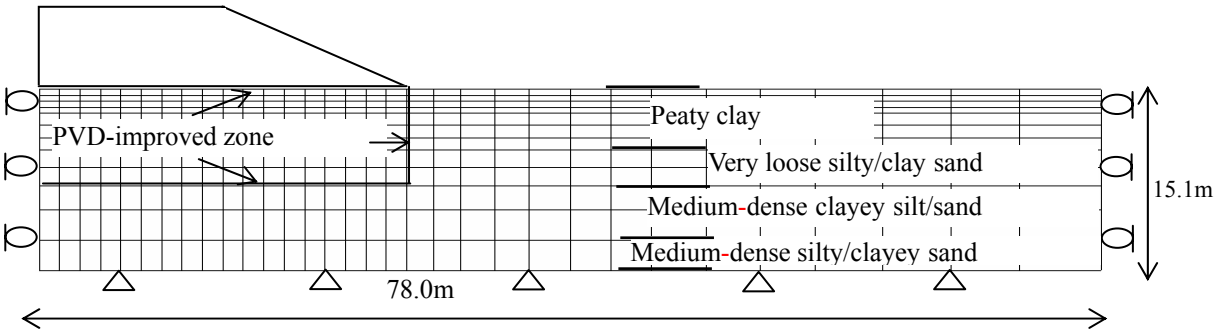

Fig. 7.6: Finite element mesh with boundary conditions

In the finite element modeling, the behavior of the peaty soil and the very loose silty/clayey sand were represented by the elasto-viscoplastic theory outlined in Chapter 3. For medium-dense clayey silt/sand, an elastic behavior was assumed. Since it is expected that the construction of the embankments exerted a high level of pressure on the subsoil and that the increase in the effective vertical stress in the subsoil was quick due to the installation of PVDs, the compressibility parameters for peaty soil were varied in accordance with Eqs. 3.33 and 3.34 during the analysis. The grass mat existing on the original ground surface, which gave additional strength to the subsoil, was modeled as a thin elastic element.

Table 7.3: Parameters used in the PVD-improved embankment foundation analysis

Parameters		Values for peaty soil	Values for very loose silty/clay sand
Initial void ratio	e_0	5.8#	1.5*
Initial vertical effective stress	$\sigma'_{22(0)}$ (kPa)	10.0#	27.0*
Coefficient of earth pressure at rest	K_0	0.53	0.5
Coefficient of permeability	k_0 (m/s)	1.0 x 10^{-7}#	1.0 x 10^{-8}*
Change in permeability index	C_k	1.0	0.9
Initial elastic shear modulus	G_0 (kPa)	800#	5000*
Compression index	λ	1.315	0.103
Swelling index	κ	0.087	0.006
Stress ratio at critical state	M^*	0.95	1.0
Compression yield stress	$\sigma'_{mbi}(\sigma'_{mai})$ (kPa)	10.0#	27.0*
Viscoplastic parameter	m'	22	25
Viscoplastic parameter	C (1/s)	1.0x 10^{-9}	1.0x 10^{-11}
Structural parameter	σ'_{maf} (kPa)	0.7 σ'_{mbi}	18.9
Structural parameter	β	5	5.0

At a depth of 1 m * At a depth of 6 m

The soil parameters were determined using the data reported by Ketheeswaravenayagam (2006), Soil Investigations for the Colombo-Katunayake Expressway Project (1999, 2001), and literature related to amorphous peaty soil. The derivation of the compressibility parameters is based on the empirical correlations for the physical and the mechanical properties of Sri Lankan peaty soil. The in situ permeability is based on the results of field permeability tests. It should be noted that the permeability in the horizontal and the vertical directions is assumed to be equal in the analysis. This is a realistic assumption considering the behavior of amorphous peaty soil which has a highly humified structure (Hobbs 1986). The initial vertical effective stress for each layer, $\sigma'_{22(0)}$, is determined based on the results of in situ density profiles. In the analysis, a surcharge load of magnitude 10 kN/m^2 was introduced over the foundation to enable the computation of the elasto-viscoplastic finite element analysis based on the finite deformation for a reason similar to that mentioned in Chapter 6. The viscoplastic parameters, the structural parameters, the initial shear modulus, the critical state parameter, and the permeability change index are the same as those used in the embankment analysis described in Chapter 6.

The type of drain used at the site was a prefabricated band drain with a cross section of 101 mm x 3 mm. According to Eq. (7.6), the equivalent drain diameter was 0.0515 m. As mentioned previously, PVDs were installed in a square pattern with a spacing of 1.1 m. With respect to that, the equivalent effective drain area was evaluated using Eq. (7.7). The diameter of smear zone d_e and the permeability ratio between the undisturbed and the disturbed zones were assumed as described in Section 7.2. In the analysis, the permeability ratio between horizontal and vertical directions was assumed to be equal. The parameters related to the PVD behavior are listed in Table 7.4.

Table 7.4: Drain parameters used in the analysis

d_w(m)	D_e(m)	d_s(m)	k_h / k_s	k_h / k_v	q_w(m^3/yr)
0.0515	1.25	0.4	5	1	100

The finite element analysis, based on the finite deformation theory, was carried out to model the actual construction sequence for the embankment (Fig. 7.5). The values of the unit weights of sand and the subsequent gravel fill were assumed to be the same as those in the previous embankment analysis (Chapter 6). Also, the same time increment scheme as shown in Fig. 6.5 in Chapter 6 was adopted in the present analysis.

7.3.3 Results of the Finite Element Analysis

The results of the finite element analysis for the settlement and the excess pore water pressure predictions are presented with the corresponding measured data. The lateral deformation pattern and the influence of the deformation pattern of the subsoil, due to the installation of the PVDs, are also verified.

7.3.3.1 Settlements

Predicted settlements just under the center and under the crest (12.5 m away from center) of the embankment are presented together with representative field measurements in Fig. 7.7. Predictions made for the settlements under the center of the embankment, without considering the PVD effect, are shown in this same figure to demonstrate the effectiveness of the PVD installation in expediting the field settlements. As shown in the figure, the predicted rate of settlement, considering the PVD effect, is much less than the predicted rate for the case in which the PVD effect is not considered, at the end of the embankment construction (around 350 days). This indicates that the time required to complete the primary consolidation, after the final load has been placed, is very short in the PVD-improved subsoil, whereas it takes a considerably long time in the case of the unimproved subsoil. The predicted excess pore water pressure, presented in the next section, will further confirm this behavior of the PVD-improved subsoil.

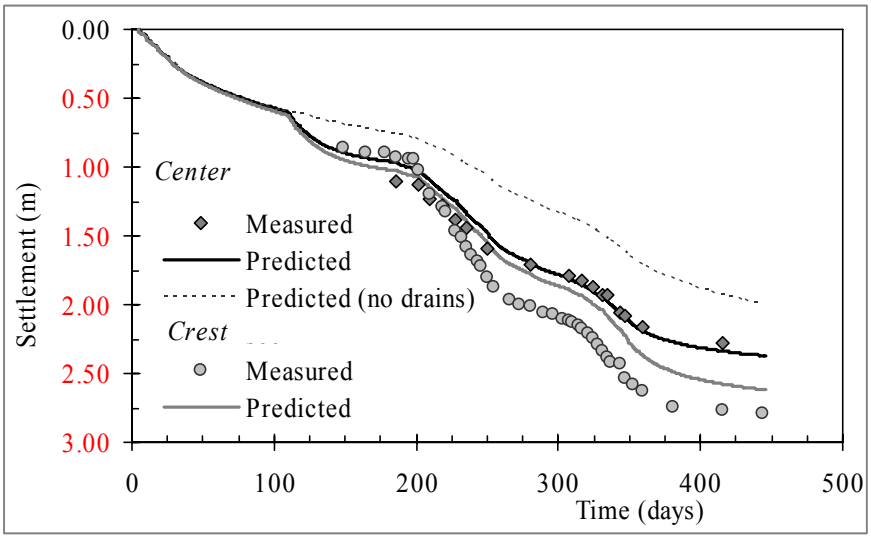

Fig. 7.7: Comparison of settlements

The instruments were installed after the construction of the sand mat, and thus, no field measurements are available for the initial period. According to the field measurements that are available, the maximum settlement occurred not under the center, but under the crest area of the embankment. This pattern was predicted accurately by the model, and

possible reasons for this kind of settlement pattern in the embankment foundation have already been discussed in Chapter 6. The predicted settlements just under the center have also shown a good quantitative agreement with the measured settlements. The model prediction for the settlements under the crest of the embankment is underestimated by about 0.2 m from the measured value. However, this is acceptable considering the non-homogeneous nature of peaty soil which has not been considered in the present analysis.

7.3.3.2 Excess pore water pressure

The excess pore water pressure predicted 1.25 m below the embankment and the excess pore water pressure measured 1 m below the bottom of the embankment are compared in Fig. 7.8. The predicted results clearly show that the PVD installation has caused a significant improvement in the rate of excess pore water pressure dissipation. As shown in the figure, before the PVDs had been installed, it took almost 110 days for the excess pore water pressure of about 10 kPa to dissipate during the initial loading stage. After the PVDs were installed, however, it took only 60 days for the excess pore water pressure of about 18 kPa to dissipate after the placement of the final load. It should be noted that this significant increase in excess pore water pressure was obtained with the prevailing lower permeability during the final stage of loading compared to that of the initial stage, as a result of the physical reduction in the void ratio during the consolidation.

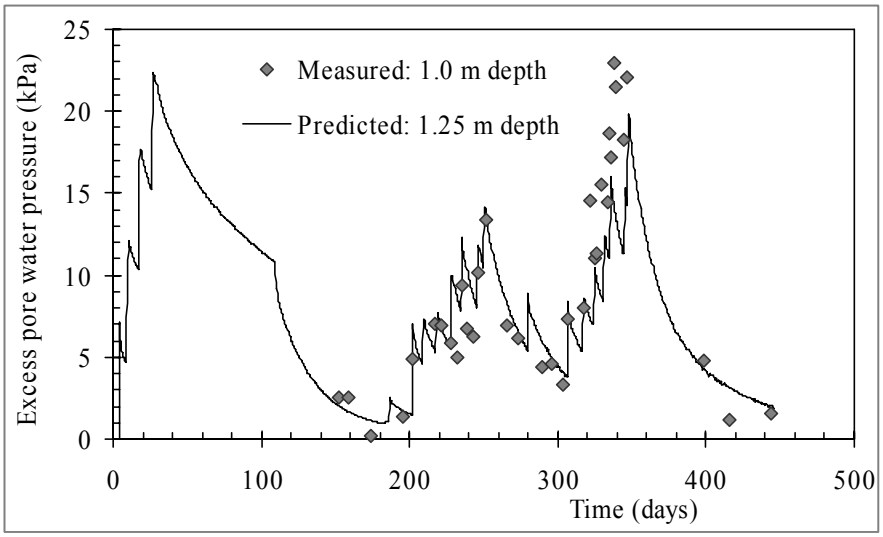

Fig. 7.8: Comparison of the excess pore water pressure

Since the piezometers were installed after the PVDs, the sudden drop in excess pore water pressure indicated in the prediction due to the PVD installation could not be captured in the field monitoring data. Also, none of the sharp peaks of the numerical predictions, which accurately represent the sudden rises in pore pressure associated with loading, are seen in the field measurements, as some dates of the field measurements do not coincide

with the exact times for which the maximum peaks are predicted. However, the agreement is generally good for the generation and the dissipation of excess pore water pressure; the results could be further improved by considering the well resistance, the different k_h / k_v ratios, or by using different discharge capacities for the drains.

Fig. 7.9 shows the predicted excess pore water pressure during the embankment construction with and without consideration given to the PVD improvement. The excess pore water pressure (u_w) is presented as a function of the applied stress (γH) of the embankment at the ground surface. It should be noted that the effect of the PVDs was considered in the analysis 108 days after the initial sand mat was constructed in order to simulate the actual construction sequence in the field. Therefore, the predicted excess pore water pressure due to the initial sand mat was the same in both cases, as shown in Fig. 7.9. After the PVDs were installed in the ground, the increase in excess pore water pressure due to the loading was significantly reduced and became very much less than the increase in total stress. On the other hand, the predicted results for the subsoil without the PVD improvement show that the increase in excess pore water pressure is approximately equal to the increase in total stress. Another important feature seen in Fig. 7.9 is the variation in the increase in excess pore water pressure with depth. As shown, the difference in the increase in excess pore water pressure with depth is lessened when PVDs have been installed.

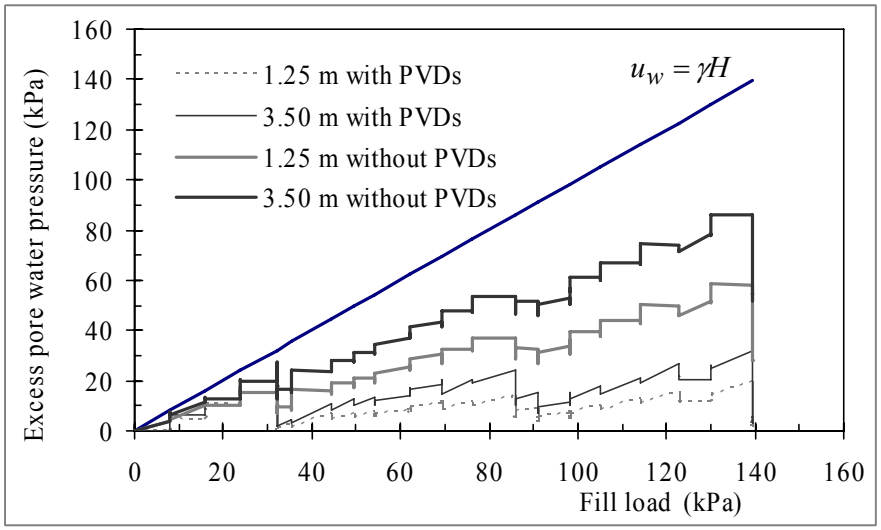

Fig. 7.9: Predicted excess pore water pressure under the center of the embankment as a function of the embankment load

7.3.3.3 Lateral Deformation

The predicted lateral displacement profiles for the PVD-improved subsoil under the embankment toe are shown in Fig. 7.10. However, the corresponding horizontal

displacement profiles from the inclinometers in the field are not available for comparison. The maximum computed lateral displacements are located at a depth ratio of z/H in the order of 0.25-0.375. H is the compressible layer thickness; it is around 8 m in this case.

It has been reported that vertical drains not only increase the settlement rate, but they also influence the magnitude of the lateral displacement of the subsoil (Chai et al. 1995). To verify this fact, lateral displacement profiles predicted under the toe of the embankment with and without PVD-improved subsoil are presented in Fig. 7.11. Comparing the results, the analysis without drains indicates larger lateral displacements at the ground surface than the analysis with drains. The effect of the drains on the lateral displacement can be more clearly seen by comparing the lateral displacement at the same surface settlement during the consolidation period. A comparison of the lateral displacement profile for a surface settlement of about 1.5 m is also presented in Fig. 7.11. It shows that although the analysis without drains yielded smaller settlements, it calculated a larger maximum lateral displacement than the case with drains.

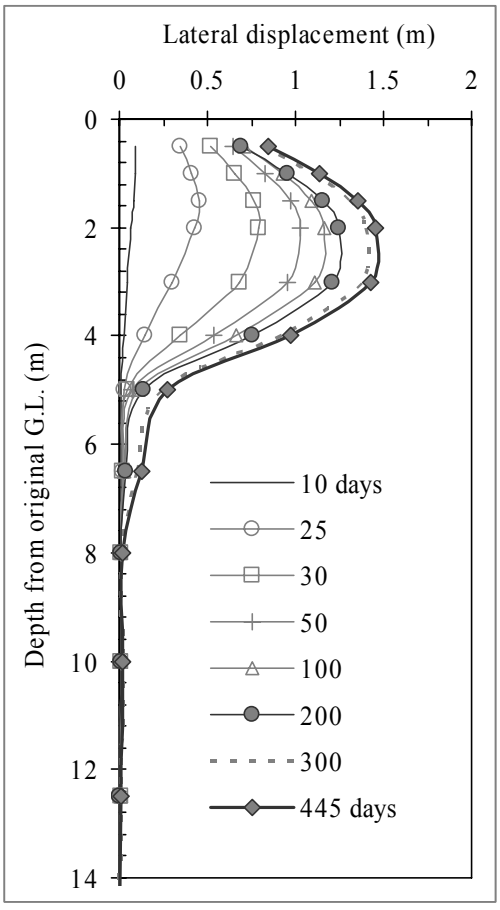

Fig. 7.10: Predicted lateral displacement profiles for the PVD-improved subsoil

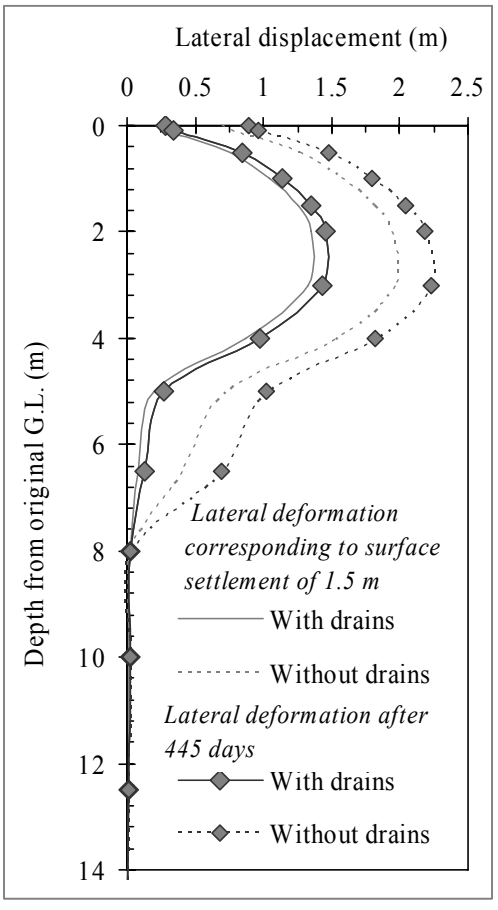

Fig. 7.11: Graph showing the influence of PVDs on lateral displacement

7.4 Stability of the Embankment

The stability of the embankment during and after construction is of major concern in the design of embankments over soft soil like peaty clay which has a low bearing capacity and low shear strength under in situ conditions. It has been seen that the installation of PVDs not only increases the settlement rate, but also significantly improves embankment stability (Li and Rowe 2001). In this section, the effect of PVDs on embankment stability is examined using the method proposed by Matsuo and Kawamura (1977).

7.4.1 Diagram for the Construction Control of Embankments

Matsuo and Kawamura (1977) introduced a chart after observing the deformations of many embankments and plotted the process of the displacement during the construction of each embankment. They proposed a method in which the degree of safety at present is ascertained and then the successive failures are predicted by observing the vertical settlement in the central area under an embankment and the horizontal displacement near the toe of the slope. It is astonishing that most of the embankments failed near the one curve even though they were constructed under different conditions from each other, such as section and unit weights, soil properties, soft layer thicknesses, and other surrounding conditions. This curve can be regarded as the "failure criterion line", as shown in Fig. 7.12. Therefore, the failure of embankments can be predicted by plotting the observed settlements and the horizontal displacements on this diagram. In Fig. 7.12, s indicates the settlement under the center and δ is the horizontal deformation at the toe of the embankment.

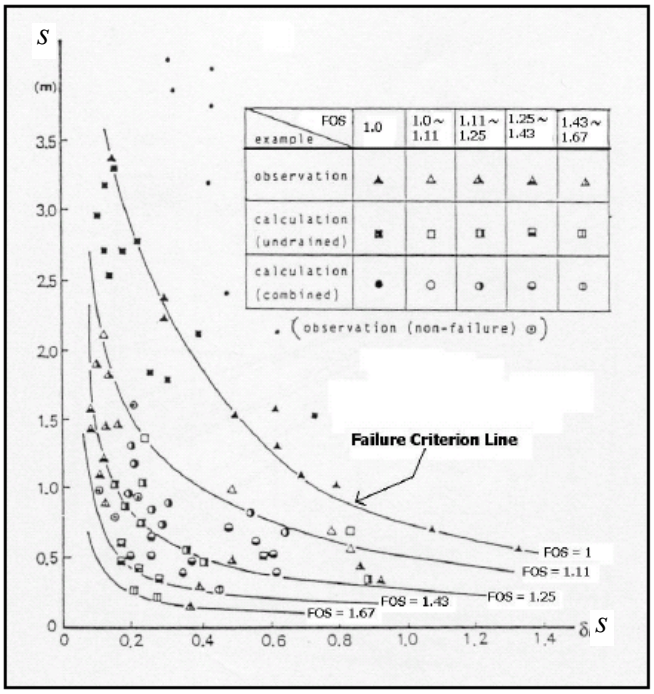

Fig. 7.12: Modified Matsuo stability plot

Embankments on soft grounds are usually constructed with smaller safety factors than other structures because changes in the design during construction are comparatively easy to make in the earth work. This requires that the embankment construction be controlled in a safe and timely manner using the information obtained from the practically possible measurements. For this purpose, the "Matsuo stability plot" provides a very useful tool for practicing geotechnical engineers.

7.4.2 Effect of PVDs on Embankment Stability

The stability evaluation for the embankment considered in the present chapter is examined using the procedure described by Matsuo and Kawamura (1977). The stability was checked for three different cases, namely, (1) a case with the same field conditions as when PVDs were installed 108 days after the construction was started, (2) a case which does not consider PVD improvement in the embankment construction, and (3) a case which considers that PVDs had been installed before the embankment filling was started. The obtained results are shown in Fig. 7.13.

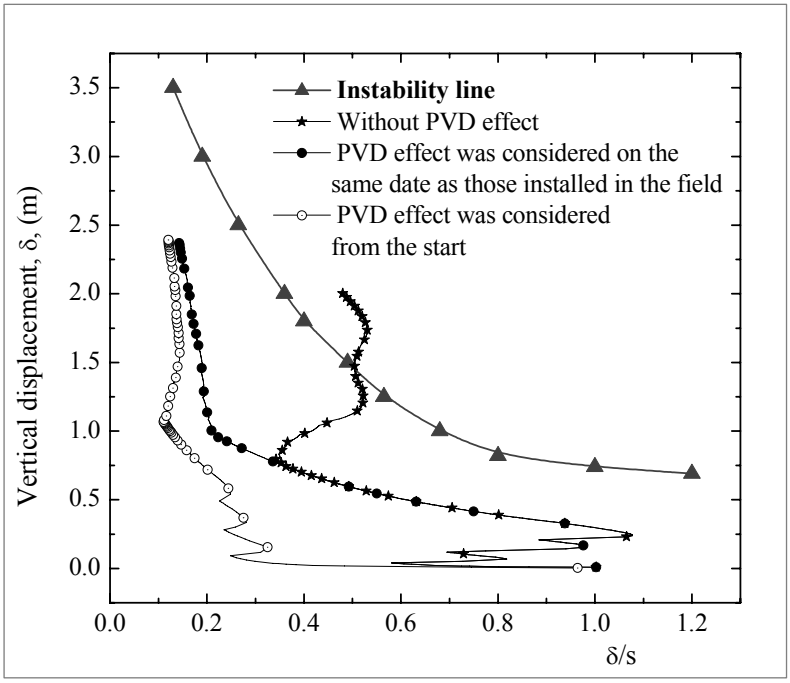

Fig. 7.13: Improvement in embankment stability due to the PVD installation

Matsuo and Kawamura (1977) reported that the instability of an embankment can occur when the plot of s and δ / s is above the instability line. As shown in Fig. 7.13, for an embankment constructed without PVDs, the predicted plot rises above the "instability line" indicating that if this embankment had been constructed without the installation of

PVDs, it would have failed during the construction period. It seems that without PVDs, large lateral deformations occur in the subsoil due to the shear stress induced by the embankment loading, and this shear stress will lead to embankment failure. In the field, PVDs were installed some time after the embankment filling was initiated and the construction was successfully completed without any risk of failure. A plot representing the exact field conditions shows this behavior, thus confirming the validity of the method to evaluate the stability of embankments constructed on peaty clay. From the results shown in the figure, it can be concluded that the stability of an embankment is significantly improved by the installation of PVDs.

7.5 Modeling of Sand Compaction Piles in the Finite Element Analysis

The sand compaction pile (SCP) method is frequently used in construction to form compacted sand piles by vibration, dynamic impact, or static excitation in soft grounds. Originally developed in Japan to improve stability or compressibility and/or to prevent liquefaction failure in loose sand, the SCP method is now often applied to soft clay grounds to ensure stability and to reduce ground settlements. In particular, for construction on embankments of materials like peaty soil, which have very low shear strength, the installation of SCPs enhances the stability of the embankment slope, helps to increase the bearing capacity, and accelerates the consolidation rate of the foundation soil.

Most sand compaction pile installations are done using the vibro-replacement method. A cylindrical vertical hole is made by a vibrating probe which penetrates by jetting and by its own weight. Sand is poured into the hole in increments of 0.4-0.8 m and compacted by the probe which simultaneously displaces the material radially into the soft soil. The diameters of SCPs are usually in the range of 0.5-1.2 m. SCPs with larger diameters are used for softer grounds. In general, square or triangular grid patterns are used with a center-to-center column spacing of 1.5-3.5 m (Mitchell 1981).

It is evident that the consolidation behavior around SCPs is three dimensional and an axisymmetric unit cell model can be used for the analysis of a single stone column in FEM. To simulate an SCP-treated foundation, however, three-dimensional finite element analyses are complex and time-consuming. Therefore, it is desirable to model the foundation by two-dimensional procedures. In the present research work, the consolidation behavior when SCPs are installed in peaty soil is modeled using the method proposed by Tan and Oo (2005). The method proposes a conversion scheme which is based on a simplified analytical method for a stone column reinforced foundation by Han

& Ye (2001) and considers the composite stiffness of the unit cell and the area replacement ratio. A two-dimensional FEM model for the SCPs can be formulated incorporating the parameters derived from the conversion scheme.

In order to model the SCP-treated ground, which is under three-dimensional conditions, into a two-dimensional numerical program, the relevant plane strain parameters have to be calculated. Thus, the conventional axisymmetric SCP unit cell must be transferred into an equivalent plane strain unit cell. Fig. 7.14 shows the conversion from the axisymmetric unit cell into the equivalent plane strain unit cell. In the conversion scheme, Han & Ye (2001) assumed that the composite stiffness of the SCP- or the SC (stone column)-treated ground will be the same as that in both the axisymmetric and the plane strain cases.

The composite stiffness of the axisymmetric unit cell is calculated using the stiffness of the SCPs and the stiffness of the surrounding soil with the respective area replacement ratio.

$$E_{composite} = E_{col,axi} * a_{s,axi} + E_{soil,axi} * (1 - a_{s,axi}) \tag{7.8}$$

$$a_{s,axi} = \frac{A_{col}}{(A_{col} + A_{soil})} \tag{7.9}$$

where $a_{s,axi}$ is the area replacement ratio in the axisymmetric unit cell, $E_{composite}$ is the stiffness of the composite material in the unit cell, $E_{col,axi}$ is the stiffness of the axisymmetric sand compaction column, and $E_{soil,axi}$ is the stiffness of the surrounding soil in the axisymmetric unit cell.

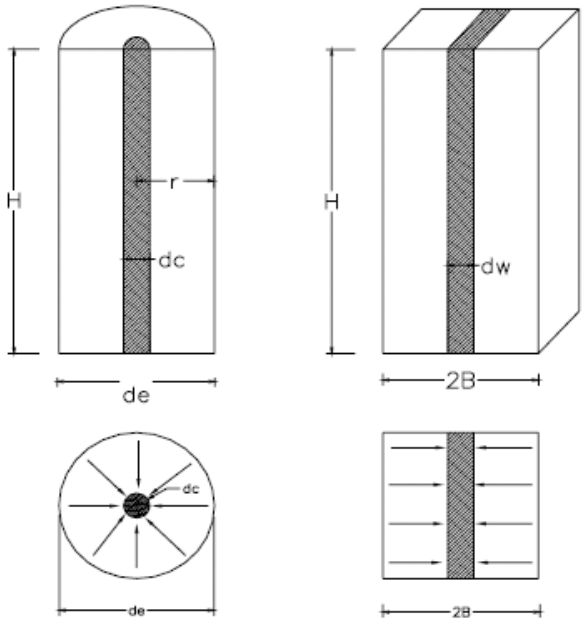

Fig. 7.14: Conversion from an axisymmetric unit cell into an equivalent plane strain (Tan and Oo 2006)

Assuming that the composite stiffness for the axisymmetric model and the plane strain model are equal, the stiffness of the sand compaction piles under plane strain conditions is calculated using Eq. (7.10), considering the area replacement ratio corresponding to the plane strain unit cell geometry. It should be noted that for this calculation, it's assumed that $E_{soil,axi} = E_{soil,pl}$.

$$E_{composite} = E_{col,pl} * a_{s,pl} + E_{soil,pl} * (1 - a_{s,pl}) \tag{7.10}$$

$$a_{s,pl} = \frac{A_{col}}{(A_{col} + A_{soil})} \tag{7.11}$$

where $a_{s,pl}$ is the area replacement ratio in the plane strain unit cell, $E_{composite}$ is the stiffness of the composite material in the unit cell, $E_{col,pl}$ is the stiffness of plane strain sand compaction wall, and $E_{soil,pl}$ is the stiffness of the surrounding soil in the plane strain unit cell.

As seen in Fig. 7.14, in transforming the sand compaction column unit cell from an axisymmetric model into a plane strain model, the compacted sand area is increased in the plane strain model. In other words, the area of the surrounding soil is reduced due to the conversion. The area reduction ratio is thought to have an impact on the determination of the stiffness of the surrounding soft soil in the plane strain model and can be expressed as

$$A_{red} = \frac{(1 - a_{s,pl})}{(1 - a_{s,axi})} \tag{7.12}$$

Incorporating the area reduction ratio for the plane strain unit cell (A_{red}), the stiffness of the soft soil in the plane strain model is modified for the stiffness matching procedure as

$$E_{soi,pl} = A_{red} * E_{soil,axi} \tag{7.13}$$

where A_{red} is the area reduction ratio due to the conversion of the axisymmetric model into the plane strain model.

In the present analysis, the permeability matching was conducted with the following equation based on the equal average degree of consolidation in the axisymmetric and equivalent plane strain unit cell, as outlined by Indraratna et al. (1986). The smear effect and the well resistance were not considered.

$$\frac{k_{h,pl}}{k_{h,axi}} = \frac{0.67}{[\ln(n) - 0.75]} \tag{7.14}$$

where $k_{h,axi}$ and $k_{h,pl}$ are the permeability in the axisymmetric and the equivalent plane strain conditions, respectively. $n = R / r_w$ in which R is the radius of the axisymmetric influence zone around a single drain, r_w is the axisymmetric radius of the sand compaction pile.

In the present analysis, the SCPs are modeled to behave as an elastic material.

7.6 Prediction of the Consolidation Behavior of an Embankment Constructed using SCPs

The embankment at Ch 19+190 in the Colombo-Katunayake Expressway (CKE) project was constructed on SCP-improved subsoil. This area has a peat layer of greater thickness than the other areas (Fig. 7.15). The virgin ground consists of peaty soil, 1.0 m in thickness, followed by a loose, silty sand layer up to a depth of 2.0 m. Lying below that, a very soft peaty soil, 6.0 m in thickness, is encountered. Below that, there exists a loose to medium-dense silty sand layer, 2.0 m in thickness. Immediately below that, a medium-dense sand layer occurs up to a depth of 14.0 m. Beneath this layer, sand layers were found down to an investigation depth of 20 m (Ketheeswaravenayagam et al. (2006).

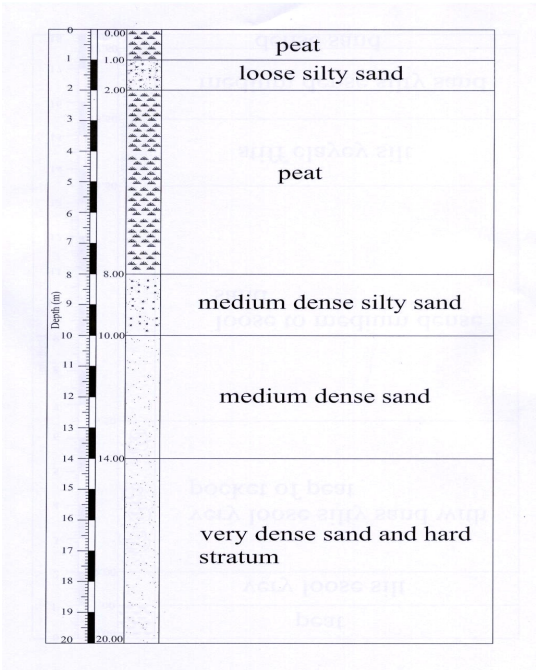

Fig. 7.15: Subsurface profile at the site

The embankment has a height of 7.5 m with a crest width of 13.6 m and 1:2 side slopes. The SCPs were installed in the field 79 days after the initial sand mat construction was started. They were installed to a depth of around 8 m from the original ground surface in a

square pattern with spacing of 1.6 m. The diameter of the SCPs was 0.6 m and they were installed to the full width of the embankment.

The foundation soil was modeled up to a depth of 16.5 m below the ground surface and 75 m horizontally from the embankment centerline. The finite element mesh, indicating the SCPs and the subsurface profile relevant to this analysis, are shown in Fig. 7.17. The loading curve showing the construction sequence for the embankment is presented in Fig. 7.16. The material parameters used for the subsoil are listed in Table 7.5. The material parameters for the peaty soil were almost the same as those for the previous embankment analysis for PVD-improved soil, except for the soil stiffness. The original soil stiffness (shear modulus) was modified for the plane strain analysis in accordance with the procedure outlined in Section 7.4.

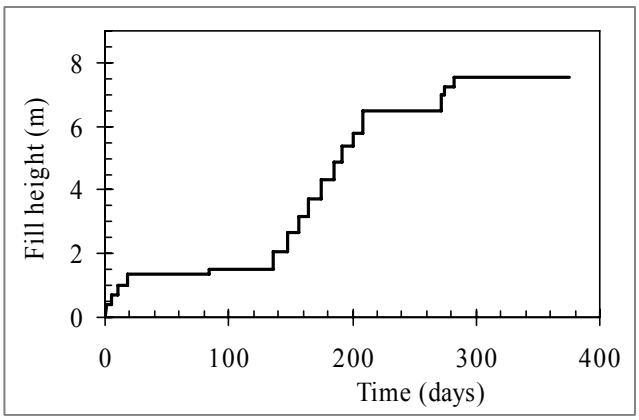

Fig. 7.16: Loading curve

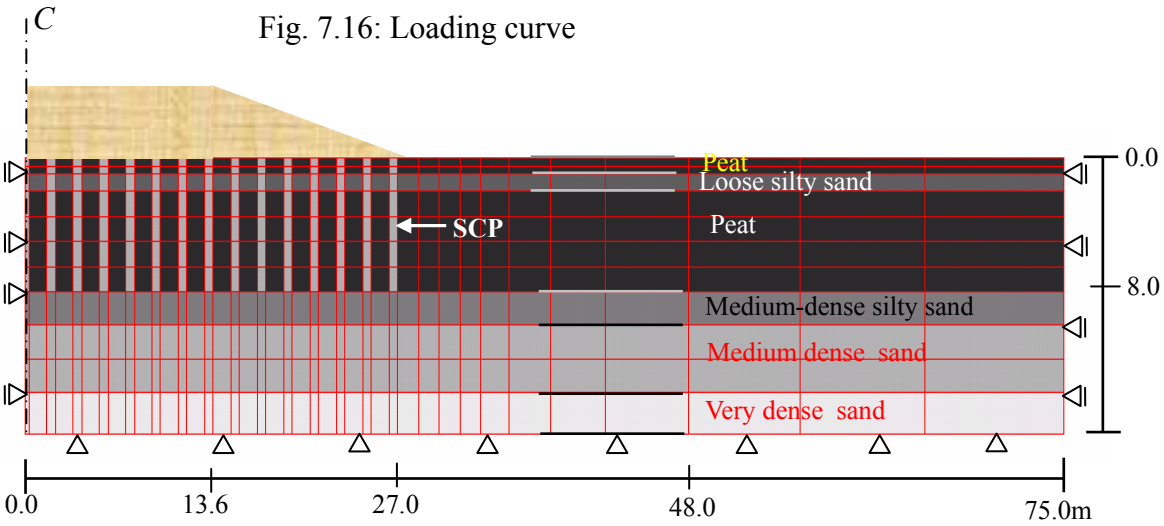

Fig. 7.17: Finite element mesh showing the locations of the SCPs

Analyses were carried out by considering the finite deformation theory. The effect of structural degradation was considered for the compressible soil. The compressibility parameters were varied in accordance with Eqs. (3.33) and (3.34) in order to consider the nonlinear nature of the $e - \log \sigma'_{\mathrm{v}}$ curve and the decreasing compressibility associated

with the peat consolidation process at higher stress levels. In the modeling, elasto-viscoplastic behavior was assumed for the peaty soil, and the elastic behavior was assumed for the other soils including the SCPs. The displacement and the drainage boundary conditions were the same as for the previous analysis described in Section 7.3.2.

Table 7.5: Parameters used for the SCP-improved peaty clay subsoil

Parameters		Values for peaty soil
Initial void ratio	e_0	5.0#
Initial vertical effective stress	$\sigma'_{22(0)}$ (kPa)	12.0#
Coefficient of earth pressure at rest	K_0	0.53
Coefficient of permeability	k_0 (m/s)	1.5 x 10^{-7}#
Change in permeability index	C_k	1.0
Initial elastic shear modulus	G_0 (kPa)	560#
Compression index	λ	1.315
Swelling index	κ	0.087
Stress ratio at critical state	M^*	0.95
Compression yield stress	$\sigma'_{mbi}(\sigma'_{mai})$ (kPa)	12.0#
Viscoplastic parameter	m'	22
Viscoplastic parameter	C (1/s)	1.0x 10^{-9}
Structural parameter	σ'_{maf} (kPa)	0.7 σ'_{mbi}
Structural parameter	β	5

At a depth of 1 m

The SCPs installed under the embankment were modeled with the equivalent plane strain properties described in Section 7.4. In the modeling, the shear modulus of the peat was assumed to be equal to 800 kPa based on the previous analysis (Chapter 5-7). SCPs were installed in the field in a square pattern with a grid spacing (s) of 1.6 m, and the equivalent diameter of the unit cell for each SCP was 1.8 m ($D_e = 1.13s$). Since reliable data were not available for the in situ stiffness ($E_{col,axi}$) or permeability ($k_{h,axi}$) of the SCPs, realistic respective values of 11,000 kPa and 1.0 x 10^{-6} m/s were assumed. Accordingly, the values required for the conversion scheme to transform the axisymmetric behavior into equivalent plane strain conditions are listed in Table 7.6.

Table 7.6: Parameters for the SCPs

a_s, axi	$E_{comp.}$ (kPa)	$E_{col,pl}$ (kPa)	a_s, pl	A_{red}	ν	K_0	k_0 (m/s)	$\sigma'_{22(0)}$ (kPa)
0.11	1922	4169	0.333	0.74	0.3	0.5	2.0 x 10^{-6}	15.0

Another analysis was conducted using a higher stiffness of 15,000 kPa for the SCPs. The equivalent $E_{col,pl}$ became 5400 kPa, and the analysis was conducted while keeping all other parameters the same as in the case with a lower stiffness value (11,000 kPa) for the SCP.

It should be noted that SCPs were implemented in the modeling from the start of the filling process, even though they were installed in the field 79 days after the start of the construction.

7.6.1 Results and Discussion

The predicted and the measured settlements for just under the embankment and for 12.5 m away from the center are shown in Figs. 7.18 and 7.19, respectively. The recorded field settlements just under the center and 12.5 m away from the center of embankments were 0.937 m and 0.813 m, respectively. These values show that the settlements of peaty soil can be greatly reduced by the installation of SCPs.

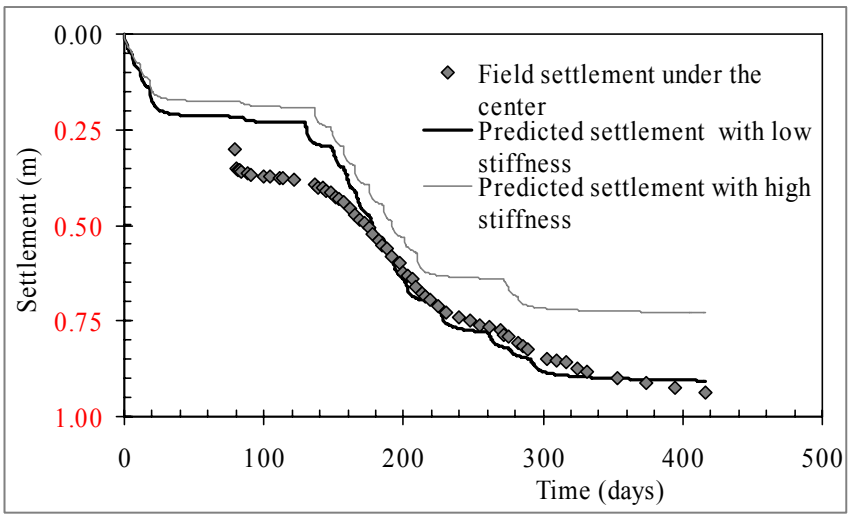

Fig. 7.18: Predicted settlement under the center of the embankment

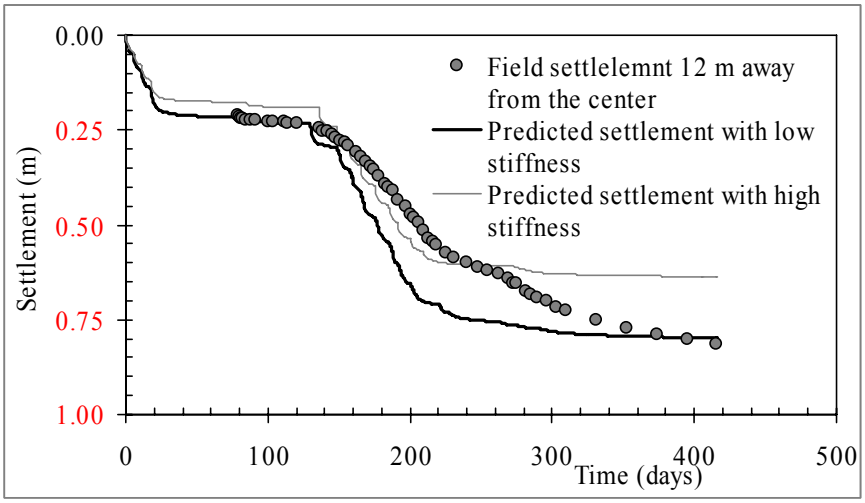

Fig. 7.19: Predicted settlement under the crest of the embankment

The monitoring was started 79 days after the filling was begun, and therefore, settlement data for this period were not available. In the modeling, the SCP behavior was considered from the beginning, whereas in the field, SCPs were installed 79 days after the construction was started. As expected, the predicted settlements for the initial period are much less than the corresponding field settlements, as indicated in Figs. 7.18 and 7.19. However, the observed settlements after the installation of the SCPs in the field show a reasonable agreement with the predicted settlements with the low stiffness value for the SCPs (Fig. 7.18). The results obtained from the predictions clearly indicate that the settlements of the surrounding peaty soil greatly depend on the stiffness of the SCPs. SCPs with higher stiffness levels yield lower ground settlements of the surrounding soil.

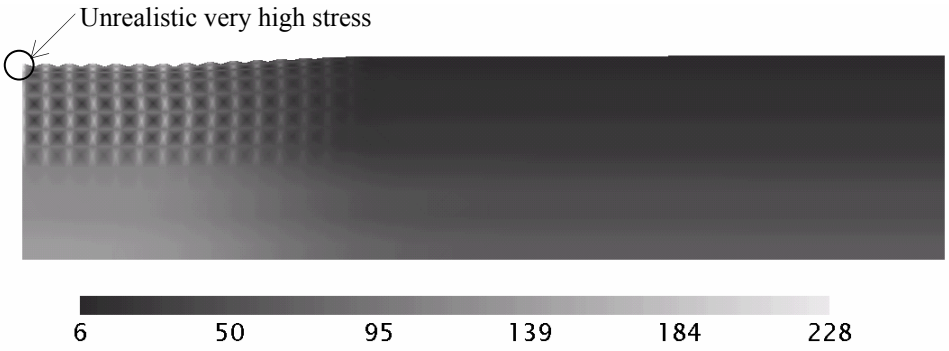

Fig. 7.20: Mean effective stress distribution in the foundation due to embankment loading (kPa)

Fig. 7.20 shows how the applied foundation loads are carried by the SCPs and the surrounding soil. The stress is shared between the SCPs and the surrounding peaty soil in proportion to the relative stiffness of the two materials and the area replacement ratio. However, it seems that a majority of the loads are supported by the SCPs due to the very soft nature of peaty soil. The very high level of stress that occurs in the top half width of the SCPs placed along the center seems to be unrealistic. This might be due to the applied constraint of the displacements in the horizontal direction used in the modeling to maintain the symmetricity of the embankment which makes the SCPs too rigid with its half width.

The predicted excess pore water pressure with a low stiffness value for the SCPs, at depths of 2 m and 4.5 m, are shown in Fig. 7.21 with the available corresponding measured data. The recorded maximum excess pore water pressure in the field was less than 10 kPa; this indicates that the excess pore water pressure was very rapidly dissipated in the subsoil due to the SCP installation. However, the field measurements do not seem to be completely accurate as the sudden increase expected due to the embankment loading was not indicated in the field data during some loading stages. In the field data, zero

excess pore water pressure was recorded between certain loading stages. Corresponding predicted values show a good agreement by predicting an excess pore water value of less than 1 kPa. In general, the results indicate that the predicted rate of excess pore water pressure dissipation is higher than the observed one. This might be due to the fact that: (a) the smear effect (the reduction in the permeability of the surrounding soil due to the disturbance occurring in the SCP installation process) was not taken into account or (b) there was a limitation of the modeling method on the SCP behavior. In the field, SCPs work in close axisymmetric drainage (three-dimensional) conditions. In the present analysis, plain strain (two-dimensional) conditions were assumed.

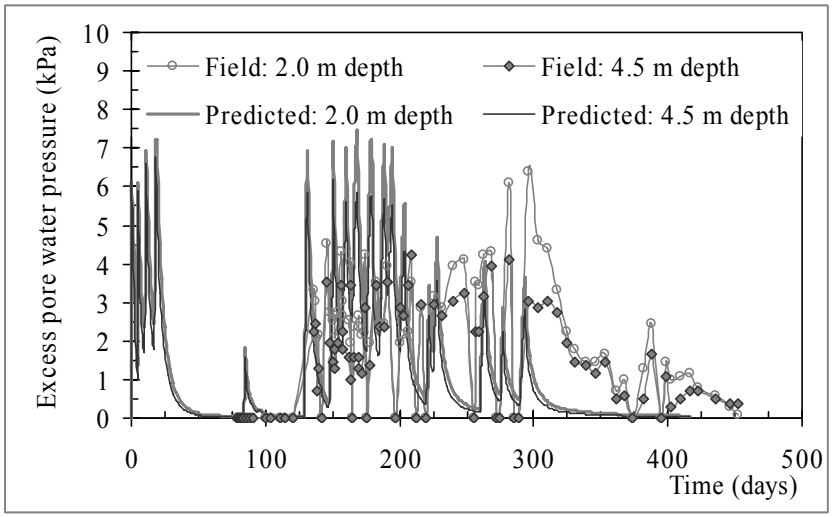

Fig. 7.21: Comparison of excess pore water pressure

The predicted results for both the settlements and the excess pore water pressure indicate that major settlements had already occurred in the subsoil. The field data also confirm these findings. The analysis and the observed data indicate that the settlements of the peaty layer are significantly reduced by the SCP installation. The predicted settlement pattern for the embankment foundation at the end of loading is shown in Fig. 7.22. The figure shows that no strong geometrical distortion occurred anywhere in the embankment foundation. Also, the outward lateral displacements of the subsoil due to the embankment loading are very small. All these features indicate that the installation of SCPs improves the bearing capacity of the subsoil and the stability of the embankment.

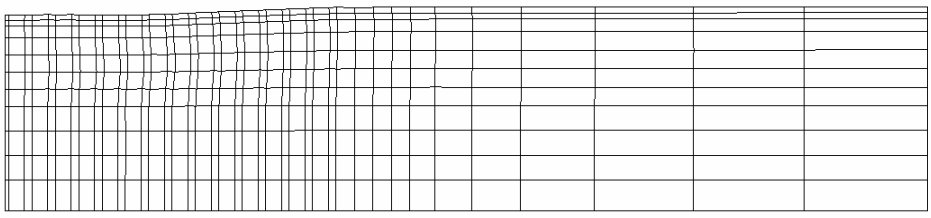

Fig. 7.22: Predicted deformation pattern for the embankment at the end of construction

7.7 Prediction of the Consolidation Behavior of an Embankment Constructed with both SCPs and PVDs

SCPs are sometimes used under slopes to improve the embankment stability. SCPs are also installed along the edges of embankments to strengthen the foundations and to reduce the influence of ground movement on adjacent structures, such as buildings and foundation area between the center of the embankment and the crest (13 m away from center) was improved by PVDs by increasing the consolidation rate, and SCPs were installed under the slope to strengthen the ground. The PVDs were installed in a square pattern with a spacing of 1.1 m up to a depth of 12.3 m where stiff clay was found. The SCPs were installed to a depth of 11.8 m from the original ground surface in a square pattern with a spacing of 1.6 m. The diameter of each SCP was 0.6 m. The finite element mesh, indicating the PVD-improved zone and the SCP locations, is shown in Fig. 7.23. The considered subsurface profile is also shown in this figure.

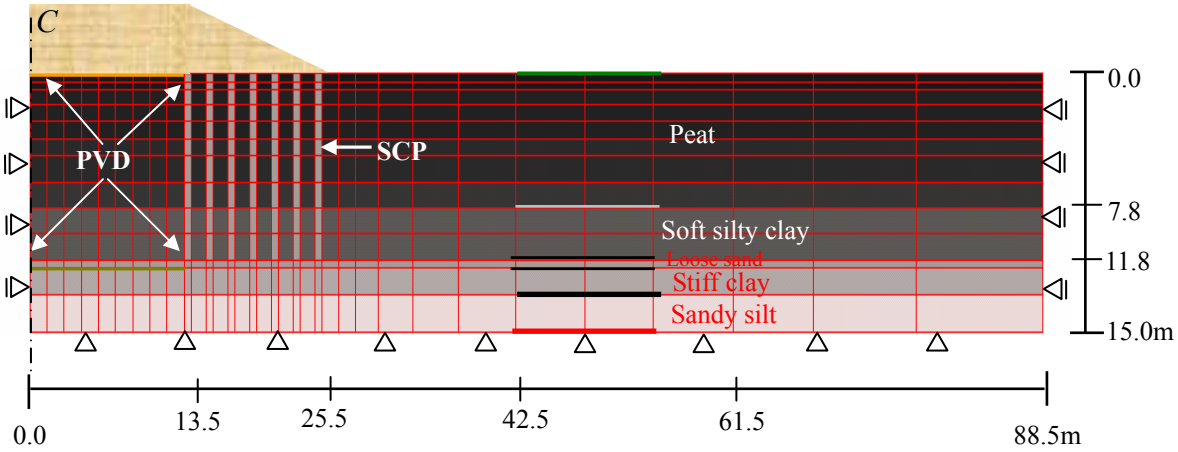

Fig. 7.23: Finite element mesh with a PVD-improved zone and SCP locations

The PVDs and the SCPs were installed in the field 48 days after the construction was started. In the modeling, the behavior of the PVDs was simulated on the same date as the field installation. For convenience, however, the SCPs were implemented in the modeling from the start of the filling process. The parameters used in the analysis were the same as those mentioned in the previous section.

The predicted settlements just under the center of the embankment are shown in Fig. 7.24 together with the corresponding measured field values. The figure shows an excellent agreement between the predicted and the measured values during the monitoring period.

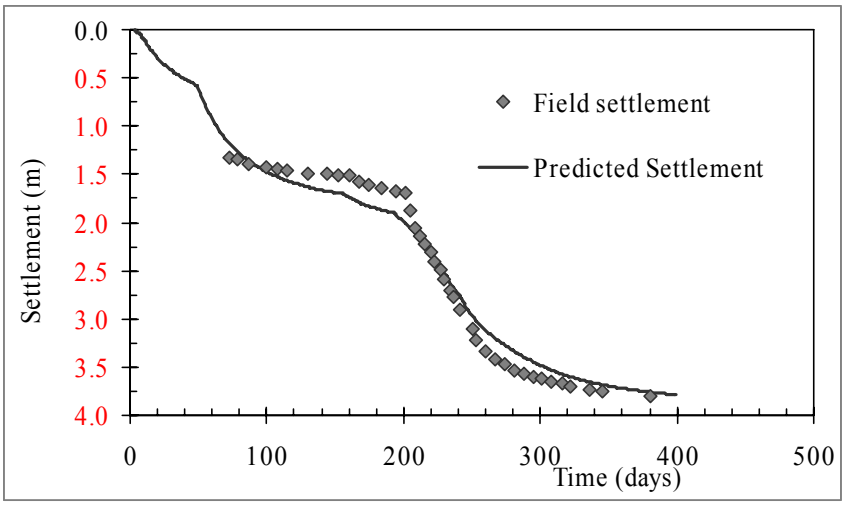

Fig. 7.24: Comparison of settlements under the embankment center

The predicted pore water pressure and the corresponding field data taken under the center of the embankment are shown in Fig. 7.25. Since the piezometers were installed after the PVDs and the SCPs, the sudden drop in excess pore water pressure indicated in the prediction could not be captured in the field monitoring data. Fig. 7.25 shows an excellent agreement between the available field data and the predicted values.

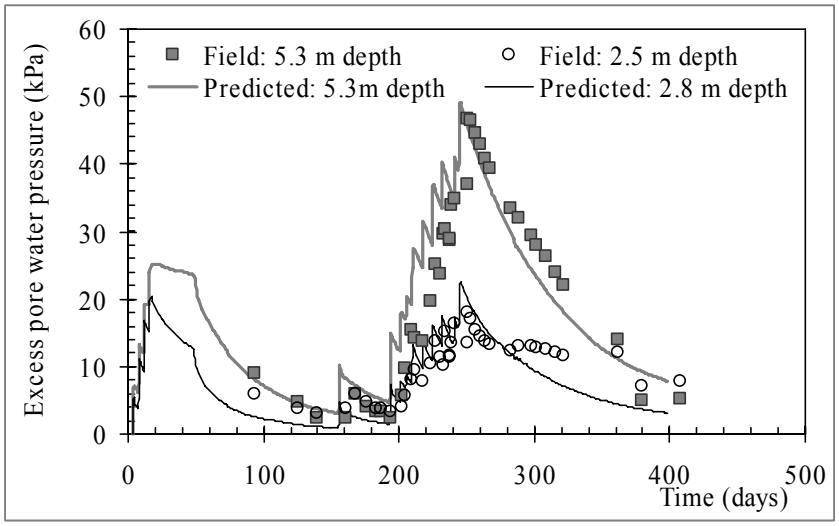

Fig. 7.25: Comparison of excess pore water pressure

The predicted pore water pressure and the corresponding field data taken under the center of the embankment are shown in Fig. 7.25. Since the piezometers were installed after the PVDs and the SCPs, the sudden drop in excess pore water pressure indicated in the prediction could not be captured in the field monitoring data. Fig. 7.25 shows an excellent agreement between the available field data and the predicted values.

Fig. 7.26 shows the distribution of excess pore water pressure under the embankment. It shows that more excess pore water pressure develops at the center and that the pore water tries to migrate outward from the center.

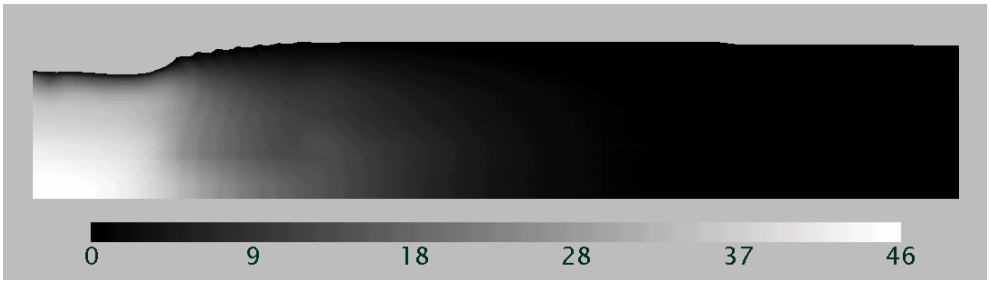

Fig. 7.26: Distribution of excess pore water pressure in the foundation (kPa)

Fig. 7.27 shows the distribution of mean effective stress under the embankment foundation. Very high stress is concentrated in the innermost SCP installed under the embankment. Appreciable horizontal movements in the peaty soil in the PVD-improved zone accompany embankment loading. Subsequent loading leads to large deformations in the soil under the slope where rotational movements are anticipated. These movements are mostly resisted by the innermost SCP. As a result, a rise in the excess pore water pressure in this area and in the effective stress of the SCPs are both possible. The same embankment was analyzed considering the effect of the PVD in the center, but without considering the SCPs under the slope. Fig. 7.28 shows that the catastrophic failure of an embankment can be prevented by the increase in shear resistance provided by the improvement.

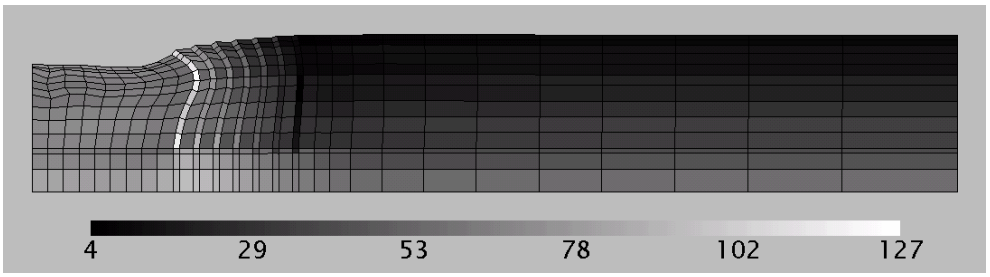

Fig. 7.27: Distribution of mean effective stress for embankment foundation (kPa)

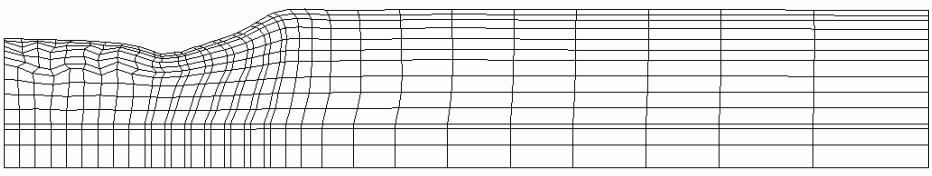

Fig. 7.28: Deformation pattern of the embankment foundation without considering SCP improvement under the slope

7.8 Summary and Remarks

A constitutive model was applied to predict the subsoil behavior due to an embankment constructed using prefabricated vertical drains (PVDs) and sand compacted piles (SCPs). Finite element analyses were carried out for all the cases by converting the actual three-dimensional conditions around the drains into simplified two-dimensional plane strain conditions. The field behavior when the PVDs were installed in the peaty clay was simulated using the equivalent vertical permeability. In the case of SCPs, a conversion scheme was used to transform the axisymmetric nature of the compacted sand columns into equivalent plane strain conditions.

Through the analyses made in this chapter, the following conclusions are drawn:

1. The laboratory consolidation model test data indicated that the prefabricated vertical drains (PVDs) significantly accelerated the peat consolidation process. The observed improvement due to the installation of the PVDs was captured well by the model.
2. The model incorporating equivalent vertical permeability for the PVD-improved embankment foundation yielded acceptable results in terms of the observed excess pore water pressure and the settlements. The maximum settlement was recorded in the field under the slope of the embankment (12.5 m away from the center); this settlement pattern was accurately predicted by the model.
3. The correlation between the predicted and the observed excess pore water pressure was generally good, but the results can be further improved.
4. The analysis indicates that the installation of PVDs not only accelerates the consolidation rate, but also influences the deformation pattern of the subsoil due to embankment loading. The lateral deformation of the embankment subsoil was greatly reduced by the installation of PVDs.
5. The effect of PVDs on embankment stability was studied using the Matsuo stability plot. It was found that the stability of the embankment was significantly improved by the installation of PVDs.
6. Analyses carried out to simulate the behavior of embankment foundations treated by SCPs indicate that the foundation stress was shared by the SCPs and the surrounding soil in proportion to the relative stiffness of the two materials and the area replacement ratio. Therefore, ground stiffness and the area replacement ratio used in the conversion scheme play vital roles in predicting the behavior of SCP-improved subsoil.

7. The analyses reveal that the installation of SCPs under the embankment slope can improve embankment stability.
8. Due to the good agreement obtained between the measured and the predicted settlements and excess pore water pressure levels, the proposed method for considering variable compressibility seems to be realistic in the analysis of stage-constructed embankments which exert high levels of pressure on the peaty subsoil.

From these comparisons, it can be seen that the elasto-viscoplastic model incorporating the described methods in the present chapter can be used to analyze the behavior of an embankment on subsoil improved with prefabricated vertical drains and sand compaction piles.

Chapter 8

CONCLUSIONS AND RECOMMENDATIONS

8.1 Summary and Conclusions

The consolidation behavior of peaty clay found in Sri Lanka was studied using the elasto-viscoplastic model (Kimoto and Oka 2005). Analyses were performed considering all the main features involved in the peat consolidation process, namely, finite strain, variable permeability and compressibility, and the effect of secondary compression which is assumed as a continuous process. In addition to these main features, the effect of structural degradation on the consolidation was considered by introducing viscoplastic strain softening in addition to strain hardening with viscoplastic volumetric strain. In the model, the secondary compression was taken into account by viscoplastic parameter m', which is related to the C_α / C_c ratio of the soil. The value of permeability was varied with the void ratio throughout the consolidation process. The variable compressibility was considered in the analysis of stage-constructed embankments which exert high levels of pressure on the peaty subsoil, in order to take into account the nonlinear nature of the $e - \log \sigma'_v$ curve of peaty soil and the decreasing compressibility associated with the peat consolidation process at higher stress levels. Finite element analyses were carried out considering finite deformation using the updated Lagrangian method. The material parameters were obtained using the available laboratory and field test results, and empirical correlations were used in cases where there was a lack of test data. The conclusions obtained from this study are as follows:

1) The composition of natural deposits of peaty soil may vary considerably among different sites, as do their mechanical properties. Therefore, it is necessary to identify the type of peat under consideration, as the resulting consolidation behavior may be region-

specific. Investigations reveal that the peaty soils found in Sri Lanka are generally of the amorphous type. Some useful relationships could be established between the physical and the mechanical properties of Sri Lankan peaty clay. Also, correlations between compression index and swelling index, and coefficient of secondary consolidation could be observed. The pattern agrees well with similar results reported elsewhere, but the numerical values of the correlations are different. This might be due to the lower organic matter content reported in Sri Lankan peaty soil.

2) The experimental results confirmed that viscoplastic parameter m', which is related to secondary compression, can be evaluated through the consolidation test results. The model assumption for the occurrence of creep (or secondary) settlement as a continuous process agrees well with the observed consolidation behavior under laboratory conditions. The effect of using the results of laboratory tests on a thin soil specimen to predict the development of strain with time for thick soil layers in the field can be successfully taken into consideration with the model by keeping in mind the difference in initial strain rates.

3) In the finite strain analysis, changes in geometry affect the ground rigidity and the rate of consolidation. Therefore, the finite strain analysis always predicts lower levels of excess pore water pressure and settlements than the infinitesimal strain analysis. The difference between the two methods becomes significant with the occurrence of large strain. The simulation of the field consolidation behavior of peaty clay due to the construction of compacted earth fill reveals that the finite deformation theory is more representative than the infinitesimal strain theory for the consolidation analysis of materials like peat which is highly compressible in nature. Also, the effect of structural degradation has a significant influence on the predictions of the observed settlements and the stagnated excess pore pressure occurring simultaneously in the field. The results of the analysis confirm that when analyzing the consolidation behavior of natural soil deposits, it is essential to consider the effect of the degradation of the structure of the deposits in order to describe realistic in situ behavior.

4) The embankment analysis of natural peaty clay indicates that the model can be successfully applied to predict both deformation and stability aspects of structures constructed on peaty clays. The predicted settlements have shown a good agreement with the measured data indicating that the observed large strain in the field was captured by the model. The predicted settlement pattern for the embankment was different from a typical one in which always the maximum settlement occurs at the center. Here, the calculated settlement under the crest area (12.5 m away from the center) was greater than that of the central area of the embankment during the construction period. This might be due to the

stress conditions in the central area of the foundation, which are approximately one dimensional, and to the edge area, which is two dimensional, as the embankment has a large width compared to its height. The higher settlement that was predicted under the shoulder area of the embankment foundation was possibly due to the result of local shear-induced displacement. The stress-strain characteristics of the embankment foundation indicated signs of instability in the foundation soil under the slope of the embankment. The stress paths of the elements under the center area moved along the K_0 path, whereas the stress paths of the elements under the toe area rose towards the critical state line indicating that the toe area was more prone to plastic instability than the center region under this embankment geometry. This was further illustrated by the distribution of accumulated viscoplastic shear strain of the embankment foundation and the viscoplastic volumetric strain vs. shear strain graphs.

5) The constitutive model was applied to predict the subsoil behavior due to an embankment constructed with prefabricated vertical drains (PVDs). Two-dimensional plane strain finite element analyses were carried out by the model using the equivalent vertical permeability for the PVD-improved soil. This method permits the effect of enhanced drainage to the PVDs, without subdividing any element into small pieces. It can also be used to analyze the improved subsoil in the same way as that for the unimproved subsoil. The model incorporating equivalent vertical permeability for the PVD-improved embankment foundation yielded acceptable results in terms of the observed excess pore water pressure and the settlements. The analysis also indicates that the installation of PVDs not only accelerates the consolidation rate, but also influences the deformation pattern of the subsoil due to embankment loading. The effect of the PVD installation on the embankment stability was examined; it was found that the stability of the embankment was greatly improved by the PVD installation. A comparison of the predicted and the observed embankment behavior confirmed the applicability of the Matsuo stability plot to evaluate the stability of embankments constructed over peaty soils.

6) The behavior when sand compaction piles (SCP) are installed in peaty clay was predicted by the model using the conversion scheme which approximates the actual three-dimensional conditions that exist around the drain into simplified two-dimensional plane strain conditions. Analyses carried out to simulate the behavior of embankment foundations treated by SCPs indicate that the stiffness and the area replacement ratio used in the conversion scheme play vital roles when predicting the behavior of SCP-improved grounds. Moreover, the analyses reveal that the installation of SCPs under an embankment slope can improve the embankment stability.

The work presented in this study indicates that the applied elasto-viscoplastic constitutive model and the analysis methods can successfully take into account the main features of the consolidation behavior of amorphous type of peaty soil. In addition, the constitutive model and the analysis methods used here can be recommended for practical applications to construction projects on Sri Lankan peaty clays because of the generally good agreement obtained between laboratory and field conditions.

8.2 Recommendations for Future Work

In the present study, a comprehensive analysis was carried out to simulate the consolidation behavior of peaty soils found in Sri Lanka. The conclusions stated above are limited by the scope of the research. The following recommendations are made for future research.

The results indicate that the constitutive model and the analysis methods adopted in the present study can predict the consolidation behavior of the amorphous type of peat. Having successfully predicted the consolidation behavior of amorphous peat, it would be worthwhile to extend the model to describe the consolidation behavior of fibrous peat which behaves significantly different from amorphous peat. Fibrous peat has a typical anisotropic character due to the fresh organic fiber content. Therefore, it is necessary to consider the anisotropic behavior in the stress-strain characteristics as well as in the soil properties.

As described in the present research work, when constructing an embankment over materials like peat, which consists of soft subsoil with low shear strength and high compressibility, certain engineering procedures must be followed in order to prevent the failure of the embankment and to control the subsoil deformation. Placing a layer of reinforcement at the base of the embankment is one of the other methods that was not described in the present research. The functions of a layer of reinforcement are: (i) to provide tensile basal reinforcement, which contributes to the stability of the embankment and (ii) to provide confinement to the embankment fill and foundation soil adjacent to the reinforcement. This confining effect can reduce the lateral distortion of the subsoil due to the embankment load, and therefore, the shear stress level in the soft soil. Therefore, an analysis of the behavior of an embankment foundation with reinforcement on peaty soil would be advantageous in these types of construction projects.

In the present research work, embankment loading was simulated by applying incremental vertical loads to the upper boundary for simplicity in the finite element mesh

and the modeling. However, it is better to simulate the embankment filling by adding element layers of the embankment together with a gradual increase in the weight with time, as it can produce a more representative stress increase with the highly deformed upper boundary surface normally associated with the peat foundations.

References

Aboshi, H. (1973) An experimental investigation on the similitude of consolidation of a clay including secondary creep settlement, In *Proceedings of 8th International Conference on Soil Mechanics and Foundation Engineering,* Moscow*,* **4**(3), 88.

Adachi, T. and Oka, F. (1982) Constitutive equations for normally consolidated clay based on elasto-viscoplasticity, *Soils and Foundations*, **22**-4, 57-70.

Adachi, T. and Okano, M. (1974) A constitutive equation for normally consolidated clay, *Soils and Foundations*, **14**, 55-73.

Adachi, T., Oka, F. and Mimura, M. (1984) Study on secondary compression of clays, In *Proceedings of Symposium on Sedimentation Consolidation Model-Prediction and Validation,* San Francisco, ASCE, 69-83.

Adams, J.I. (1965) The engineering behavior of a Canadian Muskeg, In *Proceedings of 6th International Conference on Soil Mechanics and Foundation Engineering,* Montreal*,* **1**, 3-7.

Akai, K. and Tamura, T. (1978) Numerical analysis of multi-dimensional consolidation accompanied with elasto-plastic constitutive equation, *Tans. of Japan Society of Civil Engineers*, **269**, 995-104(in Japanese).

Barden, L. (1969) Time dependent deformation of normally consolidated clays and peats, *Journal of Soil Mechanics and Foundation Division*, ASCE, **95**(1), 1-31.

Berry, P.L. (1983) Application of consolidation theory for peat to the design of a reclamation scheme by preloading, *Quarterly Journal of Engineering Geology*, *London*, **16**, 103-112.

Berry, P.L. & Poskitt, T.J. (1972) The consolidation of peat, *Geotechnique*, **22**(1), 27-52.

Biot, M.A. (1962) Mechanics of deformation and acoustic propagation in porous media, *Journal of Applied Physics*, **33**(4), 1482-1498.

Brinkgreve, R.B.J. and Vermeer, P.A. (1994) Constitutive aspects of an embankment widening project, In *Proceedings of International Workshop on Advances in Understanding and Modeling the Mechanical Behavior of Peat,* Delft, Netherlands*,* eds. den Haan, Termaat & Edil, 143-158, Balkema, Rotterdam.

Burland, J.B. (1990) On the compressibility and shear strength of natural clays, *Geotechnique*, **40**(3), 329-378.

Carrillo, N. (1942) Simple two and three dimensional cases in the theory of consolidation of soils, *Journal of Mathematics and Physics,* **21**, 1-5.

Chai, J.C. and Miura, N. (1999) Investigation of factors affecting vertical drain behavior, *Journal of Geotechnical and Geoenvironmental Engineering***,** ASCE, **125**(3), 216-226.

Chai, J.-C., Shen, S.-L., Miura, N., Sakajo, S. and Bergado, D.T. (1995) Behavior of vertical drain improved subsoil under embankment loading*, Soils and Foundations*, **35**-4, 49-61.

Chai, J.-C., Shen, S.-L., Miura, N. and Bergado, D.T. (2001) Simple method of modeling PVD improved subsoil, *Journal of Geotechnical Engraining,* ASCE, **127**(11), 965- 972.

Chew, S.H. and Ng, T.G.. (2003) Consolidation, In *Proceedings of 12th Asian Regional Conference on Soil Mechanics & Geotechnical Engineering,* Singapore, eds. Lung et al., **2,** 1265-1270, World Scientific Publishing Co.

Dafalias, Y.F. and Herrmann L.R. (1986) Boundary surface plasticity, II: application to isotropic cohesive soils, *Journal of Engineering Mechanics,* ASCE, **112**(12), 1292-1318.

Edil, T.B. and Dhowian, A.W. (1981) At-rest lateral pressure of peat soils, *Journal of Geotechnical Engineering,* ASCE, **107**(2), 201- 217.

Edil, T.B. and den Haan, E.J. (1994) Settlement of peats and organic soils, In *Proceedings of the Conference on Vertical and Horizontal Deformations of Foundations and Embankments,* Texas, USA, eds. Albert T. Yeung and Guy Y. Felio, ASCE, Part 2, 1543-1572.

Forrest, J.B. and MacFarlane, I.C. (1969) Field studies of response of peat to plate loading, *Journal of Soil Mechanics and Foundation Division*, ASCE, **95**, SM4, 949-968.

Han, J. and Ye, S.L. (2001) Simplified method for consolidation rate of stone column reinforced foundations, *Journal of Geotechnical and Geoenvironmental Engineering***,** ASCE, **127**(7), 597-603.

Hansbo, S. (1981) Consolidation of fine-grained soils by prefabricated drains, In *Proceedings of 10th International Conference on Soil Mechanics and Foundation Engineering,* Stockholm*,* **3**, 677-682.

Hansbo, S. (1987) Design aspects of vertical drains and lime column installations, In *Proceedings of 9th Southeast Asian Geotechnical Conference,* Bangkok*,* Vol. 2(8), 1-12*,* Southeast Geotechnical Society.

Higo,Y ., Oka,F., Kodaka,T. and Kimoto,S. (2006), Three-dimensional strain localization of water-saturated clay and numerical simulation using an elasto- viscoplastic model, Philosophical Magazine, **86**, Nos.21-22, 3205-3240.

Hird, C.C., Pyrah, I.C., and Russell, D. (1992) Finite element modeling of vertical drains beneath embankments on soft ground, *Geotechniques, London,* **42**(3), 499-511.

Hobbs, N.B. (1986) Mire morphology and the properties and behavior of some British and foreign peats, *Quarterly Journal of Engineering Geology*, *London*, **19**, No. 1, 7-80.

Hobbs, N.B. (1987) A note on the classification of peat, *Geotechnique*, **37**(3), 405-407.

Hsi, J., Gunasekara, C., and Nguyen, V. (2005) Characteristics of soft peats, organic soils and clays, Colombo-Katunayake expressway, Sri Lanka, In *Ground Improvement-Case Histories,* eds. Indraratna, B. and Chu, J., **3,**681-722.

Indraratna, B., Balasubramaniam, A.S. and Balachandran, S. (1992) Performance of test embankment constructed to failure on soft marine clay, *Journal of Geotechnical Engineering,* ASCE, **118**(1), 12- 33.

Indraratna, B., Bamunuwita, C., Redana, C., Balasubramaniam, A.S. (2001) Modeling of vertical drains in soft clay, In *Proceedings of 3rd International Conference on Soft Soil Engineering,* Hong Kong, eds. Lee et al., 329-338, Balkema Publishers.

Jamiolkowski, M., Ladd, C.C., Germaine, J.T. & Lancellota, R. (1985) New developments in field and laboratory testing of soils, In *Proceedings of 11th* International *Conference on Soil Mechanics and Foundation Engineering*, San Francisco, 1, 57-153.

Jaky, J. (1948) State of stress at great depth, In *Proceedings of 2nd International Conference on Soil Mechanics and Foundation Engineering,* **1**, 103-107.

Jardine, R.J and Hight, D.W. (1987) The behavior and analysis of embankments on soft clay, *Embankments on Soft Ground,* 195-244, Public Works Research Center, Greece.

Johnson, S.J. (1970) Precompression for improving foundation soils, *Journal of Soil Mechanics and Foundation Division***,** ASCE, **96,** SM5, 111-44.

Jonas, E. (1964) Subsurface stabilization of organic silty clay by precompression, Journal *of Soil Mechanics and Foundation Division***,** ASCE, **90,** SM5, 363-376.

Kabbaj, M., Oka, F., Leroueil, S. and Tavenas, F. (1986) Consolidation of natural clays and laboratory testing, In *Consolidation of Soils: Testing and Evaluation,* ASTM Special Technical Publication 892, eds. R.N. Yong and F.C. Townsend , 378-404.

Kaliakin,V.N. and Dafalias, Y.F. (1990) Theoretical aspects of the elastoplastic-viscoplastic boundary surface model for cohesive soils, *Soils and Foundations*, **30-**3, 11-24.

Karunawardena, W.A. (2000) A Study of Consolidation Characteristics of Colombo Peat, In Proceedings *of 1st International Young Geotechnical Engineering Conference,* Southampton, United Kingdom.

Karunawardena, W.A. (2002) *Improvement of engineering properties of peat by preconsolidation – A comparative of field and laboratory test results,* Master Thesis, University of Moratuwa, Sri Lanka.

Karunawardena, W.A. and Kulatilaka, S.A.S. (2003) Field monitoring of a fill on peaty clay and its modeling, In *Proceedings of 12th Asian Regional Conference on Soil Mechanics & Geotechnical Engineering,* Singapore, eds. Lung et al., **1**, 159-162, World Scientific Publishing Co.

Katona, M.G. (1984) Evaluation of viscoplastic Cap model, *Journal of Geotechnical Engineering,* ASCE, **123**(5), 411- 421.

Ketheeswaravenayagam, R. (2006) *Finite element modeling of highway embankments over soft subsoil conditions,* Master Thesis, University of Moratuwa, Sri Lanka.

Kimoto, S. (2002) *Constitutive models for geomaterials considering structural changes and anisotropy*, Doctoral Thesis, Kyoto University, Japan.

Kimoto, S. and Oka, F. (2005) An elasto-viscoplastic model for clay considering destructuralization and consolidation analysis of unstable behavior, *Soils and Foundations*, **45**-2, 29-42.

Kimoto, S., Oka, F., Higo, Y. (2004) Strain localization analysis of elasto- viscoplastic soil considering structural degradation, In *Computer Methods in Applied Mechanics and Engineering*,**193**,2845-2866.

Kim, Y.T. and Leroueil, S. (2001) Modeling the viscoplastic behavior of clays during the consolidation: application to Berthierville clay in both laboratory and field conditions, *Canadian Geotechnical Journal,***38**(3),484-497.

Kogure, K. (1999) Consolidation and settlement of peat under loading, In *Proceedings of International Conference on Problematic Soils*, eds. Eiji Yanagisawa, Moroto, N. & Mitach , **2**, 817-831, Balkema, Rotterdam.

Kugan, R., Puswewala, U.G.A., Kulathilaka, S.A.S., and Peiris, T.A. (2004) Consolidation testing of peaty clay, In *Proceedings of Engineering Research Unit,* University of Moratuwa, Sri Lanka.

Kugan, R., Puswewala, U.G.A., Kulathilaka, S.A.S., and Peiris, T.A. (2003) Peaty clay improvement with prefabricated vertical drains, In *Proceedings of Engineering Research Unit,* University of Moratuwa, Sri Lanka.

Kulathilaka, S.A.S. (1999) Improvement of engineering properties of peat by precompression, In *Proceedings of 11th Asian Regional Conference on Soil Mechanics & Geotechnical Engineering,* Seoul, Korea, eds. Hong et al., **1,** 97-100, Balkema, Rotterdam.

Ladd, C.C., Foott, R., Ishihara, K., Schlosser, F. & Poulos, H.G. (1977) Stress-deformation and strength characteristics, In *Proceedings of 9th International Conference on Soil Mechanics and Foundation Engineering*, Tokyo, **2**, 421- 494.

Lambe, T. W. (1967) Stress path method, *Journal of Soil Mechanics and Foundation Division*, ASCE, **93**, SM6, 399-331.

Landva, A.O. (1980) Vane testing of peat, *Canadian Geotechnical Journal*, 17(1) 1-19.

Lavallee, J.G., St-Arnaud, G., Gervais, R. and Hammamji, Y. (1992) Stability of the Olga C test embankment, *ASCE Geotechnical Special Publication No. 31, Stability and Performance of Slopes and Embankments II,* Berkeley, California, eds. Seed and Boulanger, **2** ,1006-1021, ASCE, New York.

Laval Samson and Pierre La Rochlle (1972) Design and performance of an expressway constructed over peat by preloading, *Canadian Geotechnical Journal*, **9**, 447-446.

Lea, N.D. (1958) Notes on mechanical properties of peat, In *Proceedings 4th Muskeg Research Conference*, *Ottawa*, ACSSM, Technical Memo 54, 53-57, National Research Council of Canada.

Lea, N.D. and Brawner, C.O. (1963) Highway design and construction over peat deposits in Lower British Colombia, Highway Research Board, *Research Record* **7**, 1–33.

Leroueil, S. (1996) Compressibility of clays: Fundamental and practical aspects, *Journal of Geotechnical Engineering,* ASCE, **122**(7), 534- 543.

Leroueil, S. and Hight, D.W. (2003) Behavior and properties of natural soils and soft rocks, In *Characterization and Engineering Properties of Natural Soils*, eds. Tan et al., 29-254., Swets & Zeitlinger, Lisse, The Netherlands.

Li, A.L. and Rowe, R.K. (2001) Combined effects of reinforcement and prefabricated vertical drains on embankment performance, *Canadian Geotechnical Journal,* **38**(6), 1266-1282.

MacFarlance, I.C. and Radforth, N.W. (1965) A study of the physical behavior of peat derivatives under compression. In *Proceedings 10th Muskeg Research Conference*, *Ottawa*, 159, National Research Council of Canada.

Matsuo, M. and Kawamura, K. (1977) Diagram for construction control of embankment on soft ground, *Soils* and *Foundations*, **17**(3), 37-52.

Mesri, G. (1973) Coefficient of secondary compression, *Journal of Soil Mechanics and Foundation Division*, ASCE, **99**(1), 123-137.

Mesri, G., and Castro, A. (1987) The C_α/C_c concept and K_0 during secondary compression, Journal of Geotechnical Engineering, ASCE, 112(3), 230-247.

Mesri, G. and Choi, Y.K. (1979) Excess pore water pressure during consolidation, In *Proceedings of 6th Asian Regional Conference on Soil Mechanics & Foundation Engineering,* Taipei, Taiwan, **1**,151-154.

Mersi, G, and Choi, Y.K. (1985) Settlement analysis of embankments on soft clays, *Journal of Geotechnical Engineering,* ASCE, **111**(4), 441- 464.

Mesri, G., and Choi, Y.K. (1985) The uniqueness of the end-of-primary (EOP) void ratio-effective stress relationship, In *Proceedings of 11th International Conference on Soil Mechanics and Foundation Engineering*, San Francisco, **2**, 587- 590.

Mesri, G.. and Feng, T.W (1991) Surcharging to reduce secondary settlements, In *Proceedings of International Conference on Geotechnical Engineering for Coastal Development ,* Yokohama, **1**, 359-364.

Mesri, G. & Godlewski, P.M. (1977) Time- and stress-compressibility interrelationship, *Journal of Soil Mechanics and Foundation Division*, ASCE, **103**(5), 417-430.

Mesri, G. & Godlewski, P.M. (1979) Closure: Time- and stress-compressibility interrelationship, *Journal of Soil Mechanics and Foundation Division*, ASCE, **105**(1), 106.

Mesri, G. and Lo, D.O.K. (1991) Field performance of prefabricated vertical drains, In *Proceedings of International Conference on Geotechnical Engineering for Coastal Development (GEO-COAST),*Yokohama, Japan, ed. Port and Harbour Research Institute, **1**, 231-236.

Mesri, G., Shahien, M. & Feng, T.W. (1995) Compressibility parameters during primary consolidation, In *Proceedings of International Symposium on Compression and Consolidation of Clay soils- IS – Hiroshima's 95* , Japan , **2**, 1021-1037, Balkema, Rotterdam, The Netherlands.

Mesri, G., Stark, T.D., Ajlouni, M.A. & Chen, C.S. (1997) Secondary compression of peat with or without surcharging, *Journal of Geotechnical Engineering*, ASCE, **123**(5), 411- 421.

Mitchell, J.K. (1981) Soil improvement – State of the art report, In *Proceedings of 10th International Conference on Soil Mechanics and Foundation Engineering,* Stockholm*,* **4**, 509-565.

Mitchell, J.K. (1986) Practical problems from surprising soil behavior, *20th Terzaghi Lecture*, *Journal of Geotechnical Engineering,* ASCE, **112**(3), 255- 289.

Munasinghe, W.G.S. (2001) *Method for improvement of engineering properties of peat – A comparative study,* Master Thesis, University of Moratuwa, Sri Lanka.

Oka, F. (1981) Prediction of time dependent behavior of clay, In *Proceedings of 10th International Conference on Soil Mechanics and Foundation Engineering,* Stockholm*,* **1**, 215-218.

Oka, F. (2005) Computational modeling of large deformations and the failure of geomaterials, Theme lecture, In *Proceedings of 16th International Conference on Soil Mechanics and Geotechnical Engineering*, Osaka, **1**, 47-95.

Oka, F., Adachi, T., Okano, Y. (1986) Two-dimensional consolidation analysis using an elasto-viscoplastic constitutive equation, *International Journal for Numerical and Analytical Methods in Geomechanics*, **10**, 1-16.

Oka, F., Higo, Y., Kimoto, S. (2002) Effect of dilatancy on the strain localization of water-saturated elasto-viscoplastic soil, In *International Journal of Solids and Structures*, **39**, 3625-3647.

Oka, F., Yashima, A., Sawada, K., Aifantis, E.C. (2000) Instability of gradient- dependent elastoviscoplastic model for clay and strain localization, In *Computer Methods in Applied Mechanics and Engineering*, **183**,67-86.

O'Loughlin, C.D. and Lehane, B.M. (2001) Modeling the time-dependent compression of peat and organic soils, In *Proceedings of 3rd International Conference on Soft Soil Engineering,* Hong Kong, eds. Lee et al., 369-375, Balkema.

Olson, R. (1998) Settlements of embankments on soft clays, *Journal of Geotechnical and Geoenvironmental Engineering***,** ASCE, **124**(4), 278-288.

Perzyna, P. (1963) The constitutive equations for work-hardening and rate sensitive plastic materials, In *Proceedings of Vibrational Problems,* Warsaw*,* **4**(3), 281-290.

Rashid, M.A. and Brown, J.D. (1975) Influence of marine organic compounds on the engineering properties of a remolded sediment, *Engineering Geology*, **9**, 141-154.

Rixner, J.J., Kraemer, S.R., and Smith, A.D. (1986) *Prefabricated vertical drains-Vol. I: Engineering Guidelines,* Federal Highway Administration, Report No. FHWA-RD-86/169, Washington D.C.

Roscoe, K.H. and Burland , J.B. (1968) On the generalized stress-strain behavior of 'wet' clay, *Engineering plasticity* (Cambridge University Press), eds. Heyman, J. and Leckie, F.A., 535-609.

Roscoe, K. H., Schofield, A. N. and Thurairajah, A. (1963), Yielding of clays in states wetter than critical, *Geotechnique*, **13**(3), 211-240.

Roscoe, K.H. and Schofield, A.N. (1963) Mechanical behavior of an idealized 'wet' clay, In *Proceedings of the European Conference on Soil Mechanics and Foundation Engineering,* Wiesbaden*,* **1**, 47-54.

Samson, L. and La Rochelle, P. (1972) Design and performance of an expressway constructed over peat by preloading, *Canadian Geotechnical Journal,* **9,** 447-467.

Sekiguchi, H. and Ohta , H. (1977) Induced anisotropy and time dependency in clays, Constitutive Equation of Soils, In *Proceedings of Specialty Session 9, 9th* International *Conference on Soil Mechanics and Foundation Engineering,* Tokyo, 306-315.

Sekiguchi, H., Shibata, T., Fujimoto, A., and Yamaguchi, H. (1986) A macro-element approach to analyzing the plane strain behavior of soft foundation with vertical drains, In *Proceedings of 31st Japan National Conference on Geotechnical Engineering,* 111-116 (in Japanese), Japanese Soil Mechanics and Foundation Engineering Society, Tokyo.

Suklje, L. (1969) *Rheological Aspects of Soil Mechanics,* Wiley-Interscience, A division of John Wiley & Sons Ltd.

Tamura, T. (1979) *Theory of multi-dimensional consolidation and numerical analysis of non-linear soil problem*, Doctoral Thesis, Kyoto University, Japan.

Tan, S.A. and Oo, K.K. (2005) Finite element modeling of stone columns – a case history, In *Proceedings of 16th International Conference on Soil Mechanics and Foundation Engineering*, Osaka, **3**, 1425- 1428.

Tan, Y.X. and Imai, G. (1995) A constitutive relation with creep and its application to numerical analysis of one dimensional consolidation, In *Proceedings of International Symposium on Compression and Consolidation of Clayey Soils,* eds. H. Yoshikuni and O. Kusakabe, **1**, 465-472, Balkema.

Taylor, D.W. (1948) *Fundamentals of Soil Mechanics*, Wiley, New York.

Vermeer, P.A. and Neher, H.P. (1999) A soft soil model that accounts for creep, In *Proceedings of the International Symposium "Beyond 2000 in Computational Geotechnics"* Amsterdam, eds. Brinkgreve R.B.J, 249-261, Balkema.

Yamaguchi, H., Ohira, Y., Kogure, K. and Mori, S. (1985) Undrained shear characteristics of normally consolidated peat under triaxial compression and extension conditions, *Soils and Foundations*, **25** (3), 1-18.

Yin, J.-H. and Graham, J. (1989) Viscous-elastic-plastic modeling of one-dimensional time-dependent behavior of clays. *Canadian Geotechnical Journal*, **26**, 199-209.

Zeng, G.X., Xie, K.H. and Shi, Z.Y. (1987) Consolidation analysis of sand drained ground by FEM, In *Proceedings of 8th Asian Regional Conference on Soil Mechanics & Geotechnical Engineering,* Kyoto, Japan, **1,**139-142.

Zhang, L. (1999) Settlement patterns of soft soil foundations under embankments, *Canadian Geotechnical Journal,* **36**(4), 774-781.

Appendix A1

Finite Element Formulation for an Infinitesimal Strain Analysis

The basic equation for incremental boundary value problems, based on the infinitesimal deformation theory, can be expressed as

$$\dot{\sigma}_{ij,j} + \dot{\overline{F}}_i^b = 0 \quad \text{in} \quad V \tag{A1.1}$$

where σ_{ij} is the total stress tensor and $\overline{F}_i^b$ is the body force vector for problem domain V. The superimposed dots denote the time derivatives.

Effective stress tensor σ'_{ij} and its rate form $\dot{\sigma}'_{ij}$ are defined as

$$\sigma_{ij} = \sigma'_{ij} + u_w \delta_{ij} \tag{A1.2}$$

$$\dot{\sigma}_{ij} = \dot{\sigma}'_{ij} + \dot{u}_w \delta_{ij} \tag{A1.3}$$

where σ_{ij} is the total stress tensor and u_w is the pore water pressure.

Consider a bounded domain with the Dirichlet condition on a part of the boundary and the Neumann condition on its complement.

$$\Gamma = \Gamma_p + \Gamma_u \tag{A1.4}$$

On the stress boundary (Neumann condition)

$$\dot{\sigma}_{ij} n_j = \dot{\overline{T}}_i \quad \text{on} \quad \Gamma_p \tag{A1.5}$$

On the displacement boundary (Dirichlet condition)

$$\dot{u}_i = \dot{\overline{u}}_i \quad \text{on} \quad \Gamma_u \tag{A1.6}$$

where n_i is the i^{th} component of the unit vector normal to the surface.

Applying the principal of virtual work to the equilibrium equation (Eq.A1.1) and incorporating the relationships mentioned in the above equations, it is possible to obtain the following:

$$\int_V \dot{\sigma}_{ij}\delta\dot{\varepsilon}_{ij}dV = \int_V \dot{\sigma}'_{ij}\delta\dot{\varepsilon}_{ij}dV + \int_V \dot{u}_w\delta_{ij}\delta\dot{\varepsilon}_{ij}dV = \int_V \dot{\bar{F}}_i^b\delta\dot{u}_i dV + \int_\Gamma \dot{\bar{T}}_i\delta\dot{u}_i d\Gamma \tag{A1.7}$$

where $\delta\dot{\varepsilon}_{ij}$ is the virtual strain rate tensor and $\delta\dot{u}_i$ is the virtual displacement rate vector. In the finite element formulation, Eq. (A1.7) is written in matrix-form as

$$\begin{aligned}\int_V \{\delta\dot{\varepsilon}\}^T\{\dot{\sigma}\}dV &= \int_V \{\delta\dot{\varepsilon}\}^T\{\dot{\sigma}'\}\,dV + \int_V \{\delta\dot{\varepsilon}\}^T\{\dot{u}_w\}dV \\ &= \int_V \{\delta\dot{u}\}^T\left\{\dot{\bar{F}}^b\right\}dV + \int_\Gamma \{\delta\dot{u}\}^T\left\{\dot{\bar{T}}\right\}d\Gamma\end{aligned} \tag{A1.8}$$

In the above equation, total stress rate vector $\{\dot{\sigma}\}$, effective stress rate vector $\{\dot{\sigma}'\}$, and strain rate vector $\{\dot{\varepsilon}\}$ are defined as follows:

$$\{\dot{\sigma}\} = \{\dot{\sigma}_{xx}\ \ \dot{\sigma}_{zz}\ \ \dot{\sigma}_{xz}\}^T,\ \{\dot{\sigma}'\} = \{\dot{\sigma}'_{xx}\ \ \dot{\sigma}'_{zz}\ \ \dot{\sigma}'_{xz}\}^T,\ \{\dot{\varepsilon}\} = \{\dot{\varepsilon}_{xx}\ \ \dot{\varepsilon}_{zz}\ \ \dot{\gamma}_{xz}\}^T \tag{A1.9}$$

In Eq. (A1.8), $\{\dot{u}\}$ is the displacement rate vector, $\left\{\dot{u}^*\right\}$ is the nodal displacement rate, and $\{\dot{u}_w\}$ is the pore pressure rate vector.

$$\{\dot{u}\} = \{\dot{u}_{xx}\ \ \dot{u}_{zz}\}^T\ ,\quad \left\{\dot{u}^*\right\} = \left\{\dot{u}^*_{xx}\ \ \dot{u}^*_{zz}\right\}^T\ ,\quad \{u_w\} = \{\dot{u}_w\ \ \dot{u}_w\ \ 0\}^T \tag{A1.10}$$

The term $\int_V \{\delta\dot{\varepsilon}\}^T\{\dot{u}_w\}dV$ in Eq. (A1.8) can be expressed as

$$\int_V \{\delta\dot{\varepsilon}\}^T\{\dot{u}_w\}dV = \int_V \{\delta\dot{\varepsilon}_{xx}, \delta\dot{\varepsilon}_{zz}, \delta\dot{\gamma}_{xz}\}\begin{Bmatrix}\dot{u}_w\\ \dot{u}_w\\ 0\end{Bmatrix}dV = \{\dot{u}_w\}\int_V \delta\dot{\varepsilon}_v\,dV \tag{A1.11}$$

which gives

$$\int_V \{\delta\dot{\varepsilon}\}^T\{\dot{\sigma}'\}dV + \{\dot{u}_w\}\int_V \delta\dot{\varepsilon}_v\,dV = \int_V \{\delta\dot{u}\}^T\left\{\dot{\bar{F}}^b\right\}dV + \int_\Gamma \{\delta\dot{u}\}^T\left\{\dot{\bar{T}}\right\}d\Gamma \tag{A1.12}$$

Displacement rate vector $\{\dot{u}\}$ in the element is approximated by shape function $[N]$ as

$$\{\dot{u}\} = [N]\left\{\dot{u}^*\right\}\ ,\quad \{\delta\dot{u}\} = [N]\left\{\delta\dot{u}^*\right\} \tag{A1.13}$$

Similarly, strain rate vector $\{\dot{\varepsilon}\}$ and volumetric strain rate $\{\varepsilon_v\}$ in any element are given by

$$\{\dot{\varepsilon}\} = [B]\{\dot{u}^*\} \quad , \quad \{\delta\dot{\varepsilon}\} = [B]\{\delta\dot{u}^*\} \tag{A1.14}$$

$$\dot{\varepsilon}_v = \{B_v\}^T \{\dot{u}^*\} \quad , \quad \delta\dot{\varepsilon}_v = \{B_v\}^T \{\delta\dot{u}^*\} \tag{A1.15}$$

where $[B]$ is the matrix which transforms the nodal displacement into strain and $\{B_v\}$ is the vector which transforms the nodal displacement into volumetric strain.

Using the nonlinear stress-strain relations of the geomaterials outlined in Section (3.2.1), the following relationship between the effective stress rate vector and the strain rate vector is established:

$$\{\dot{\sigma}\} = [D]\{\dot{\varepsilon}\} - \{\dot{\sigma}^*\} \tag{A1.16}$$

in which $[D]$ is the elastic modulus and $\{\dot{\sigma}^*\}$ is the relaxation stress vector given as

$$\{\dot{\sigma}^*\} = [D]\{\dot{\varepsilon}^{vp}\} \tag{A1.17}$$

Substituting Eqs. (A1.13)-(A1.16) into Eq. (A1.12) and dividing by $\{\delta\dot{u}^*\}^T$ yields

$$[K]\{\dot{u}^*\} + \dot{u}_w\{K_v\} = \{\dot{F}^*\} + \{\dot{\bar{F}}\} + \{\dot{F}^b\} \tag{A1.18}$$

where

$$[K] = \int_V [B]^T [D][B]\, dV \tag{A1.19}$$

$$\{K_v\} = \int_V \{B_v\}\, dV \tag{A1.20}$$

$$\text{relaxation force} \sim \{\dot{F}^*\} = \int_V [B]^T \{\dot{\sigma}^*\} dV \tag{A1.21}$$

$$\text{external force} \sim \{\dot{\bar{F}}\} = \int_\Gamma [N]^T \{\dot{\bar{T}}\} d\Gamma \tag{A1.22}$$

$$\text{body force} \sim \{\dot{F}^b\} = \int_V [N]^T \{\dot{\bar{F}}^b\} d\Gamma \tag{A1.23}$$

The pore water pressure increment in the equilibrium equation (Eq. A1.18) can be transformed by the following finite difference technique:

$$\dot{u}_w = \frac{u_{w,t+\Delta t} - u_{w,t}}{\Delta t} \tag{A1.24}$$

Similarly, the derivative of the displacement can be written as

$$\dot{u}^* = \frac{\Delta u^*}{\Delta t} \tag{A1.25}$$

Using Eqs. (A1.24) and (A1.25), the final weak-form of the equilibrium equation becomes

$$[K]\{\Delta u^*\} + [K_v]\{u_{w,t+\Delta t}\} = [K_v]\{u_{w,t}\} + \Delta t\{Q\} \tag{A1.26}$$

where

$$\{Q\} = \{\dot{F}^*\} + \{\dot{\bar{F}}\} + \{\dot{F}^b\} \tag{A1.27}$$

Next, the equation of continuity is formulated. This is derived from the equation for the balance of mass and the equation for the motion of the fluid phase (Darcy`s law).

Assuming the net outflow per unit time from region V is equal to the volumetric strain of the same region per unit time, the following relationship can be derived:

$$\dot{\varepsilon}_v = \dot{\varepsilon}_{ii} = \frac{\partial v_i}{\partial x_i} = div\{\mathrm{v}\} \tag{A1.28}$$

where ε_v is the volumetric strain assumed to be positive in the volumetric compression and v_i is the velocity vector.

From Darcy's law, a flow velocity vector $\{\mathrm{v}\}$ can be expressed as

$$\{\mathrm{v}\} = -k\frac{\partial h}{\partial\{\mathrm{x}\}} \tag{A1.29}$$

where k is the coefficient of permeability and h is the total head defined as

$$h = \frac{u_w}{\gamma_w} + \frac{u_s}{\gamma_w} + z \tag{A1.30}$$

in which u_w is excess pore water pressure, u_s is static water pressure, z is potential head and γ_w is unit weight of water.

Since, $u_s / \gamma_w + z$ is constant, substituting Eq. (A1.30) for Eq. (A1.29), the flow velocity vector $\{\mathrm{v}\}$ is as follows:

$$\{\mathrm{v}\} = -\frac{k}{\gamma_w}\frac{\partial u_w}{\partial\{\mathrm{x}\}} \qquad (v_i = -\frac{k}{\gamma_w}\frac{\partial u_w}{\partial x_i}) \tag{A1.31}$$

As a result, the following continuum equation can be obtained:

$$\dot{\varepsilon}_v = \frac{\partial v_i}{\partial x_i} = -\frac{k}{\gamma_w}\frac{\partial}{\partial x_i}\left(\frac{\partial u_w}{\partial x_i}\right) \tag{A1.32}$$

Integrating Eq. (A1.28) in elemental region V^e and using the Gaussian divergence theory, the volumetric strain in each element can be calculated.

$$\int_{V^e} \dot{\varepsilon}_v dV = \int_{V^e} div\{\mathrm{v}\}dV = \int_{\Gamma^e} \{\mathrm{v}\}^T \{\mathrm{n}\}d\Gamma = \int_{\Gamma^e} v_j n_j d\Gamma \tag{A1.33}$$

Under 2D plane strain conditions, the above equation can be expanded to

$$\int_{V^e} \dot{\varepsilon}_v \, dV = \int_{\Gamma^e} v_j n_j d\Gamma = \sum_{i=1}^{4} \int_{b_i} (v_x^i n_x^i + v_y^i n_y^i) db \tag{A1.34}$$

in which i is the number of elements next to the element under consideration.

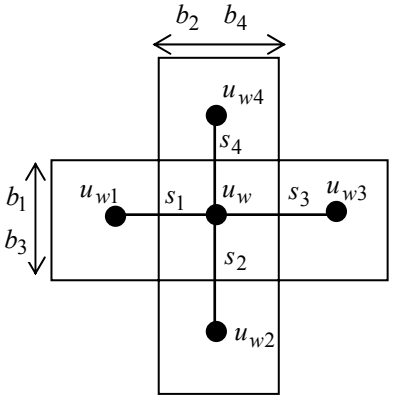

Fig. A1.1: Drainage distance used to evaluate the rate of flow (Tamura 1979)

Using the implicit backward finite difference scheme, the excess pore water pressure indicated on the right-hand side of Eq. (A1.34) is approximated. In the approximation, the pore water pressure is defined at the center of each element. It can be assumed to flow

between the centers of the neighboring two elements due to the excess pore water pressure. In case all elements in V are rectangular in shape, Eq. (A1.34) can be simply expressed as

$$\int_V div\{\mathrm{v}\}dV = \beta u_{w,t+\Delta t} - \sum_{i=1}^{4} \beta_i u_{wi,t+\Delta t} \tag{A1.35}$$

where

$$\beta_i = \frac{k}{\gamma_w}\frac{b_i}{s_i} \quad , \quad \beta = \sum_{i=1}^{4} \beta_i \tag{A1.36}$$

On the other hand, the left-hand side of Eq. (A1.34) can be written as

$$\int_{V^e} \dot{\varepsilon}_v \, dV = \frac{1}{\Delta t}\{K_v\}^T \left\{\Delta u^*\right\} \tag{A1.37}$$

From Eqs. (A1.35) and (A1.37), the continuity equation can be formed as follows:

$$[K_v]^T \left\{\Delta u^*\right\} = \Delta t \beta u_{w,t+\Delta t} - \sum_{i=1}^{4} \beta_i u_{wi,t+\Delta t} \tag{A1.38}$$

The discretized form of the continuity equation finally becomes

$$[K_v]^T \left\{\Delta u^*\right\} + \Delta t\{\beta\}\left\{u_{w,t+\Delta t}\right\} = \{0\} \tag{A1.39}$$

Combining Eqs. (A1.26) and (A1.39), the generalized force-stiffness formulation for the infinitesimal strain analysis is obtained as

$$\begin{bmatrix} [K] & [K_v] \\ [K_v]^T & \beta \end{bmatrix} \begin{Bmatrix} \left\{\Delta u^*\right\} \\ \left\{u_{w,t+\Delta t}\right\} \end{Bmatrix} = \begin{Bmatrix} \{K_v\}u_{w,t} + \{\Delta Q\} \\ \sum_{i=1}^{4} \beta_i u_{wi,t+\Delta t} \end{Bmatrix} \tag{A1.40}$$

Appendix A2

Evaluation of Equivalent Vertical Permeability for PVD-improved Subsoil

The evaluation of equivalent vertical permeability for PVD-improved subsoil proposed by Chai et al. (2001) can be derived as follows.

Using Carrillo's theoretical solution (1942), the effects of vertical and radial drainage can be combined as

$$U_{vr} = 1 - (1 - U_v)(1 - U_r) \tag{A2.1}$$

U_{vr} = average degree of consolidation of PVD-improved subsoil

U_r = average degree of consolidation due to radial drainage

U_r = average degree of consolidation due to vertical drainage

According to Hansbo's solution (1981), which was derived from the equal vertical strain assumption and disregards the vertical drainage of natural subsoil,

$$U_r = 1 - \exp\left(-\frac{8}{\mu} T_h\right) \tag{A2.2}$$

where T_h is the time factor and can be expressed as

$$T_h = C_h t / D_e^2 \tag{A2.3}$$

in which

C_h = coefficient of consolidation in the horizontal direction

D_e = diameter of the unit cell

t = time

The value of μ can be expressed as

$$\mu = \ln\frac{n}{s} + \frac{k_h}{k_s}\ln(s) - \frac{3}{4} + \pi\frac{2l^2 k_h}{3q_w} \tag{A2.4}$$

where

$n = \dfrac{D_e}{d_w}$ d_w = diameter of drain $s = \dfrac{d_s}{d_w}$ d_s = diameter of the smear zone

k_h and k_s = horizontal hydraulic conductivity of natural and smear zones

l = drainage path

q_w = discharge capacity of PVD

The average degree of vertical consolidation (U_v) is calculated using an approximation of Terzaghi's solution

$$U_v = 1 - \exp(-C_d T_v) \tag{A2.5}$$

where T_v is the time factor for the vertical consolidation

$$T_v = C_v t / H^2 \tag{A2.6}$$

in which

C_v = coefficient of consolidation in the vertical direction

H = vertical drainage length

c_d = constant that can be determined by curve fitting by Terzaghi's exact solution and the approximation solution used here.

By substituting the values from Eqs. (A2.2) - (A2.6) into Eq. (A2.1)

$$U_{vr} = 1 - \exp\left(-\frac{8}{\mu}T_h\right) + 1 - \exp(-C_d T_v) - \left(1 - \exp\left(-\frac{8}{\mu}T_h\right)\right)\left(1 - \exp(-C_d T_v)\right)$$

$$= 1 - \exp\left(-\frac{8}{\mu}T_h\right)\exp(-C_d T_v) \tag{A2.7}$$

Assuming $U_{vr} = 1 - \exp(-C_d T_{vr})$, Eq. (A2.7) can be written as

$$C_d T_{vr} = \frac{8}{\mu} T_h + C_d T_v \tag{A2.8}$$

The following relationships also exist:

$$T_v = C_v t / H^2 , \quad T_h = C_h t / D_e^2 \ , \ T_{vr} = C_{vr} t / H^2 \tag{A2.9}$$

$$C_v = k_v / m_v \gamma_w \ , \quad C_h = k_h / m_h \gamma_w \ , \ C_{vr} = k_{ve} / m_{vr} \gamma_w \tag{A2.10}$$

Assuming $m_v = m_h = m_{vr}$,

$$k_{ve} = \frac{8H^2}{C_d \mu D_e^2} k_h + k_v \tag{A2.11}$$

When C_d = 3.2 (Chai et al. 2001),

$$k_{ve} = \left(1 + \frac{2.5H^2}{\mu D_e^2} \frac{k_h}{k_v} \right) k_v \tag{A2.12}$$